2014

Magnetic phase transitions and novel materials for magnetocaloric effect

Muhamad Faiz Md Din
University of Wollongong

Magnetic Phase Transitions and Novel Materials for Magnetocaloric Effect

This thesis is presented as part of the requirements for the

Award of the Degree of Doctor of Philosophy

from the

University of Wollongong

by

Muhamad Faiz Md Din

BEng (Hons), MSc

Institute for Superconducting and Electronic Materials

October 2014

DECLARATION

I, Muhamad Faiz Md Din, declare that this thesis, submitted in partial fulfilment of the requirements for the award of Doctor of Philosophy, in the Institute for Superconducting & Electronic Materials (ISEM), Faculty of Engineering, University of Wollongong, Australia, is wholly my own work unless otherwise referenced or acknowledged. This document has not been submitted for a qualification at any other academic institution.

Muhamad Faiz Md Din

October, 2014

ACKNOWLEDGEMENTS

First and foremost, I give gratitude to the Almighty Lord for His mercy and blessing on me to accomplish this study in spite of the numerous constraints that I encountered.

I am deeply would like to express my deepest gratitude to my principal supervisor Dr Jianli Wang, for giving me the opportunity to embark on this PhD study with his intellectual guidance, invaluable support, continual encouragement, and patience throughout this work. His inspirational knowledge and understanding of physics accompany with continuous support of any idea or suggestion always finding the best solution in my ramblings situation. To be your student has been a real pleasure for me. I also would like to express my deepest gratitude to my co-supervisors, Prof. Shi Xue Dou and Dr Rong Zeng for their invaluable advice and supervision for providing me with the guidance and encouragement to finish this thesis. I thank you for your patience and kindness and most importantly your willingness to share your knowledge during my PhD study.

In addition, I have been very privileged to get the opportunity to collaborate with many other great scientists as Prof. Shane Kennedy from the Bragg Institute, Australian Nuclear Science and Technology Organisation (ANSTO), Prof. Stewart Campbell from University of New South Wales Canberra at the Australian Defence Force Academy (UNSW@ADFA) and Associate Prof. Zhen Xiang Cheng from University of Wollongong. I'm much appreciated for sacrificing time out of your incredibly busy schedule to perform experiments with me, analyse data and correct numerous manuscripts as well as this thesis. I would also like to thank the following scientists, Dr Maxim Adveev (ANSTO), Dr Andrew Studer (ANSTO) and Dr Qinfen Gu (Australian Synchrotron) during valuable experiment with them.

I would like to thank the Malaysian Government, especially the Ministry of Education Malaysia for the scholarship support during my studies at the University of Wollongong. I am also grateful to National Defence University of Malaysia for granting me study leave and a generous stipend for my family during my doctoral studies in Australia. I am also grateful to University of Wollongong for providing me High Degree Research (HDR) top-up scholarship.

I wish to express appreciation for the assistance I received from all the other student and staff at Institute of Superconducting and Electrnic Material (ISEM), especially Dr Jotish Debnath, Dr Precious Shamba, Dr Germanas Peleckis, Dr Xun Xu, Mr. Rob Morgan, and Miss Crystal Longin for their useful advice and technical assistance. Special thanks also go to Dr. Tania Silver for critical reading of my manuscript and this thesis. Many thanks should also go to my best friend Fathul Hakim, Mohammad Ismail, Zahir Hassan, Azman Ahmad and Taufik Jusoh for providing the support and friendships.

Lastly and most importantly, I wish to express my gratitude thanks to my lovely wife, Noor Fadzilah Mohamed Sharif, my newborn son, Danish Iman and my parents Md Din Zainal Abidin and Wan Samsiah Wan Ahmed for their prayers and moral support. Their patience, encouragement, and understanding enabled me to really consistently concentrate on my PhD study, as was greatly appreciated.

Abstract

The magnetic and structural properties of some selected magnetocaloric materials such as La (Fe, Si)$_{13}$ series compounds, RMn_2X_2 series (R=rare earth and X=Si or Ge) compounds and typical MM′X series (M, M′ = transition metal, X = Si, Ge, Sn) have been systematically investigated in this thesis with total 7 chapters being included. After a general introduction in Chapter 1, the description of theoretical aspects of the research and experimental techniques are given in Chapters 2 and 3, respectively.

In Chapter 4, the investigation on structure and magnetic properties of the $La_{0.7}Pr_{0.3}Fe_{11.4-x}Cu_xSi_{1.6}$ and $La_{0.7}Pr_{0.3}Fe_{11.4-x}Cr_xSi_{1.6}$ compounds is presented. Cu substitution for Fe in $La_{0.7}Pr_{0.3}Fe_{11.4-x}Cu_xSi_{1.6}$ (x = 0, 0.06, 0.12, 0.23, 0.34) leads to a reduction in hysteresis loss, a decrease in magnetic entropy change but an increase in Curie temperature (T_C). The influences of annealing processes at different temperatures on T_C, magnetic hysteresis, and the magnetocaloric effect (MCE) of $La_{0.7}Pr_{0.3}Fe_{11.4}Si_{1.6}$ are also investigated in detail. It has been found that a short-time and high temperature annealing process has benefits for the formation of the $NaZn_{13}$ types as phase compared to a long-time and low temperature annealing process.

Furthermore, the effects of substitution Fe by Cr in $NaZn_{13}$-type $La_{0.7}Pr_{0.3}Fe_{11.4-x}Cr_xSi_{1.6}$ (x=0, 0.06, 0.12, 0.26, and 0.34) compounds have been investigated by high intensity of X-ray and neutron diffraction, scanning electron microscopy, specific heat, and magnetization measurement. It has been found that a substitution of Cr for Fe in this compounds leads to a decrease in the lattice parameter *a* at room temperature and a variation on T_C. While the first order nature of magnetic phase transition around T_C does not change with increasing Cr

content up to x=0.34. High intensity X-ray and neutron diffraction study at variable temperatures for highest Cr concentration x=0.34 confirmed the presence of strong magneto-volume effect around T_C and indicated the direct evidence of coexistence of two magnetic phases across magnetic transition as characteristic of first order nature. The values of $-\Delta S_M$ around T_C found to decrease from 17 J $kg^{-1}K^{-1}$ for x=0 to 12 J $kg^{-1}K^{-1}$ for x=0.06 and then increases with further increasing Cr content up to 17.5 J $kg^{-1}K^{-1}$ for x=0.34 under a change of 0–5 T magnetic field. The relative cooling power (RCP) also indicated the similar behaviour which is decrease from 390 J kg^{-1} for x=0 to 365 J kg^{-1} for x=0.06 at the beginning and then increases up to 400 J kg^{-1} for x=0.34 at the same field applied.

Chapter 5 describes the investigation on magnetic behaviour and magnetocaloric effects of RMn_2X_2-based materials (R=rare earth and X=Si or Ge). The RMn_2X_2 series has attracted significant interest in recent years due primarily to their natural layered structure in which R and Mn atoms lie in alternate layers, separated by layers of X atoms. The strong dependence of the Mn–Mn magnetic exchange interaction on the intralayer near neighbour distance, and the interplay between the magnetism of the Mn and R layers lead to a fascinating arrangement of magnetic phases for these compounds. Firstly, in order to clarify the effect of substitution Mn with other transition metal (T) in $NdMn_2Si_2$ compound, structural and magnetic properties of the intermetallic compounds $NdMn_{2-x}T_xSi_2$ (T=Ti, Cr, Cu and V) have been studied.

The Curie temperature and N´eel temperature of $NdMn_2Si_2$ decrease from T_C = 36 K and T_N = 380 K to T_C = 14 K and T_N = 360 K, respectively, on substitution of Ti (x = 0.3*)* for Mn. The magnetocaloric effect around T_C, has been investigated in detail. Under a change of magnetic field of 0–5 T, the maximum value of the magnetic entropy change is 27 J $kg^{-1}K^{-1}$

for x = 0, reducing to 15.3 J $kg^{-1}K^{-1}$ for x = 0.1 and 10 J $kg^{-1}K^{-1}$ for x = 0.3; importantly, no thermal or field hysteresis losses occur with increase in Ti concentration. Combined with the lack of any hysteresis effects, these findings indicate that $NdMn_{1.9}Ti_{0.1}Si_2$ compound offers potential as a candidate for magnetic refrigerator applications in the temperature region below 35 K.

In substitution Mn with Cr in $NdMn_{2-x}Cr_xSi_2$ compound, a giant magnetocaloric effect has been observed around Curie temperature, T_C~42 K, in $NdMn_{1.7}Cr_{0.3}Si_2$ with no discernible thermal and magnetic hysteresis losses. Detailed study shown that below 400 K, three magnetic phase transitions take place around 380 K, 320 K and 42 K. High resolution synchrotron and neutron powder diffraction (10–400 K) analysis confirmed the magnetic phases transitions as follows: T_N^{intra}~380 K denotes the transition from paramagnetism to intralayer antiferromagnetism (AFl), T_N^{inter}~320 K represents the transition from the AFl structure to the canted antiferromagnetic spin structure (AFmc), while T_C~42 K denotes the first order magnetic transition from AFmc to canted ferromagnetism (Fmc+F(Nd)) due to ordering of the Mn and Nd sub-lattices. The maximum values of the magnetic entropy change and the adiabatic temperature change, around T_C for a field change of 5 T are evaluated to be $-\Delta S_M$~15.9 J $kg^{-1}K^{-1}$ and ΔT_{ad}~5 K, respectively. The first order magnetic transition associated with the low levels of hysteresis losses (thermal <~0.8 K; magnetic field < ~0.1 T) in $NdMn_{1.7}Cr_{0.3}Si_2$ offers potential as a candidate for magnetic refrigerator applications in the temperature region below 45 K.

Furthermore, the structural and magnetic properties of $NdMn_{2-x}Cu_xSi_2$ compounds (x=0–1.0) also have been investigated. Substitution of Cu for Mn leads to an increase in the lattice parameter *a* but a decrease in *c* at room temperature. Two magnetic phase transitions have

been found for $NdMn_{2-x}Cu_xSi_2$ compounds with T_N for the antiferromagnetic ordering of Mn-sublatttice and T_C for the Nd-sublattice ferromagnetic ordering. T_C increases significantly with increasing Cu content from 36 K at x=0 to 100 K at x=1.0. Moreover, it is found that the order of magnetic phase transition around T_C also changes from first order at x<0.6 to second order transition for x≥0.6. The spontaneous magnetization found to decrease with the increase in Cu concentration which can be understood in the term of the dilution effect of Cu for Mn. The values of $-\Delta S_M$ around T_C decrease with increasing x from 27 J $kg^{-1}K^{-1}$ for x=0 to 0.5 J $kg^{-1}K^{-1}$ for x=1.0 under 0–5 T field. Refinement of neutron diffraction patterns for x=0.2 confirms the magnetic states detected by magnetic study and also indicates that the lattice constants *a* and *c* show a distinct variation around T_C. Moreover, further study on substitution Mn with V in $NdMn_2Si_2$ compound shown the similar behaviour with the replacement Mn by Ti. Both T_C and T_N are found decrease with increasing V concentration accompany with decreasing magnetic entropy change as discussed in more detail in Chapter 5.

Secondly, we carry out investigations of the $Pr_{1-x}Y_xMn_2Ge_2$ magnetic phase diagram as functions of both composition and Mn–Mn spacing using X-ray and neutron diffraction, magnetization and differential scanning calorimetry measurements. $Pr_{1-x}Y_xMn_2Ge_2$ exhibits an extended region of re-entrant ferromagnetism around x=0.5 with re-entrant ferromagnetism at T_C^{Pr}~ 50 K for $Pr_{0.5}Y_{0.5}Mn_2Ge_2$. The entropy values $-\Delta S_M$ around the ferromagnetic transition temperatures T_C^{inter} from the layered antiferromagnetic AFl structure to the canted ferromagnetic structure Fmc (typically T_C^{inter}~330–340 K) have been derived for $Pr_{1-x}Y_xMn_2Ge_2$ with x=0.0, 0.2, and 0.5 for ΔB=0–5 T. The changes in magnetic states due toY substitution for Pr are also discussed in terms of chemical pressure, external pressure, and electronic effects.

Thirdly, the structural and magnetic properties of $CeMn_2Ge_{2-x}Si_x$ compounds with Si concentrations in the range x = 0.0–2.0 have been investigated. Substitution of Ge with Si leads to a monotonic decrease of both *a* and *c* along with concomitant contraction of the unit cell volume and significant modifications to the magnetic states - a crossover from ferromagnetism at room temperature for Ge-rich compounds to antiferromagnetism for Si-rich compounds. The magnetic phase diagram has been constructed over the full range of $CeMn_2Ge_{2-x}Si_x$ compositions and co-existence of ferromagnetism and antiferromagnetism has been observed in both $CeMn_2Ge_{1.0}Si_{1.0}$ and $CeMn_2Ge_{0.8}Si_{1.2}$ compounds with novel insight provided by high resolution X-ray synchrotron radiation studies. This study has enabled the large variety of magnetic structures and magnetic phase transitions of $CeMn_2Ge_{2-x}Si_x$ compounds and their related magnetic properties to be determined by controlling chemical concentration.

Finally in Chapter 6, the MnCoGe-based materials, as a typical MM′X (M, M′ = transition metal, X = Si, Ge, Sn) compound which undergoes a second-order phase transition as well as a crystallographic phase transition from the low temperature orthorhombic TiNiSi-type to the high temperature hexagonal Ni_2In-type structure have been studied. An investigation on substituting Ge by other metalloids in $MnCoGe_{1-x}T_x$ compounds (T = Al and Si) has been implemented in this thesis and it was found that an appropriate T concentration successfully shifted the structural change and magnetic phase transition into the temperature range of interest, leading to the attainment of a high contribution to the giant magnetocaloric effect (GMCE). $MnCoGe_{1-x}T_x$ provides the best example for control of the temperature window in order to investigate the effects of the structural and magnetic transition on the total entropy change, providing an excellent vehicle for investigation of the field-induced martensitic transformation in GMCE materials. Thus, in an effort to understand the nature of the

magnetic transition in $MnTiGe_{0.97}Al_{0.03}$, critical exponent analysis in the vicinity of the ferromagnetic (FM)–paramagnetic (PM) region has been performed. The outcomes revealed that this material undergoes a structural transition at ~ 420 K as well as a second-order ferromagnetic–paramagnetic transition at ~ 350 K. Finally, a temperature dependent neutron diffraction experiment has been performed and confirmed that there is a coupling of the structural transition and the magnetic phase transition.

Structural, magnetic and magnetocaloric properties of the $Mn_{1-x}Ti_xCoGe$ also have been investigated using X-ray diffraction, DC magnetization and neutron diffraction measurements in order to define the effect of substitution Mn with Ti in MnCoGe compound. Substitution of Ti for Mn in the parent MnCoGe compound leads to a significant reduction in both structure change temperature, T_{str} (from ~ 645 K for MnCoGe to ~ 235 K for $Mn_{0.94}Ti_{0.06}CoGe$ and ~ 178 K for $Mn_{0.9}Ti_{0.1}CoGe$) and Curie temperature, T_C (from ~ 345 K for MnCoGe to ~ 270 K for $Mn_{0.94}Ti_{0.06}CoGe$ and ~ 280 K for $Mn_{0.9}Ti_{0.1}CoGe$). Moreover, all the critical exponents for $Mn_{0.94}Ti_{0.06}CoGe$ and $Mn_{0.9}Ti_{0.1}CoGe$ fulfil the Widom scaling law. The validity of the calculated critical exponents was confirmed by the scaling equation, with the magnetization, field, and temperature data obtained below and above T_C collapsing onto two different curves. Thus, the scaling of the magnetization data above and below T_C was obtained using the respective critical exponents, and the consistency of the values of the critical exponents determined by different methods confirm that the calculated exponents are unambiguous and intrinsic. The critical exponents determined are close to those predicted by the mean-field theory for long range interactions.

List of Figures

List of Tables

List of Contents

Chapter 1

INTRODUCTION

1.1 General Introduction

Modern society relies on cooling technology for food safety, comfort, and medical applications. For example, in the US about 34 % of the electricity is consumed by cooling appliances [1], and 15 % of total worldwide energy consumption involves the use of refrigeration (air conditioning, refrigeration, freezing, chilling, etc.) [2]. Nowadays, most cooling devices are based on vapour-compression technology, which was originally developed in the 19th century. As this technique uses strong greenhouse gases and the energy efficiency has reached its limit, rising international concerns about global warming due to ever increasing energy consumption call for a change. Recently, several solid-state cooling technologies, such as optical refrigeration [3], thermoelectric refrigeration [4]-[5], electric refrigeration [6]-[7], and magnetic refrigeration [8]-[9], have been considered as viable alternative techniques because they are becoming increasingly efficient and affordable. For a technique to become a fully mature alternative, however, clever engineering and more detailed studies on the fundamental physical properties are needed.

Conventional refrigerators have become omnipresent in a large number of cooling applications, but the use of chlorofluorocarbons (CFCs) and hydro chlorofluorocarbons (HCFCs) as working fluids has raised serious environmental concerns, mainly because of their contributions to destruction of the ozone layer and global warming [10, 11].

Replacement by fluid HFCs which contain no chlorine and therefore have no ozone depletion potential, is not without problems because HFCs are greenhouse gases [12] with higher global warming potential than CO_2. Thus, due to serious concerns for the environment, alternative technology should be a more attractive solution to the environmental problems.

By using solid magnetic materials as coolants instead of conventional gases, magnetic refrigeration avoids all harmful gases, including ozone-depleting gases, greenhouse-effect gases that contribute to global warming, and other hazardous gaseous refrigerants. A solid coolant can easily be recycled. Furthermore, it has been demonstrated that magnetic cooling is energetically more energy efficient than conventional gas-compression cooling. This is of particular interest in view of the global energy problems [13]. In addition, magnetic refrigerators make very little noise and may be built to be very compact. Therefore, magnetic refrigeration has attracted attention in recent years as a promising environmentally-friendly alternative to conventional gas-compression cooling.

1.2 The Magnetocaloric Effect

Magnetic refrigeration is based on the magnetocaloric effect (MCE), which was discovered by Warburg in 1881 [14]. In magnetic materials, a change in the degrees of freedom of the spins induces thermal effects. If the magnetic field is applied adiabatically, the material temperature rises, and when the field is removed, the material temperature is consequently decreased. These warming and cooling phenomena in response of an external magnetic field define the magnetocaloric effect (MCE), which can be used in refrigeration technology. The magnitude of the MCE in a magnetic material is defined by the isothermal magnetic entropy change (ΔS_M) or by the adiabatic temperature change (ΔT_{ad}) as the magnetic field is applied

or removed. Both of these points are very important factors for ideal magnetic material selection to produce a high performance magnetic refrigerator.

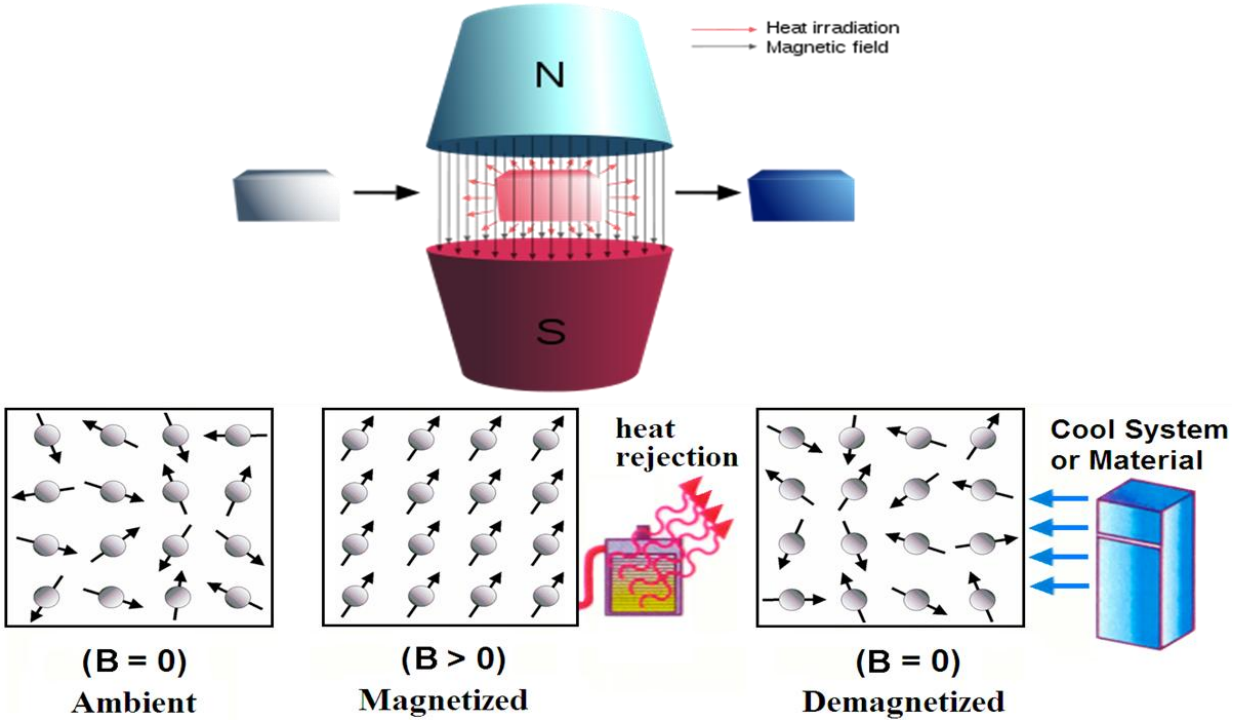

Figure 1.1 Gadolinium alloys heats up inside the magnetic field and loses thermal energy by irradiation, so that it is cooler than when it entered the field. This is a magneto-thermodynamic phenomenon, in which a reversible change in temperature of a suitable material is caused by exposing the material to a changing magnetic field [15].

Magnetic materials can order their magnetic moments in a variety of ways, such as ferromagnetic, ferromagnetic, and antiferromagnetic orderings, depending on the characteristics of the material. The moments of a magnetic material are aligned parallel to the magnetic field, as shown in Figure 1.1, when a magnetic field is applied to a magnetic material and affects the spin ordering, leading to lower entropy of the system as disorder decreases. To compensate for the aligned spins, the atoms of the material start to vibrate in an attempt to randomize the spin and lower the entropy of the system again, which contributes to increasing the temperature of the magnetic material. The opposite behaviour occurs when the material is removed from the magnetic field, which decreases the temperature of the magnetic

material. All the moments may be aligned, and increasing the applied field will not yield a further increase in the magnetization at very low temperature and very high field. Magnetization is defined by how much the magnetic moment is aligned, and this behaviour occurs around the phase transition temperature of the material.

1.3 The Magnetic Refrigerator

The magnetic refrigerator (MR) is based on the magnetocaloric effect (MCE), which occurs due to the coupling of a magnetic sublattice with an external magnetic field. With the magnetic spin system aligned by magnetic field, the magnetic entropy changes by ΔS_M as a result of isothermal magnetization of a material. On the other hand, the sum of the lattice and electronic entropies of a solid must be changed by ΔS_M as a result of adiabatically magnetizing the material, thus resulting in an increase in the lattice vibrations and the adiabatic temperature change, ΔT_{ad}. Both the isothermal entropy change ΔS_M and the adiabatic temperature change ΔT_{ad} are important parameters in quantifying the MCE and the performance of magnetocaloric materials (MCM).

In general, ΔS_M and ΔT_{ad} are obtained by using magnetization and heat capacity data in conjunction with the Maxwell equations. Although the Maxwell equations can be used to calculate MCE for first order magnetic transition (FOMT) materials due to the fact that the transition is not truly discontinuous, there can be some errors depending on the numerical integration method used. Thus, direct measurements of ΔT_{ad} are both useful and required to better understand the nature of the giant magnetocaloric effect (GMCE). Moreover, the direct measurements of ΔT_{ad} allow investigation of the dynamic performance of FOMT materials experiencing repeated magnetization/demagnetization cycles.

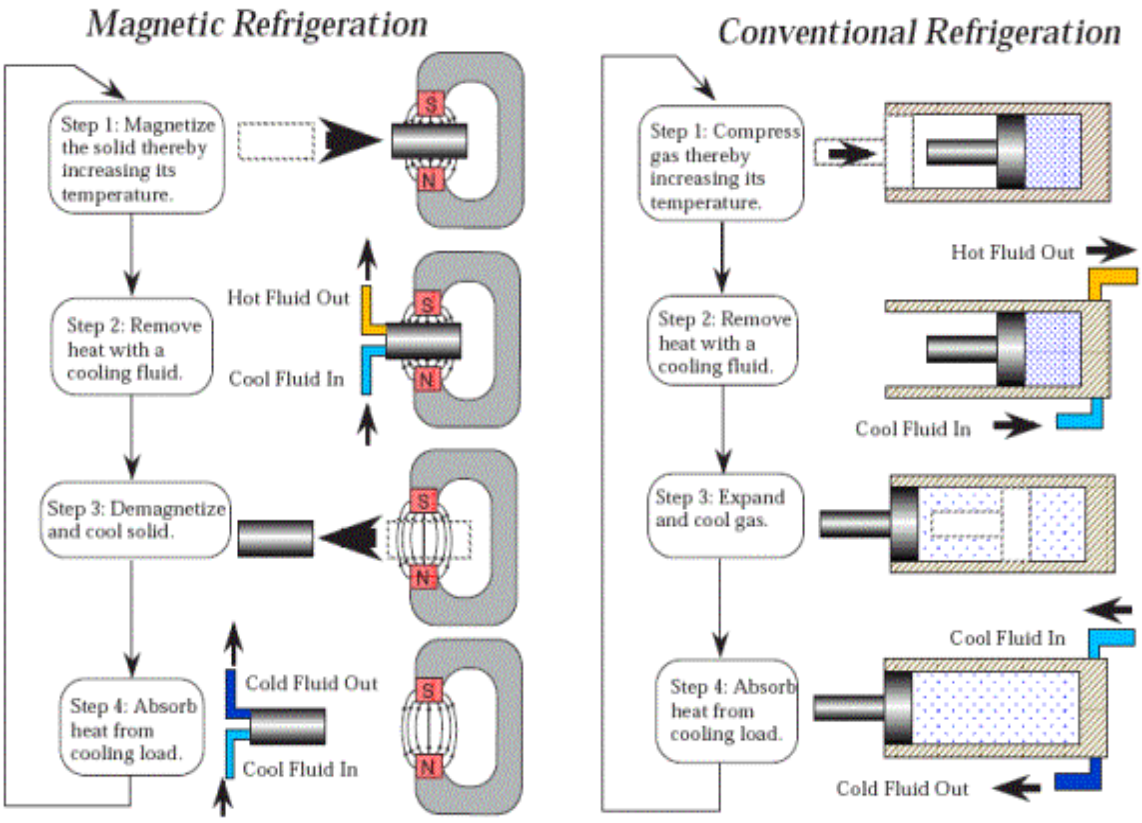

Figure 1.2 Magnetic refrigeration process and its analogy to conventional refrigeration [16].

In the magnetic-refrigeration cycle depicted in Figure 1.2, initially randomly (or nearly randomly)-oriented magnetic moments are aligned by a magnetic field, resulting in heating of the magnetic material. This implies a reduction of the entropy of the spin system. The entropy is transferred via the spin-lattice coupling to the lattice, resulting in heating of the magnetic material. The heat is removed from the material to the ambient environment by a heat transfer fluid. In a conventional vapour refrigeration system, the gas medium is compressed, thereby increasing its pressure and temperature, which is followed by a condensation process to transfer the heat to the ambient environment. Upon the removal of the field, as shown in step 3 of Figure 1.2, the magnetic moments randomize, which leads via spin-lattice coupling to cooling of the material below the ambient temperature. Heat from the system to be cooled can then be extracted by using a heat transfer medium. In a conventional refrigeration system, a

high pressure liquid expands and absorbs heat from the space to be cooled. When the magnetic field is generated by superconducting solenoids or permanent magnets, high-energy efficiency can be achieved as entropy is transferred to and from the quantum spin system.

Simultaneous occurrence of changes in degrees of freedom of the spins, magnetovolume effects, and changes in valence may bring about a giant MCE and thus a much more efficient magnetocaloric refrigeration system. Magnetic refrigeration (MR) is potentially a high efficiency, low-cost, and greenhouse-gas-free refrigeration technology, and with the looming phase out of HCFC and hydrofluorocarbon (HFC) refrigerants, is drawing more attention as an alternative to the existing vapour compression refrigeration.

1.4 Objectives of Research

The objective of the present thesis is to explore novel magnetic materials that possess a considerable MCE for real application in magnetic refrigerators. It is the aim of this work to contribute to a better understanding of their fundamental material characteristics, with an emphasis on understanding the relationships between the defined structure, the crystallographic phase, and the magnetic phase structure. The specific objectives are:

1. Study the effects of stoichiometric modifications or atomic substitutions to tune the transition temperature, T_C, for phase transitions in order to produce the giant MCE.
2. Develop new MCE material compositions and fabrication conditions for the different types of magnetic phase transitions and the related magneto-structural coupling.

3. Explore the properties of these systems, by quantifying the MCE using magnetic measurements to determine the magnetic entropy change (ΔS_M) and conduct magnetic thermal measurements to determine the adiabatic temperature change (ΔT_{ad}).
4. Study the behaviour of the lattice structure and magnetic moment using high technology neutron and synchrotron diffraction equipment.
5. The ultimate aim of the study is to synthesize high quality magnetocaloric materials suitable for use in magnetic refrigeration and to achieve a deep understanding of how to produce novel materials for MCE.

1.5 Organization of Thesis

The present study aims to provide guidance on the optimization of novel magnetic materials for MCE in order to implement them in real applications in magnetic refrigeration. This thesis is organised as follows:

The general introduction with an explanation of the magnetocaloric effect and magnetic refrigeration related to this research study, as well as the specific objectives of the work, are outlined in Chapter 1. A literature review of the variation in the magnetocaloric effect from theoretical aspects, especially in terms of the Gibbs free energy, magnetic entropy, specific heat, chemical pressure, and critical exponent analysis, is presented in Chapter 2.

Chapter 3 is devoted the synthesis procedures for the various material systems investigated in this study and the main characterization techniques to determine the structure and physical properties of the materials. A detailed study of the the effects on the magnetic properties and

magnetocaloric effect of $La_{0.7}Pr_{0.3}Fe_{11.4}Si_{1.6}$ compound by partial substitution of Cu and Cr for Fe at specific concentrations is outlined in Chapter 4.

Chapter 5 details the results of an intensive research study on the effects of other metal transition elements (Cu, Cr, Ti, and V) when substituted for Mn in the $NdMn_2Si_2$ interlayer compound. This study proposes a new fundamental idea on the role of other metal transition elements in tuning the giant magnetocaloric effect properties of $NdMn_2Si_2$ compound, as this layered structure is very significantly sensitive to the Mn-Mn distance. A significant enhancement of the Curie temperature, T_C, and the refrigerant capacity was achieved in $NdMn_2Si_2$ due to the replacement of Mn with other metal transition elements. Furthermore, ethe ffects of partially replacing Pr with Y in $PrMn_2Ge_2$ compound are also investigated in this Chapter. An intensively study of the effects of external pressure accompanied by a high applied magnetic field produced significant outcomes, which are also discussed. Finally, the effects of replacement of Ge by another metalloid (Si) in $CeMn_2Ge_2$ compound are included to complete the whole story of ternary intermetallic compounds of the RT_2X_2 series (R = rare earth, T = transition metal, X = Si or Ge). This study demonstrates the variety of magnetic transition and chemical pressure effects with different substitutions in the composition.

In Chapter 6, the results on the magnetic properties and the critical behaviour analysis of $Mn_{0.94}Ti_{0.06}CoGe$ and $Mn_{0.9}Ti_{0.1}CoGe$ alloys are presented. The results of a temperature dependent neutron diffraction study of both $Mn_{0.94}Ti_{0.06}CoGe$ and $Mn_{0.9}Ti_{0.1}CoGe$ alloys are also presented in this Chapter so as to elucidate the existence of a coupling in the magneto-structural transition. Moreover, variations in the lattice parameters and phase fractions with temperature change also were detected from the neutron diffraction patterns based on Fullprof refinement.

Finally, Chapter 7 describes the conclusions drawn and outlook based on this study, as well as recommendations regarding future work.

References

[1] Craig B. Smith and K. E. Parmenter, Handbook of Energy Efficiency and Renewable Energy edited by Frank Kreith and D. Yogi Goswami (CRC press, Taylor & Francis, 2007) Chapter 10. (2007)

[2] K. A. Gschneidner Jr and V. K. Pecharsky, International Journal of Refrigeration 31 (2008) 945.

[3] M. Sheik-Bahae and R. I. Epstein, Nat Photon 1 (2007) 693.

[4] B. C. Sales, Science 295 (2002) 1248.

[5] L. E. Bell, Science 321 (2008) 1457.

[6] A. S. Mischenko, Q. Zhang, J. F. Scott, R. W. Whatmore, and N. D. Mathur, Science 311 (2006) 1270.

[7] B. Neese, B. Chu, S.-G. Lu, Y. Wang, E. Furman, and Q. M. Zhang, Science 321 (2008) 821.

[8] V. K. Pecharsky and J. K. A. Gschneidner, Physical Review Letters 78 (1997) 4494.

[9] J. Glanz, Science 279 (1998) 2045.

[10] F. Drake, M. Purvis, and J. Hunt, Public Understand. Sci 10 (2001)

[11] United Nation (UN) New York ,NY (1987)

[12] United Nation (UN) New York, NY (1997)

[13] G. V. Brown, J. Appl. Phys 47 (1976) 3673.

[14] E. Warburg, Ann. Phys. (Leipzig) 13 (1881) 141.

[15] http://en.wikipedia.org/wiki/Magnetic_refrigeration.

[16] https://www.ameslab.gov/news/ins01-11Magnetic.htm,

Chapter 2

THEORETICAL ASPECTS

2.1 Magnetic Entropy

The magnetocaloric effect (MCE) is the response of a magnetic solid to a changing magnetic field, which manifests itself by a change in the temperature of the solid [1, 2]. The essential part of any magnetic refrigeration device is the magnetocaloric material that undergoes a temperature change when subjected to a magnetic field. It is worth noting that all magnetic materials exhibit the magnetocaloric effect. This effect indicates that paramagnetic (PM) or soft ferromagnetic (FM) materials absorb heat, and their magnetic entropy decreases when the magnetic field is applied isothermally or heat is otherwise expelled, and their magnetic entropy increases when the magnetic field is reduced isothermally. In order to understand the physics behind the magnetocaloric effect, it is important to gain insight into the behaviour of magnetic materials under the influence of a magnetic field.

The MCE is quantified through the definition of the entropy at constant pressure in a system as a function of temperature and magnetic field, $S(T, H)$. The entropy of a magnetic material consists of the magnetic entropy S_M, the lattice entropy S_L, and the electronic entropy S_E, as shown below:

$$S(T,H) = S_M(T,H) + S_L(L) + S_E(T) \tag{2.1}$$

where S_M is a function of both H and T, whereas S_L and S_E are both functions of T only. Thus, only the magnetic entropy S_M can be controlled by changing the strength of the magnetic field. Figure 2.1 is an S-T diagram for a ferromagnetic solid, showing the total entropy in magnetic fields H_F and H_1 ($H_1 < H_F$). The diagram also illustrates the MCE, which is represented by ΔT_{ad} or ΔS_M in the vicinity of the magnetic ordering temperature (Curie temperature, T_C). The vertical arrow shows the isothermal magnetic entropy change, ΔS_M whilst the horizontal arrow shows the adiabatic temperature change, ΔT_{ad} [3]. These arrows represent two different transformations, described in the preceding paragraph, which elucidate further the thermodynamics of the magnetocaloric effect [3].

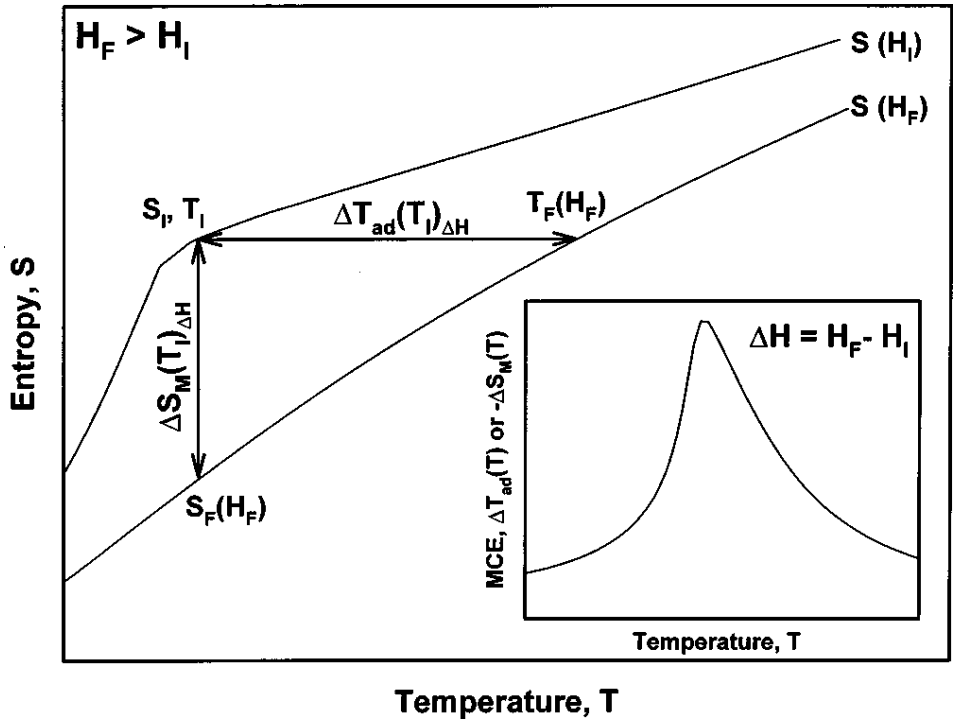

Figure 2.1 *S* - *T* diagram demonstrating the magnetocaloric effect [3].

2.2 Gibbs Free Energy

The MCE is essentially the application of the first and second laws of thermodynamics to a magnetic system. A description of the MCE in a magnetic system involves the use of thermodynamic functions such as the Gibbs free energy, which is a function of $T, H,$ and the pressure, $p,$ and is used for systems with constant pressure. It can be expressed as:

$$G = U - TS + pV - \mu_0 MH \tag{2.2}$$

Here, U is the internal energy and V is the volume. Equation (2.2) is a very important expression, as is it possible to define the first order and second order phase transitions on the basis of this equation. A phase transition is defined to be first order if the first derivative of the Gibbs free energy is discontinuous at the phase transition. Generally, in a first order transition the volume, magnetization, and entropy of the magnetic material might be discontinuous.

For a second order phase transition, the first derivative of the Gibbs free energy, as well as the entropy, is continuous at the phase transition.

The differentials of $U, S,$ and G are given below as:

$$dU = TdS - pdV - \mu_0 HdM \tag{2.3}$$

$$dS = -SdT - pdV - \mu_0 HdM \tag{2.4}$$

$$dG = Vdp - SdT - \mu_0 MdH \tag{2.5}$$

Considering the free energy, F, the following equations determine the internal parameters $S, p,$ and H.

$$S(T,H,V) = -\left(\frac{\partial F}{\partial T}\right)_{H,V} \tag{2.6}$$

$$H(T,M,V) = -\left(\frac{\partial F}{\partial M}\right)_{V,T} \tag{2.7}$$

$$p(T,H,V) = -\left(\frac{\partial F}{\partial V}\right)_{H,T} \tag{2.8}$$

Considering the Gibbs free energy, the following equations determine the internal parameters S, M, V:

$$S(T,H,p) = -\left(\frac{\partial G}{\partial T}\right)_{H,p} \tag{2.9}$$

$$M(T,H,p) = -\left(\frac{\partial G}{\partial H}\right)_{T,p} \tag{2.10}$$

$$V(T,H,p) = -\left(\frac{\partial G}{\partial p}\right)_{T,p} \tag{2.11}$$

Replacing the magnetic field H with the magnetic moment M as the external variable we get:

$$H = \left(\frac{\partial G}{\partial M}\right)_{T,p} \tag{2.12}$$

Deriving the Maxwell equations using Equations (2.9) and (2.10), (2.9) and (2.11), and (2.9) and (2.12) we get:

$$\left(\frac{\partial S}{\partial H}\right)_{T,p} = \left(\frac{\partial M}{\partial T}\right)_{H,p} \tag{2.13}$$

$$\left(\frac{\partial S}{\partial p}\right)_{T,H} = \left(\frac{\partial V}{\partial T}\right)_{H,p} \tag{2.14}$$

$$\left(\frac{\partial S}{\partial M}\right)_{T,p} = -\left(\frac{\partial H}{\partial T}\right)_{M,p} \tag{2.15}$$

2.3 Specific Heat

From the second law of thermodynamics, the enthalpy variation of a reversible process can be expressed as

$$\partial S = \left(\frac{\partial Q}{T}\right) \tag{2.16}$$

Accordingly, the heat capacity C_x of a system at constant parameter x is defined by:

$$C_x = \left(\frac{\partial Q}{\partial T}\right)_x \tag{2.17}$$

Where ∂Q is the amount of heat exchanged by the solid at temperature T giving rise to a temperature change ∂T. Since $\partial Q = TdS$, the heat capacity of the system can be expressed as:

$$C_x = T\left(\frac{\partial S}{\partial T}\right)_x \tag{2.18}$$

From Equation (2.20), the differential of the total entropy can be expressed as:

$$dS(T)_x = \frac{C(T)_x}{T} dT \tag{2.19}$$

The total differential of the total entropy of a magnetic system as a function of $T, p,$ and H can be written as:

$$dS = \left(\frac{\partial S}{\partial T}\right)_{H,p} dT + \left(\frac{\partial S}{\partial H}\right)_{T,p} dH + \left(\frac{\partial S}{\partial p}\right)_{T,H} dp \tag{2.20}$$

Considering an adiabatic $(dS = 0)$ and isobaric $(dp = 0)$ process and using the Maxwell relations (2.13) and (2.18), the temperature change due to a change in the magnetic field is expressed as:

$$dT = -\frac{T}{C_{H,p}}\left(\frac{\partial M}{\partial T}\right)_{H,p} dH \tag{2.21}$$

Using Equations (2.15) and (2.19) the temperature change caused by an adiabatic and isobaric change of magnetization is given by:

$$\partial T = -\frac{T}{C_{M,p}}\left(\frac{\partial H}{\partial T}\right)_{M,p} dM \tag{2.22}$$

$C_{H,p}$ and $C_{M,p}$ are the heat capacity of the material at constant pressure and constant field or constant magnetization, respectively.

If the total entropy of the system is expressed a function of T, p, and M, respectively, its total differential can be written as:

$$dS = \left(\frac{\partial S}{\partial T}\right)_{M,p} dT + \left(\frac{\partial S}{\partial M}\right)_{T,p} dM + \left(\frac{\partial S}{\partial p}\right)_{T,M} dp \tag{2.23}$$

To obtain the finite temperature change ΔT_{ad} for an adiabatic magnetization, Equations (2.21) and (2.22) are integrated as shown below:

$$\Delta T_{ad}(T, \Delta H) = -\int_{H_1}^{H_2}\left(\frac{T}{C(T,H)}\right)_H \left(\frac{\partial M(T,H)}{\partial T}\right)_H dH \tag{2.24}$$

$$\Delta T_{ad}(T, \Delta M) = -\int_{M_1}^{M_2}\left(\frac{T}{C(T,M)}\right)_M \left(\frac{\partial H(T,M)}{\partial T}\right)_H dM \tag{2.25}$$

The integration of the Maxwell relation, Equation (2.13), to give the finite entropy change under isothermal and isobaric conditions is expressed below:

$$\Delta S_M(T,\Delta H) = \int_{H_1}^{H_2}\left(\frac{\partial M(T,H)}{\partial T}\right)_H dH \tag{2.26}$$

From these equations, it follows that the MCE (absolute value of $\Delta S_M(T)_{\Delta H}$ or $\Delta T_{ad}(T)_{\Delta H}$) is large when $\left|\frac{\partial M}{\partial T}\right|$, which is sometimes written as $\left|\frac{\partial \sigma}{\partial T}\right|$, is large, that is, the magnetization changes rapidly with temperature.

2.4 Critical Exponent Analysis

Analysis of the critical behaviour is one of the methods used to clarify the nature of the FM – PM phase transition. According to the criterion proposed by Banerjee [4], the order of a magnetic transition can be determined from the slope of the isothermal plot. If the *H*/*M* versus M^2 curve shows a negative slope, the transition is first order, while a positive slope corresponds to a second order transition. The scaling hypothesis postulates that a second order magnetic phase transition near T_C is characterized by a set of critical exponents, namely, β, γ, and δ [5]. The modified Arrott plots (MAPs), Kouvel-Fisher method, critical isotherm analysis and the Widom scaling relation are the commonly used methods for determining the critical exponents. The first method used to calculate the critical exponents is the MAP method, which is based on the Arrott-Noakes equation of state [6]. Quantitative fits are made to the Arrott plots using the following equations [7]:

$$M_S(T) = \lim_{H\to 0}(M) = M_0\,(-\varepsilon)^{\beta}, \varepsilon < 0 \tag{2.27}$$

where M_0 and h_0 are constants and ε (= $(T\text{-}T_C)/T_C$) is the reduced temperature. Initial values of β and γ are selected, then a plot of $M^{1/\beta}$ versus $(H/M)^{1/\gamma}$ is obtained. M_S is then determined from the intersection of the linearly extrapolated curve with the $M^{1/\beta}$ axis.

$$\chi_0{}^{-1}(T) = \lim_{H\to 0}(H/M) = (h_0/M_0)\varepsilon^{\gamma}, \varepsilon > 0 \tag{2.28}$$

Here, χ_0 is the limit of the susceptibility at zero magnetic field. It is imperative to note that only the high field linear region is used for the analysis because MAPs tend to deviate from linearity at low field due to the mutually misaligned magnetic domains [8]. Next, M_S is plotted as a function of temperature. To determine $\chi_0{}^{-1}(T)$, a similar procedure is used in conjunction with the $(H/M)^{1/\gamma}$ axis. These new critical exponent values are then used to construct new MAPs. These steps are repeated until the iterations converge to the optimum β, γ, and T_C values.

The Kouvel-Fisher (KF) method, which makes use of Equations (2.29) and (2.30) shown below, is a more accurate way of determining the critical exponents β and γ [9].

$$\frac{M_S(T)}{\frac{dM_S(T)}{dT}} = \frac{T-T_C}{\beta} \tag{2.29}$$

$$\frac{\chi_0^{-1}(T)}{d\chi_0^{-1}(T)dT} = \frac{T-T_C}{\gamma} \tag{2.30}$$

According to Equations (2.29) and (2.30), plotting $M_S(T)[dM_S/dT]^{-1}$ and $\chi_0^{-1}(T)[d\chi_0^{-1}/dT]^{-1}$ versus temperature yields straight lines with slopes of $1/\beta$ and $1/\gamma$, respectively. The value of T_C is obtained from the intercepts on the x-axis. A comparison of the critical exponents β and γ obtained using the MAPs and those obtained using the KF method reveals

that these values match extremely well. The value of the critical component δ can be determined directly from the critical isotherm $M(T_C, H)$ according to Equation (2.31) below as D is the critical amplitudes.

$$M_{T_C} = DH^{1/\delta}, \varepsilon = 0, T = T_C \tag{2.31}$$

From Equation (2.31), a plot of log (M) versus log (H) is expected be a straight line with slope 1/δ. Another way of obtaining the critical component δ is by using the Widom scaling relation shown in Equation (2.32):

$$\delta = 1 + \frac{\gamma}{\beta} \tag{2.32}$$

Thus, the Widom scaling relation has confirmed the reliability of the critical exponents deduced from the experimental data. The reliability of the calculated exponents β and γ can be confirmed by using the scaling theory. In the critical region, according to the scaling theory, the magnetic equation of state can be written as:

$$M\,(H, \varepsilon) = \varepsilon^{\beta} f_{\pm}\,(H / \varepsilon^{\beta+\gamma}) \tag{2.33}$$

Where ε is the reduced temperature $(T - T_C) / T_C$ and f_+ and f_- are regular analytical functions above and below T_C respectively. Using β and γ obtained from the Kouvel-Fisher method, the plots of M / ε^{β} versus $H / \varepsilon^{(\beta+\gamma)}$ yield two universal curves, one for temperatures above T_C and the other one for temperatures below T_C, in agreement with the scaling theory. This therefore confirms that the obtained values of the critical exponents as well as the T_C are reliable and in agreement with the scaling hypothesis.

2.5 Recent International Progress on Magnetocaloric Materials

The discovery of the giant MCE (GMCE) in $Gd_5(Si,Ge)_4$ compounds has triggered vast interest in magnetic cooling. In addition, in 1997 the first near-room-temperature magnetic refrigerator was demonstrated by Zimm et al. at the Astronautics Corporation of America [10]. These two events attracted interest from both scientists and private companies, which started developing new kinds of room-temperature materials and magnetic-refrigerator designs. Figure 2.2 shows the number of publications on magnetic cooling since 1992 to 2010 and Figure 2.3 presents the number of magnetic refrigerators developed per year since 1970.

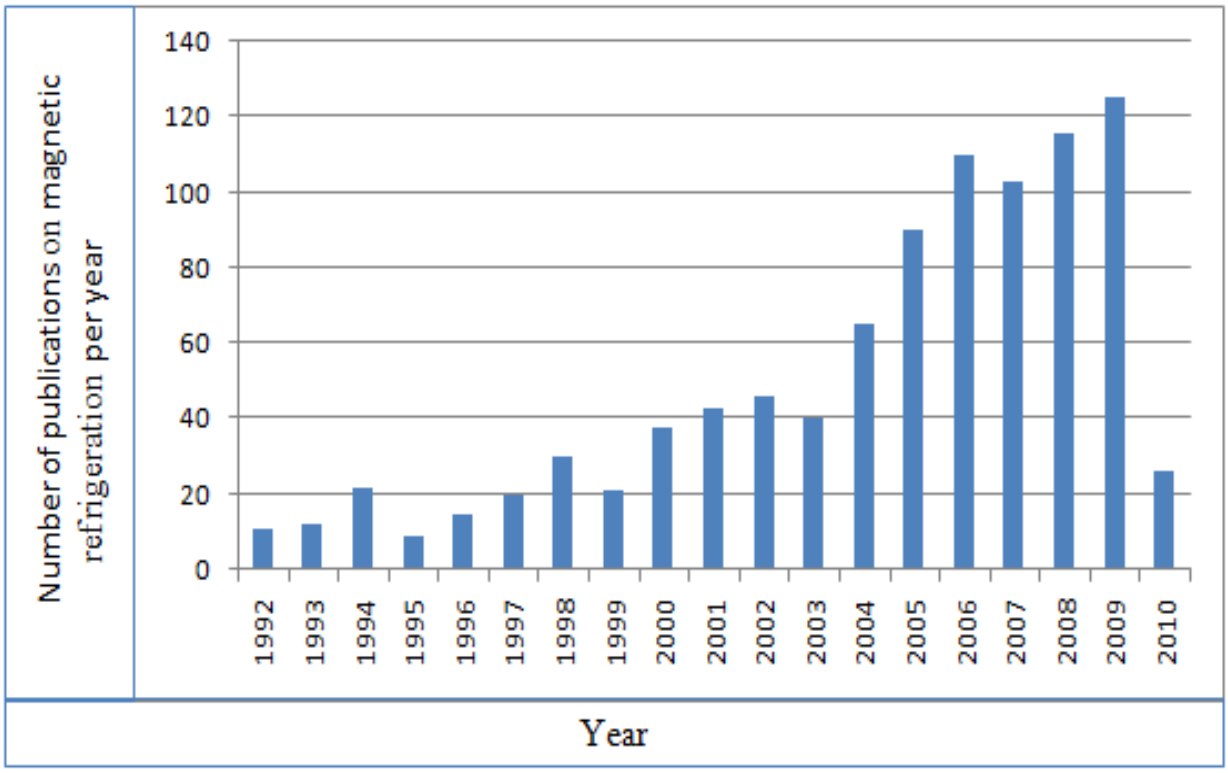

Figure 2.2 Publications on magnetic refrigeration since 1992 (Source: ISI web, *Science*, May 5, 2010).

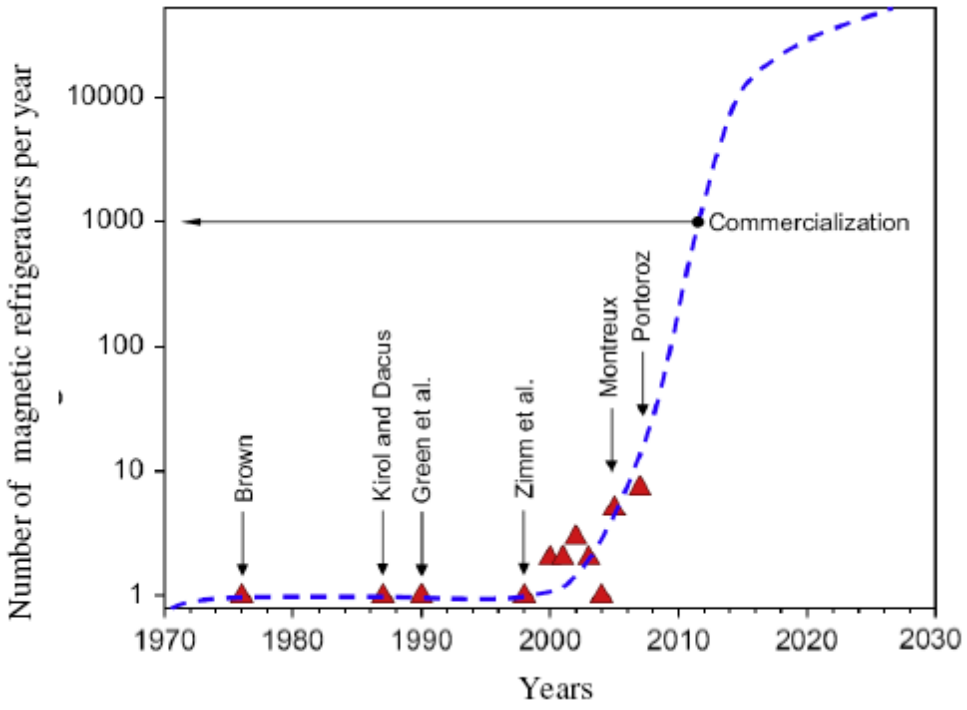

Figure 2.3 Number of magnetic refrigerators developed per year [11].

For room-temperature applications such as refrigerators and air-conditioners, compounds containing manganese or iron should be a good alternative. Manganese and iron are transition metals with high abundance. Also, in contrast to rare-earth compounds, there exist an almost unlimited number of manganese and iron compounds with critical temperatures near room temperature. The magnetic moment of manganese generally is only about half the size of those for heavy rare-earth elements and the magnetic moment of iron is even less. Enhancement of the caloric effects associated with magnetic moment alignment may be achieved through the induction of a first order phase-transition, or better, a very rapid change of magnetisation at the critical temperature, which will lead to much higher efficiency of the magnetic refrigerator.

In combination with currently available permanent magnets [12], based on modern rare-earth transition-metal compounds [13], this opens the path to the development of small-scale

magnetic refrigerators, which need no longer rely on rather costly and service-intensive superconducting magnets. Another prominent advantage of magnetocaloric refrigerators is that the cooling power can be varied by scaling from miliwatts to a few hundred watts or even kilowatts. To increases the temperature span of the refrigerator, in comparison with the temperature change in a single cycle, all demonstrator models or prototypes nowadays are based on active magnetic regenerator design [14].

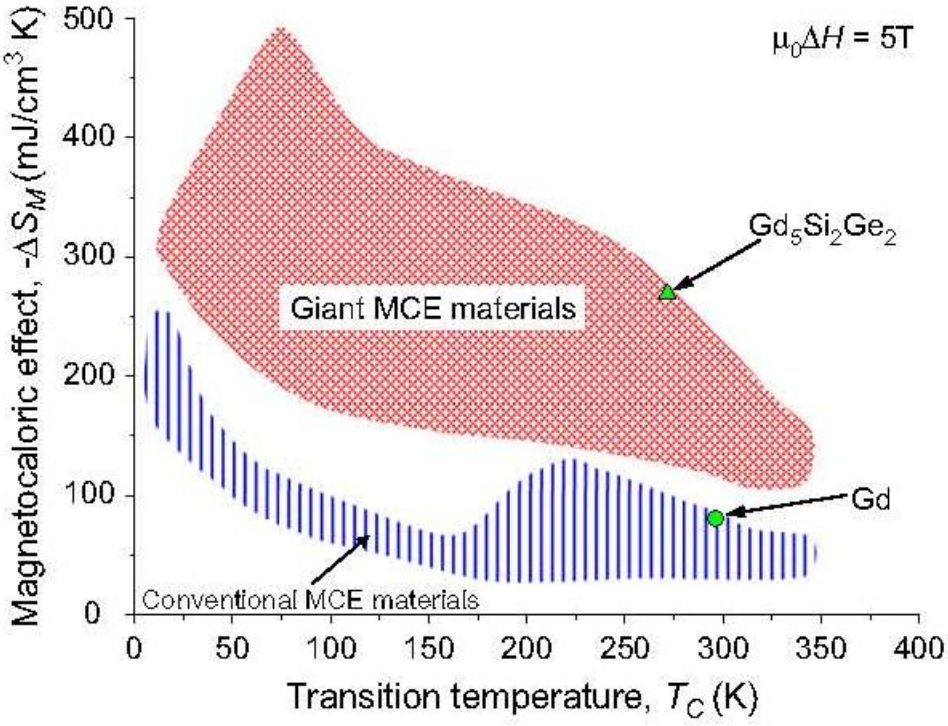

Figure 2.4 Comparison between GMCE materials and conventional MCE materials at $\mu_0\Delta H$ = 5 T [14]

2.5.1 $Gd_5Ge_2Si_2$ type compounds

Following the discovery of a sub-room-temperature giant-MCE in the ternary compound $Gd_5(Ge_{1-x}Si_x)_4$ ($0.3 \leq x \leq 0.5$) [15], as shown in Figure 2.4, there has been strongly increased interest from both fundamental and practical points of view in studying the MCE in these materials [16-17]. The most prominent feature of these compounds is that they undergo a

first-order structural and magnetic phase transition, which leads to a giant magnetic field-induced entropy change across their ordering temperature. We now therefore will discuss to some extent the structural properties of these compounds. At low temperatures for all *x*, $Gd_5(Ge_{1-x}Si_x)_4$ adopts an orthorhombic Gd_5Si_4-type structure (Pnma), and the ground state is ferromagnetic[18].

At room temperature, however, depending on *x*, three different crystallographic phases are observed. For $x > 0.55$, the aforementioned Gd_5Si_4 structure is stable, while for $x < 0.3$, the materials adopt the Sm_5Ge_4-type structure with the same space group (Pnma) but a different atomic arrangement and a somewhat larger volume, and finally, in between these two types of structure, the monoclinic $Gd_5Si_2Ge_2$ type with space group P1121/a is formed, which has an intermediate volume. The latter structure type is stable only below about 570 K, where again, the orthorhombic Gd_5Si_4-type structure is formed in a first-order phase transition [19].

As one may guess, the three structure types are closely related; the unit cells contain four formula units and essentially only differ in the mutual arrangement of identical building blocks, which are either connected by two, one, or no covalent-like Si-Ge bonds, resulting in successively increasing unit-cell volumes. The giant magnetocaloric effect is observed for the compounds that exhibit a simultaneous paramagnetic to ferromagnetic and structural phase transition that can be induced by a change in temperature, applied magnetic field, or applied pressure [20-21].

In contrast to most magnetic systems, the ferromagnetic phase has a 0.4% smaller volume than the paramagnetic phase, which results in an increase in T_C on application of pressure of about 3 K/kbar. The structural change at the phase transition also leads to a very large

magneto-elastic effect, and the electrical resistivity behaves anomalously. The strong coupling between the lattice degrees of freedom and the magnetic and electronic properties is rather unexpected, because the magnetic moment in Gd originates from spherical symmetric s-states that, in contrast to other rare-earth elements, hardly couple with the lattice. First principles electronic structure calculations on the atomic level and local-density approximation calculations with spin-orbit coupling added variationally could reproduce some distinct features of the phase transition [22].

Total energy calculations for the monoclinic and orthorhombic phases show different temperature dependences and the structural change occurs at the temperature where the energies are equal. A distinct difference appears in the effective exchange-coupling parameter for the monoclinic and orthorhombic phases, respectively. This difference could be directly related to the change in the Fermi level in the structural transition. Thus, the fact that the structural and magnetic transitions are simultaneous is somewhat accidental, as the exchange energy is of the same order of magnitude as the thermal energy at the structural phase-transition. The electrical resistivity and magnetoresistance of $Gd_5Ge_2Si_2$ also shows unusual behaviour, indicating a strong coupling between the electronic structure and the lattice.

For several compounds in the series, a very large magnetoresistance effect is reported next to a cusp-like anomaly in the temperature dependence of the resistivity [23-26]. From the point of view of building a refrigerator based on $Gd_5(Ge_{1-x}Si_x)_4$, there are a few points to consider. The largest magnetocaloric effect is observed considerably below room temperature, while a real refrigerator should expel heat at least at about 320 K. Because the structural transition is connected with sliding of the building blocks, impurities can play an important role, especially at the sliding interface. The thermal hysteresis and the size of the magnetocaloric

effect connected with the first-order phase transition strongly depend on the quality of the starting materials and the sample preparation [27].

For the $Gd_5(Ge_{1-x}Si_x)_4$ compounds with *x* around 0.5, small amounts of impurities may suppress the formation of the monoclinic structure near room temperature. These alloys then show only a second order phase transition at a somewhat higher temperature, but with a lower magnetocaloric effect [19],[28-29]. This sensitivity to impurities such as carbon, oxygen and iron strongly influences the production costs of the materials, which may hamper broad-scale application. Next to the thermal and field hysteresis, the magneto-structural transition in $Gd_5(Ge_{1-x}Si_x)_4$ appears to be rather sluggish [30, 31]. This will also influence the optimal operation frequency of a magnetic refrigerator and its efficiency.

2.5.2 La(Fe,Si)$_{13}$ and related compounds

Another interesting type of material is the rare-earth - transition-metal compounds crystallizing in the cubic $NaZn_{13}$ type of structure. $LaCo_{13}$ is the only binary compound, from the 45 possible combinations of a rare-earth and iron, cobalt, or nickel, that exists in this structure. It has been shown that with an addition of at least 10% Si or Al this structure can also be stabilized with iron and nickel [32].

The $NaZn_{13}$ structure contains two different Zn sites. The Na atoms at 8*a* and Zn atoms at 8*b* form a simple CsCl type of structure. Each ZnI atom is surrounded by icosahedra composed of 12 ZnII atoms at the 96*i* site. In $La(Fe,Si)_{13}$, La occupies the 8*a* site, while the 8*b* site is fully occupied by Fe and the 96*i* site is shared by Fe and Si. The iron rich compounds $La(Fe,Si)_{13}$ show typical Invar behaviour, with magnetic ordering temperatures around 200 K

that increase to 262 K with lower iron content [33]. Thus, although the magnetic moment is diluted and also decreases per Fe atom, the magnetic ordering temperature increases. Around 200 K, the magnetic ordering transition is found to be also distinctly visible in the electrical resistivity, where a chromium-like cusp in the temperature dependence is observed. In contrast to $Gd_5Ge_2Si_2$, this phase transition is not accompanied by a structural change, and thus, above and below T_C, the material is cubic.

Recently, because of the extremely sharp magnetic ordering transition, the (La,Fe,Si,Al) system was reinvestigated by several research groups, and a large magnetocaloric effect was reported [34-36]. The largest effects are observed for the compounds that show a field- or temperature-induced phase transition of first order. Unfortunately, these large effects only occur up to about 210 K, as the magnetic sublattice becomes more and more diluted. When using standard melting techniques, preparation of homogeneous single-phase samples appears to be rather difficult, especially for alloys with high transition metal content. Almost single phase samples are reported when, instead of normal arc melting, rapid quenching by melt spinning and subsequent annealing is employed [37-39]. Samples prepared in this way also show a very large magnetocaloric effect.

To increase the magnetic ordering temperature without losing too much magnetic moment, one may replace some Fe by other magnetic transition metals. Because the isostructural compound $LaCo_{13}$ has a very high critical temperature, substitution of Co for Fe has been widely studied. The compounds $La(Fe,Co)_{13-x}Al_x$ and $La(Fe,Co)_{13-x}Si_x$ with $x \approx 1.1$ and thus a very high transition-metal content, show a considerable magnetocaloric effect near room temperature [40-43]. This is achieved with only a few percent Co, and the Co content can

easily be varied to tune the critical temperature to the desired value. It should be mentioned, however, that near room temperature, the values for the entropy change drop steeply.

Hydrogen is the most promising interstitial element. In contrast to other interstitial atoms, interstitial hydrogen not only increases the critical temperature, but also leads to an increase in magnetic moment [35], [44-48]. The lattice expansion due to the addition of three hydrogen atoms per formula unit is about 4.5%. The critical temperature can be increased up to 450 K, as the average magnetic moment per Fe increases from 2.0 μB up to 2.2 μB and the field- or temperature-induced phase transition is found to be of first order for all hydrogen concentrations.

For a certain Si percentage, this all results in an almost constant value of the magnetic entropy change per mass unit over a broad temperature span. From the materials cost point of view, the $La(Fe,Si)_{13}$ type alloys appear to be very attractive. La is the cheapest from the rare-earth series, and both Fe and Si are available in large amounts. The processing will be a little more elaborate than for a simple metal alloy, but this can be optimized. For use in a magnetic refrigerator, next to the magnetocaloric properties, the mechanical properties and chemical stability may also be of importance.

The hydrogenation process in rare-earth transition-metal compounds almost always produces granular material due to the strong lattice expansion. In the case of the cubic $NaZn_{13}$ type of structure, however, this does not seem to be the case. At the phase transition in $La(Fe,Si)_{13}$ type alloys, a volume change of 1.5% is also observed [49]. If this volume change is performed very frequently, the material will definitely become very brittle and probably break into even smaller grains. This can have a distinct influence on the corrosion resistance

of the material and thus on the lifetime of a refrigerator. The suitability of this material definitely needs to be tested.

2.5.3 RT_2X_2 interlayer compounds

Ternary rare-earth (R) compounds of the type RT_2X_2, where T = transition metal and X = Si, Ge, exhibit a large variety of structural and physical properties (Refs.[50-52]) and as such continue to attract interest. The interplay between the R-T and T-T exchange interactions in these RT_2X_2 compounds, combined with the extensive ranges of solubility of the R, T and X elements, enables structural and magnetic behaviours to be controlled through elemental substitution [53-56]. Given this scope to tune their physical and magnetic properties and related magnetic phase transitions, RT_2X_2-based compounds have attracted attention in exploring their magnetocaloric effect behaviour [57-59].

The ternary intermetallic compounds of the RT_2X_2 series have attracted considerable attention because of the rich variety of interesting phenomena, including superconductivity, magnetism, mixed valence, heavy fermions, and Kondo behaviour [60, 61]. RT_2X_2 compounds form mainly in the $ThCr_2Si_2$ structure (space group *I*4/*mmm*), with the layered nature of this crystal structure leading to strong dependence of the magnetic interactions on the interplanar and intraplanar interatomic distances [53]. From this point of view, RMn_2X_2 compounds with X= Si or Ge have attracted special attention, due mainly to the interesting interplay between the magnetism of the layers of 3*d* and 4*f* atoms and the strong dependence of the magnitude of the Mn moment and the magnetic state of the Mn sublattice on the Mn-Mn interatomic distances [57, 61-66].

As a general guide, for intraplanar distance, $d_{Mn\text{-}Mn}$ below ~ 2.87 Å, the coupling between Mn layers is antiferromagnetic while above this value, the coupling is ferromagnetic [67-69]. In $NdMn_2Si_2$, below T_N ~ 380 K the Mn sublattice orders antiferromagnetically, while below T_C ~ 36 K the compound is ferromagnetic with ordered moments at both the Nd and the Mn sublattices [70, 71]. These magnetic behaviours with different temperature dependences reflect different types of exchange interactions with different mechanisms with both the Ruderman-Kittel-Kasuya-Yosida (RKKY) exchange interaction *via* conduction electrons, and super exchange between magnetic atoms *via* the Si or Ge atoms contributing. Generally, the exchange interactions in RMn_2X_2 compounds can be divided into four classes: Mn–Mn within the Mn layers, Mn–Mn between the Mn layers, and Mn–R and R–R interactions [72].

Investigations of the RMn_2X_2 magnetic phase diagram as functions of both composition and Mn–Mn spacing using x-ray and neutron diffraction, magnetisation and differential scanning calorimetry measurements. For example, $Pr_{1-x}Y_xMn_2Ge_2$ exhibits an extended region of re-entrant ferromagnetism around x~0.5 with re-entrant ferromagnetism at T_c^{Pr} ~ 50 K for $Pr_{0.5}Y_{0.5}Mn_2Ge_2$. The entropy values $-\Delta S_M$ around the ferromagnetic transition temperatures T_C^{inter} from the layered antiferromagnetic AF*l* structure to the canted ferromagnetic structure F*mc* (typically T_C^{inter} ~ 330-340 K) have been derived for $Pr_{1-x}Y_xMn_2Ge_2$ with x=0.0, 0.2 and 0.5 for ΔB=0-5 T. The changes in magnetic states due to Y substitution for Pr are discussed in terms of chemical pressure, external pressure and electronic effects.

2.5.4 MnCoGe based compounds

Materials which experience simultaneous crystallographic and magnetic phase transitions have garnered a lot of interest owing to their promising applications as multifunctional

materials [73, 74]. The intermetallic compounds $MnCo_{1-x}Ge$, with ($0 \leq x \leq 0.1$) have an orthorhombic TiNiSi –type structure at room temperature whilst the compositions with $x > 0.1$ have a Ni_2In-type structure [75].

MnCoGe behaves like a typical ferromagnet with a second-order magnetic phase transition. It has previously been shown that, the magnetic saturation moment M_S and the magnetic ordering temperature T_C are different for these two phases. In the orthorhombic structure, the values of M_S and T_C are 4.13 μ_B and 345 K, respectively [76]. The hexagonal form, on the other hand exhibits a lower M_S and also a lower T_C, namely 2.76 μ_B and 275 K, respectively [77]. It has been established that for the MnCoGe compound, the structural transition temperature, T_{str} between the orthorhombic and hexagonal phase can be changed by either changing the composition [78], or applying an external pressure [79, 80].

Kanomata *et al.*[75] clearly point out that the structural transition in MnCoGe, as shown in Figure 2.7, is accompanied by strong thermal hysteresis (ΔThys ~ 40 K) and a large volume change ($\Delta V/V$ ~ 4%). In order to modify the interatomic distances resulting in the tuning of the magnetostructural coupling in MnCoGe compound, several different ways such as substitutions, dopings and the application of physical pressure have been used [81, 82].

Compared to the $La(Fe,Si)_{13}$ based group of compounds, the MnCoGe compounds have not been studied as much, however several research groups worldwide have reported on the MCE of MnCoGe and related alloys, some of these finding are discussed in detail below. Wang *et al.* reported on the *ab initio* total energy calculations on the first-order structural transition of the ferromagnetic $MnCo_{1-x}Ge$ intermetallic compound. They show that increasing Co vacancies induce a transition from an orthorhombic structure to a hexagonal structure they also observed that a concomitant high to low moment magnetic transition and a large

magnetovolume effect occur due to the change of the symmetry and the resulting coupling distance between the magnetic atoms.

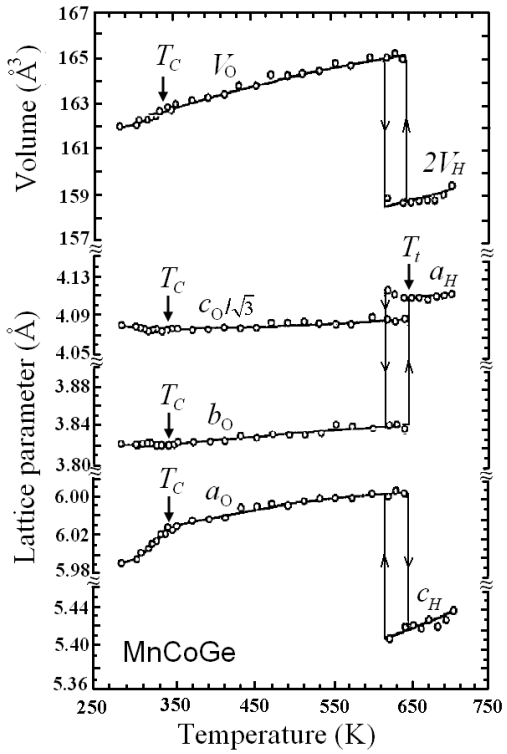

Figure 2.5 Volume and lattice parameters of the MnCoGe alloy as a function of temperature [45].

Markin *et al.* studied the concentrational dependences of the lattice parameters, spontaneous magnetic moment, and magnetic ordering temperature of nonstoichiometric $Mn_{1.9-x}Co_xGe$ ($0.8 < x < 1.65$) compounds with a hexagonal crystal structure [83]. On increasing the Co content, x from 1.1 to 1.2, the Curie temperature and magnetic moment were found to increase abruptly.

Lin *et al.* [76], reported on the iron doping where a structural transformation from the orthorhombic to the hexagonal phase was observed in the $MnCo_{1-x}Fe_xGe$ alloys. For undoped MnCoGe, the maximum magnetic entropy change is about -5.6 $Jkg^{-1}K^{-1}$ for a magnetic field change ΔB = 0-5 T. Meanwhile, an enhanced ΔS_M value up to -9 $Jkg^{-1}K^{-1}$ was reported for

the x = 0.2 sample. For Sn and Ge doped MnCoGe compounds for low magnetic field change, moderate values of magnetic entropy change were obtained [84, 85].

Trung *et al.* systematically studied the structural, magnetic and magnetocaloric properties of MnFe(P,Ge) and related compounds on both bulk samples and melt-spun ribbons. By changing either the compositions or the annealing conditions, the critical behavior of the phase transition can be controlled. Also, the thermal hysteresis is tunable to very small values while maintaining a large MCE in a large range of working temperatures [86].

Trung *et al*. studied the substitution of some Cr for Mn atoms in MnCoGe to control the magnetic and structural transitions in this alloy to coincide, leading to a single first-order magnetostructural transition from the ferromagnetic to the paramagnetic state with a giant magnetocaloric effect observed near room temperature. Further increase in the Cr content in the $Mn_{1-x}Cr_xCoGe$ alloys induces another first-order magnetoelastic transition from the antiferromagnetic to the ferromagnetic state occurring at lower temperature.

Caron *et al.*[87] investigated the effects of physical and chemical pressures in the $Mn_{1-x}Cr_xCoGe$ series of compounds. Cr substitution and hydrostatic pressure play similar roles in displacing T_C to lower temperatures and coupling or decoupling magnetic and crystallographic transitions. In this work the similarities and differences between the effects of chemical and physical pressures were explored, helping unveil the nature of the first-order phase transition presented by MnCoGe-based compounds [82].

2.5.5 MnAs based compounds

MnAs is similar to $Gd_5Ge_2Si_2$ in having two distinct crystallographic structures [88]. At low and high temperature the hexagonal NiAs structure is found, and for the narrow temperature range of 307 K to 393 K, the orthorhombic MnP structure exists. The high temperature transition in the paramagnetic region is of second order. The low temperature transition is a combined structural and ferro-paramagnetic transition of first order with large thermal hysteresis.

The change in volume at this transition amounts to 2.2% [89]. The transition from paramagnetic to ferromagnetic occurs at 307 K, and the reverse transition from ferromagnetic to paramagnetic occurs at 317 K. Very large magnetic entropy changes are observed in this transition [90, 91]. Similar to the application of pressure [92, 93], substitution of Sb for As leads to lowering of T_C [94, 95], and 25% Sb gives a transition temperature of 225 K. The thermal hysteresis, however, is affected quite differently by hydrostatic pressure or Sb substitution.

In Mn(As,Sb), the hysteresis is strongly reduced, and at 5% Sb, it is reduced to about 1 K. In the concentration range of 5 to 40% of Sb, T_C can be tuned between 220 and 320 K without losing much of the magnetic entropy change [96, 97]. Direct measurements of the temperature change confirm a ΔT of 2 K/T [98]. On the other hand, MnAs under pressure shows an extremely large magnetic entropy change [99] in conjunction with large hysteresis.

The materials costs of MnAs are quite low, but processing of As containing alloys is complicated due to the biological activity of As. In the MnAs alloy, the As is covalently

bound to the Mn and would not be easily released into the environment. This should be experimentally verified, however, especially because second phases frequently form in an alloy that may be less stable. The change in volume in Mn(As,Sb) is still 0.7%, which may result in aging after frequent cycling of the material.

2.5.6 Heusler Alloys

Heusler alloys frequently undergo a martensitic transition between the martensitic and the austenitic phase, which is generally temperature induced and of first order. Ni_2MnGa orders ferromagnetically, with a Curie temperature of 376 K and a magnetic moment of 4.17 μB, which is largely confined to the Mn atoms, with only a small moment of about 0.3 μB associated with the Ni atoms [100]. As may be expected from its cubic structure, the parent phase has a low magnetocrystalline anisotropy energy (H = 0.15 T). In its martensitic phase, however, the compound exhibits a much larger anisotropy (H = 0.8 T). The martensitic-transformation temperature is near 220 K.

This martensitic transformation temperature can be easily varied to around room temperature by modifying the composition of the alloy from the stoichiometric one. The low temperature phase evolves from the parent phase by a diffusionless, displacive transformation leading to a tetragonal structure, $a = b$ = 5.90 Å, c = 5.44 Å. The martensitic phase generally accommodates the strain associated with the transformation (6.56% along the c-axis for Ni_2MnGa) by the formation of twin variants. This means that a cubic crystallite splits up into two tetragonal crystallites sharing one contact plane. These twins pack together in compatible orientations to minimize the strain energy (in much the same way as the magnetization of a

ferromagnet may take on different orientations by breaking up into domains to minimize the magnetostatic energy).

Alignment of these twin variants by the motion of twin boundaries can result in large macroscopic strains. In the tetragonal phase with its much higher magnetic anisotropy, an applied magnetic field can induce a change in strain, which is why these materials may be used as actuators. Next to this ferromagnetic shape memory effect, very close to the martensitic transition temperature, one observes a large change in magnetization for low applied magnetic fields. This change in magnetization is also related to the magnetocrystalline anisotropy. This change in magnetization results in a moderate magnetic entropy change of a few J/mol K, which is enhanced when measured on a single crystal [101, 102]. When the composition in this material is tuned in such a way that the magnetic and structural transformations occur at the same temperature, the largest magnetic entropy changes are observed [103-105].

For magnetocaloric applications, the extremely large length changes in the martensitic transition will definitely result in aging effects. It is well known for the magnetic shape-memory alloys that only single crystals can be frequently cycled, while polycrystalline materials spontaneously powderize after several cycles.

2.5.7 Fe_2P based compounds

The binary intermetallic compound Fe_2P can be considered as the parent alloy for an interesting class of materials. This compound crystallizes in the hexagonal non-centrosymmetric Fe_2P type structure with space group P 6 2 m. In this structure, Fe and P

occupy four different crystallographic sites, Fe occupies the 3*g* and 3*f* sites, and P occupies the 1*b* and 2*c* sites. Thus, one has a stacking of alternating P-rich and P-poor layers. Neutron diffraction has revealed that the magnetic moment of Fe on the 3*g* sites is about 2 μB, whereas the moment on the 3*f* sites is about 1 μB [106]. The Curie temperature of this compound is 216 K, and the magnetic transition is of first order [107].

The magnetic-ordering transition from the paramagnetic state to the ferromagnetic state is accompanied by a discontinuous change in the volume of 0.05%. Thus, the ferromagnetic state has a bigger volume than the paramagnetic one. This phase transition is found to be extremely sensitive to changes in pressure or magnetic field. Application of pressure first reduces the Curie temperature, and at pressures exceeding 5 kbar, antiferromagnetic ordering preceding the ferromagnetic ordering is observed [108]. Substitution of As, B, or Si into the P sublattice results in an increase in the Curie temperature [109], which can easily be lifted to above room temperature for As or Si concentrations of 10% or by 4% for B. Substitution of Mn for Fe on the 3*g* sites further increases the magnetic moment to about 4 μB.

To stabilize the Fe_2P-type of structure, simultaneouslywith the Mn substitution, part of the P should also be replaced. The most extensively studied series of alloys is of the MnFe(P,As) type. The magnetic phase diagram for the MnFeP-MnFeAs system [110] shows a rich variety of crystallographic and magnetic phases. The most striking feature is the fact that for As concentrations between 30 and 65% the hexagonal Fe_2P type of structure is stable, and the ferromagnetic order is accompanied by a discontinuous change in the volume. While the total magnetic moment is not affected by changes in the composition, the Curie temperature increases from about 150 K to well above room temperature. We reinvestigated this part of

the phase diagram [111, 112] and investigated possibilities for partially replacing the As [113-115].

The large MCE observed in Fe_2P based compounds originates from a field-induced first order magnetic phase transition. The magnetisation is reversible depending on the temperature and in alternating magnetic field. The magnetic ordering temperature of these compounds is tuneable over a wide temperature interval (200 K to 450 K). The excellent magnetocaloric features of the compounds of the MnFe (P,Si,Ge,As) type, in addition to the very low material costs, make it an attractive candidate material for a commercial magnetic refrigerator. In the same way as for MnAs alloys, however, it should be verified that materials containing as do not release it to the environment. The fact that the magnetoelastic phase-transition is rather a change of *c*/*a* than a change of volume, makes it feasible that this alloy, even in polycrystalline form, will not experience severe aging effects after frequent magnetic cycling [81].

References

[1] K. A. Gschneidner and V. K. Pecharsky, Journal of Applied Physics 85 (1999) 5365.
[2] L. von Moos, C. R. H. Bahl, K. K. Nielsen, K. Engelbrecht, M. Küpferling, and V. Basso, Physica B: Condensed Matter 435 (2014) 144.
[3] B. F. Yu, Q. Gao, B. Zhang, X. Z. Meng, and Z. Chen, International Journal of Refrigeration 26 (2003) 622.
[4] B. K. Banerjee, Physics Letters 12 (1964) 16.
[5] H. E. Stanley, (Oxford University Press, London) (1971)
[6] A. Arrott and J. E. Noakes, Physical Review Letters 19 (1967) 786.
[7] M. Sahana, U. K. Rössler, N. Ghosh, S. Elizabeth, H. L. Bhat, K. Dörr, D. Eckert, M. Wolf, and K. H. Müller, Physical Review B 68 (2003) 144408.
[8] A. Aharoni, (Oxford University Press, New York,) (1971)
[9] J. S. Kouvel and M. E. Fisher, Physical Review 136 (1964) A1626.
[10] Zimm and e. al., Advanced in Cryogenic Engineering 43 (1998) 1759.
[11] K. A. Gschneidner Jr and V. K. Pecharsky, International Journal of Refrigeration 31 (2008) 945.
[12] W. Dai, B. G. Shen, D. X. Li, and Z. X. Gao, Journal of Magnetism and Magnetic Materials 218 (2000) 25.
[13] J.A. Barclay and W. Steyert, in U.S. Patent (1981)
[14] J. A. Barclay and W. Steyert, U.S. Patent. (1981)
[15] V. K. Pecharsky and J. K. A. Gschneidner, Physical Review Letters 78 (1997) 4494.
[16] W. Choe, V. K. Pecharsky, A. O. Pecharsky, K. A. Gschneidner, Jr., V. G. Young, Jr., and G. J. Miller, Physical Review Letters 84 (2000) 4617.
[17] L. Morellon, J. Blasco, P. A. Algarabel, and M. R. Ibarra, Physical Review B 62 (2000) 1022.
[18] A. O. Pecharsky, K. A. Gschneidner Jr, V. K. Pecharsky, and C. E. Schindler, Journal of Alloys and Compounds 338 (2002) 126.
[19] Y. Mozharivskyj, A. O. Pecharsky, V. K. Pecharsky, and G. J. Miller, Journal of the American Chemical Society 127 (2005) 317.
[20] L. Morellon, P. A. Algarabel, M. R. Ibarra, J. Blasco, B. GarcÃa-Landa, Z. Arnold, and F. Albertini, Physical Review B 58 (1998) R14721.
[21] L. Morellon, Z. Arnold, P.A. Algarabel, C. Magen, M.R. Ibarra, and Y. Skorokhod, Journal of Physics-Condensed Matter 16 (2004) 1623.
[22] V. K. Pecharsky, G. D. Samolyuk, V. P. Antropov, A. O. Pecharsky, and K. A. Gschneidner, Journal of Solid State Chemistry 171 (2003) 57.
[23] L. Morellon, P. A. Algarabel, C. Magen, and M. R. Ibarra, Journal of Magnetism and Magnetic Materials 237 (2001) 119.
[24] E. M. Levin, V. K. Pecharsky, K. A. Gschneidner, Jr., and G. J. Miller, Physical Review B 64 (2001) 235103.
[25] H. Tang, V. K. Pecharsky, G. D. Samolyuk, M. Zou, J. K. A. Gschneidner, V. P. Antropov, D. L. Schlagel, and T. A. Lograsso, Physical Review Letters 93 (2004) 237203.
[26] L. Morellon, J. Stankiewicz, B. Garcia-Landa, P. A. Algarabel, and M. R. Ibarra, Applied Physics Letters 73 (1998) 3462.
[27] A. O. Pecharsky, K. A. Gschneidner, Jr., and V. K. Pecharsky, Journal of Applied Physics 93 (2003) 4722.
[28] V. K. Pecharsky and K. A. Gschneidner Jr, Journal of Magnetism and Magnetic Materials 167 (1997) L179.
[29] V. Provenzano, A. J. Shapiro, and R. D. Shull, Nature 429 (2004) 853.
[30] A. GiguÃ¨re, M. Foldeaki, B. Ravi Gopal, R. Chahine, T. K. Bose, A. Frydman, and J. A. Barclay, Physical Review Letters 83 (1999) 2262.

[31] K. A. Gschneidner, Jr., V. K. Pecharsky, E. BrÃ¼ck, H. G. M. Duijn, and E. M. Levin, Physical Review Letters 85 (2000) 4190.
[32] P.I. Kripyakevich, O.S. Zarechnyuk, E.I. Gladyshevsky, and O.I. Bodak, Z. Anorg. Chem. 358 (1968) 90.
[33] T. T. M. Palstra, J. A. Mydosh, G. J. Nieuwenhuys, A. M. van der Kraan, and K. H. J. Buschow, Journal of Magnetism and Magnetic Materials 36 (1983) 290.
[34] F.X. Hu, B.G. Shen, J.R. Sun, and X.X. Zhang, Chinese Physics. 9 (2000) 550.
[35] S. Fujieda, A. Fujita, and K. Fukamichi, Applied Physics Letters 81 (2002) 1276.
[36] H. Feng-Xia, S. Bao-Gen, S. Ji-Rong, A. B. Pakhomov, C. Y. Wong, X. X. Zhang, Z. Shao-Ying, W. Guang-Jun, and C. Zhao-Hua, Magnetics, IEEE Transactions on 37 (2001) 2328.
[37] X.B. Liu, Z. Altounian, and G.H. Tu, Journal of Physics-Condensed Matter. 16 (2004) 8043.
[38] X. B. Liu, X. D. Liu, Z. Altounian, and G. H. Tu, Journal of Alloys and Compounds 397 (2005) 120.
[39] O. Gutfleisch, A. Yan, and K. H. Muller, Journal of Applied Physics 97 (2005) 10M305.
[40] F.X. Hu, B.G. Shen, J.R. Sun, and Z.H. Cheng, Physical Review B. 6401 (2001) 012409012409.
[41] F. X. Hu, J. Gao, X. L. Qian, M. Ilyn, A. M. Tishin, J. R. Sun, and B. G. Shen, Journal of Applied Physics 97 (2005) 10M303.
[42] J.R. Proveti, E.C. Passamani, C. Larica, A.M. Gomes, A.Y. Takeuchi, and A. Massioli, Journal Of Physics D-Applied Physics. 38 (2205) 1531.
[43] J. Shen, Y.X. Li, F. Wang, G.J. Wang, and S.Y. Zhang, Chinese Physics. 13 (2004) 1134.
[44] A. Fujita, S. Fujieda, Y. Hasegawa, and K. Fukamichi, Physical Review B. 67 (2003) 104416.
[45] K. Irisawa, A. Fujita, K. Fukamichi, Y. Yamazaki, Y. Iijima, and E. Matsubara, Journal Of Alloys And Compounds. 316 (2001) 70.
[46] S. Fujieda, A. Fujita, and K. Fukamichi, Materials Transactions. 45 (2004) 3228.
[47] K. Mandal, O. Gutfleisch, A. Yan, A. Handstein, and K.H. Muller, Journal Of Magnetism And Magnetic Materials. 290 (2005) 673.
[48] S.A. Nikitin, I.S. Tereshina, V.N. Verbetsky, A.A. Salamova, and E.V. Anosova, Journal Of Alloys And Compounds. 367 (2004) 266.
[49] F.W. Wang, G.J. Wang, F.X. Hu, A. Kurbakov, B.G. Shen, and Z.H. Cheng, Journal of Physics-Condensed Matter. 15 (2003) 5269.
[50] M. Hofmann, S. J. Campbell, and A. V. J. Edge, Physical Review B 69 (2004) 174432.
[51] A. M. Bebb, J. W. Taylor, J. A. Duffy, Z. F. Banfield, M. J. Cooper, M. R. Lees, J. E. McCarthy, and D. N. Timms, Physical Review B 71 (2005) 024407.
[52] E. G. Gerasimov, N. V. Mushnikov, and T. Goto, Physical Review B 72 (2005) 064446.
[53] G. Venturini, R. Welter, E. Ressouche, and B. Malaman, Journal of Magnetism and Magnetic Materials 150 (1995) 197.
[54] R. Welter and B. Malaman, Journal of Alloys and Compounds 354 (2003) 35.
[55] J. L. Wang, S. J. Campbell, J. M. Cadogan, O. Tegus, A. J. Studer, and M. Hofmann, Journal of Physics: Condensed Matter 18 (2006) 189.
[56] J. L. Wang, L. Caron, S. J. Campbell, S. J. Kennedy, M. Hofmann, Z. X. Cheng, M. F. Md Din, A. J. Studer, E. Brück, and S. X. Dou, Physical Review Letters 110 (2013) 217211.
[57] J L Wang, S J Campbell, A J Studer, M Avdeev, R Zeng, and S. X. Dou, Journal of Physics: Condensed Matter 21 (2009) 124217.
[58] J. L. Wang, S. J. Campbell, R. Zeng, C. K. Poh, S. X. Dou, and S. J. Kennedy, Journal of Applied Physics 105 (2009) 07A909.
[59] R. Zeng, S. X. Dou, J. L. Wang, and S. J. Campbell, Journal of Alloys and Compounds 509 (2011) L119.
[60] A. Szytuła and J. Leciejewicz, in Handbook on the Physics and Chemistry of Rare Earths, Vol. Volume 12 (Karl A. Gschneidner, Jr. and E. LeRoy, eds.), Elsevier, 1989, p. 133.
[61] B. Emre, S. Aksoy, O. Posth, M. Acet, E. Duman, J. Lindner, and Y. Elerman, Physical Review B 78 (2008) 144408.

[62] G. Venturini, R. Welter, E. Ressouche, and B. Malaman, Journal of Alloys and Compounds 224 (1995) 262.
[63] T. Samanta, I. Das, and S. Banerjee, Applied Physics Letters 91 (2007) 152506.
[64] P. Kumar, K. G. Suresh, A. K. Nigam, A. Magnus, A. A. Coelho, and S. Gama, Physical Review B 77 (2008) 224427.
[65] J. L. Wang, S. J. Campbell, J. M. Cadogan, A. J. Studer, R. Zeng, and S. X. Dou, Applied Physics Letters 98 (2011) 232509.
[66] J. L. Wang, S. J. Campbell, J. M. Cadogan, A. J. Studer, R. Zeng, and S. X. Dou, Journal of Physics: Conference Series 303 (2011) 012022.
[67] A. Szytuła and S. Siek, Journal of Magnetism and Magnetic Materials 27 (1982) 49.
[68] H. Fujii, T. Okamoto, T. Shigeoka, and N. Iwata, Solid State Communications 53 (1985) 715.
[69] H. Fujii, M. Isoda, T. Okamoto, T. Shigeoka, and N. Iwata, Journal of Magnetism and Magnetic Materials 54–57, Part 3 (1986) 1345.
[70] R. Welter, G. Venturini, D. Fruchart, and B. Malaman, Journal of Alloys and Compounds 191 (1993) 263.
[71] Y.-g. Wang, F. Yang, C. Chen, N. Tang, and Q. Wang, Journal of Alloys and Compounds 257 (1997) 19.
[72] N. P. Kolmakova, A. A. Sidorenko, and R. Z. Levitin, Low Temperature Physics 28 (2002) 653.
[73] C.-B. Rong and J. P. Liu, Applied Physics Letters 90 (2007)
[74] H. Wada and Y. Tanabe, Applied Physics Letters 79 (2001) 3302.
[75] T. Kanomata, H. Endo, S. Mori, H. Okajima, T. Hihara, K. Sumiyama, T. Kaneko, and K. Suzuki, Journal of Magnetism and Magnetic Materials 140–144, Part 1 (1995) 133.
[76] S. Lin, O. Tegus, E. H. Brück, W. Dagula, T. J. Gortenmulder, K. H. J. Buschow, and W. Sadowski, IEEE TRANSACTIONS ON MAGNETICS 42 (2006) 3776.
[77] J.T. Wang, D.S. Wang, C. Chen, O. Nashima, T. Kanomata, H. Mizuseki, and Y. Kawazoe, Applied Physics Letters 89 (2006)
[78] V. Johnson, Inorganic Chemistry 14 (1975) 1117.
[79] S. Nizioł, A. Zięba, R. Zach, M. Baj, and L. Dmowski, Journal of Magnetism and Magnetic Materials 38 (1983) 205.
[80] S. NizioŁ, R. Zach, J. P. Senateur, and J. Beille, Journal of Magnetism and Magnetic Materials 79 (1989) 333.
[81] N. T. Trung, V. Biharie, L. Zhang, L. Caron, K. H. J. Buschow, and E. Brück, Applied Physics Letters 96 (2010)
[82] N. T. Trung, L. Zhang, L. Caron, K. H. J. Buschow, and E. Brück, Applied Physics Letters 96 (2010)
[83] P. E. Markin, N. V. Mushnikov, V. I. Khrabrov, and M. A. Korotin, The Physics of Metals and Metallography 106 (2008) 481.
[84] J. B. A. Hamer, R. Daou, S. Özcan, N. D. Mathur, D. J. Fray, and K. G. Sandeman, Journal of Magnetism and Magnetic Materials 321 (2009) 3535.
[85] Y. K. Fang, C. C. Yeh, C. W. Chang, W. C. Chang, M. G. Zhu, and W. Li, Scripta Materialia 57 (2007) 453.
[86] N. T. Trung, Z. Q. Ou, T. J. Gortenmulder, O. Tegus, K. H. J. Buschow, and E. Brück, Applied Physics Letters 94 (2009)
[87] L. Caron, Z. Q. Ou, T. T. Nguyen, D. T. Cam Thanh, O. Tegus, and E. Brück, Journal of Magnetism and Magnetic Materials 321 (2009) 3559.
[88] L. Pytlik and A. Zieba, J. Magn. Magn. Mater. 51 (1985) 199.
[89] H. Fjellvag and K. A., Acta Chem. Scand. A. 38 (1984) 1.
[90] H. Wada and Y. Tanabe, Applied Physics Letters. 79 (2001) 3302.
[91] C. Kuhrt, T. Schittny, and K. Barner, Phys. Stat. Sol. (a). 91 (1985) 105.
[92] N. Menyuk, J.A. Kafalas, K. Dwight, and J.B. Goodenough, Physical Review. 177 (1969) 942.

[93] H. Yamada, K. Terao, K. Kondo, and T. Goto, Journal Of Physics-Condensed Matter. 14 (2002) 11785.
[94] H. Wada, T. Morikawa, K. Taniguchi, T. Shibata, Y. Yamada, and Y. Akishige, Physica B-Condensed Matter. 328 (2003) 114.
[95] H. Wada, K. Taniguchi, and Y. Tanabe, Materials Transactions. 43 (2002) 73.
[96] H. Wada and T. Asano, Journal Of Magnetism And Magnetic Materials. 290 (2005) 703.
[97] T. Morikawa, H. Wada, R. Kogure, and S. Hirosawa, Journal of Magnetism and Magnetic Materials. 238 (2004)
[98] H. Wada, C. Funaba, T. Asano, M. Ilyn, and A.M. Tishin, Sci. Tech. Froid comptes rendus. 2005-4 (2005) 37.
[99] S. Gama, A.A. Coelho, A. de Campos, A.M.G. Carvalho, F.C.G. Gandra, P.J. von Ranke, and N.A. de Oliveira, Physical Review Letters. 93 (2004)
[100] P.J. Webster, K.R.A. Ziebeck, S.L. Town, and M.S. Peak, Philosophical Magazine B. 49 (1984) 295.
[101] F.X. Hu, B.G. Shen, J.R. Sun, and G.H. Wu, Phys. Rev. B 64 (2001) 132412.
[102] J. Marcos, A. Planes, L. Manosa, F. Casanova, X. Batlle, A. Labarta, and B. Martinez, Physical Review B. 66 (2002) 224413.
[103] Y.K. Kuo, K.M. Sivakumar, H.C. Chen, J.H. Su, and C.S. Lue, Physical Review B. 72 (2005) 054116.
[104] X.Z. Zhou, W. Li, H.P. Kunkel, G. Williams, and S.H. Zhang, Journal Of Applied Physics. 97 (2005) Part 3 10M515.
[105] Y. Long, Z.Y. Zhang, D. Wen, G.H. Wu, R.C. Ye, Y.Q. Chang, and F.R. Wan, Journal Of Applied Physics. 98 (2005) 033515046102.
[106] H. Fujii, S. Komura, T. Katega, T. Okamoto, I. Y., and J. Akimitsu, J. Phys. Soc. Jpn. 46 (1979) 1616.
[107] H. Fujii, T. Hokabe, T. Komigaichi, and T. Okamoto, J. Phys. Soc. Jpn. 43 (1977) 41.
[108] H. Kadomatsu, M. Isoda, K. Tohma, H. Fujii, T. Okamoto, and H. Fujiwara, J. Phys. Soc. Jpn. 54 (1985) 2790.
[109] P. Jernberg, A. Yousif, and L. Hägström, J. Solid State Chem. 53 (1984) 313.
[110] O. Beckmann and L. Lundgren, Compounds of transition elements with nonmetals 181.
[111] E. Brück, O. Tegus, X.W. Li, F.R. de Boer, and K.H.J. Buschow, Physica B Condensed Matter. 327 (2003) 431.
[112] O. Tegus, E. Brück, L. Zhang, Dagula, K.H.J. Buschow, and F.R. de Boer, Physica B. 319 (2002) 174.
[113] O. Tegus, E. Brück, W. Dagula, X.W. Li, L. Zhang, K.H.J. Buschow, and F.R. de Boer, Journal Of Applied Physics. 93 (2003) 7655.
[114] O. Tegus, B. Fuquan, W. Dagula, L. Zhang, E. Brück, P.Z. Si, F.R. de Boer, and K.H.J. Buschow, Journal Of Alloys And Compounds. 369 (2005) 6.
[115] L. Zhang, O. Moze, K. Prokes, O. Tegus, and E. Brück, Journal Of Magnetism And Magnetic Materials. 290 (2005) 679.

Chapter 3

EXPERIMENTAL METHODS AND PROCEDURES

3.1 Sample Preparation

The basic principles of the equipment used to prepare the materials presented in this thesis are outlined in this chapter. All the materials used for measurement in this thesis are polycrystalline and were prepared using the arc melting method at UNSW@ADFA, Canberra and the ball-milling method at ISEM, University of Wollongong.

3.1.1 Bulk sample Preparation – Arc melting

Stoichiometric amounts of the starting elements, typically with purity greater than 99.9%, were melted using an argon arc furnace with a tungsten electrode and water cooled copper hearth. The furnace was flushed 3-4 times with high purity argon gas to minimise the amount of oxygen in the tube and hence prevent oxidation during the melting process. The gas pressure was initially set slightly lower than ambient pressure to allow for its increase due to the high temperatures experienced during melting. The process commenced with the melting of a titanium getter, for further reduction of the residual oxygen in the furnace, before proceeding to the actual starting materials. The preparations were carried out with sets of smaller masses (approximately 1 - 2.5 g), and each specimen was melted, turned, and remelted at least 6 times to ensure homogeneity of the specimens. Due to the sensitivity of all specimens, it was found that vacuum annealing was required to obtain a good quality

structure. To do this, the specimens were wrapped in Ta foil, sealed in an evacuated quartz tube, and annealed at a specific temperature and time before quenching in water.

3.1.2 Bulk sample Preparation – Ball milling

In order to investigate which method is most beneficial to produce the desired structure in $Mn_{1-x}Co_xGe$ alloys, ball milling was performed as a comparison with arc melting. All the powders, which were of high purity (> 99.9%), were mixed in an agate mortar and loaded into a stainless steel vial under high purity Ar atmosphere inside a glove box. Before sealing the vial, stainless steel balls 5 mm in diameter were added, with a powder-to-ball ratio of 1:10. The ball milling was performed in a planetary crushing Fritsch Pulverisette 7. A low energy ball milling at 200 rpm for 30 minutes was conducted before high energy ball milling at 500 rpm for 6 hours. The fine powder was then pressed into pellets and sealed in quartz ampoules in an Ar atmosphere of 200 mbar. Finally, the as-milled alloy was annealed at 1423 K for 1 hour before a quenching in water.

3.2 Structural and Characterization Analysis of the Samples

In order to determine the structural properties as well as the quantification of the phases and impurities therein, X-ray diffraction (XRD), neutron diffraction, and scanning electron microscopy (SEM) were carried out. These characterizations needed to be done as a first step before measuring the physical properties of the samples, as if the impurity content is more than 5%, it means that the sample is not suitable for further investigation. All these techniques are elaborated in detail below.

3.2.1 Neutron and Synchrotron (X-ray) Diffraction

The neutron diffraction technique is used not only for the determination of the atomic structure, but also for the magnetic structure and moment of a material as well. We performed our neutron experiments at the Australian Nuclear Science and Technology Organisation (ANSTO), which houses the Open Pool Australian Lightwater (OPAL) reactor, which is a state-of-the-art 20 Megawatt reactor that uses low enriched uranium fuel. A high continuous flux of neutrons is produced in the core of this fission reactor. These neutrons are moderated to thermal velocities close to the source and then transported to the neutron scattering instruments in neutron guide systems that direct them to targets in a series of instruments. The Echidna and Wombat neutron beam instruments were used in this study for a few selected materials, as this equipment offers very limited beam time. A schematic diagram of the Echidna and Wombat neutron diffractometers is shown in Figure 3.1.

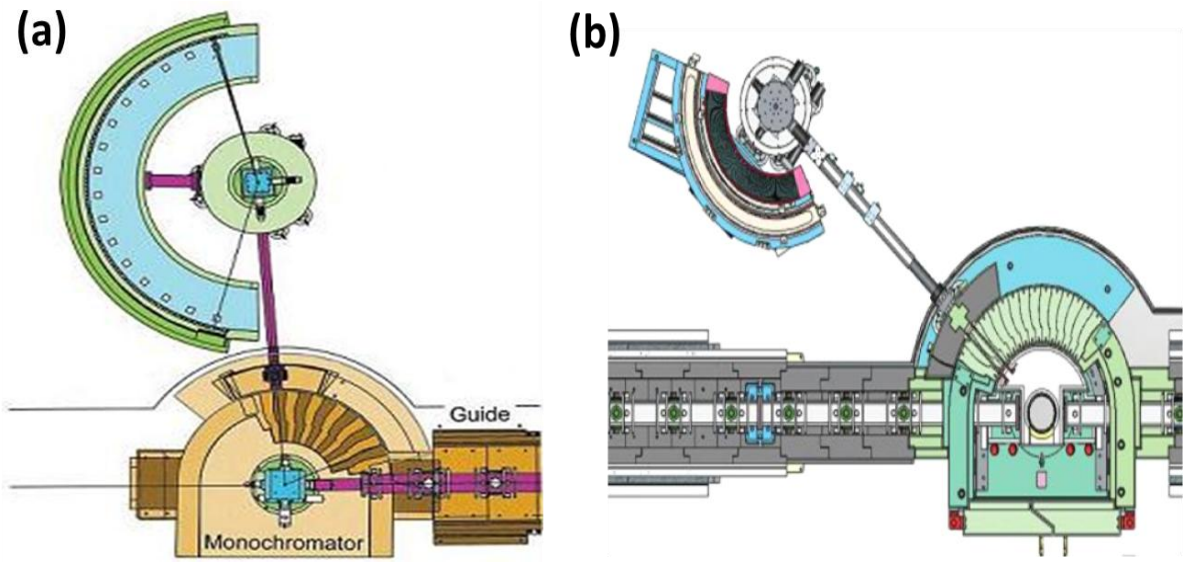

Figure 3.1 Schematic diagrams of the (a) Echidna and (b) Wombat diffractometers as cited from ANSTO website.

As mentioned previously, an intense beam of neutrons is produced at the nuclear reactor, and this neutron beam is channelled through a collimator that narrows the beam so that only neutrons travelling normal to the reactor surface are used. The neutron beam is then targeted on a monochromator (usually graphite), which will reflect neutrons with a wavelength close to a value determined by the angular setting of the monochromator. The monochromatic beam is then directed to the sample under investigation. When these neutrons strike the target material, they scatter, producing distinctive patterns that deliver information to the researchers. The Echidna provided high resolution diffraction patterns and Wombat has high intensity. These are among the most powerful diffractometers in the world, promising high quality outcomes for the present research study.

Synchrotron X-ray diffraction equipment located at the Australian Synchrotron was used in order to identify change of structure of samples, especially with regards to strain, the magnetic contribution, and valence effects. Because it probides high resolution and a sophisticated facility for powder diffraction, all the physical and chemical behaviour that takes place at critical transitions can be explored and efficiently clarified.

The powder diffraction beamline as shown in Figure 3.2 is located on a bending magnet source and has been designed to operate over the energy range of 5-30 keV. The beamline consists of three hutches and a user cabin. The first hutch contains the optics, including mirrors and a double crystal monochromator. The centre hutch houses the primary end station where the majority of powder diffraction experiments are undertaken. Finally, the third hutch contains a large optical table which allows a variety of alternative configurations, primarily centred on engineering applications.

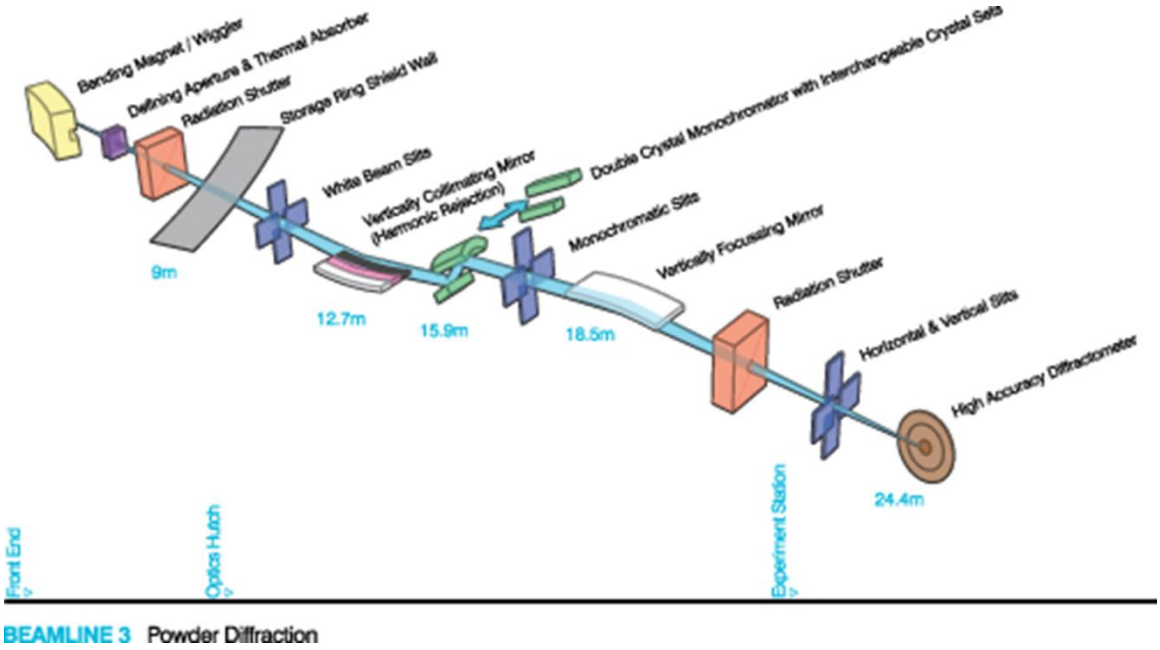

Figure 3.2 Schematic layout of the 10-BM-1 powder diffraction beamline as cited from Australian Synchrotron website.

3.2.2 Scanning Electron Microscopy

The scanning electron microscope (SEM) generates a variety of signals at the surface of solid specimens by using a focused beam of high energy electrons. Electron and sample interactions generate a signal which reveals information about the sample, such as the morphology, chemical composition, and crystalline structure, for in this study.

A precise measurement of very small features of the sample down to the nanometer (nm) size was possible using SEM (JEOL Model JSM-6490) for this study, and the basic operation is shown in Figure 3.3. The SEM is also capable of quantitatively determining the chemical composition using energy dispersive x-ray spectroscopy (EDS). In this technique, only solid samples can be analysed. For electrically insulating samples, the low vacuum mode is used or an electrically conductive coating is applied to the sample.

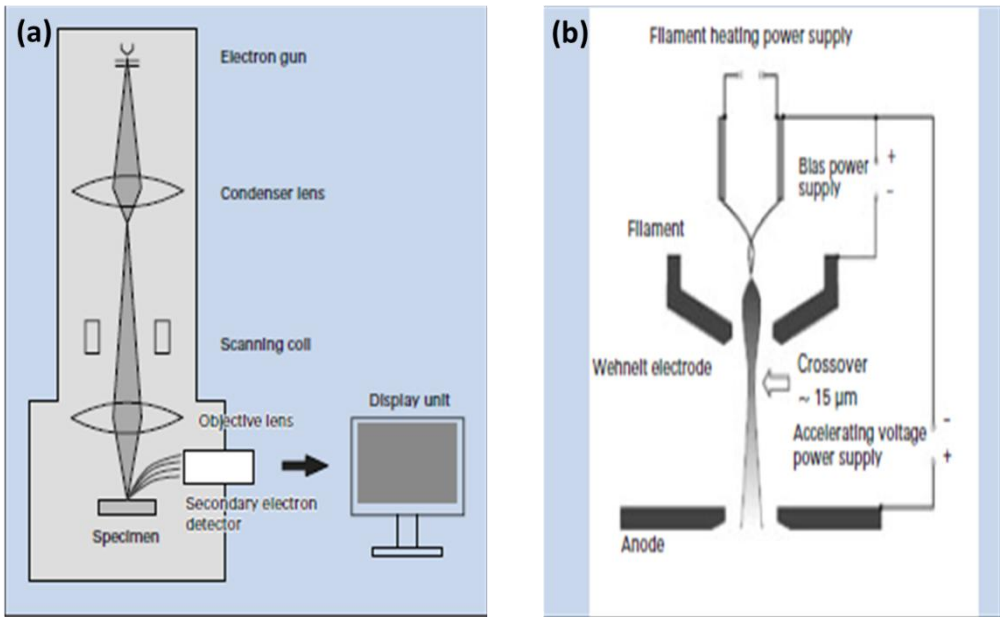

Figure 3.3 (a) Basic construction of SEM and (b) construction of an electron gun.

3.2.3 Diffraction Analysis

In order to analyse all the diffraction patterns collected from X-rays and neutrons in this study, refinement with the FullProf program was performed as this software package is very efficient and user-friendly. The FullProf program has been mainly developed for Rietveld analysis (structure profile refinement) of neutron (constant wavelength, time-of-flight, nuclear and magnetic scattering) or X-ray powder diffraction data collected with constant or variable steps at scattering angle 2θ.

The program can be also used as a profile matching (or pattern decomposition using the Le Bail method) tool, without detailed knowledge of the structure as in Figure 3.4. Single crystal refinement can also be performed alone or in combination with powder data. Time-of-flight (TOF) neutron data analysis is also available. Energy dispersive X-ray data can also be treated, but only for profile matching.

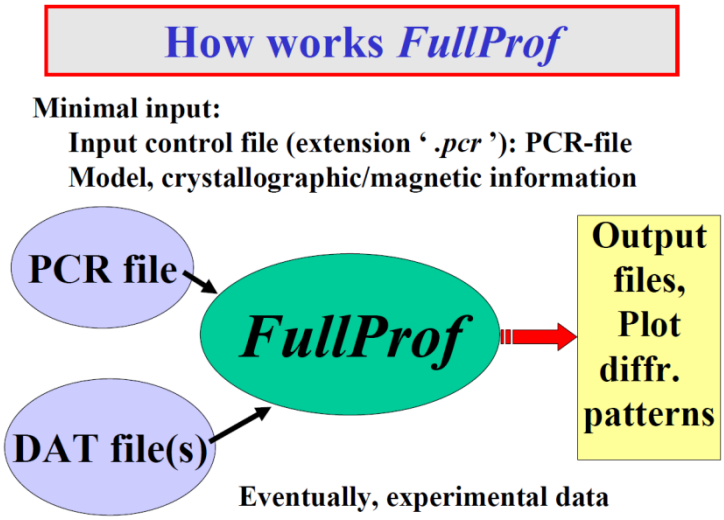

Figure 3.4 Schematic diagram of refinement using FullProf program.

3.3 Physical Properties Measurement System (PPMS)

Physical properties measurement has an important role in verifying the behaviour and characteristics of every single sample in this study. Furthermore, the effects of the doping concentration in the parent compound are clearly shown using this method.

3.3.1 Vibrating Sample Magnetometer (VSM)

The vibrating sample magnetometer (VSM) measurement system for the PPMS is a fast, sensitive, and fully automated DC magnetometer. The sensitivity of the VSM detection coils is not significantly affected by large magnetic fields, so the PPMS VSM can perform sensitive measurements up to the maximum field of 14 T that is available from PPMS magnet equipment. The VSM detection coil is inserted into the PPMS sample chamber by using the standard PPMS sample interface design. This procedure will make it easy to reconfigure the VSM option with alternate pick-up coil designs in the future. If the temperature range is over

360 K, the oven chamber is inserted, with the VSM oven allowing measurements up to the 1000 K temperature limit.

3.3.2 Superconducting Quantum Interference Device (SQUID)

The Quantum Design MPMS 5XL SQUID uses a superconducting quantum interference device (SQUID) magnetometer to monitor very small changes in magnetic flux and so discover the magnetic properties of the samples in this study. It is extremely sensitive for all kinds of AC and DC magnetic measurements. The SQUID detects and measures the magnetic moment of a sample. From this, the magnetization and magnetic susceptibility can be determined. Applications of the SQUID magnetometer include measurements of small quantities of paramagnetic ions, characterization of all kinds of magnetic materials, and quantitative determination of the number of unpaired electrons in samples. The MPMS-XL provides solutions for a unique class of sensitive magnetic measurements in key areas such as high-temperature superconductivity, biochemistry, and magnetic recording media.

3.3.3 Specific Heat Measurements

This type of measurement is very essential in this study, as the physics of various types of behaviour at some stages will need to be explained in detail, for example, adiabatic temperature, Debye temperature, phonon and electron contributions, and other unexpected outcomes. Unprecedented ease of use is the first feature of the PPMS Heat Capacity system (Model P650) that has been implemented during this study. Following a simple sample-mounting procedure, the sample mount is inserted into the PPMS sample chamber, the measurement parameters are entered into the software package and the measurement is

initiated. The system automatically accommodates all the necessary temperature, field, and vacuum settings; the data acquisition and analysis; and the data plotting. The option uses a hybrid adiabatic relaxation method that combines excellent measurement accuracy with robust error analysis. The PPMS Heat Capacity option uses the basic PPMS to control environmental variables, such as the temperature and magnetic field, while specialized components perform the heat capacity measurements. The Heat Capacity option includes hardware and software that allow fully automated high-sensitivity heat capacity measurements to be routinely performed between 1.9 K and 400 K (< 0.4 K to 350 K with the Helium-3 System) in magnetic fields up to 14 T.

3.3.4 Resistivity Measurements

Resistivity measurement is an additional method applied in order to confirm that something has happened at a transition temperature or some special stage and can be used to calculated magnetocaloric effect (MCE) values as well. The DC resistivity measurement option to the PPMS used in this study adds resistance bridge capability to the Model 6000 PPMS Controller, featuring a current range of 5 nA to 5 mA, and with voltage sensitivity as low as 20 nV. This bridge provides four independent channels that can be used for measuring up to four samples at one time, which is a very advantage for saving time.

3.3.5 Differential scanning calorimetry (DSC)

Differential scanning calorimeters (DSC) measure the temperatures and heat flows associated with thermal transitions in a material. This method is particularly valuable, as it is not influenced by magnetic field. This type of measurement includes the investigation, selection,

comparison, and end-use performance evaluation of materials in this research, with a view to real applications. TA Instruments Q100 DSC technology was used in this study as a more accurate way of measuring heat flow. It provides significant improvements in baseline flatness, transition resolution, and sensitivity. This advanced equipment allows direct measurement of heat capacity and makes Modulated® DSC experiments both faster and more accurate in the temperature range from 77 K to 550 K.

Chapter 4

MAGNETIC PROPERTIES AND MAGNETOCALORIC EFFECT OF $La_{0.7}Pr_{0.3}Fe_{11.4}Si_{1.6}$

4.1 Effect of Substitution on Fe with Others Metal Transition in $La_{0.7}Pr_{0.3}Fe_{11.4}Si_{1.6}$

The $La_{0.7}Pr_{0.3}Fe_{11.4}Si_{1.6}$ compound which formed in $NaZn_{13}$ type structure attracted many researchers to further investigate regarding to how interesting its behaviour is with tuning or substitution effect. Investigation on how the replacement of transition metal (Fe) in this compound with another transition metal modifies the physical properties and the limitation in the $NaZn_{13}$ type structure with substitution has been reported in this study.

4.1.1 Introduction

Magnetic refrigeration is becoming more reliable, which will enable it to replace conventional refrigeration systems, a change which is desirable because of the advantages of using the magnetocaloric effect (MCE) for applications. This technology has significant advantages - high refrigeration efficiency, environmental friendliness, small volume requirement, low cost, lack of toxicity, and no noise pollution, which makes it attractive for further research, compared with the widely used gas compression refrigeration technology. The MCE was originally discovered by Warburg [1] in 1881, and since the discovery of the giant magnetocaloric effect at room temperature in 1997 [2], magnetic materials with large MCE have been extensively studied experimentally and theoretically, especially over the past

two decades. Up to the present time, a number of materials with giant magnetic entropy changes have been discovered, such as MnFe(As, P) [3], MnCoGeB [4],MnNiGe:Fe [5], $Gd_5Si_2Ge_2$ [2], $(Mn, Fe)_2(P, Ge)$ [6], $MnAs_{1-x}Sb_x$ [7], and $La(Fe,Si)_{13}$ [8-10].

Cubic $NaZn_{13}$-type $La(Fe,Si)_{13}$ has become one of the most interesting systems for exploring large MCE because its magnetic properties are strongly doping dependent, and it shows large enough spontaneous magnetization for applications, as well as soft ferromagnetism [11-13]. These effects can be ascribed to the itinerant-electron metamagnetic (IEM) transition in the vicinity of the first order transition temperature. Doping other magnetic rare-earth elements, such as Pr, Nd, Ce, Er, and Gd, into the La site has been used to change the temperature and to reduce the critical field of the 3d-metamagnetic transition in $La(Fe,Si)_{13}$ compound [14-16] because the rare earth-Fe magnetic coupling displays a strong dependence on the type rare earth. The cubic $NaZn_{13}$-type compound is hard to form by the common solidification process due to the intrinsic incompleteness of the peritectic reaction, $\gamma\text{-Fe+L} \rightarrow La(Fe,Si)_{13}(\tau_{1a})$, which often results in a mixed microstructure of α-Fe + $La(Fe,Si)_{13}(\tau_{1a})$ + $LaFeSi(_{\tau 4})$ [17]. Recent study indicated that silicon (Si) concentration also plays the role to form $NaZn_{13}$ type structure [18]. Moreover stability of $La(Fe_xSi_{1-x})_{13}$ is governed by reaction diffusion according to magnetic and electronic states contribution [19]. Many groups have prepared this compound through annealing at temperatures in the range of 1173-1323 K for ten or more days to form the $NaZn_{13}$-type structure [20-22]. However the peritectic reaction temperature in $La(Fe,Si)_{13}$ is around 1673 K, according to the La-Fe quasi binary diagram [23], and the temperature was found to have an effective role in shortening the phase transformation process [24], as demonstrated by Liu et al. [25] and Chen et al. [26]. Both groups reported that preparation in the temperature range of 1323-1623 K can produce the greatest phase fraction of the $NaZn_{13}$-type structure.

According to Shen et al. [27], the replacement of La by other rare earth elements can lead to remarkable enhancements in the magnetic entropy change. However these phenomena always are accompanied by an increased hysteresis loss because of the features of the first order transition. In the $LaFe_{13-x}Si_x$ structure there are 3 in equivalent atomic sites: (8*a*) occupied by La, (8*b*) occupied by Fe1 and (96*i*) occupied by Fe2 and Si [31]. It was reported that the substitution of Cu for Si can lead to a remarkable reduction in both thermal and magnetic hysteresis in $LaFe_{11.7}(Si_{1-x}Cu_x)_{1.3}$ with reduction the lattice parameter [28]. This present study investigates how the replacement of transition metal (Fe) with another transition metal (Cu and Cr) modifies the physical properties and the limitation of substitution content in the $NaZn_{13}$ type structure. The effects of annealing at different temperatures on the structure and magnetic properties of $La_{0.7}Pr_{0.3}Fe_{11.4}Si_{1.6}$ were also investigated.

4.1.2 Experimental and Procedures

Samples polycrystalline with the nominal compositions $La_{0.7}Pr_{0.3}Fe_{11.4-x}Cu_xSi_{1.6}$ and $La_{0.7}Pr_{0.3}Fe_{11.4-x}Cr_xSi_{1.6}$ (x = 0, 0.06, 0.12, 0.23, 0.34) were prepared by arc melting appropriate amounts of high purity constituent elements under a high purity argon atmosphere in a water-cooled copper crucible. The starting materials were pure elements ($\geqslant$ 99.9%), and excesses of 10 at. % for La were used to compensate for the weight loss during the arc melting [29]. The ingots were turned over and re-melted several time to ensure their homogeneity. The resulting ingots were wrapped in tantalum foil and sealed under vacuum in a quartz tube, then annealed by the following processes: a $La_{0.7}Pr_{0.3}Fe_{11.4}Si_{1.6}$ sample was annealed at 1323 K for 14 days, while $La_{0.7}Pr_{0.3}Fe_{11.4-x}Cu_xSi_{1.6}$ and $La_{0.7}Pr_{0.3}Fe_{11.4-x}Cr_xSi_{1.6}$ samples with x = 0, 0.06, 0.12, 0.23, 0.34 were annealed at 1523 K for 4 hours, respectively, to improve crystallization of the samples. Afterwards, the samples were quenched in water.

Room temperature powder x-ray diffraction (XRD) measurements were performed using Cu $K_{\alpha 1}$ radiation to identify phase purity. The crystal structures of the samples were checked by room temperature powder XRD with the diffraction patterns refined using the Fullprof software package [30], scanning electron microscopy (SEM) and energy dispersive spectrometer (EDS). The vibrating sample magnetometer option of a Quantum Design 14 T physical property measurement system (PPMS) and an MPMS XL magnetic property measurement system (MPMS) were used to determine the magnetic and MCE properties. The crystallographic and magnetic structural behaviors of the set of $La_{0.7}Pr_{0.3}Fe_{11.06}Cr_{0.34}Si_{1.6}$ samples were investigated over the temperature range 3-450 K by neutron powder diffraction experiments using the high intensity powder diffractometer Wombat (2.4205(2) Å) at OPAL, and high intensity x-ray diffraction (λ = 0.8265(8) Å) at Australian Synchrotron.

4.1.3 Result and Discussion

4.1.3.1 $La_{0.7}Pr_{0.3}Fe_{11.4-x}Cu_xSi_{1.6}$

It is well accepted that the phase percentage of impurity phases in the $NaZn_{13}$-type compounds is particularly related to the preparation process [25, 26]. Recently systematic study on phase stability of $NaZn_{13}$-type was carried out on the basis of various cross section of the ternary phase diagram [18]. From this point of view, $La_{0.7}Pr_{0.3}Fe_{11.4}Si_{1.6}$ was selected to be prepared by two different annealing treatments to clarify which method is more practical and produces better quality samples. Results from the XRD data (as shown in Figure 4.1) indicate that high temperature annealing (HTA) over a short time can form more $NaZn_{13}$–type phase than low temperature annealing (LTA) over a longer time. LTA produces much more LaFeSi and the α-Fe phase in $La_{0.7}Pr_{0.3}Fe_{11.4}Si_{1.6}$. It is clearly shown in Table 4.1 that

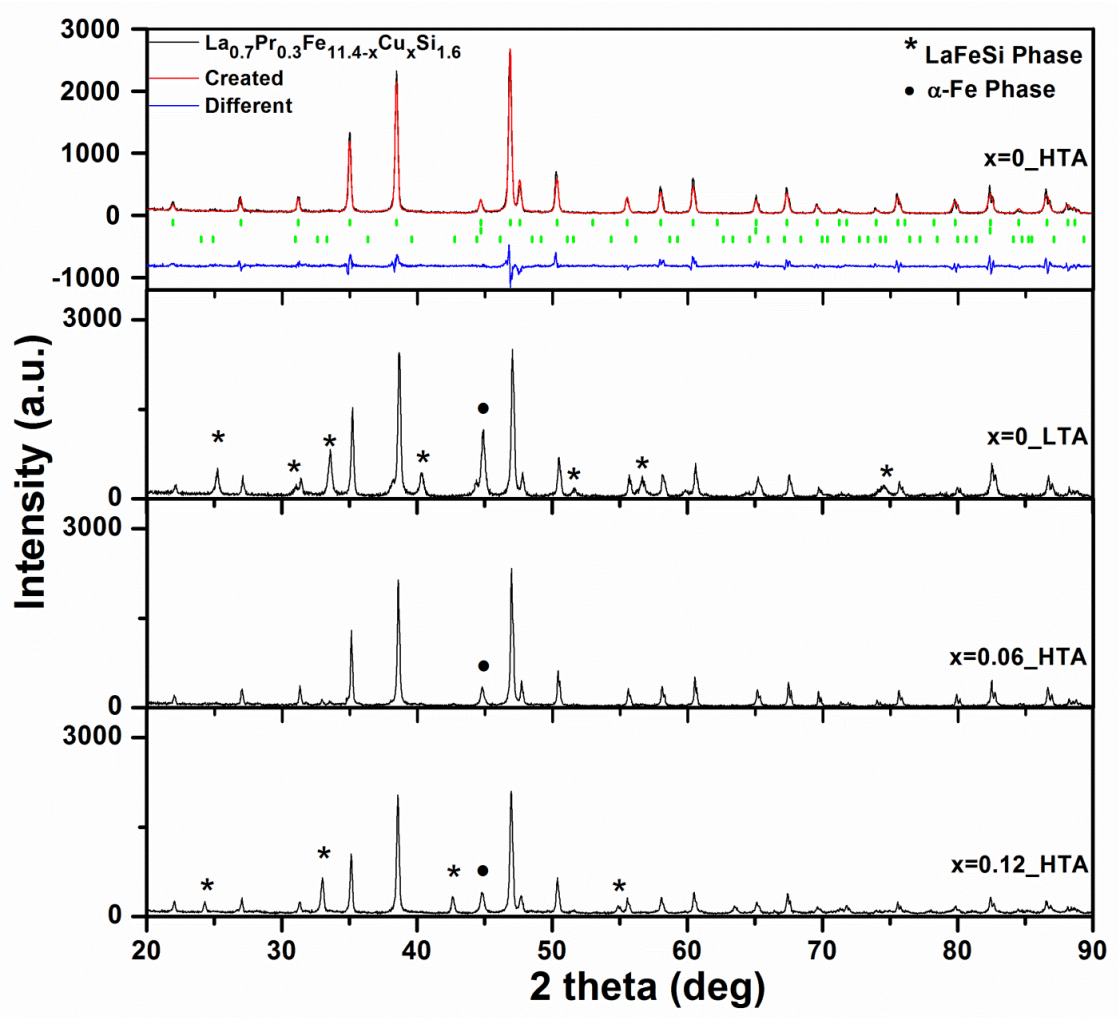

Figure 4.1 Room temperature x-ray diffraction patterns of $La_{0.7}Pr_{0.3}Fe_{11.4-x}Cu_xSi_{1.6}$ (x = 0, 0.06, 0.12) produced by the HTA and LTA processes. Rietveld refinements to the experimental diffraction patterns for x=0 sample by the HTA are shown as a typical example. The lines show the calculated profiles through the experimental data and the residuals. The markers for the crystallographic structures (top for $NaZn_{13}$ phase, middle for α-Fe and bottom for LaFeSi) are indicated.

the LTA process results in smaller amounts of the $NaZn_{13}$ phase through a peritectic reaction. (The results refer to the refined composition). This phenomenon regarding non-equilibrium solidification behaviour is the result of an incomplete peritectic reaction, γ-Fe+L → $La(Fe,Si)_{13}(\tau_{1a})$ [17]. This behaviour similar to Niitsu et al. [18] where below 1373 K the $NaZn_{13}$–type phase is difficult to be formed even being annealed after 45 days. When the annealing temperature is higher, the speed of diffusion of atoms is higher during the high temperature and solid phase diffusion reaction process. Thus, on increasing the annealing

temperature to 1523 K and annealing for 4 hours (HTA), the amount of the $NaZn_{13}$ phase gradually increases, eliminating almost all of the LaFeSi phase and decreasing the amount of the α-Fe phase. The Rietveld refinement results are listed in Table 4.1, and it can be clearly seen that the weight fraction of the $NaZn_{13}$ phase increases from 69 % for LTA to 96 %, while the weight fractions of LaFeSi and α-Fe phase for HTA are reduced. Indicated to obtain single $NaZn_{13}$–type phase by a peritectic reaction is quite difficult using conventional melting [18] and substitution of Fe by Cu in $NaZn_{13}$–type phase contribute to change stability of metallic, magnetic and electronic state [19]. The constituents of the $NaZn_{13}$ phase obtained at 1523 K after 4 hours annealing are in agreement with reports from other groups [25, 26].

$La_{0.7}Pr_{0.3}Fe_{11.4-x}Cu_xSi_{1.6}$ (x = 0, 0.06, 0.12, 0.23, 0.34) compounds were prepared using HTA at 1523 K for 4 hours. The XRD patterns in Figure 4.1 clearly show that Cu doping contributes to an increased amount of α-Fe and LaFeSi phases in $La_{0.7}Pr_{0.3}Fe_{11.4-x}Cu_xSi_{1.6}$. It was been found when the amount of Cu in $La_{0.7}Pr_{0.3}Fe_{11.4-x}Cu_xSi_{1.6}$ increases, the peak intensities of the α-Fe and LaFeSi phases gradually start to increase. We suggest that this behaviour is related to bulk diffusion rate controlling factor of homogenization in $NaZn_{13}$–type phase by substitution Cu for Fe. From Table 4.1, it can be seen that the weight fraction of the $NaZn_{13}$ phase decreases from 96 % at x = 0 to 85 % at x = 0.34, while the LaFeSi and α-Fe phase fractions in $La_{0.7}Pr_{0.3}Fe_{11.4-x}Cu_xSi_{1.6}$ increase with the increasing Cu substitution. In the La-Fe-Si ternary system, the chemical affinity is very strong for La-Si, while it is just moderate for Fe-Si. The enthalpy of mixing for La-Fe is positive, which means no formation of binary La-Fe phase [31]. The introduction of Cu into $La_{0.7}Pr_{0.3}Fe_{11.4-x}Cu_xSi_{1.6}$ starts to produce large differences in affinity between the La-Si and the La-Fe pairs, gradually changing the interatomic distances of the pairs, while the structural stability of clusters (domains of $NaZn_{13}$ structure) will be lowered. Recently the study by Fujita et al. [19] shown

that diffusion is also sensitive to modification of both the electronic structure and lattice spacing which agrees with the fact that Cu atomic radius (1.28 Å) is larger than Fe atomic

Table 4.1 Synthesis conditions (heat treatment process) and results of the structural characterization (phase observed, analysed compositions, lattice parameter of the $NaZn_{13}$, α-Fe, and LaFeSi phases; and atomic distances (Fe1-Fe2 and Fe2-Fe2) of $NaZn_{13}$) from XRD. (Statistical uncertainties are given in parentheses)

Nominal composition	Heat treatment (T(K)/t)	Phase	Wt%	Refined composition	Lattice parameter, *a* (Å)	Atomic Distance (Å) for Fe1-Fe2	Fe2-Fe2
$La_{0.7}Pr_{0.3}Fe_{11.4}Si_{1.6}$	1323K/14 days	$NaZn_{13}$	69.1(1)	$La_{0.7}Pr_{0.3}Fe_{14.1(2)}Si_{2.1(2)}$	11.4510(3)	-	
		α-Fe	19.4(8)				
		LaFeSi	11.5(4)				
$La_{0.7}Pr_{0.3}Fe_{11.4}Si_{1.6}$	1523K/4 hours	$NaZn_{13}$	96.1(2)	$La_{0.7}Pr_{0.3}Fe_{11.(3)}Si_{1.6(2)}$	11.4585(5)	2.4508(2)	2.5522(3)
		α-Fe	3.5(6)				
		LaFeSi	0.4(5)				
$La_{0.7}Pr_{0.3}Fe_{11.34}Cu_{0.06}Si_{1.6}$	1523K/4 hours	$NaZn_{13}$	91.7(2)	$La_{0.7}Pr_{0.3}Fe_{11.03}Cu_{0.06}Si_{1.62}$	11.4604(3)	2.4512(3)	2.5527(2)
		α-Fe	7.3(4)				
		LaFeSi	1.0(4)				
$La_{0.7}Pr_{0.3}Fe_{11.28}Cu_{0.12}Si_{1.6}$	1523K/4 hours	$NaZn_{13}$	88.2(2)	$La_{0.7}Pr_{0.3}Fe_{11.05}Cu_{0.12}Si_{1.67}$	11.4627(4)	2.4517(2)	2.5531(2)
		α-Fe	9.1(5)				
		LaFeSi	2.7(3)				
$La_{0.7}Pr_{0.3}Fe_{11.17}Cu_{0.23}Si_{1.6}$	1523K/4 hours	$NaZn_{13}$	86.8(1)	$La_{0.7}Pr_{0.3}Fe_{11.08}Cu_{0.23}Si_{1.68}$	11.4650(4)	2.4521(2)	2.5536(2)
		α-Fe	10.2(8)				
		LaFeSi	3.0(2)				
$La_{0.7}Pr_{0.3}Fe_{11.06}Cu_{0.34}Si_{1.6}$	1523K/4 hours	$NaZn_{13}$	85.2(8)	$La_{0.7}Pr_{0.3}Fe_{11.12}Cu_{0.34}Si_{1.71}$	11.4662(4)	2.4525(2)	2.5540(1)
		α-Fe	10.6(4)				
		LaFeSi	4.2(4)				

radius (1.24 Å) in this study. If the amount of replacement of Fe by Cu further increases, it contributes to an increased amount of α-Fe and LaFeSi, making it impossible to form the $NaZn_{13}$ phase structure. This situation is proved by the high magnification SEM image in Figure 4.2, which shows that the percentage of $NaZn_{13}$ phase starts to decrease with increasing Cu content in $La_{0.7}Pr_{0.3}Fe_{11.4-x}Cu_xSi_{1.6}$. Figure 4.2(b) with the highest Cu concentration shows clearly how the substitution of Cu into the Fe site reduces the weight fraction of $NaZn_{13}$ phase indicating the presence of the limitations of Cu substitution for the structural stability of $NaZn_{13}$ phase.

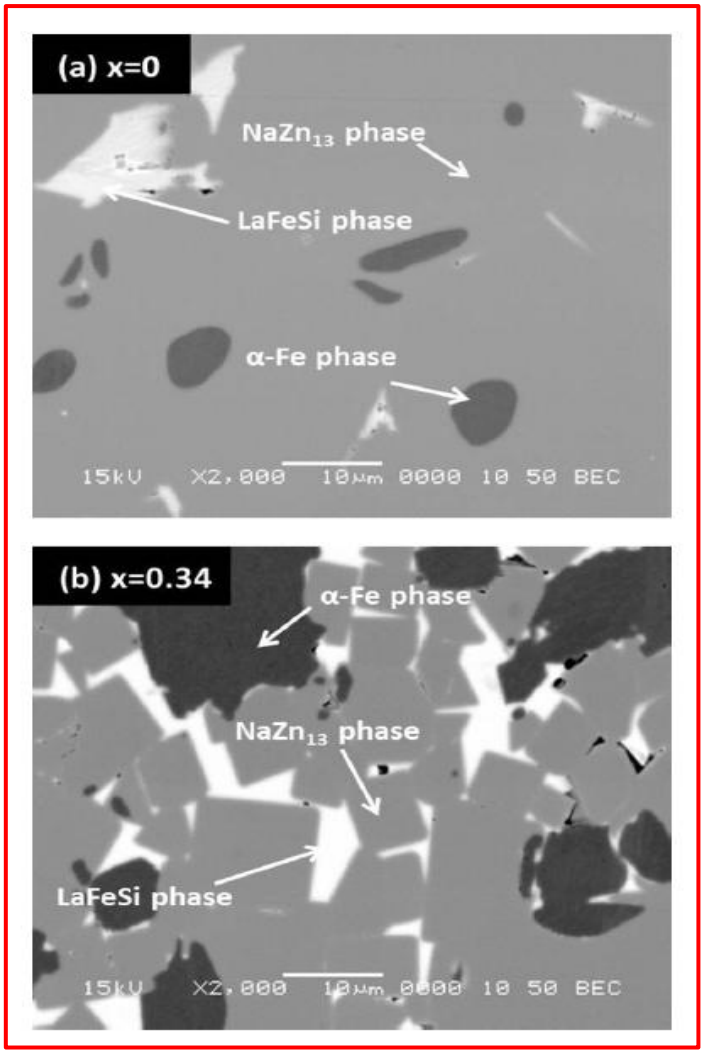

Figure 4.2 High magnification backscattered SEM images of $La_{0.7}Pr_{0.3}Fe_{11.4-x}Cu_xSi_{1.6}$ samples: (a) x = 0 and (b) x = 0.34.

Figure 4.3 shows the temperature dependence of the magnetization of $La_{0.7}Pr_{0.3}Fe_{11.4-x}Cu_xSi_{1.6}$ for x = 0, with preparation by LTA and HTA, and the lowest level of Cu substitution, x = 0.06, with preparation by HTA, measured under the low magnetic field of 0.01 T in the temperature range from 100-300 K. The T_C shown in the inset was defined by the minimum of dM/dT. T_C of $La_{0.7}Pr_{0.3}Fe_{11.4}Si_{1.6}$ produced by the LTA method is 10 K higher than by HTA and has different magnetic phase transition characteristics because of the different Si concentration in the $NaZn_{13}$ phase, which is that the LTA method forms higher Si composition and contributes to increase T_C and changes the nature of transition from first to

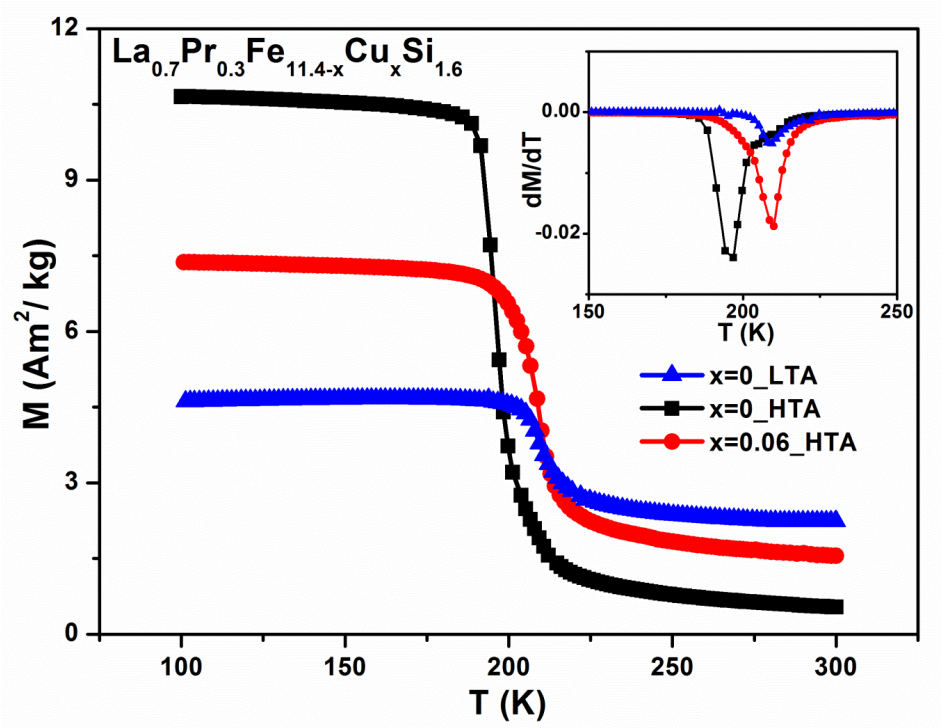

Figure 4.3 Temperature dependence of magnetization of $La_{0.7}Pr_{0.3}Fe_{11.4-x}Cu_xSi_{1.6}$ for x = 0 with LTA, and x = 0, x = 0.06 with HTA, measured in a field of 0.01 T. The inset shows the values of the Curie temperature (T_C) for the different samples.

second order characteristic [12]. We assume the LTA treatment interacts to form more α-Fe and LaFeSi phase but decreases $NaZn_{13}$ phase content regarding to temperature and time during annealing process difficulty in solution treatment at low temperature contribute to increase Si composition. In Table 4.1, it is indicated from XRD data refinement that the proportion of Si in the $NaZn_{13}$ phase for LTA is higher than for HTA. In terms of the effects of increasing the Si concentration in $NaZn_{13}$ phase, we assume that this phenomenon contributes to increasing the value of T_C and changes the phase transition behaviour. Similar behaviour has also been reported by Bo Liu *et al.* [31] where the effects of Cu doping were found to increase the T_C and change the magnetic phase transition from first to second order type. It was accepted that two types of exchange interactions exist between Fe-Fe in the Fe-rich rare earth intermetallic compounds: when the separation of the Fe–Fe pair is smaller than 2.45 Å, the exchange interaction is negative, while the interaction is positive at larger Fe–Fe

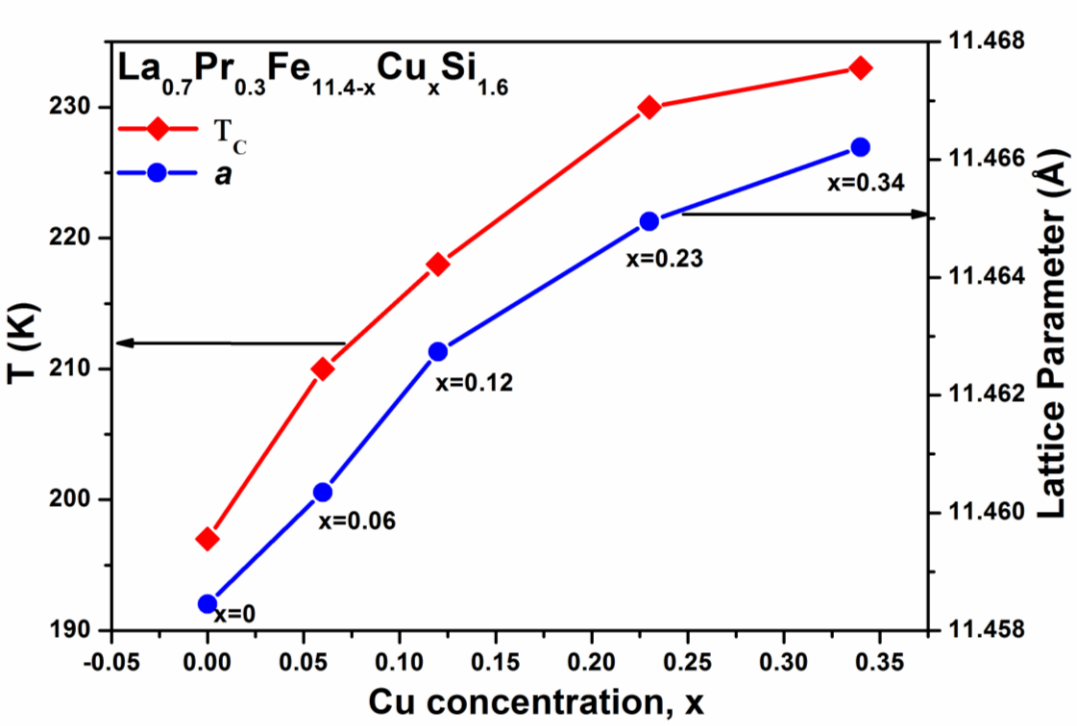

Figure 4.4 Curie temperature and lattice parameter for $La_{0.7}Pr_{0.3}Fe_{11.4-x}Cu_xSi_{1.6}$ samples as functions of copper concentration.

distances. It was reported [31] that in the $La(Fe,Si)_{13}$ structure, there exist one La site (8*a* site), two Fe sites Fe1 (8*b* site) and Fe2 (96*i* site). It was reported that in the $LaFe_{13-x}Si_x$ compounds the La atom (8*a*) has 24 near neighbours of Fe2 (Fe or Si) atoms (96*i*), but no near neighbours of Fe1 atoms (8*b*) while the Fe2 atom has nine near neighbours of Fe2 in addition to two neighbours of La and one neighbour of Fe1. The Fe1 is surrounded by 12 near neighbours of Fe2 (Fe or Si) atoms. The interatomic distances of Fe-Fe between the near neighbours Fe1–Fe2 and Fe2–Fe2 can be directly derived from Wigner–Seitz calculations. For $LaFe_{11.4}Si_{1.6}$, it was found that the Fe1–Fe2 atomic distance, is 2.443 Å and the Fe2-Fe2 being about 2.53 Å [31]. Based on the fact that the atomic radius of Cu (1.28 Å) is bigger than that of Fe (1.24 Å), Cu doping will lead to an increase in the lattice parameter and the Fe-Fe distance, which will enhance the positive interactions, thus increasing T_C. The composition dependences of T_C and the lattice parameter are shown in Figure 4.4. The Fe1-Fe2 and Fe2-Fe2 distances have been obtained with the BLOKJE program [32] using the

structural and positional parameters and listed in Table 4.1. It can be seen clearly that the substitution of Cu for Fe leads to a monotonic increase in both T_C and lattice parameter resulting in an increment of Fe1-Fe2 and Fe2-Fe2 distance even though the Cu substitution for Fe results in a dilution of magnetic atom (Fe) content.

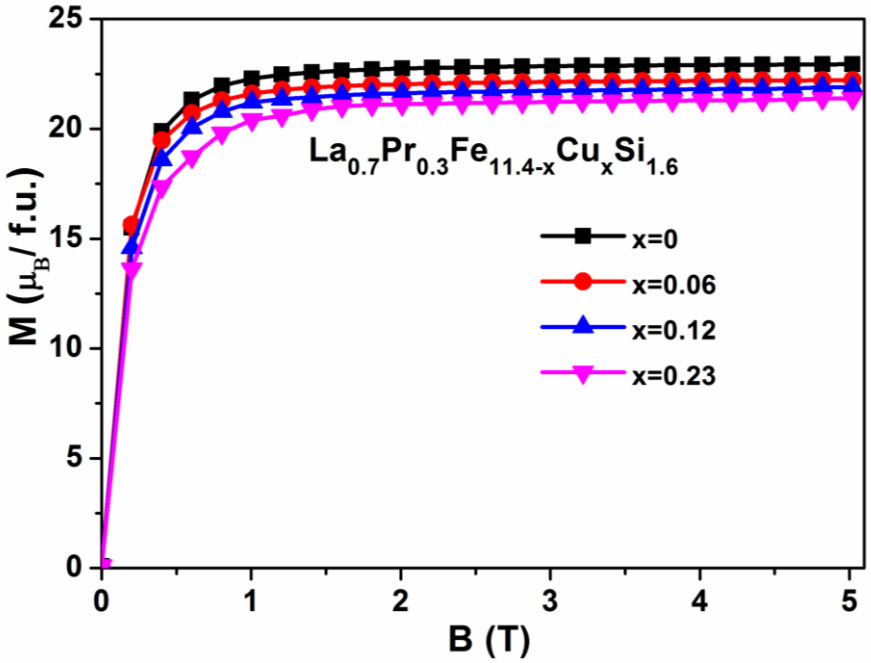

Figure 4.5 Magnetization (M) as a function of a magnetic field (H) for $La_{0.7}Pr_{0.3}Fe_{11.4-x}Cu_xSi_{1.6}$ samples with x = 0, 0.06, 0.12, 0.23 at T = 10 K.

Figure 4.5 shows the magnetization versus magnetic field from 0-5 T for $La_{0.7}Pr_{0.3}Fe_{11.4-x}Cu_xSi_{1.6}$ (x = 0, 0.06, 0.12, 0.23) at 5 K. All the compounds were found to exhibit ferromagnetic behaviour with a magnetization below 24 μ_B/f.u. at field applied less than 2 T. According to the characteristics of Cu as a diamagnetic element, the replacement of Fe by Cu will reduce the saturation magnetization field in $La_{0.7}Pr_{0.3}Fe_{11.4-x}Cu_xSi_{1.6}$ compound as clearly shown in Table 4.2. If we assume that the Pr moment contribution does not change with increasing Cu content, the average moment of the Fe can be derived from the total moment. It is found that the replacement of Fe by Cu leads to a decrease in the average moment of the Fe in $La_{0.7}Pr_{0.3}Fe_{11.4-x}Cu_xSi_{1.6}$. For the sample with x = 0.34, the value of the saturation

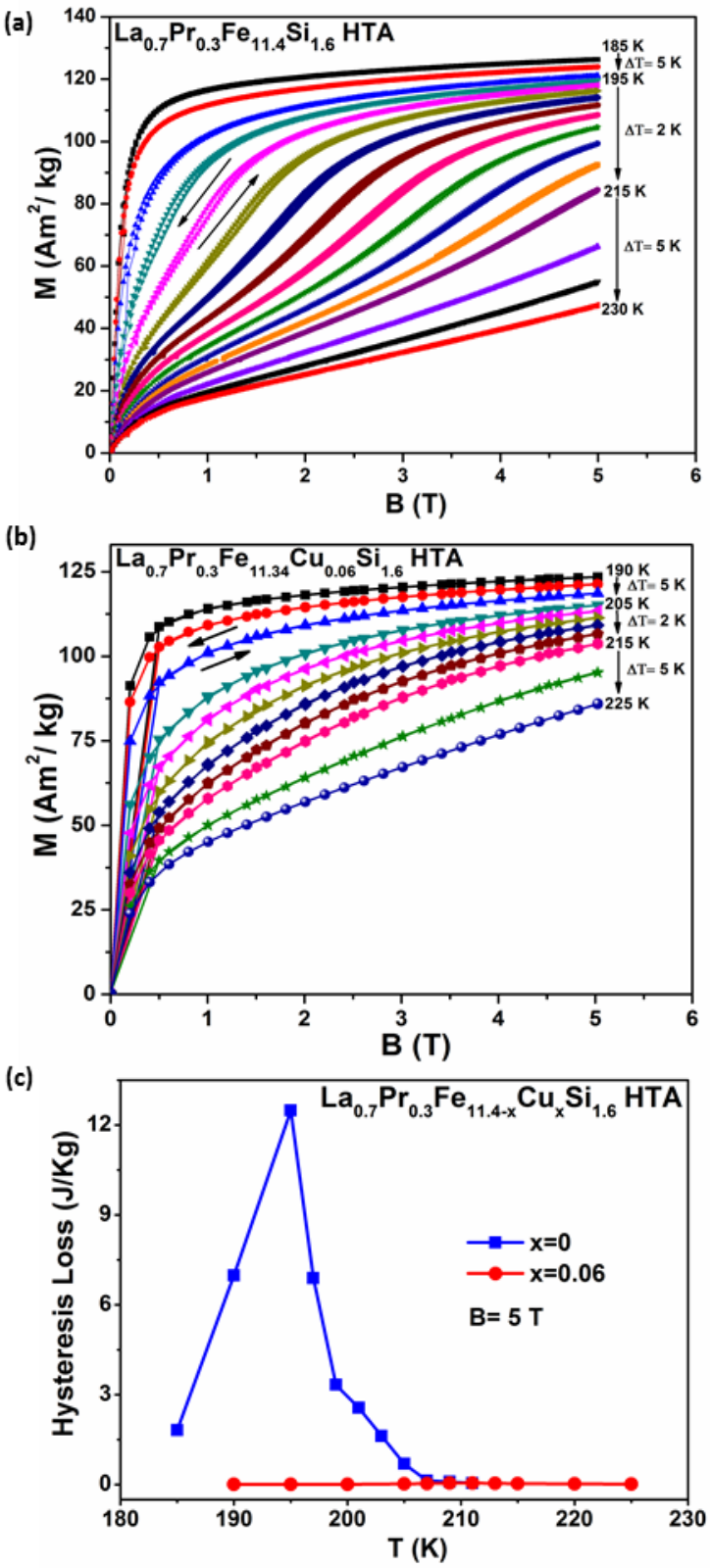

Figure 4.6 Isothermal magnetization curves M (H) in the vicinity of T_C for (a) $La_{0.7}Pr_{0.3}Fe_{11.4}Si_{1.6}$ and (b) $La_{0.7}Pr_{0.3}Fe_{11.34}Cu_{0.06}Si_{1.6}$, both produced by the HTA process. (c) Magnetic hysteresis loss for both at 5 T field applied.

magnetization is higher than expected, which can be ascribed to the contribution from the large amount of α-Fe moment in $La_{0.7}Pr_{0.3}Fe_{11.06}Cu_{.34}Si_{1.6}$.

Table 4.2 Results of the magnetic characterization of HTA $La_{0.7}Pr_{0.3}Fe_{11.4-x}Cu_xSi_{1.6}$ (x = 0, 0.06, 0.12, 0.23, 0.34) and of LTA x = 0 compound. The Curie temperature is given for a magnetic field of 0.01 T, order of magnetic transition, the saturation magnetization is given at 10 K, and the magnetic entropy change and the relative cooling power are given for a field of 0-5 T. (Statistical uncertainties are given in parentheses)

Refined composition	T_C (K)	Order of Transition	M_S (μ_B/ f.u.) at 5K	$-\Delta S_M$ (J/kg K)	RCP (J/Kg) for 5T
$La_{0.7}Pr_{0.3}Fe_{14.10}Si_{2.10}$_LTA	210	Second	-	7(2)	220(1)
$La_{0.7}Pr_{0.3}Fe_{11.0}Si_{1.60}$_HTA	197	First	22.8(3)	17(2)	400(2)
$La_{0.7}Pr_{0.3}Fe_{11.03}Cu_{0.06}Si_{1.62}$_HTA	210	Second	22(2)	12(1)	330(2)
$La_{0.7}Pr_{0.3}Fe_{11.05}Cu_{0.12}Si_{1.67}$_HTA	218	Second	21.6(2)	9(2)	300(1)
$La_{0.7}Pr_{0.3}Fe_{11.08}Cu_{0.23}Si_{1.68}$_HTA	224	Second	21(1)	7(2)	280(1)
$La_{0.7}Pr_{0.3}Fe_{11.12}Cu_{0.34}Si_{1.71}$_HTA	230	Second	21.4(2)	5(1)	245(2)

The corresponding Arrott plots (M^2 versus B/M) are drawn in Figure 4.7. It was well accepted that the positive slopes in the isotherm Arrott plots indicate the second-order nature of the phase transition around T_C while negative aslope for first order transition according to I-S model [26]. It can be seen from Figure 4.7 that the replacement of Fe by Cu in $La_{0.7}Pr_{0.3}Fe_{11.4}Si_{1.6}$ has changed the slope from negative to positive and reduced the characteristics of the IEM transition above T_C [12] (summary in Table 4.2) .

Magnetic entropy change, $-\Delta S_M$, is defined from the magnetization curve by the Maxwell relation [33, 34]:

$$-\Delta S_M(T,H) = \int_0^H \left(\frac{\partial M}{\partial T}\right)_H dH \qquad (4.1)$$

The values of $-\Delta S_M$ around T_C have been derived from the magnetic data and are shown in Figure 4.8 (a) as a function of temperature with a 0-5 T change in field for $La_{0.7}Pr_{0.3}Fe_{11.4-}$

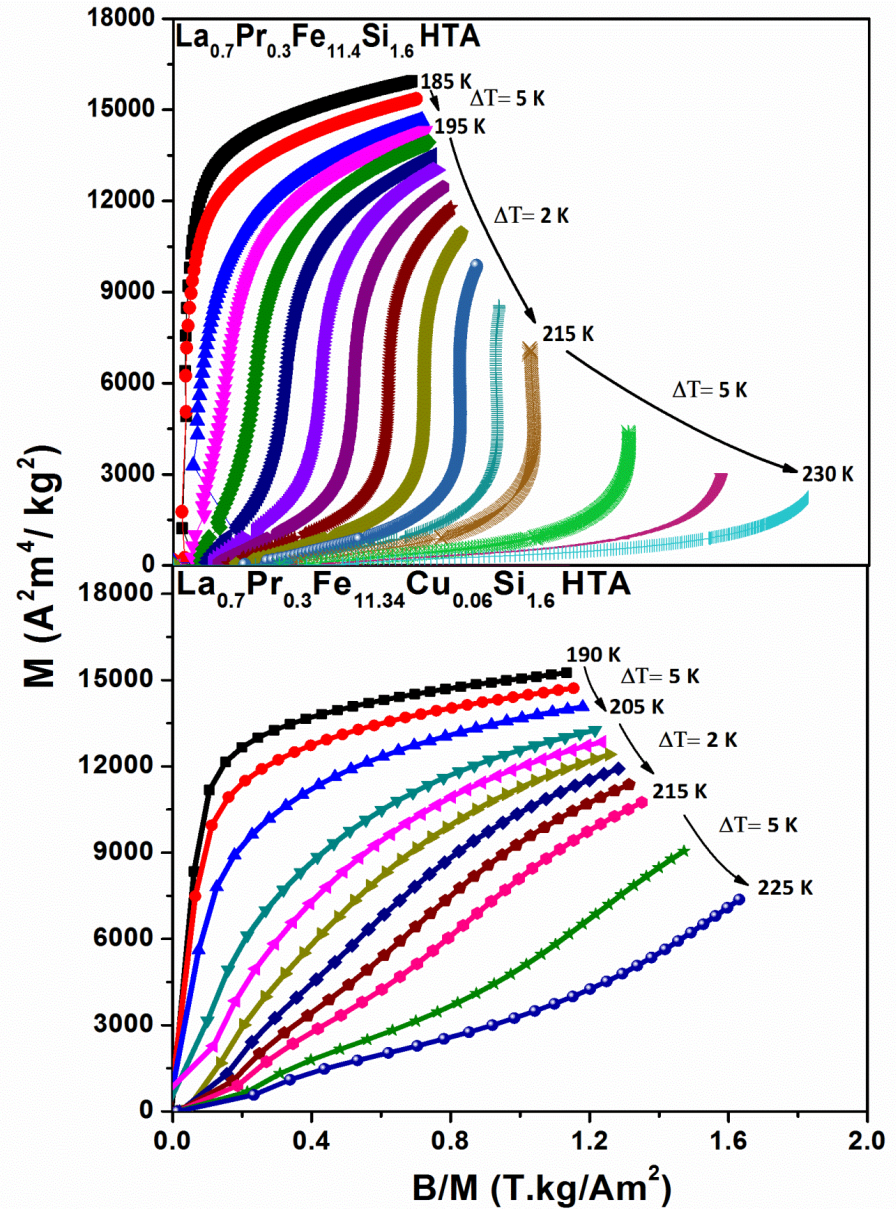

Figure 4.7 Arrott plots for $La_{0.7}Pr_{0.3}Fe_{11.4-x}Cu_xSi_{1.6}$ (x = 0 and 0.06) compounds.

$_xCu_xSi_{1.6}$ (x = 0, 0.06, 0.34) for HTA and (x = 0) for LTA compounds. It can be seen clearly that the $-\Delta S_M$ peak gradually becomes broader at higher temperature with increasing magnetic field from 1 to 5 T, which is a characteristic of the field induced IEM transition from the paramagnetic to the ferromagnetic state at temperatures above T_C. This is clearly evident for the HTA compound with x = 0 in Figure 4.8 (b). The value of $-\Delta S_M$ for the LTA x = 0 compound is very small, around 7 J/kgK compared to 17 J/kgK for the HTA x = 0 sample,

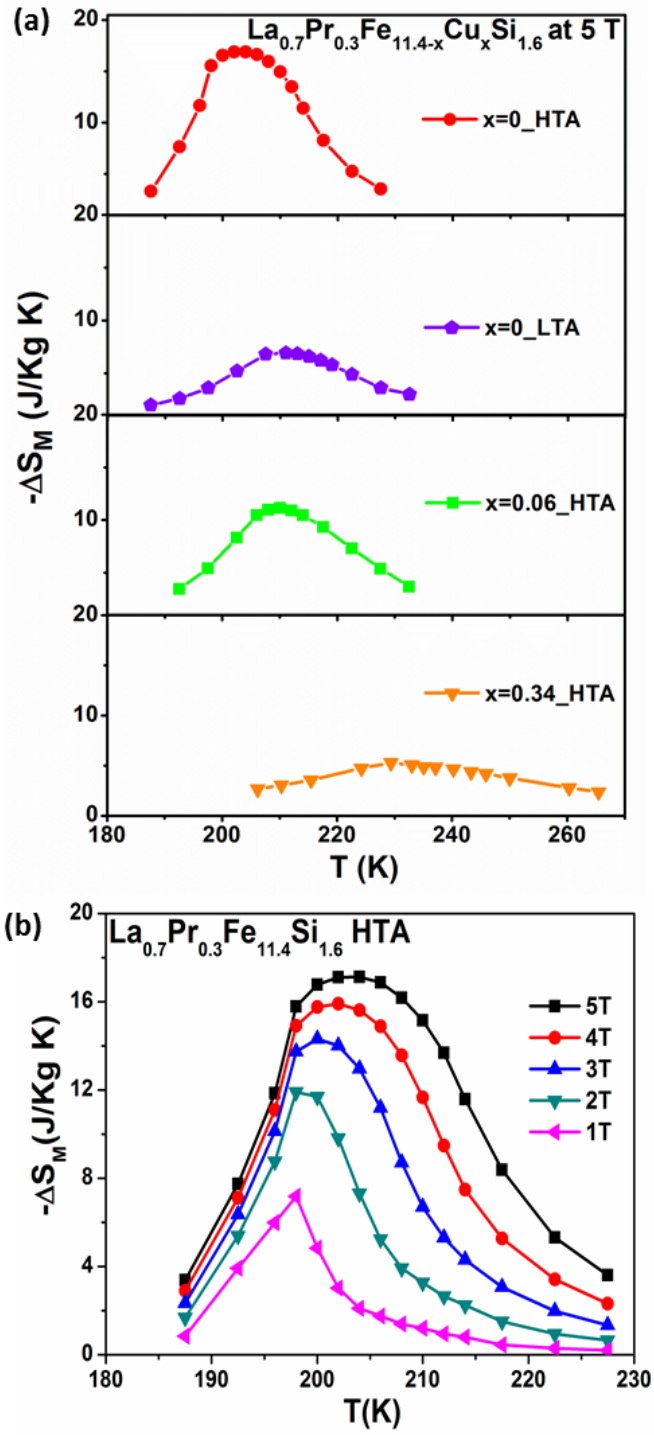

Figure 4.8 Magnetic entropy change, $-\Delta S_M$, (a) for a 0-5 T change in field of $La_{0.7}Pr_{0.3}Fe_{11.4-x}Cu_xSi_{1.6}$ (x = 0, 0.06, 0.34) for HTA and x = 0 for LTA compounds and (b) from 0 to 1, 2, 3, 4 and 5 T change in field of $La_{0.7}Pr_{0.3}Fe_{11.4}Si_{1.6}$ compound for HTA as a function of temperature.

which is larger than that observed in Gd (10.2 J/kgK). We ascribe this effect to the lower percentage of the $NaZn_{13}$ type phase in the LTA sample with x = 0. Moreover, it has been

found that the replacement of Fe by Cu decreases $-\Delta S_M$ from 12 J/kgK for x = 0.06 to 5 J/kgK for x = 0.34.

The relative cooling power (RCP) is a very important aspect of the MCE, and it is directly related to the magnetic refrigerator application. Using the maximum of the entropy variation $-\Delta S_M^{max}$ and the full width at half maximum of the peak in the temperature dependence of the magnetic entropy change $-\Delta S_{M,}$ one can derive the value of RCP as defined by the following formula [22, 35]:

$$RCP = -\Delta S_M^{max} \delta T^{FWHM} \quad (4.2)$$

A summary of RCP values and other magnetic characterization parameters for HTA $La_{0.7}Pr_{0.3}Fe_{11.4-x}Cu_xSi_{1.6}$ (x = 0, 0.06, 0.12, 0.23, 0.34) and LTA x = 0 compounds are listed in Table 4.2. It can be seen that the HTA process yields a significant improvement in sample quality compared to LTA, considering the superior values of $-\Delta S_M$ and RCP. However, the value of the saturation magnetization was reduced by increasing the Cu content. This lead to a decrease in the magnetic entropy change when the concentration of Cu increases from x = 0 to x = 0.34. The RCP shows the same behaviour with MCE, even though an increase in Cu content changes the type of magnetic phase transition from first order to second order and increases the temperature span. It was found that the RCP decreases from 400 J/kg for x = 0 to 245 J/kg for x = 0.34 on application of a 0 to 5 Tesla magnetic field change.

4.1.3.2 $La_{0.7}Pr_{0.3}Fe_{11.4-x}Cr_xSi_{1.6}$

The room temperature diffraction analysis in Table 4.3 shown that the Cr substitution first contributes to an increase the amount of α-Fe and LaFeSi phases from beginning to x=0.06 then decrease until x=0.34 in $La_{0.7}Pr_{0.3}Fe_{11.4-x}Cr_xSi_{1.6}$ compounds. We suggest this behavior may be related to bulk diffusion rate controlling factor of homogenization in cubic $NaZn_{13}$– type phase structure (space group *Fm3c*) by substitution Cr for Fe. From Table 4.3, it can be seen that the weight fraction of the $NaZn_{13}$ structure decreases from 96 % at x = 0 to 85 % at x = 0.06 then increase to 97 % with increasing Cr content till x=0.34.

Table 4.3 Results of the structural characterization (type and weight of phase observed, lattice parameter of the $NaZn_{13}$, α-Fe, and LaFeSi phases; and atomic distances (Fe1-Fe2 and Fe2-Fe2) of $NaZn_{13}$) from room temperature x-ray diffraction analysis and Curie temperature, T_C for $La_{0.7}Pr_{0.3}Fe_{11.4-x}Cr_xSi_{1.6}$ compounds.

Nominal composition	Phase	Wt%	Lattice parameter, *a* (Å)	Atomic Distance (Å) for Fe1-Fe2	Fe2-Fe2	T_C (K)
$La_{0.7}Pr_{0.3}Fe_{11.4}Si_{1.6}$	$NaZn_{13}$	96.1(2)	11.4585(5)	2.4508(2)	2.5522(3)	197
	α-Fe	3.5(6)				
	LaFeSi	0.4(5)				
$La_{0.7}Pr_{0.3}Fe_{11.34}Cr_{0.06}Si_{1.6}$	$NaZn_{13}$	85.9(1)	11.4556(4)	2.4506(3)	2.5521(2)	180
	α-Fe	10.6(6)				
	LaFeSi	3.5(3)				
$La_{0.7}Pr_{0.3}Fe_{11.28}Cr_{0.12}Si_{1.6}$	$NaZn_{13}$	92.6(1)	11.4540(3)	2.4505(4)	2.5517(2)	185
	α-Fe	6.0(3)				
	LaFeSi	1.4(6)				
$La_{0.7}Pr_{0.3}Fe_{11.17}Cr_{0.23}Si_{1.6}$	$NaZn_{13}$	94.0(1)	11.4524(3)	2.4501(3)	2.5515(2)	190
	α-Fe	4.7(6)				
	LaFeSi	1.3(2)				
$La_{0.7}Pr_{0.3}Fe_{11.06}Cr_{0.34}Si_{1.6}$	$NaZn_{13}$	97.6(6)	11.4518(2)	2.4996(3)	2.5511(1)	195
	α-Fe	2.3(3)				
	LaFeSi	0.2(4)				

As mentioned by Liu Xu *et al.*,[31] in the La-Fe-Si ternary system, the chemical affinity is very strong for La-Si, while it is just moderate for Fe-Si. The enthalpy of mixing for La-Fe is

positive, which means no formation of binary La-Fe phase. The introduction of Cr into $La_{0.7}Pr_{0.3}Fe_{11.4-x}Cr_xSi_{1.6}$ starts to produce large differences in affinity between the La-Si and the La-Fe pairs, gradually changing the interatomic distances of the pairs, while the structural stability of clusters (domains of $NaZn_{13}$ structure) will be lowered. That diffusion also sensitive to modification of both the electronic structure and lattice spacing [19] agree with phenomena of lattice parameter *a*, which decreases from 11.458(3) Å at x=0 to 11.451(5) Å at x=0.34 even Cr atomic radius (1.3 Å) is larger than Fe atomic radius (1.26 Å) and different electronic environment (Fe ~ $3d^64s^2$ and Cr ~ $3d^54s^1$) in this study. This situation is proved by the high magnification SEM image in Figure 4.9(a) and (b), which shows that the percentage of $NaZn_{13}$ phase for x=0.34 are higher than x=0.06 presence of the advantage in increasing Cr concentration. In order to justify if the Cr entered in the $NaZn_{13}$ phase structure, EDS analysis has been performed and proved that Cr exists in the $NaZn_{13}$ phase structure as expected by using comparison for x=0 and highest Cr concentration x=0.34.

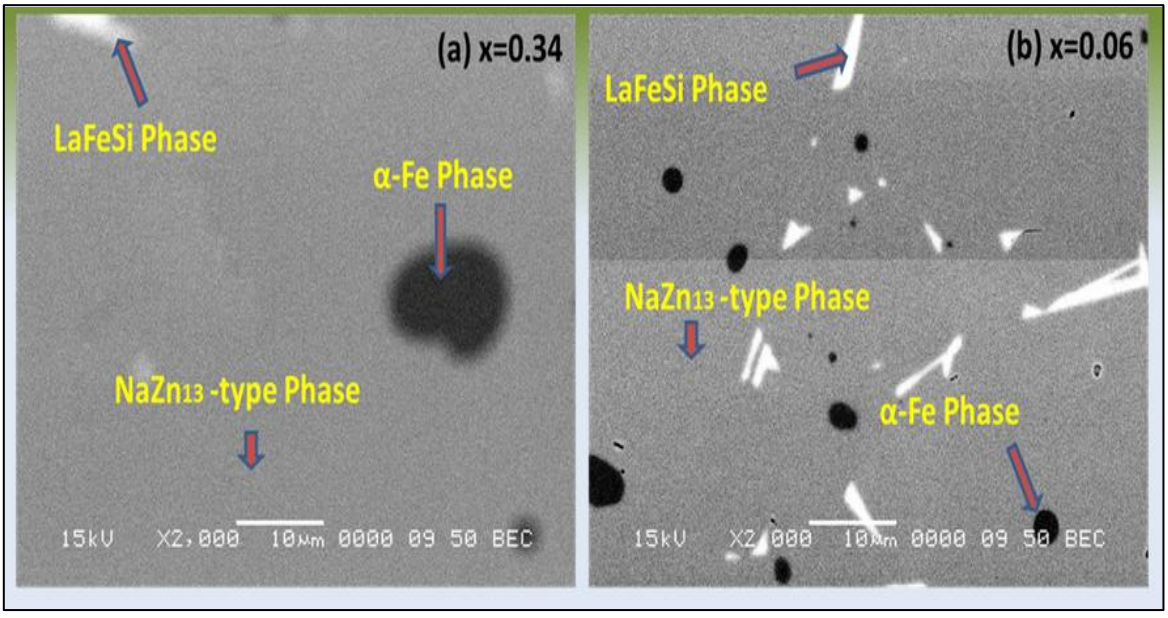

Figure 4.9 High magnification backscattered SEM images of $La_{0.7}Pr_{0.3}Fe_{11.4-x}Cr_xSi_{1.6}$ samples: (a) x = 0.34 and (b) x = 0.06.

The temperature dependence of the magnetization of $La_{0.7}Pr_{0.3}Fe_{11.4-x}Cr_xSi_{1.6}$ compound is measured under the low magnetic field of 0.01 T. The T_C shown in Table 4.3 was defined by

the minimum of dM/dT. T_C was found to decrease first from 197 K at x=0 to 180 K at x=0.06 but start to increase to 185 K at x=0.12 until 195 K at higher Cr concentration x=0.34. We assume more presence of α-Fe and LaFeSi phase at lower Cr concentration is responsible for the variation in value of T_C as both of these phases are impurity. However, both of these phases are not critical to the nature of magnetic phase transition as we found that the first order phase transition behaviour did not change compared to other study [36]. The variation of the T_C values with the Cr content in these compounds happen accordingly to two types of exchange interactions exist between Fe-Fe in the Fe-rich rare earth intermetallic compounds: when the separation of the Fe–Fe pair is smaller than 2.45 Å, the exchange interaction is negative, while the interaction is positive at larger Fe–Fe distances. The Fe1-Fe2 and Fe2-Fe2 distances have been obtained with the BLOKJE program [32] using the structural and positional parameters and listed in Table 4.3. It can be seen clearly that the substitution of Cr for Fe leads to a decrease lattice parameter *a*, resulting in an decrement of Fe1-Fe2 and Fe2-Fe2 distance as confirmed the replacement Fe by Cr results in a dilution of magnetic atom (Fe) content.

Magnetization curves as a function of magnetic field up to 5 T for $La_{0.7}Pr_{0.3}Fe_{11.4-x}Cr_xSi_{1.6}$ (x = 0 and 0.34) have been measured under increasing and decreasing field at various temperatures and are shown in Figure 4.10 (a) and (b). The measurements were performed over a wide range of temperature around T_C. Magnetic hysteresis is one characteristic of the first order magnetic transition, which is defined as the enclosed area between the ascending and descending branches of the magnetization curve. It can be seen that the M-B curves exhibit almost no magnetic hysteresis for x = 0.34 which is found same of the characteristic at x = 0. Furthermore it indicates that the field induced first order transition from

paramagnetic to ferromagnetic notably slightly increases by the introduction of Cr. The advantage of the sample with higher itinerant-electron metamagnetic (IEM) transition will

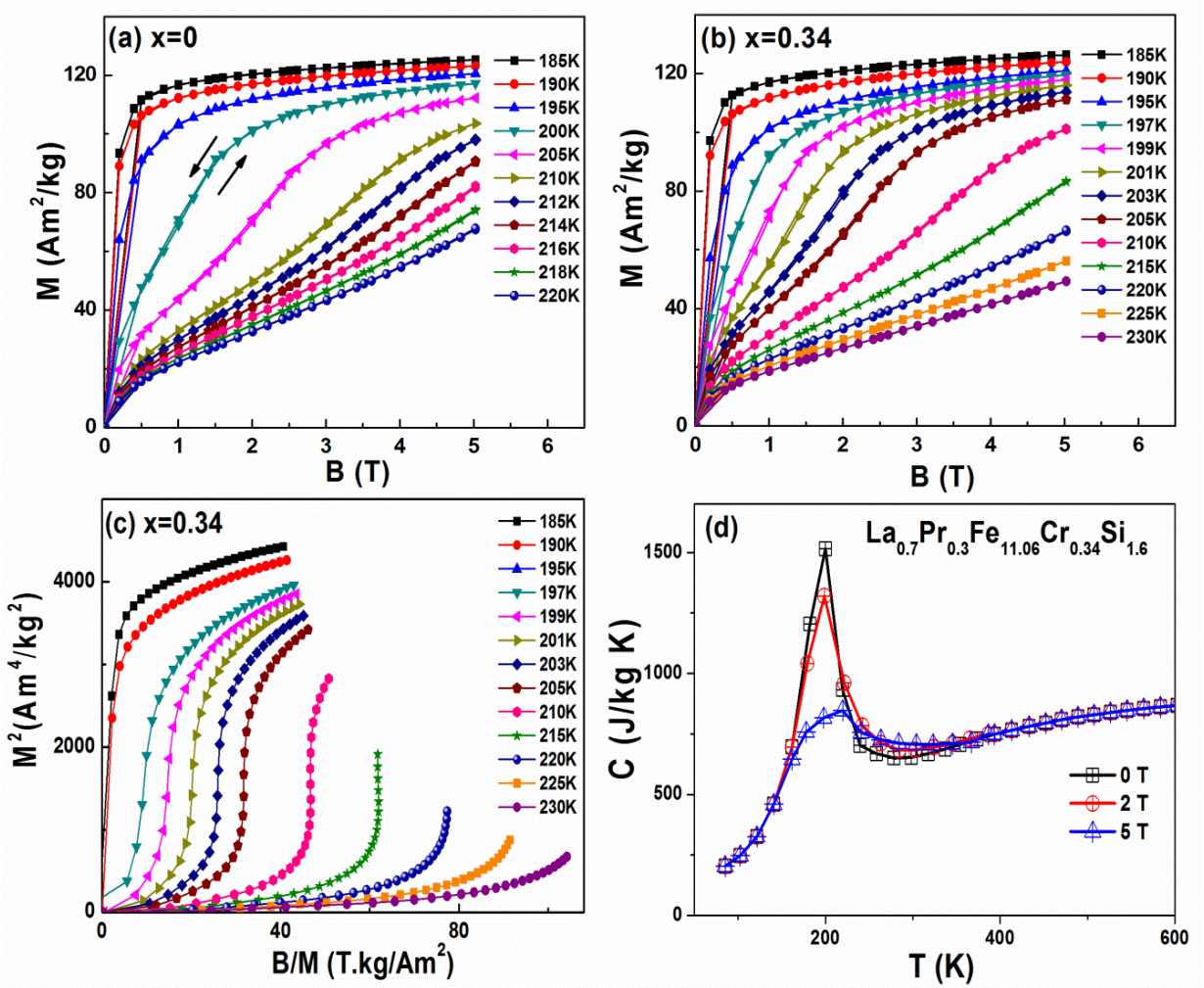

Figure 4.10 Isothermal magnetization curves in the vicinity of the ferromagnetic ordering temperatures for: (a) $La_{0.7}Pr_{0.3}Fe_{11.4}Si_{1.6}$ and (b) $La_{0.7}Pr_{0.3}Fe_{11.06}Cr_{0.34}Si_{1.6}$; (c) Arrott plots of M^2 versus B/M and (d) heat capacity measurement for the set of $La_{0.7}Pr_{0.3}Fe_{11.06}Cr_{0.34}Si_{1.6}$.

contribute to enhance the value of magnetic entropy change. The corresponding Arrott plots (M^2 versus B/M) are drawn in Figure 4.10 (c) depicted the negative slopes in the isotherm Arrott plots indicate the first-order nature of the phase transition around T_C according to I-S model for highest concentration x=0.34 [12, 26]. It has been reconfirmed that the first order nature consistent by others method (heat capacity measurement those that involve a latent heat) as shown in Figure 4.10 (d) and mixed peaks appear around T_C indicating the

coexistence of phases across magnetic transition defined by high intensity x-ray diffraction as will discuss later.

In order to satisfy the suitability of different experimental and related analytical approaches to establish the isothermal entropy change, $-\Delta S_M$, is defined from the magnetization curve by the Maxwell relation in equation 4.1 [33, 34]. The values of $-\Delta S_M$ around T_C have been derived from the magnetic data and are shown in Figure 4.11 (a) as a function of temperature with a 0-5 T change in field for $La_{0.7}Pr_{0.3}Fe_{11.4-x}Cr_xSi_{1.6}$ (x = 0, 0.06, 0.12, 0.23 and 0.34) compounds. $-\Delta S_M$ found to decrease from 17 J kg^{-1} K^{-1} at x=0 to 12 J kg^{-1} K^{-1} at x=0.06 then begin to increase to 14.2 J kg^{-1} K^{-1} at x=0.12 until reach 17.5 J kg^{-1} K^{-1} at x=0.34 which is larger than Gd (10.2 J kg^{-1} K^{-1}). It can be seen clearly that the $-\Delta S_M$ peak gradually becomes broader at higher temperature with increasing magnetic field from 2 to 5 T, which is a characteristic of the field induced IEM transition from the paramagnetic to the ferromagnetic state at temperatures above T_C as shown for x = 0.34 in Figure 4.11 (b) and agree well with the $-\Delta S_M$ values which are determined from heat capacity measurement. The peak value of the adiabatic temperature change is derived to be ΔT_{ad}^{max} = 8.4 K for ΔB = 0-5 T and 5.5 K for ΔB = 0-2 T as can be evaluated from $-\Delta S_M(T, B)$ and the heat capacity data as:

$$\Delta T_{\mathrm{ad}}(T,B) = \int_0^B \frac{T}{C_{B,P}} \left(\frac{\partial M}{\partial T}\right)_B dB \qquad (4.3)$$

The relative cooling power (RCP) is directly related to the magnetic refrigerator application. Using the maximum of the entropy variation $-\Delta S_M^{\max}$ and the full width at half maximum of the peak in the temperature dependence of the magnetic entropy change $-\Delta S_M$, one can derive the value of RCP as defined by the equation 4.2 [22, 35]. It can be seen at Figure 4.11 (a) that the RCP values increase from 365 J kg^{-1} at x=0.06; 372 J kg^{-1} at x=0.12; 384 J kg^{-1} at x=0.23 and 420 J kg^{-1} at x=0.34 under 0-5 T field applied. The RCP value at x=0.34 is slightly

higher than parent compound as indicated the promising material of $La_{0.7}Pr_{0.3}Fe_{11.06}Cr_{0.34}Si_{1.6}$ compound.

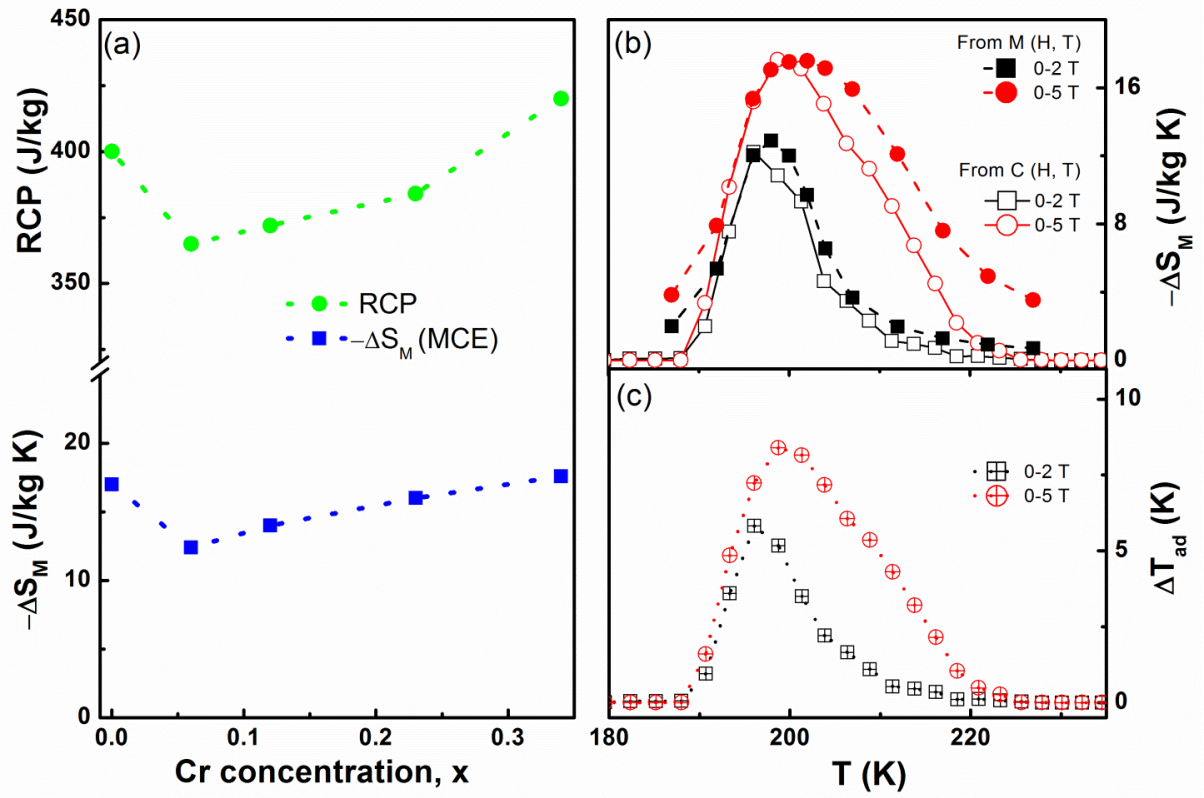

Figure 4.11 (a) The relative cooling power, RCP and the temperature dependence of the isothermal magnetic entropy change, $-\Delta S_M$, for $La_{0.7}Pr_{0.3}Fe_{11.4-x}Cr_xSi_{1.6}$ compounds with x = 0, 0.06, 0.12, 0.23 and 0.34 as measured from magnetization isotherms (ΔB = 0-5 T from decreasing field curves). (b) The magnetic entropy change, $-\Delta S_M$, determined from magnetization and the heat capacity measurements for $La_{0.7}Pr_{0.3}Fe_{11.06}Cr_{0.34}Si_{1.6}$ (ΔB = 0-5 and 0-2 T). (c) The adiabatic temperature change, ΔT_{ad}, for $La_{0.7}Pr_{0.3}Fe_{11.06}Cr_{0.34}Si_{1.6}$ as determined from the heat capacity measurements.

The high intensity of neutron and x-ray diffraction over 10-300 K has been studied for $La_{0.7}Pr_{0.3}Fe_{11.06}Cr_{0.34}Si_{1.6}$ compound in order to investigate the magneto-volume effect producing large magnetic entropy change, MCE. Neutron diffraction patterns indicated the shift of the peaks position to higher angle around T_C confirm the contraction of unit cell volume as shown in Figure 4.12 (a) and agree well with the x-ray diffraction analysis in Figure 4.12 (b) together with coexistence of two phases (paramagnetic and ferromagnetic phases) across magnetic transition as indicator for first order magnetic behaviour. The

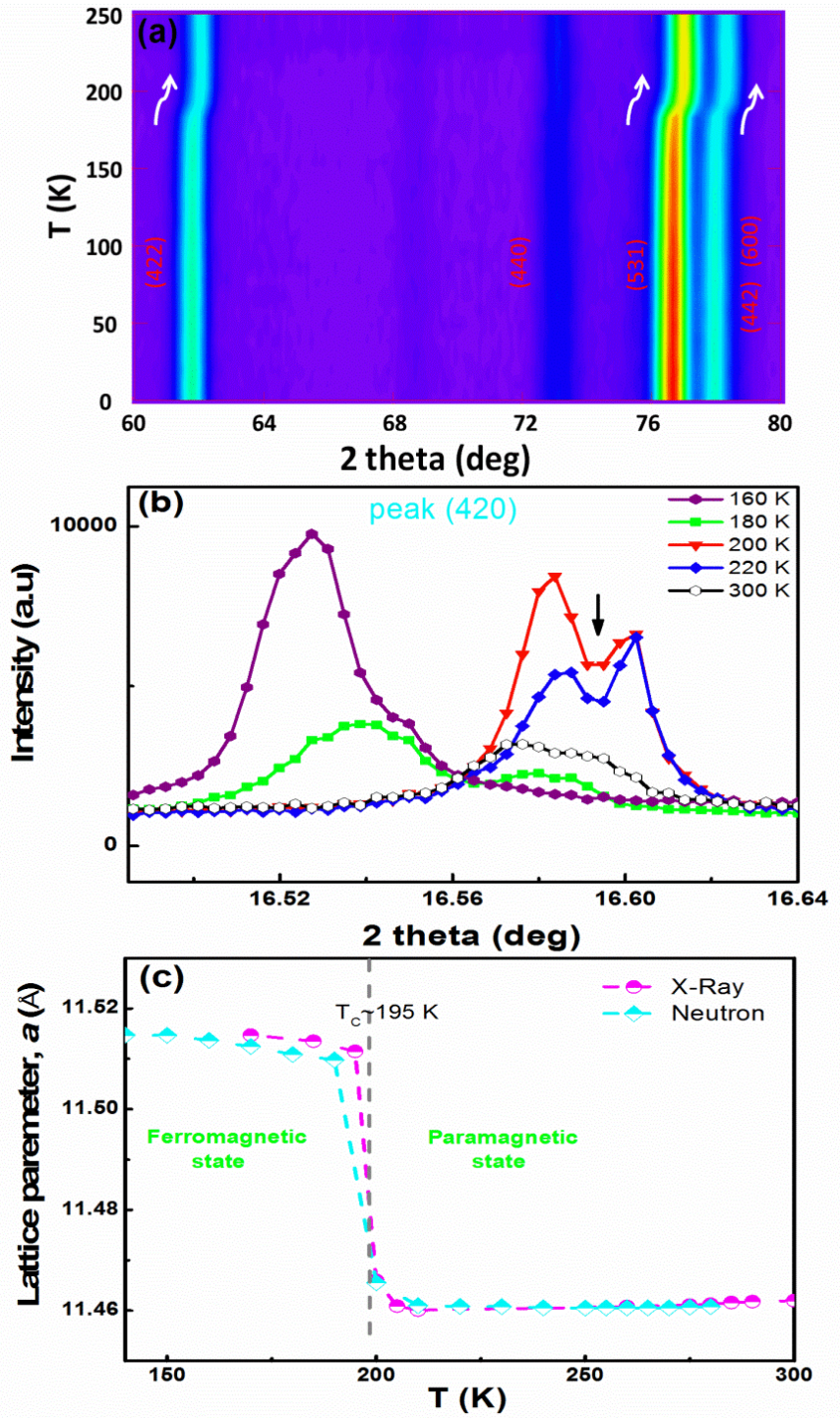

Figure 4.12 (a) Neutron diffraction patterns for $La_{0.7}Pr_{0.3}Fe_{11.06}Cr_{0.34}Si_{1.6}$ over temperature range 10-250 K (wavelength λ = 2.4205(2) Å) respectively. (b) High intensity x-ray diffraction pattern at selected temperature range 170-300 K (wavelength λ = 0.866(1) Å). The coexistence peaks appear as shown by arrow; (c) The lattice parameters change around T_C of $La_{0.7}Pr_{0.3}Fe_{11.06}Cr_{0.34}Si_{1.6}$ compound as a function of temperature.

variation in decrease of the lattice parameter, *a* has been found from 11.5148(3) Å at 170 K to 11.4608(2) Å at 200 K as depict in Figure 4.12 (c). The changes in lattice parameter at T_C

~ 195 K according to magnetic state changes from ferromagnetic to paramagnetic structure [37], indicates the presence of strong magneto-volume behaviour as contribute to the increase of the total of entropy change around T_C. It been found that around $-\Delta S_{structural}$ ~ 3.15 J kg^{-1} K^{-1} is estimated using the method from Gschneidner *et al.* [38] under ΔB = 0-5 T.

4.1.4 Conclusion

A systematic investigation of the structural and magnetic characterization of $La_{0.7}Pr_{0.3}Fe_{11.4-x}Cu_xSi_{1.6}$ (x = 0, 0.06, 0.12, 0.23, 0.34) for HTA and x = 0 for LTA samples has been carried out. The results show that the HTA process resolves the problem of non-equilibrium solidification behaviour due to the incomplete peritectic reaction γ-Fe+L $\rightarrow$ La(Fe,Si)$_{13}$(τ_{1a}) that occurs in the LTA process. The HTA sample with x = 0 shows promising values of $-\Delta S_M$ and RCP with very small hysteresis loss. This indicates the elevated temperature in HTA plays an important role to form the $NaZn_{13}$ type structure in the $La_{0.7}Pr_{0.3}Fe_{11.4}Si_{1.6}$ compound. However, the substitution of Cu for Fe leads to a decrease in the magnetic entropy change and eliminates hysteresis loss. Increasing the Cu concentration (starting from x = 0.06) also results in a change in the magnetic phase transition type from first to second order and reduces the characteristics of the IEM transition. The Curie temperature, T_C, increases with increasing Cu content, which can be ascribed to the increase in the lattice parameter and the modification of the composition. The compound with a small amount of Cu substitution shows a promising magnetic performance for magnetic refrigerator application, with no hysteresis loss and reasonable RCP.

Substitution of Cr for Fe $La_{0.7}Pr_{0.3}Fe_{11.4-x}Cr_xSi_{1.6}$ compounds leads to decreases in lattice parameter but variation behaviour on temperature transition, $T_{C.}$ The variation in the value of

T_C with increasing Cr concentration can be understood in terms of sensitive changes of Fe1-Fe2 and Fe2-Fe2 distances. Analysis of the magnetisation data demonstrates that the order of magnetic phase transition around T_C is consistent on first order type even x=0.34 for $La_{0.7}Pr_{0.3}Fe_{11.4-x}Cr_xSi_{1.6}$ compounds. Replacement of Fe by Cr leads to a reduction of the magnetic entropy change from beginning at x=0; ($-\Delta S_M$ =17 J kg^{-1} K^{-1}) to x=0.06; ($-\Delta S_M$ = 12 J kg^{-1} K^{-1}), however starts to enhance again when keep increasing Cr concentration until x=0.34; ($-\Delta S_M$ = 17.5 J kg^{-1} K^{-1}). High intensity Neutron and X-ray diffraction studies demonstrate that $La_{0.7}Pr_{0.3}Fe_{11.06}Cr_{0.34}Si_{1.6}$ compound has contraction in unit cell from ferromagnetic to paramagnetic structure which contributes to produce high magnetic entropy change. However this investigation is still incomplete as it will be the platform for us to further study, particularly further increase Cr concentration in this compound in order to confirm the ultimate of the beneficial in Cr substitution.

References

[1] E. Warburg, Ann. Phys. (Leipzig) 13 (1881) 141.
[2] V. K. Pecharsky and J. K. A. Gschneidner, Physical Review Letters 78 (1997) 4494.
[3] O. Tegus, E. Bruck, K. H. J. Buschow, and F. R. de Boer, Nature 415 (2002) 150.
[4] N. T. Trung, L. Zhang, L. Caron, K. H. J. Buschow, and E. Bruck, Applied Physics Letters 96 (2010) 172504.
[5] E. Liu, W. Wang, L. Feng, W. Zhu, G. Li, J. Chen, H. Zhang, G. Wu, C. Jiang, H. Xu, and F. de Boer, Nat Commun 3 (2012) 873.
[6] A. Yan, K. H. Muller, L. Schultz, and O. Gutfleisch, Journal of Applied Physics 99 (2006) 08K903.
[7] H. Wada and Y. Tanabe, Applied Physics Letters 79 (2001) 3302.
[8] O. Gutfleisch, A. Yan, and K. H. Muller, Journal of Applied Physics 97 (2005) 10M305.
[9] F. X. Hu, B. G. Shen, J. R. Sun, Z. H. Cheng, G. H. Rao, and X. X. Zhang, Applied Physics Letters 78 (2001) 3675.
[10] S. Fujieda, A. Fujita, and K. Fukamichi, Applied Physics Letters 81 (2002) 1276.
[11] F. X. Hu, B. G. Shen, J. R. Sun, and X. X. Zhang, Chinese Physics 9 (2000) 550.
[12] J. Shen, Y. X. Li, Q. Y. Dong, and J. R. Sun, Journal of Magnetism and Magnetic Materials 321 (2009) 2336.
[13] X. X. Zhang, G. H. Wen, F. W. Wang, W. H. Wang, C. H. Yu, and G. H. Wu, Applied Physics Letters 77 (2000) 3072.
[14] A. Fujita and K. Fukamichi, Magnetics, IEEE Transactions on 35 (1999) 1796.

[15] M. Balli, D. Fruchart, D. Gignoux, M. Rosca, and S. Miraglia, Journal of Magnetism and Magnetic Materials 313 (2007) 43.
[16] L. Jia, J. R. Sun, J. Shen, Q. Y. Dong, F. X. Hu, T. Y. Zhao, and B. G. Shen, Applied Physics Letters 92 (2008)
[17] V. Raghavan, Journal of Phase Equilibria 22 (2001) 158.
[18] K. Niitsu and R. Kainuma, Intermetallics 20 (2012) 160.
[19] A. Fujita and H. Yako, Scripta Materialia 67 (2012) 578.
[20] T. T. M. Palstra, J. A. Mydosh, G. J. Nieuwenhuys, A. M. van der Kraan, and K. H. J. Buschow, Journal of Magnetism and Magnetic Materials 36 (1983) 290.
[21] A. Fujita and K. Fukamichi, Journal of Alloys and Compounds 404–406 (2005) 554.
[22] A. Fujita, S. Fujieda, and K. Fukamichi, Journal of Magnetism and Magnetic Materials 310 (2007) e1006.
[23] J. K. A. Gschneidner, Rare Earth Alloys (D. Van Nostrand Co., Inc., Princeton, N.J.) (1961) pp187.
[24] D. V. Louzguine-Luzgin and A. Inoue, Physica B: Condensed Matter 358 (2005) 174.
[25] T. Liu, Y. Chen, Y. Tang, S. Xiao, E. Zhang, and J. Wang, Journal of Alloys and Compounds 475 (2009) 672.
[26] X. Chen, Y. Chen, and Y. Tang, Journal of Alloys and Compounds 509 (2011) 8534.
[27] J. Shen, Y.-X. Li, J.-R. Sun, and B.-G. Shen, Chinese Physics B 18 (2009) 2058.
[28] B. Gao, F. X. Hu, J. Wang, J. Shen, J. R. Sun, and B. G. Shen, Journal of Applied Physics 105 (2009) 07A916.
[29] P. Shamba, J. C. Debnath, R. Zeng, J. L. Wang, S. J. Campbell, S. J. Kennedy, and S. X. Dou, Journal of Applied Physics 109 (2011) 07A940.
[30] L. B. McCusker, R. B. Von Dreele, D. E. Cox, D. Louër, and P. Scardi, Journal of Applied Crystallography 32 (1999) 36.
[31] B. Liu Xu, Z. Altounian, and D. H. Ryan, Journal of Physics: Condensed Matter 15 (2003) 7385.
[32] L. Gelato, J. Appl. Crystallogr. 14 (1981) 151.
[33] A. H. Morrish, Wiley, New York Chapter 3 (1965)
[34] H. Feng Xia, S. Bao Gen, S. Ji Rong, C. Zhao Hua, and Z. Xi Xiang, Journal of Physics: Condensed Matter 12 (2000) L691.
[35] M. Balli, M. Rosca, D. Fruchart, and D. Gignoux, Journal of Magnetism and Magnetic Materials 321 (2009) 123.
[36] M. F. Md Din, J. L. Wang, R. Zeng, P. Shamba, J. C. Debnath, and S. X. Dou, Intermetallics 36 (2013) 1.
[37] F.W. Wang, G.J. Wang, F.X. Hu, A. Kurbakov, B.G. Shen, and Z.H. Cheng, Journal of Physics-Condensed Matter. 15 (2003) 5269.
[38] K. A. Gschneidner Jr, Y. Mudryk, and V. K. Pecharsky, Scripta Materialia 67 (2012) 572.

Chapter 5

STRUCTURAL, MAGNETIC PHASE TRANSITION AND ENTROPY CHANGE ON RT_2X_2 COMPOUND (R=RARE EARTH), (T=TRANSITION METAL) AND (X=METALLIOD)

5.1 Substitution Mn with Others Transition Metal in $NdMn_2Si_2$ Compound

Magnetic materials with first order magnetic transition (FOMT) are found to exhibit large magnetocaloric effect (MCE) compared to second order magnetic transition (SOMT) [1-4]. Among them, the tetragonal intermetallic compounds RMn_2X_2 (R=rare earth; T=transition metal and X=Si or Ge) attract special attention mainly in interesting interplay between 3*d* and 4*f* magnetism and present wide range of magnetic behaviour [5-7]. For example, $NdMn_2Si_2$ compound provides the promising prospect for enhanced magnetocaloric effect because of the crystal structure nature in layered allows to control of the intrinsic magnetism via inter and intra planar separations of the Mn atoms with Nd atoms performing the large magnetization due to ferromagnetic coupling between the Mn and Nd sublattices below the Nd ordering temperature [8].

5.1.1 Introduction

Application of the magnetocaloric effect (MCE) for magnetic refrigeration offers advantages that are well known, with increasing prospects as the basis of magnetic cooling to replace conventional refrigeration systems over appropriate temperature regions [9-11]. Given these

promising developments, magnetic materials which exhibit a large magnetocaloric effect have been studied, both experimentally and theoretically, over the past two decades [12, 13]. A number of materials which exhibit giant magnetic entropy changes at magnetic transitions have been investigated, including $Gd_5Si_2Ge_2$ [14], $(Mn, Fe)_2(P, Ge)$ [15], $MnAs_{1-x}Sb_x$ [16], and $La(Fe,Si)_{13}$ [17]. All of these materials undergo a first-order magnetic phase transition which, given the rapid change in magnetisation, enhances the scope for a large MCE. However such behaviour is often accompanied by hysteresis. For example, $La_{0.7}Pr_{0.3}Fe_{11.4}Si_{1.6}$ exhibits thermal hysteresis ~ 1.9 K and magnetic hysteresis ~ 0.2 T around T_C ~ 188 K [17]. The presence of a hysteresis effect in a material will lead to a decrease in efficiency of the energy performance during cooling and heating processes and therefore limit its use in practical applications. As such the search for suitable materials that show both a large MCE and are free from hysteresis continues.

The ternary intermetallic compounds of the RT_2X_2 series (R = rare earth, T = transition metal, X = Si or Ge) have attracted considerable attention because of the rich variety of interesting phenomena, including superconductivity, magnetism, mixed valence, heavy fermions, and Kondo behaviour [18, 19]. RT_2X_2 compounds form mainly in the $ThCr_2Si_2$ structure (space group *I*4/*mmm*), with the layered nature of this crystal structure leading to strong dependence of the magnetic interactions on the interplanar and intraplanar interatomic distances [20]. From this point of view, RMn_2X_2 compounds with X= Si or Ge have attracted special attention, due mainly to the interesting interplay between the magnetism of the layers of 3*d* and 4*f* atoms and the strong dependence of the magnitude of the Mn moment and the magnetic state of the Mn sublattice on the Mn-Mn interatomic distances [2, 3, 5, 19, 21-23]. As a general guide, for intraplanar distance, $d_{Mn\text{-}Mn}$ below ~ 2.87 Å, the coupling between Mn layers is antiferromagnetic while above this value, the coupling is ferromagnetic [24-26]. In

$NdMn_2Si_2$, below T_N ~ 380 K the Mn sublattice orders antiferromagnetically, while below T_C ~ 36 K the compound is ferromagnetic with ordered moments at both the Nd and the Mn sublattices [8, 27]. These magnetic behaviours with different temperature dependences reflect different types of exchange interactions with different mechanisms with both the Ruderman-Kittel-Kasuya-Yosida (RKKY) exchange interaction *via* conduction electrons, and super exchange between magnetic atoms *via* the Si or Ge atoms contributing. Generally, the exchange interactions in RMn_2X_2 compounds can be divided into four classes: Mn–Mn within the Mn layers, Mn–Mn between the Mn layers, and Mn–R and R–R interactions [28].

Here, the section presents a detailed investigation of the influence of replacing Mn atoms by others transition metal (Ti, Cr, Cu and V) atoms on the magnetic structure and magnetic phase transition in $NdMn_2Si_2$ compound. The main interest is to explore the effects of replacing Mn atoms of atomic radius r (Mn) = 1.35 Å and electronic configuration Mn ($3d^5 4s^2$) with different others transition metal atoms of atomic radius and electron configuration. In the case of $NdMn_{2-x}Co_xSi_2$ [29] for example, replacement of Mn by the smaller Co atoms, r(Co) = 1.25 Å of electronic configuration Co ($3d^7 4s^2$), leads to a decrease in magnetic entropy change from ~ 14.4 J kg^{-1} K^{-1} with x=0.2 to 12.4 J kg^{-1} K^{-1} with x=0.4 (ΔB = 0- 5 T) but the Curie temperature T_C ~ 45 K does not change with increasing Co concentration for $NdMn_{2-x}Co_xSi_2$ (x=0.2, 0.4, 0.8 and 1). In this study, investigation on the effects of others transition metal substitution for Mn in $NdMn_2Si_2$ compound on the structural and magnetic properties. Given that others transition metal atoms are significantly different with Mn atoms (r(Mn) = 1.35 Å) , replacement of Mn by others transition metal in $NdMn_2Si_2$ compound is expected to increase or decrease the distance between magnetic atoms, thus modifying the magnetic states of both the Nd and the Mn sublattices.

5.1.2 Experimental and Procedures

Polycrystalline samples with nominal compositions $NdMn_{2-x}T_xSi_2$ (T = Ti, Cr, Cu and V) were prepared by the arc melting of appropriate amounts of high purity constituent elements under a high purity argon atmosphere in a water-cooled copper crucible. The starting materials were pure elements (≥ 99.9%), and an excess of 3 at. % Mn was used to compensate for the loss during the arc melting and annealing processes. The ingots were turned over and re-melted several times to ensure homogeneity. The resulting ingots were wrapped in Ta foil and sealed under vacuum in a quartz tube, annealed at 900°C for 7 days to improve crystallization of the samples [6], and then quenched into water. The crystal structure of the samples were checked by room temperature powder x-ray diffraction (XRD) measurements using $CuK_{\alpha 1}$ radiation with the diffraction patterns refined using the Fullprof software package [30]. The magnetic properties were investigated over the temperature 10-300 K using the vibrating sample magnetometer option of a Quantum Design 14 T physical properties measurement system (PPMS) and an MPMS XL magnetic properties measurement system. Differential scanning calorimetry (DSC) measurements were carried out using a TA instrument DSC-Q100 over the range 300-450 K to check for possible phase transitions in the higher temperature range and investigate thermal hysteresis changes at the magnetic transitions. The crystallographic and magnetic structural behaviors of the set of $NdMn_{2-x}T_xSi_2$ samples were investigated over the temperature range 3-450 K by powder neutron diffraction experiments using the high resolution powder diffractometer Echidna (wavelength λ = 1.622(1) Å) and high intensity powder diffractometer Wombat (wavelength λ=2.4205 Å; 6-400 K) at the Open Pool Australian Light Water Reactor (OPAL), Lucas Heights, Australia.

5.1.3 Result and Discussion

5.1.3.1 $NdMn_{2-x}Ti_xSi_2$

Confirmation that all of the $NdMn_{2-x}Ti_xSi_2$ (x = 0, 0.1, 0.2, 0.3) samples crystallize in the expected $ThCr_2Si_2$ type structure with space group I4/*mmm* [31] was provided by analysis of the x-ray powder diffraction patterns. $NdMn_{2-x}Ti_xSi_2$ compounds have Nd atoms in the 2a site (0, 0, 0), while Ti and Mn share the position at the 4d site $(0, \frac{1}{2}, \frac{1}{4})$, and Si atoms occupy the 4e site (0, 0, z). The measured data from the diffraction patterns were analysed using the Rietveld refinement technique [30], and the distances between neighbouring atoms (Tables 5.1 and 5.3) have been obtained with the BLOKJE program [32], using the structural and positional parameters. Compared with pure $NdMn_2Si_2$ [22, 28], substitution of Ti for Mn does not change the crystal structure but leads to an expansion of the unit cell. The lattice constants *a* and *c*, and correspondingly the unit cell volumes, were found to increase with the Ti content consistent with the larger atomic radius of Ti compared to Mn. As shown in Table 5.1, $d_{\text{Mn-Mn}}$ increases from 2.8312(6) Å for x=0 to 2.8341(6) Å for x=0.3. However $d_{\text{Mn-Mn}}$ remains below $d_{\text{Mn-Mn}}^{\text{crit}}$ = 2.87 Å for all compositions. The geometric influence due to the size difference of Ti and Mn can be understood in the term of chemical pressure using the Murnaghan equation of state (see e.g. the case of $PrMn_{2-x}Fe_xGe_2$ compounds [6]):

$$p = \left(\frac{B_0}{B'_0}\right)\left[\left(\frac{V}{V_0}\right)^{-B_0} - 1\right] \tag{5.1}$$

where B_0 is the isothermal bulk modulus, B'_0 is its pressure derivative , and V_0 and V are the volume at ambient pressure and pressure *p*, respectively. Using the values of B_0 = 867 kbar, B'_0 = 5.1 for $CeNi_2Ge_2$ [33], the corresponding pressure can derived to be -3.35 kbar, -5.3

kbar and -6.05 kbar for the $NdMn_{2-x}Ti_xSi_2$ samples (x=0.1, 0.2 and 0.3) respectively. As discussed below these changes in d_{Mn-Mn} distances influence the magnetic properties.

Table 5.1 Lattice parameters, unit cell volume, and intralayer Mn-Mn distance of the $NdMn_{2-x}Ti_xSi_2$ compounds with x = 0, 0.1, 0.2 and 0.3 as determined from refinement of the room temperature x-ray diffraction patterns. The errors are shown for $NdMn_2Si_2$ as a typical example.

$NdMn_{2-x}Ti_xSi_2$	*a* (Å)	*c* (Å)	*V* (Å^3)	*c/a*	d_{Mn-Mn} (Å)	d_{Mn-Nd} (Å)
x=0	4.0039(5)	10.5251(6)	168.73(4)	2.6287(3)	2.8312(6)	3.3063(6)
x=0.1	4.0067	10.5515	169.39	2.6335	2.8332	3.3124
x=0.2	4.0073	10.5743	169.81	2.6388	2.8336	3.3171
x=0.3	4.008	10.5779	169.92	2.6392	2.8341	3.318

The temperature dependence of the magnetization of $NdMn_{2-x}Ti_xSi_2$ (x = 0, 0.1, 0.2, 0.3) measured in a magnetic field of B = 0.01 T over the temperature range ~ 10-300 K is shown in Figure 5.1 together with the differential scanning calorimetry (DSC) curves over the temperature range ~ 300-450 K. The inset shows the values of the Néel temperature T_N and the Curie temperature T_C, for the set of compounds as defined by 1/M versus temperature and the maxima of the dM/dT versus temperature graphs respectively. For the DSC measurements, the phase transition temperatures were determined by the maxima of the DSC signals (see figure 5.1). Comparison of results obtained under otherwise identical conditions for cooling and warming revealed almost no thermal hysteresis across all compositions (ΔT = 0.3 K at x=0 and ΔT = 0 K at x = 0.1, 0.2 and 0.3). Inspection of the insert to Figure 5.1, reveals that T_N decreases from ~ 380 K to ~ 360 K with increase in Ti concentration from x = 0 to x = 0.3 while T_C decreases from ~ 36 K to ~ 14 K. As shown in Table 5.1 d_{Mn-Mn} and d_{Mn-Nd} are found to increase from d_{Mn-Mn} = 2.8312(6) Å, d_{Mn-Nd} = 3.3063(6) Å at x = 0 to d_{Mn-Mn} = 2.8341(6) Å, d_{Mn-Nd} = 3.3180(6) Å at x = 0.3 and this expansion (size effect) will lead to enhancement of the Mn-Mn intralayer exchange interaction. On the other hand, increased Ti

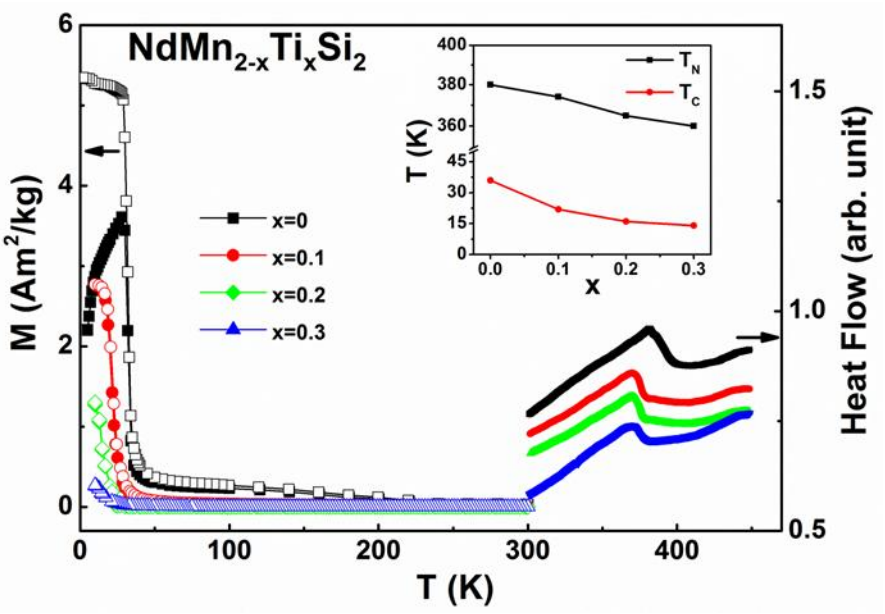

Figure 5.1 Temperature dependence of magnetization of $NdMn_{2-x}Ti_xSi_2$ compounds (x = 0, 0.1, 0.2, and 0.3) as measured in a field of 0.01 T (left axis; solid symbols for zero field cooling, ZFC, and open symbol for field cooling, FC); and differential scanning calorimetry measurements for the temperature range 300-450 K (right axis; solid symbols). The inset shows the Néel temperatures (T_N) and the Curie temperatures (T_C) for the set of samples.

concentration is also expected to weaken the exchange interactions of Mn-Mn between layers and the Mn-Nd due to the magnetic dilution effect. Moreover, the change in electronic environment on replacing Mn ($3d^5 4s^2$) by Ti ($3d^2 4s^2$) is also expected to influence the magnetic structures and states of the $NdMn_{2-x}Ti_xSi_2$ compounds. This is supported by Density Functional Theory calculations for RMn_2Ge_2 (R = Y or Ca) compounds [34] which indicate that to a large extent, the magnetic moment is determined mainly by the interatomic Mn-Mn distances, while the interstitial electron density contributes to the change in magnetic structures. Assuming the expansion of the unit cell volume due to Ti substitution (chemical pressure) to be equivalent to the influence of external pressure [26] and using dT_C/dp = -0.6 K/kbar in $NdMn_2Ge_2$ [35] (the same crystal structure), as a guide for the modulus values for $NdMn_{2-x}Ti_xSi_2$, the magnetic transition temperatures, T_C, expected from the pressure effect due to replacement of Mn atoms by the larger Ti atoms have been calculated as shown in Figure 5.2. The analysis based on the Murnaghan relationship indicates a slight increase in T_C

with Ti concentration from T_C = 36 K for x = 0 to T_C = 37 K for x = 1 whereas the experimental data reveal a decrease from T_C = 36 K for x = 0 to T_C = 14 K for x = 0.3. These results indicate that for $NdMn_{2-x}Ti_xSi_2$ compounds over the Ti concentration range x = 0.0 to 1.0, the electronic effects, rather than atomic size effects produce the observed decrease in magnetic transition temperature (T_C; Fig 2).

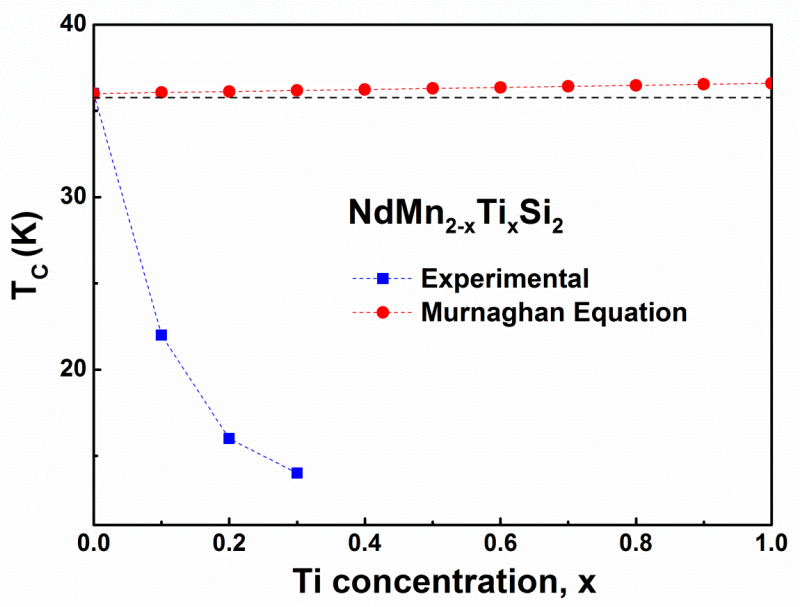

Figure 5.2 Experimental (squares) and calculated values (circles) of the Curie temperature T_C as a function of Ti concentration for $NdMn_{2-x}Ti_xSi_2$ (x = 0, 0.1, 0.2, 0.3). The T_C values were calculated using the Murnaghan equation and dT_C/dp = -0.6 K/kbar as described in the text. The dashed lines act as a guide to the eye with the horizontal dashed line included to emphasise the slight increase in the calculated T_C values, with increasing Ti concentration.

The magnetization versus field curves (B = 0-5 T) for $NdMn_{2-x}Ti_xSi_2$ (x = 0, 0.1, 0.2, 0.3) at 10 K are shown in Figure 5.3. The magnetization is not saturated up to 5 T indicating large magnetic anisotropy in these samples. This behaviour is supported by the strong uniaxial magnetic anisotropy observed for $NdMn_2Si_2$ [8] with the moment of 4.16 μ_B/f.u. inhibiting saturation in magnetization up to fields of B = 5 T. The saturation magnetization values at 10 K were derived from graphs of magnetisation M versus 1/B by extrapolation and applying the law of approach to saturation. The saturation magnetization, M_S (at 10 K) is found to decrease with increasing Ti concentration in the $NdMn_{2-x}Ti_xSi_2$ compounds (Table 5.2). With assume

that the rare earth moment does not change with Ti content, it can be derived that the substitution of Ti atoms for Mn leads to a decrease of around -4.6 μ_B per Ti atom (from linear fitting), which is much faster than that expected with a simple dilution model (in which the Ti atoms do not carry magnetic moment). This behaviour is similar to that observed in $NdMn_{2-x}Co_xSi_2$ (-2.1 μ_B per Co atom decrease of M_s at 5 K) [29], $NdMn_{2-x}Cr_xSi_2$ (-2.8 μ_B per Cr atom decrease of M_s at 4.2 K) [36] and $NdMn_{2-x}Fe_xSi_2$ [37] compounds.

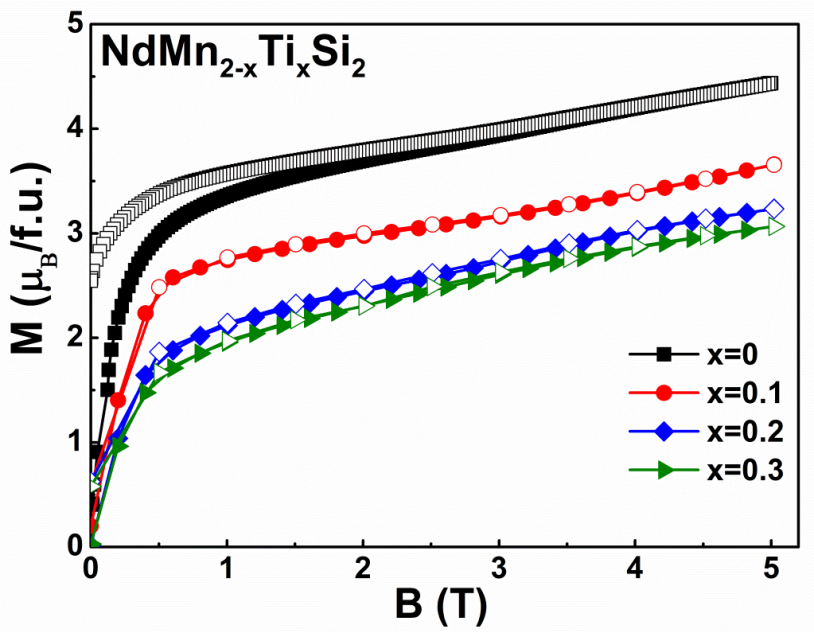

Figure 5.3 Magnetization curves (B = 0 - 5 T) for $NdMn_{2-x}Ti_xSi_2$ compounds (x = 0, 0.1, 0.2, 0.3) at T = 10 K (closed symbols denote field increasing and open symbols field decreasing).

The magnetization curves obtained for $NdMn_2Si_2$ and $NdMn_{1.9}Ti_{0.1}Si$ for fields in the range B = 0 - 8 T and B = 0 - 5 T around their ferromagnetic ordering temperatures are shown in Figures 5.4(a) and 5.4(b), respectively. These data were obtained for increasing and decreasing fields at 2 K intervals spanning a range of about 45 K around T_C, thus providing information about magnetic hysteresis loss effects as discussed below using expression [38]:

$$\text{Magnetic hysteresis loss} = \int_{decrease\ H}^{increase\ H} (\partial M)_H \ dH. \qquad (5.2)$$

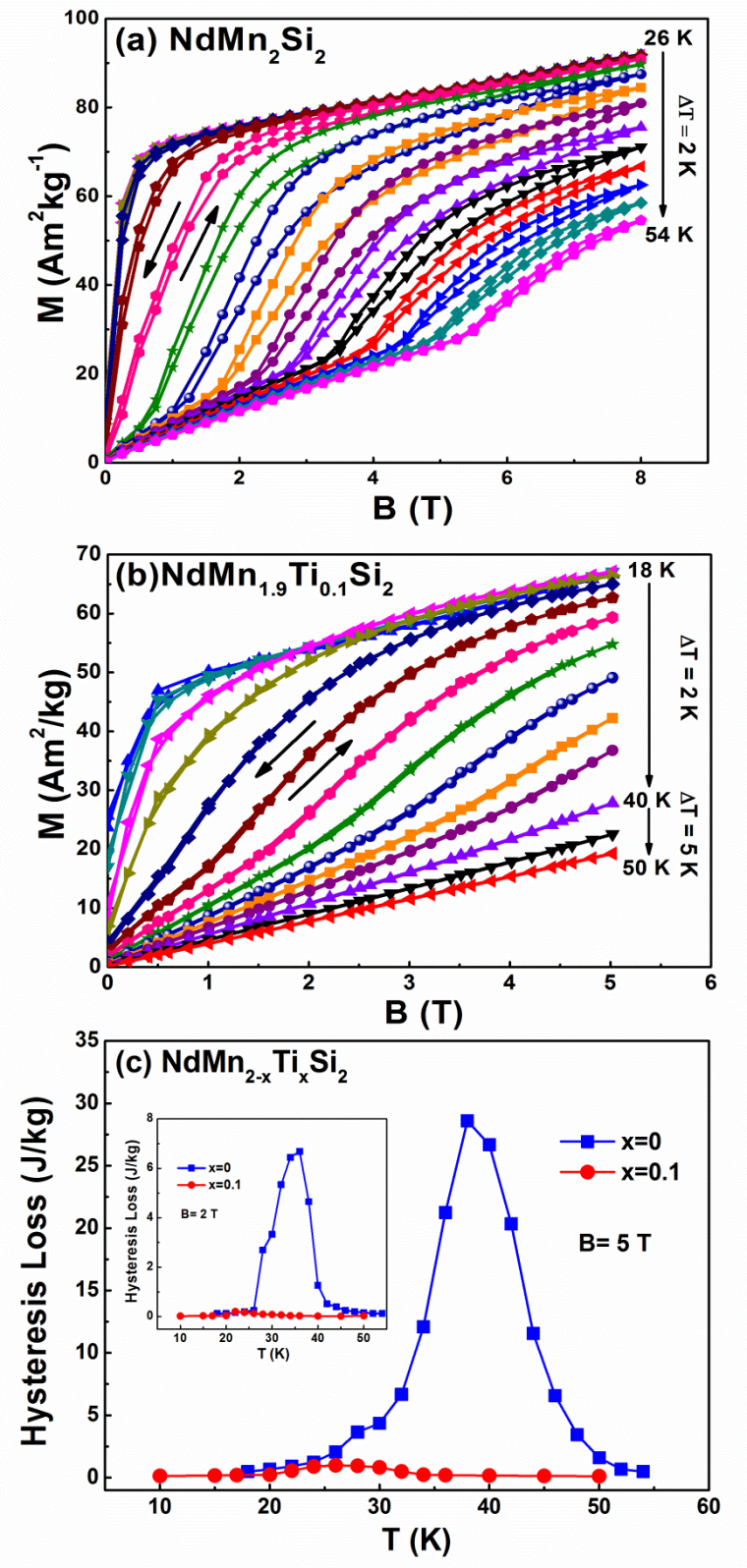

Figure 5.4 Isothermal magnetization curves in the vicinity of the ferromagnetic ordering temperatures for: (a) $NdMn_2Si_2$ (T_C = 36 K with B = 0 - 8 T) and (b) $NdMn_{1.9}Ti_{0.1}Si_2$ (T_C = 22 K with B = 0 - 5 T) (the arrows indicate the direction of the applied fields during magnetisation measurements, and (c) Comparison of the magnetic hysteresis losses for $NdMn_2Si_2$ and $NdMn_{1.9}Ti_{0.1}Si_2$ for magnetic fields over the ranges B=0-5 T (the results for B=0-2 T are shown in the insert).

Magnetic hysteresis effects (as indicated by the area enclosed between the ascending and descending branches of the magnetization curves) are also characteristic of first order

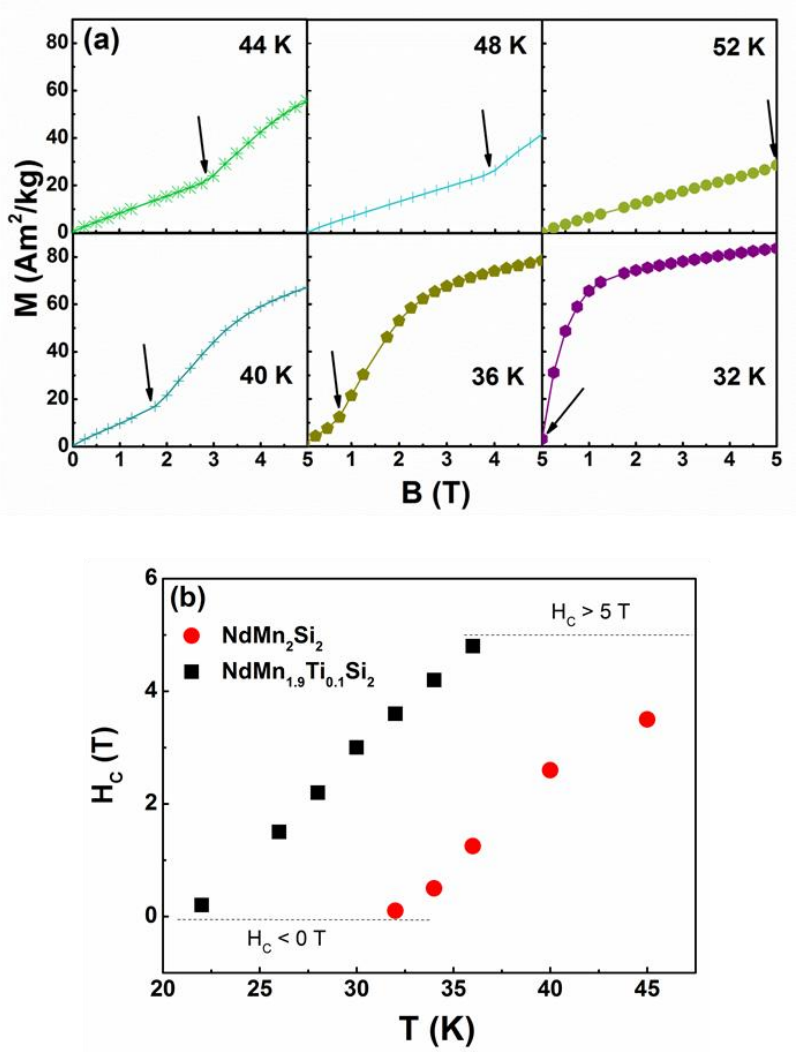

Figure 5.5 (a) Magnetic field dependence of the magnetization for applied fields in the range 0-5 T at selected temperatures for $NdMn_2Si_2$. H_C corresponds to the field at the onset of the antiferromagnetic to ferromagnetic transition, indicated by arrow; (b) Critical field values, H_C, for $NdMn_2Si_2$ and $NdMn_{1.9}Ti_{0.1}Si_2$ at selected temperatures.

magnetic transitions. As demonstrated in Figure 5.4(c), comparison of the magnetisation curves around the ferromagnetic ordering temperatures for $NdMn_2Si_2$ (figure 5.4(a)) with those for $NdMn_{1.9}Ti_{0.1}Si_2$ (figure 5.4(b)) reveal pronounced hysteresis losses of up to ~ 28.5 J kg^{-1} (indicated values for B = 0 - 5 T as suitable to comparison) for $NdMn_2Si_2$ at T_C = 36 K

while negligible hysteresis losses of ~ 0.8 J kg^{-1} are observed for $NdMn_{1.9}Ti_{0.1}Si_2$ around T_C = 22 K.

Table 5.2 Results of the magnetic characterization of $NdMn_{2-x}Ti_xSi_2$ compounds with x = 0, 0.1, 0.2 and 0.3. The magnetic features listed are: Curie temperature (T_C; determined by graphs of dM/dT versus T) and the order of the magnetic transition around T_C; Néel temperature (T_N; determined by graphs of 1/M versus T) and the saturation magnetization, M_S, as determined at 10 K. The magnetic entropy change ($-\Delta S_M$) and the relative cooling power (RCP) are given for a field change of 0-5 T. The errors are shown for $NdMn_2Si_2$ as a typical example.

Composition	T_C (K)	Nature of Transition at T_C	T_N (K)	M_S (μ_B/f.u.) (T=10 K)	$-\Delta S_M$ (J kg^{-1} K^{-1}) (B=0-5 T)	RCP (J kg^{-1}) (B=0-5 T)
$NdMn_2Si_2$	36(3)	First	380(3)	4.4(4)	27(3)	127(3)
$NdMn_{1.9}Ti_{0.1}Si_2$	22	First	374	3.6	15.3	99
$NdMn_{1.8}Ti_{0.2}Si_2$	16	First	365	3.2	13	89
$NdMn_{1.7}Ti_{0.3}Si_2$	14	First	360	3	10	70

It is demonstrated clearly in Figure 5.4(c) that magnetic hysteresis losses decrease significantly on substitution of Ti for Mn. This behaviour indicates that increasing Ti concentration contributes to a weakening of the characteristic field induced metamagnetic transition from the antiferromagnetic to the ferromagnetic state. As shown in Figure 5.5(a) for $NdMn_2Si_2$, with the applied field below the critical value field (H_C), the magnetization increases linearly with increasing field applied expected for an antiferromagnetic state. However for applied field greater than H_C, the magnetization initially increases rapidly before tending towards saturation at higher fields (similar behaviour is observed for $La_{0.5}Pr_{0.5}Mn_2Si_2$ [19] of the same $ThCr_2Si_2$ bct crystal structure) i.e. ferromagnetic behaviour. In the present investigation, as shown in Figure 5.5(b) the value of H_C is found to increase significantly with increasing the temperature and Ti concentration. Welter *et al* [8] have postulated that the ferromagnetic ordering of Nd sublattice below T_C drives the change in order of the Mn sublattice from antiferromagnetism to ferromagnetism in $NdMn_2Si_2$. It can be seen from Figures 5.4(a) and 5.4(b) that the metamagnetic transition occurs at higher temperatures and

lower values of H_C in $NdMn_2Si_2$ compared with $NdMn_{0.9}Ti_{0.1}Si_2$. Therefore the metamagnetic transition is expected to produce a larger magnetocaloric effect for x = 0, with a decrease in MCE values for x = 0.1, 0.2 and 0.3 as described below in the magnetic entropy section.

As mentioned before, significant MCE values and magnetic entropy changes are usually obtained with a first order magnetic transition due to a large rate of change of magnetisation. Although such materials have this advantage compared with materials that exhibit a second order transition, first order magnetic transitions usually exhibit considerable thermal and magnetic hysteresis. The details of this study have established that hysteresis effects have effectively been eliminated by substitution of Mn with Ti in $NdMn_{2-x}Ti_xSi_2$ compounds. Figures 5.6(a - d) show the corresponding Arrott plots (M^2 versus B/M) for the x = 0, 0.1, 0.2 and 0.3 samples, respectively. The Arrott plots are found to exhibit features characteristic of a first order transition for all of the samples. In particular the nature of the Arrott plot near T_C denotes a negative order of the sign of the coefficient c2(T) in the Landau expansion of the magnetic free energy [39], thereby denoting a first order magnetic transition. The present findings demonstrate that the ferromagnetic transition at T_C in $NdMn_{2-x}Ti_xSi_2$ remains a first order transition on substitution of Ti for Mn to Ti concentration up to x=0.3.

The magnetic entropy change, $-\Delta S_M$, has been determined for the set of $NdMn_{2-x}Ti_xSi_2$ compounds (x = 0, 0.1, 0.2 and 0.3) from their magnetization curves for both increasing and decreasing field values as functions of temperature and magnetic field (ΔB = 0-5 T). The magnetic entropy change has been derived by applying the standard Maxwell relation [40]:

$$-\Delta S_M(T,B) = \int_0^H \left(\frac{\partial M}{\partial T}\right)_B dB. \quad (5.3)$$

As shown by the curves of Figure 5.7(a), the $-\Delta S_M$ peak (closed symbols for increasing field values and open symbols for decreasing field values) gradually broadens towards higher

temperatures with increasing magnetic field (from ΔB = 0-5 T), behaviour characteristic of a field induced transition from an antiferromagnetic to a ferromagnetic state.

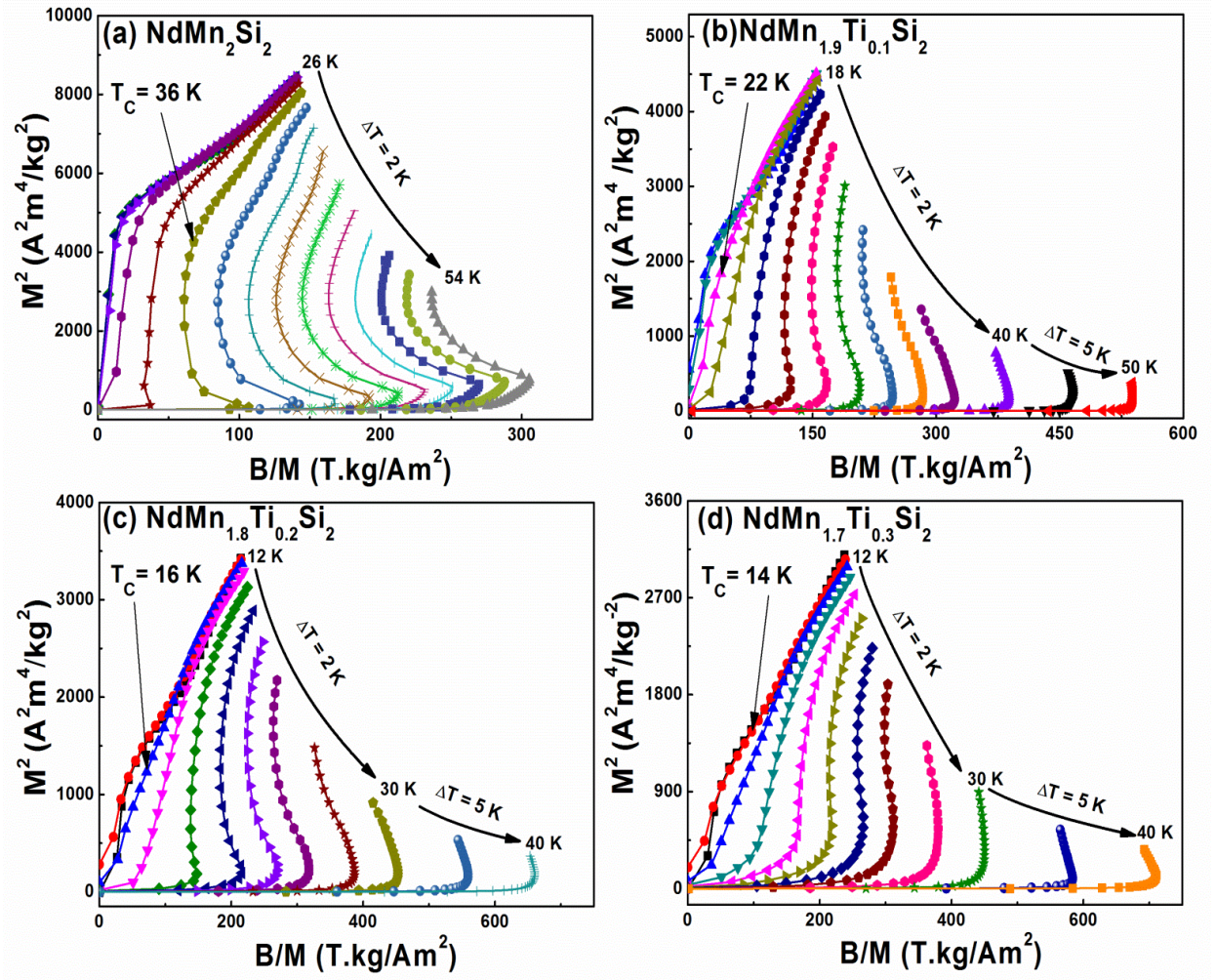

Figure 5.6 Arrott plots of M^2 versus B/M for the set of $NdMn_{2-x}Ti_xSi_2$ compounds: (a) $NdMn_2Si_2$; (b) $NdMn_{1.9}Ti_{0.1}Si_2$, (c) $NdMn_{1.8}Ti_{0.2}Si_2$, and (d) $NdMn_{1.7}Ti_{0.3}Si_2$.

The changes in magnetic entropy for the set of $NdMn_{2-x}Ti_xSi_2$ compounds (x = 0, 0.1, 0.2 and 0.3) around their ferromagnetic ordering temperatures are shown in Figure 5.7(b) as calculated from decreasing applied fields in order to satisfy the suitability of different experimental and related analytical approaches to establish the isothermal entropy change [41]. The entropy values at the respective Curie temperatures are (ΔB = 0-5 T): $-\Delta S_M \sim 27$ J kg^{-1} K^{-1} at T_C = 36 K; $-\Delta S_M \sim 15.3$ J kg^{-1} K^{-1} at T_C = 22 K; $-\Delta S_M \sim 13$ J kg^{-1} K^{-1} at T_C = 16 K

and $-\Delta S_M \sim 10$ J kg^{-1} K^{-1} at $T_C = 14$ K. The decrease in magnetization on substitution of the non-magnetic Ti for Mn, correspondingly reduces the value of $-\Delta S_M$. Never the less it is noted that the MCE values of $-\Delta S_M \sim 15.3$ J kg^{-1} K^{-1} for $NdMn_{1.9}Ti_{0.1}Si_2$ and $-\Delta S_M \sim 13$ J kg^{-1} K^{-1} for $NdMn_{1.8}Ti_{0.2}Si_2$ are comparable with MCE values for other materials with small hysteresis that exhibit transitions in the temperature region below 100 K. These materials include: $TbCoC_2$ [42] ($-\Delta S_M = 15$ J kg^{-1} K^{-1} at 28 K), GdCoAl [43] ($-\Delta S_M = 10.4$ J kg^{-1} K^{-1} at 100 K) and TbCoAl [43] ($-\Delta S_M = 10.5$ J kg^{-1} K^{-1} at 70 K), all of which - in common with $NdMn_{1.9}Ti_{0.1}Si_2$ and $NdMn_{1.8}Ti_{0.2}Si_2$ - importantly exhibit no field hysteresis losses.

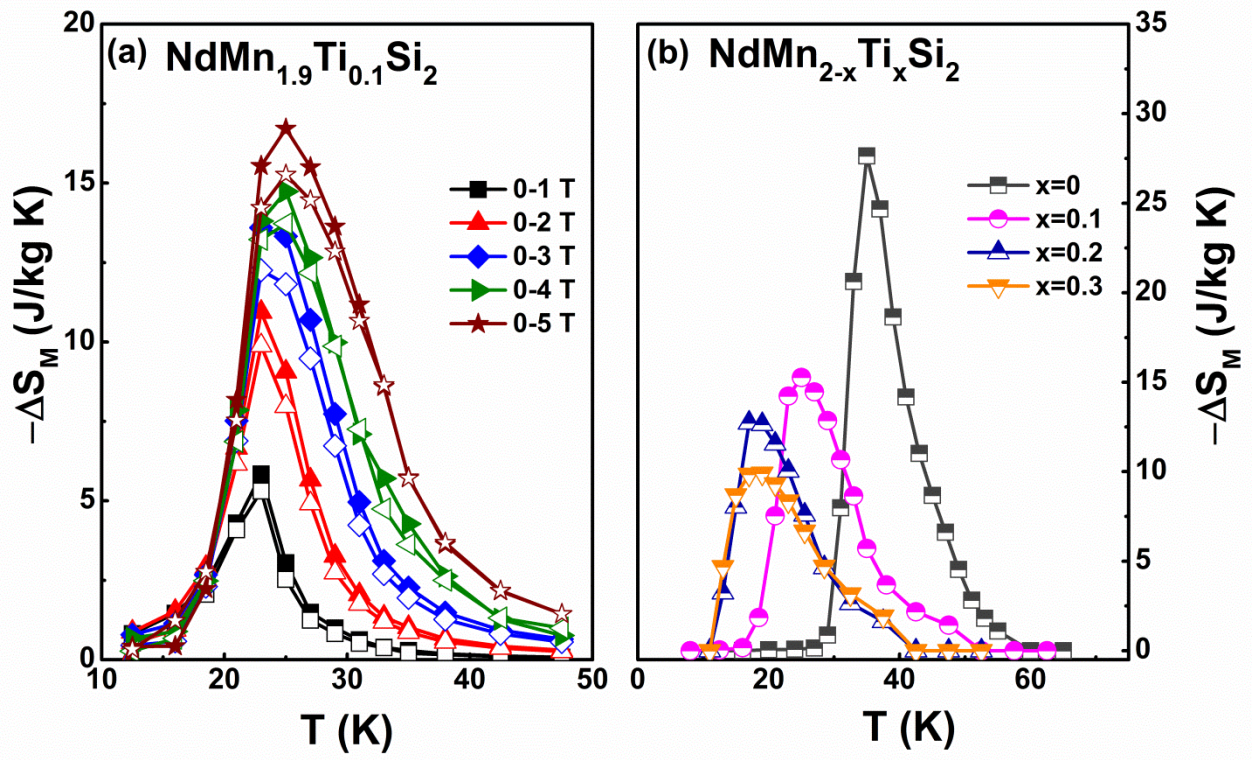

Figure 5.7 (a) The temperature dependence of the isothermal magnetic entropy change, $-\Delta S_M$, for $NdMn_{0.9}Ti_{0.1}Si_2$ as determined from the magnetization isotherms for ΔB = 0-1 T, ΔB = 0-2 T, ΔB = 0-3 T, ΔB = 0-4 T and ΔB = 0-5 T (closed symbols for increasing fields and open symbols for decreasing fields). (b) The temperature dependence of the isothermal magnetic entropy change, $-\Delta S_M$, for $NdMn_{2-x}Ti_xSi_2$ compounds with x = 0, 0.1, 0.2 and 0.3 as measured from magnetization isotherms (ΔB = 0-5 T from decreasing field curves).

The magnetic entropy change, $-\Delta S_M(T, B)$ has also been derived from heat calorimetric measurements of the field dependence of the heat capacity using the expression [10, 44, 45]:

$$-\Delta S_M(T,B) = \int_0^T \left(\frac{C(T,B)-C(T,0)}{T}\right) dT \quad (5.4)$$

where *C(T,B)* and *C(T,0)* are the values of the heat capacity measured in field *B* and zero field, respectively. The corresponding adiabatic temperature change, ΔT_{ad} can be evaluated from $-\Delta S_M(T, B)$ and the heat capacity data as:

$$\Delta T_{ad}(T,B) = \int_0^B \frac{T}{C_{B,P}} \left(\frac{\partial M}{\partial T}\right)_B dB \quad (5.5)$$

Figure 5.8(b) shows the set of heat capacity measurement obtained for $NdMn_{1.9}Ti_{0.1}Si_2$ with B = 0, 2, and 5 T. The corresponding $-\Delta S_M(T, B)$ values for $NdMn_{1.9}Ti_{0.1}Si_2$ are shown in Figure 5.8(a) with the ΔT_{ad} values shown in Figure 5.8(c) (open symbols). The peak value of the adiabatic temperature change is ΔT_{ad}^{max} = 4.7 K for ΔB = 0-5 T.

As shown in Figure 5.8(a), the maximum magnetic entropy change for $NdMn_{1.9}Ti_{0.1}Si_2$ as determined from the heat capacity measurements of $-\Delta S_M^{max}$ ~ 15 J kg^{-1} K^{-1} and 9.3 J kg^{-1} K^{-1} for ΔB = 0-5 T and 0-2 T are similar to the maximum entropy change $-\Delta S_M^{max}$ ~ 15.3 J kg^{-1} K^{-1} and 9.8 J kg^{-1} K^{-1} as determined from the magnetic measurements using the Maxwell relation. The good agreement between the two sets of measurements confirms that the $-\Delta S_M$ values derived for $NdMn_{1.9}Ti_{0.1}Si_2$ from the magnetization measurements represent the MCE behaviour within experimental errors [14, 22, 46]. Similarly, the ΔT_{ad} values determined by combing the $-\Delta S_M(T, B)$ (derved from magnetic data) and specific heat results are also drawn in Figure 5.8(c) using closed symbols to make a comparison, which are found to be consistent with the values (open symbols) derived from the specific heat only. By comparison, Nikitin *et al* [47] reported that the value of ΔT_{ad}^{max} in $NdMn_2Si_2$ compound (around T_C ~ 32 K) can be up to 8.2 K with a field change of ΔB=0-6 T.

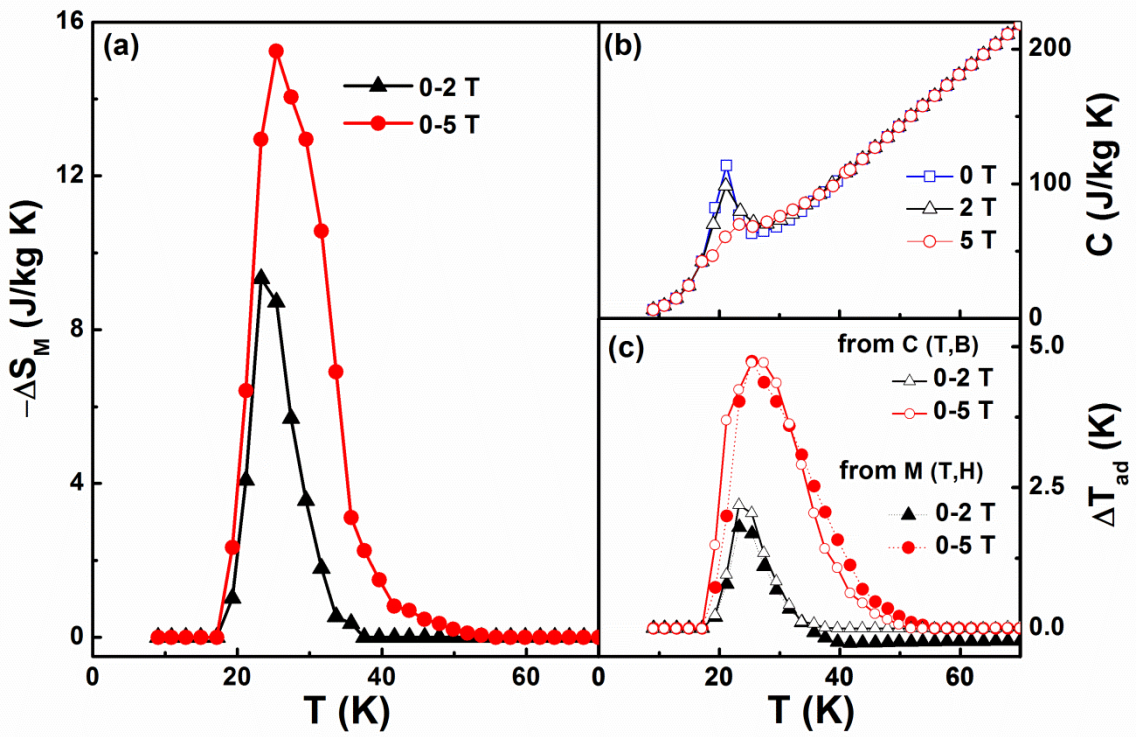

Figure 5.8 (a) The magnetic entropy change, -ΔS_M, determined from the heat capacity measurements of figure 5.8(b) for $NdMn_{1.9}Ti_{0.1}Si_2$ (ΔB = 0-2 T, ΔB = 0-5 T). (b) The heat capacity of $NdMn_{1.9}Ti_{0.1}Si_2$ as measured over the temperature range 10-70 K in magnetic fields B = 0 T, 2 T, 5 T. (c) The adiabatic temperature change, ΔT_{ad}, for $NdMn_{1.9}Ti_{0.1}Si_2$ as determined from the heat capacity(open symbol) of figure 5.8(b) and magnetization (closed symbol) measurements.

In general, the relative cooling power (RCP) is an important parameter of the magnetocaloric material, providing an accepted criterion to evaluate the refrigeration efficiency in practical application. The RCP is used to evaluate the cooling power of magnetic refrigerants by measuring how much heat can be transferred between two temperatures (low and high in temperature span range) in one ideal refrigeration cycle. The RCP is defined by the following expression [48]:

$$\mathrm{RCP} = -\Delta S_M^{max} \delta T^{FWHM} \quad (5.6)$$

-ΔS_M^{max} denotes the maximum entropy change and δT represents the full width at half maximum (FWHM) of the temperature dependence of the magnetic entropy change -ΔS_M. A summary of the RCP values and other magnetic characterization parameters for $NdMn_2$-

$_xTi_xSi_2$ (x = 0, 0.1, 0.2, 0.3) compounds is listed in Table 5.2. The RCP shows the same trend with Ti concentration as the magnetic entropy change. It is noted that δT increases with Ti content: δT = 9.5 K, δT = 12.0 K, δT = 12.4 K and δT = 12.8 K for x=0, 0.1, 0.2 and 0.3 respectively. It was found that the RCP decreases from ~127 J kg^{-1} for x = 0 to ~70 J kg^{-1} for x = 0.3 for a change in magnetic field ΔB = 0-5 T.

The $NdMn_{1.9}Ti_{0.1}Si_2$ compound was selected for investigation by neutron diffraction measurements over the temperature range 3-450 K as representative of the magnetic behaviour of the $NdMn_{2-x}Ti_xSi_2$ samples (figure 5.1). The aims were to determine the magnetic structures and to explore structural changes at the transition temperatures. The diffraction patterns (λ = 1.622(1) Å) and Rietveld refinements obtained for $NdMn_{1.9}Ti_{0.1}Si_2$ at 450 K, 150 K and 15 K are shown in Figures 5.9(a), 5.9(b) and 5.9(c), respectively. The selected temperatures typify the behaviour of $NdMn_{1.9}Ti_{0.1}Si_2$ in the three magnetic regions (paramagnetic-antiferromagnetic-ferromagnetic) as indicated from the magnetisation and DSC measurements of Figure 5.1. Rietveld refinements of the neutron diffraction pattern at 450 K (figure 5.9(a)) confirm that $NdMn_{1.9}Ti_{0.1}Si_2$ has the $ThCr_2Si_2$ structure as expected. The absence of magnetic scattering above T_N ~ 374 K (figure 5.1) in reflections such as (101), (111) and (112) is consistent with a paramagnetic (PM) state. (*cf*. e.g. the disordered magnetic states (PM) observed in $PrMn_{1.6}Fe_{0.4}Si_2$ [6], $EuMn_2Si_2$ [49] and $LaPrMn_2Si_2$ [50]). Below T_N ~ 374 K, $NdMn_{1.9}Ti_{0.1}Si_2$ is found to exhibit the antiferromagnetic interlayer coupling structure (AFil) down to T_C ~ 22 K (see e.g. the 150 K pattern of figure 5.9(b)). The AFil structure − a collinear antiferromagnetic structure between adjacent Mn planes in a + - +

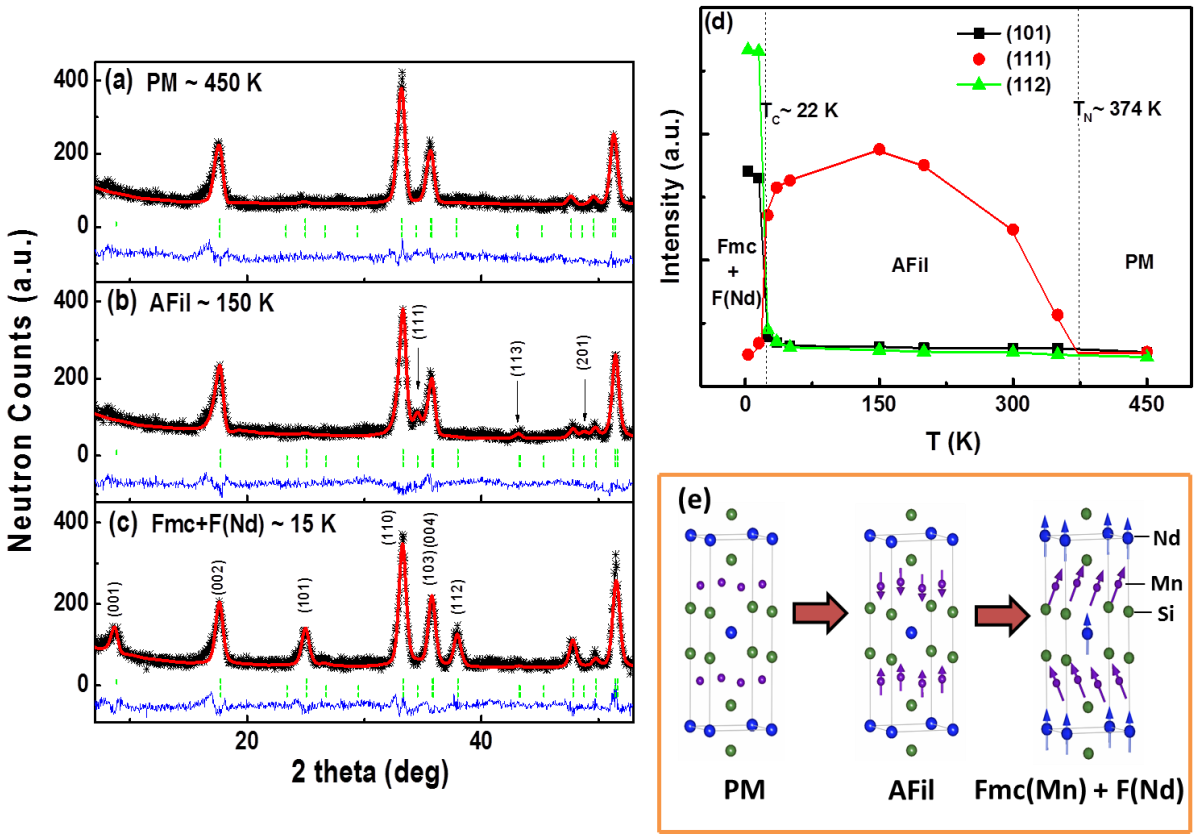

Figure 5.9 (a), (b), and (c) Neutron diffraction patterns for $NdMn_{1.9}Ti_{0.1}Si_2$ at 450 K, 150 K, and 15 K respectively. The star symbols represent the observed patterns and the red solid lines the refined patterns. The blue lines represent the differences between the observed and refined patterns; the vertical bars indicate the Bragg peak positions for the nuclear (top), F*mc* magnetic (middle) and AF*il* magnetic (bottom) structure respectively. (d) The temperature dependence of the integrated intensities of the (101), (112) and (111) reflections for $NdMn_{1.9}Ti_{0.1}Si_2$ over the temperature range 3-450 K. The T_N ~ 374 K and T_C ~ 22 K transition temperatures that delineate the paramagnetic PM, antiferromagnetic AF*il* and ferromagnetic F*mc*+F(Nd) regions, asre shown by the dashed lines. The lines through the intensity values act as guides to the eye. (e) The structure of $NdMn_{1.9}Ti_{0.1}Si_2$ and the antiferromagnetic AFil and ferromagnetic F*mc*+F(Nd) structures.

- sequence along the *c*-axis − is indicated by the magnetic scattering observed at the (111), (113) and (201) reflections; (extinction rules $h + k = 2n$ and $h + k + l = 2n+1$) in agreement with Dincer *et al* [50]. In order to draw out the changes in magnetic structures with temperature, the temperature dependence of the peak intensity for selected magnetic peaks is shown in Figure 5.9(d). Furthermore, the absence of magnetic scattering from the (111), (113) and (201) reflections at 15 K in Figure 5.9(c), combined with the increase in intensity of the

(112) and (101) peaks as in Figure 5.9(d), indicate that the interlayer spin components of the Mn moments align parallel, thus leading to a canted ferromagnetic structure (F*mc*) for the Mn sublattice. The presence of the purely magnetic peak (001) below T_C indicates the existence of antiferromagnetic component of Mn moment in the ab-plane [22]. At lower temperature (e.g. 3 K; figure 5.9(d)), the increase in the intensities of the (112) (contributions from both Nd- and Mn-sublattices) and (101) (contribution only from Nd-sublattice [22]) reflections further indicates an additional contribution from Nd moments coupled parallel to

Table 5.3 Structural and magnetic parameters of $NdMn_{1.9}Ti_{0.1}Si_2$ as derived from Rietveld refinements of the neutron diffraction patterns and the BLOKJE program. μ_{total}^{Mn} - the Mn magnetic moment; μ_c^{Mn} - the Mn moment along the c-axis; μ_{ab}^{Mn} - the Mn moment in (001) Mn layers; μ^{Nd} - the Nd moment along the c-axis; the errors for the data at T=3 K are shown as typical examples.

T (K)	3 K	15 K	25 K	35 K	50 K	150 K	200 K	300 K	450 K
a(Å)	4.001(7)	4	3.999	3.998	3.997	4.001	4.003	4.009	4.022
c(Å)	10.523(8)	10.522	10.535	10.536	10.535	10.543	10.548	10.558	10.574
V(Å^3)	168.39(8)	168.38	168.43	168.44	168.42	168.74	169.04	169.73	171.13
$d_{Mn\text{-}Mn}$(Å)	2.8286(9)	2.8285	2.8273	2.8272	2.8271	2.8288	2.8307	2.8351	2.8446
Z_{Si}	0.3793(6)	0.3813	0.3807	0.3812	0.3813	0.3789	0.3786	0.3809	0.381
μ_{total}^{Mn}	1.56(4)	1.54	1.67	1.98	2.1	1.91	1.85	1.53	-
μ_c^{Mn}	1.30(6)	1.26	1.67	1.98	2.1	1.91	1.85	1.53	-
μ_{ab}^{Mn}	0.86(2)	0.89	-	-	-	-	-	-	-
μ^{Nd}	2.56(5)	2.77	-	-	-	-	-	-	-
R_{wp}	5.46	5.87	5.99	6.21	6.59	6.93	7.35	7.75	8.05
R_{exp}	3.23	3.45	3.95	4.67	4.89	5.04	5.25	5.65	5.78

the Mn moments along *c*-axis thereby leading to the formation of F*mc*+F(Nd) magnetic structure as depicted in Figures 5.9(e). This behavior agrees well with the results of Welter *et al* [51] who demonstrated that in the RMn_2Ge_2 compounds with R= Pr and Nd rare earth moments ferromagnetically coupled with the Mn sublattice at low temperatures. This behaviour, also applicable to $NdMn_2Si_2$ [8] and $NdMn_2Si_{1.6}Ge_{0.4}$ [22] compounds, is due to the exchange interaction between the light rare earth elements and 3*d* transition metal as

reported by Coey [52]. Ordering of the Nd sublattice in $NdMn_2Si_2$ below T_C has also been confirmed by Chatterji *et al* [53] from inelastic neutron scattering.

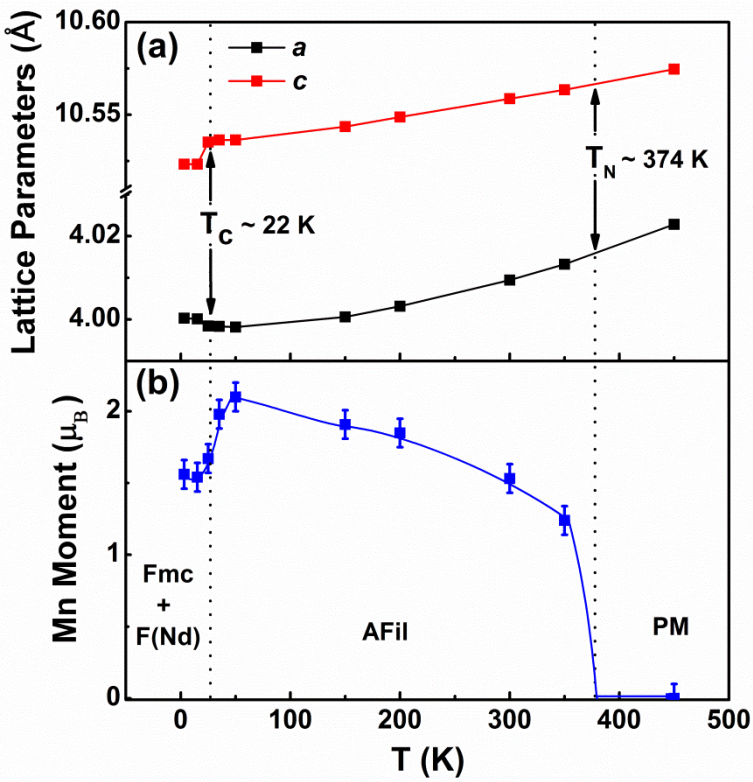

Figure 5.10 (a) The lattice parameters of $NdMn_{1.9}Ti_{0.1}Si_2$ as a function of temperature and (b) temperature dependence of the Mn magnetic moment (3-450 K). The Néel temperature T_N and Curie temperature T_C are denoted by arrows with the dotted lines delineating the paramagnetic (PM), antiferromagnetic (AF*il*-type) and ferromagnetic (F*mc*+F(Nd)) regions. The line through the moment values act as a guide to the eye.

The variation in the *a* and *c* lattice parameters with temperature are plotted in Figure 5.10(a). Both the *a* and *c* values exhibit a monotonic decrease with temperature in the region of the antiferromagnetic transition between T_N = 374 K and T_C = 22 K, while below T_C = 22 K, the *a* lattice parameter expands slightly from 3.998 Å at 35 K to 4.001 Å at 3 K whereas the *c* lattice parameter decreases from 10.536 Å at 35 K to 10.523 Å at 3 K. The variation in lattice parameters *a* and *c* shown in Figure 5.10(a) for the PM, AFil, and F*mc*+F(Nd) states is comparable with the behaviour in $NdMn_2Si_2$ [8]. The changes in lattice parameter at T_C ~ 22 K when the magnetic state changes from AFil to F*mc*+F(Nd) structure, indicates the presence

of strong magnetostructural coupling around T_C. As discussed recently [7, 54], the strong magnetostructural coupling leads to a large structural entropy change around the magnetic phase transition, thereby contributing to the total entropy change around T_C.

Figure 5.10(b) is a plot of the temperature dependence of the Mn magnetic moments as derived from the refinements. Within the AFil state region (T_N ~ 374 K > T > T_C ~ 22 K), the Mn moment increases to μ^{Mn} = 2.1 (1) μ_B at 50 K with both Nd and Mn ordering magnetically below T_C ~ 22 K. The magnetic moments for Mn and Nd have been derived to be μ_{total}^{Mn} = 1.56 (4) μ_B (of basal plane and axial components μ_{ab}^{Mn} =0.86(2) μ_B and μ_c^{Mn} =1.30(6) μ_B respectively) and μ^{Nd} = 2.56(5) μ_B at 3 K. The Nd moment and the ferromagnetic component of the Mn moment along the *c*-axis for $NdMn_{1.9}Ti_{0.1}Si_2$ are found to be 2.56(1) μ_B and 1.30(1) μ_B respectively. The resultant total moment is 3.86(1) μ_B per formula unit at 3 K which is slightly higher than that obtained from DC magnetization measurement at 10 K (3.6 μ_B per formula unit). This different value of magnetic moment is related to the non-saturation behavior shown by the magnetisation curve from DC measurements at 10 K even for a field applied of 5 T.

5.1.3.2 $NdMn_{2-x}Cr_xSi_2$

As shown by the series of x-ray diffraction patterns in Figure 5.11(a), the $NdMn_{1.7}Cr_{0.3}Si_2$ compound is single phase and exhibits the body-centred tetragonal $ThCr_2Si_2$-type structure (space group *I4/mmm*) over the temperature range ~10-300 K. No change in crystal structure is observed over this temperature range although, as discussed below, the *a* lattice parameter is found to increase slightly around T_C ~ 42(2) K while the *c* lattice parameter decreases. The patterns have been analysed using FULLPROF [30] software, and the changes in lattices

parameters *a* and *c* around T_C (volume change $\Delta V/V \sim 0.1\%$) found to agree well with the neutron data as discussed below. The temperature dependences of the magnetization of $NdMn_{1.7}Cr_{0.3}Si_2$ (6-295 K) and the differential scanning calorimetry curve obtained at higher temperatures (280-430 K) are shown in Figure 5.11(b). As is also evident from the analyses of the neutron diffraction data presented below, $NdMn_{1.7}Cr_{0.3}Si_2$ exhibits three magnetic transitions over the temperature range 6-400 K. The $T_N^{intra} \sim 380(3)$ K and $T_N^{inter} \sim 320(3)$ K antiferromagnetic transition temperatures were determined from a graph of the DSC data plotted against inverse temperature with the $T_C \sim 42(2)$ K ferromagnetic transition temperature determined from the maximum of the dM/dT versus T curve from the zero-field cooling magnetization data. Comparison of the cooling and warming magnetisation results in Figure 5.11(b) shows that the thermal hysteresis at T_C is $\Delta T < \sim 0.8$ K.

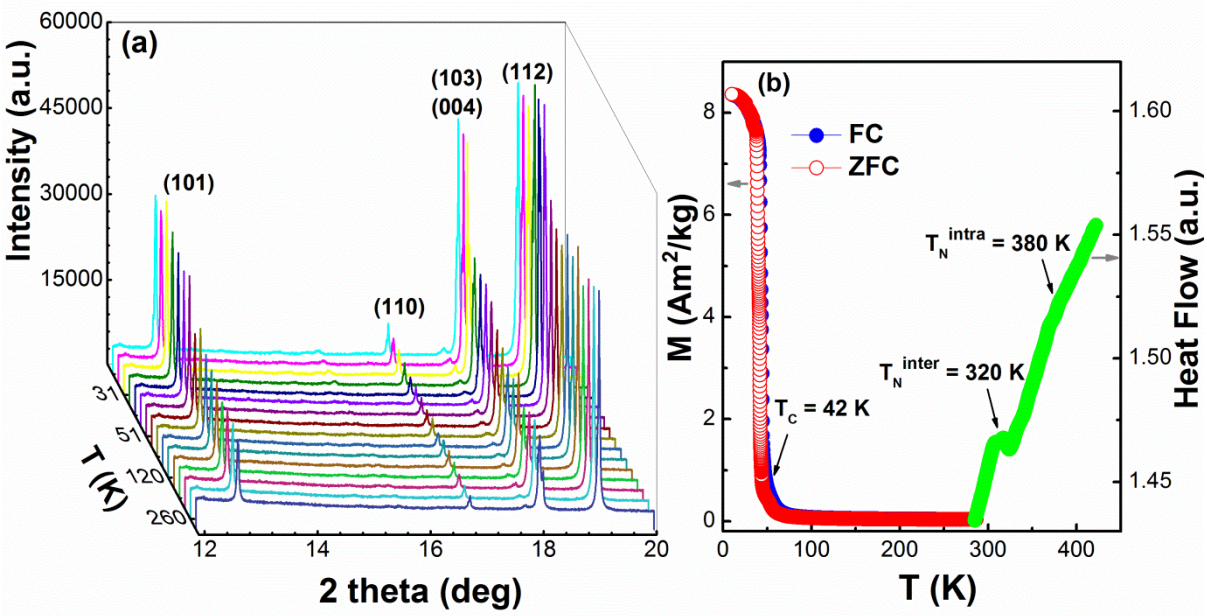

Figure 5.11 (a) X-ray diffraction patterns (synchrotron radiation) of $NdMn_{1.7}Cr_{0.3}Si_2$ over the temperature range T=10-300 K (λ=0.8265 Å). (b) Temperature dependence of the magnetization as measured in a field of 0.01 T (left axis: zero field cooling (ZFC) and field cooling (FC)); right axis: DSC results over the range T=300-420 K).

Figure 5.12(a) shows a thermal contour plot of neutron diffraction measurements on $NdMn_{1.7}Cr_{0.3}Si_2$ from 6 to 400 K. In addition to the set of patterns obtained in the warming ramp mode (step 1 K; counting time 1 min), patterns were obtained around the transition temperatures (5 K steps for 6-70 K; 10 K steps for 80-340 K; 5 K steps for 350-400 K; counting time 10 min). The neutron diffraction patterns in Figures 5.13(a-d) are representative of $NdMn_{1.7}Cr_{0.3}Si_2$ in the four regions indicated by the magnetic transition in Figure 5.11(b). The different magnetic structures indicated in Figure 5.12(b) can be discerned readily from the temperature dependence of the peak intensities for selected magnetic peaks as in Figure 5.13(e). The Rietveld refinement of the pattern at 400 K (Figure 5.13(a)) confirms that $NdMn_{1.7}Cr_{0.3}Si_2$ has the $ThCr_2Si_2$ structure as expected with the absence of

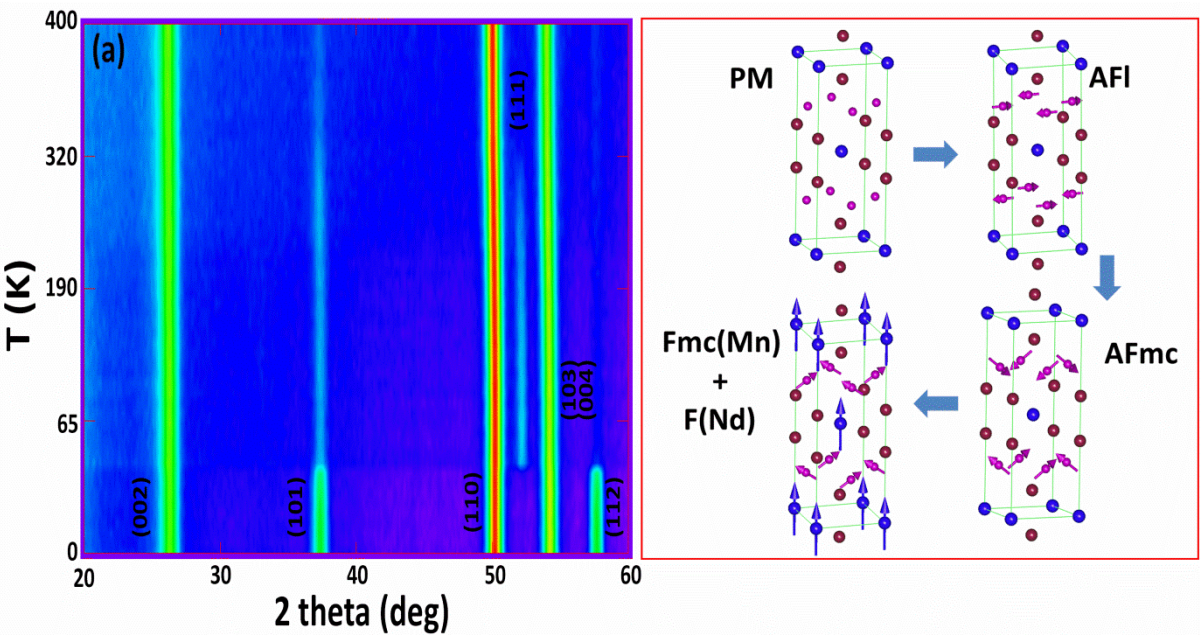

Figure 5.12 (a) Neutron diffraction patterns for $NdMn_{1.7}Cr_{0.3}Si_2$ over the temperature range 6-400 K (λ=2.4205 Å). (b) The magnetic structures of $NdMn_{1.7}Cr_{0.3}Si_2$: paramagnetism for $T>T_N^{intra}$ ~ 380(3) K; AFil ordering of the Mn sublattice for $T_N^{intra}>T>T_N^{inter}$ ~ 320(3) K; AF*mc* for $T_N^{inter}>T>T_C$ ~ 42(2) K and combined ferromagnetic state F*mc*(Mn)+F(Nd) for $T<T_C$.

coherent magnetic scattering above T_N^{intra} ~ 380(3) K consistent with paramagnetism. Below T_N^{intra} ~ 380(3) K, $NdMn_{1.7}Cr_{0.3}Si_2$ exhibits the AFil antiferromagnetic structure with

intralayer coupling (see e.g., the 375 K pattern of Figure 5.13(b) and Figure 5.13(e) with increased (101) peak intensities) down to T_N^{inter} ~ 320(3) K. On cooling below T_N^{inter} ~ 320(3) K down to T_C, $NdMn_{1.7}Cr_{0.3}Si_2$ exhibits the canted AF*mc* structure (both interlayer and intralayer antiferromagnetic coupling; see e.g. the 100 K pattern of Figure 5.13(c) and related increases in the (101) and (111) peak intensities in Figure 5.13(e)).

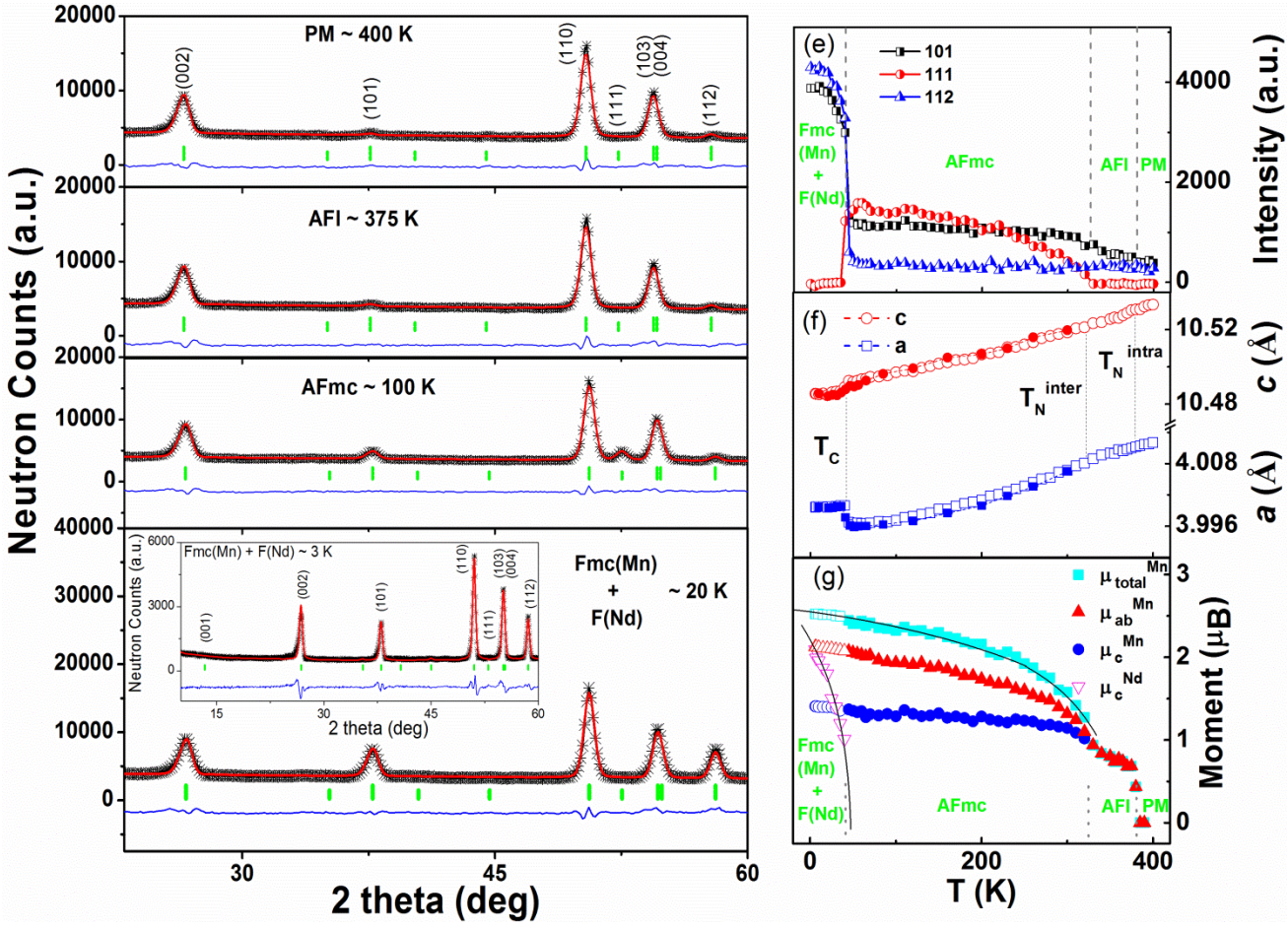

Figure 5.13 Neutron diffraction patterns (λ=2.4205 Å) for $NdMn_{1.7}Cr_{0.3}Si_2$ at: (a) 400 K; (b) 375 K; (c) 100 K; (d) 20 K (inset-3 K pattern at λ=2.4395 Å). (e) Temperature dependence of the integrated intensities of the (101), (111) and (112) reflections; (f) Lattice parameters as a function of temperature (open/closed symbols–neutron/x-ray diffraction). (g) Temperature dependence of the Mn and Nd magnetic moments (6-400 K). The full lines through the open symbols represent the Nd and Mn moments using estimation/fix Mn total moment method as discussed.

Below T_C, the absence of magnetic scattering from the (111) and (001) reflection at 20 K (Figure 5.13(d)), combined with the increase in intensity of the (112) and (101) peaks (Figure

5.13(e)), indicate that the interlayer spin components of the Mn moments have a parallel alignment, thus leading to a canted ferromagnetic structure (F*mc*) for the Mn sublattice. The additional high resolution neutron diffraction pattern at T=3 K (inset to Figure 5.13(d)) confirms the absence of the purely magnetic (001) peak and any antiferromagnetic component of the Mn moment in the *ab*-plane below T_C.

The further increase in intensities of the (112) and (101) peaks below T_C (Figure 5.13(e)) indicates an additional contribution from Nd moments coupled parallel to the Mn moments along the *c*-axis, thereby leading to the formation of the F*mc*(Mn)+F(Nd) magnetic structure. The present results agree well with the findings of Chatterji *et al*.[53], who demonstrated the ordering of the Nd sublattice in $NdMn_2Si_2$ below T_C from inelastic neutron scattering. It should be noted that the F*mc*(Mn)+F(Nd) configuration in $NdMn_{1.7}Cr_{0.3}Si_2$ differs from that of $NdMn_2Si_2$ [8], $NdMn_{1.9}Ti_{0.1}Si_2$ [55] and $NdMn_{1.8}Co_{0.2}Si_2$ [29] for which the (001) peak is present. As shown in Figure 5.13(f), both the *a* and *c* lattice parameters exhibit monotonic decreases with temperature in the antiferromagnetic region between T_N^{intra} ~ 380(3) K and T_N^{inter} ~ 320(3) K, down to T_C ~ 42(2) K. Below T_C ~ 42(2) K, the *a* lattice parameter expands slightly from 3.996(4) Å at 45 K (AF*mc*) to 3.999(5) Å at 6 K (F*mc*(Mn)+F(Nd)), whereas the *c* lattice parameter decreases from 10.492(6) Å to 10.485(5) Å. Good agreement is found with the results of the synchrotron radiation experiments (closed symbols in Figure 5.13(f)). The anomalous changes in lattice parameter around T_C ~ 42(2) K indicates the presence of strong magnetostructural coupling.

Figure 5.13(g) is a plot of the variation of the Mn magnetic moments with temperature as derived from the refinements. Within the AF*il* and AF*mc* antiferromagnetic regions, the Mn total moment increases from μ_{total}^{Mn} = 0.82(4) μ_B at T_N^{inter} ~ 320 K to μ_{total}^{Mn} = 2.04(5) μ_B at

T_C ~ 42(2) K due to the fact that, with decreasing temperature, thermal disorder becomes weaker compared with magnetic interaction. The sudden rise of Mn moment around T_N^{inter} is due to the appearance of *c*-axis components of Mn moment. Below T_C, $NdMn_{1.7}Cr_{0.3}Si_2$ has the magnetic structure shown in Figure 5.12(b). The contributions of the Mn and Nd moments to the ferromagnetic peaks of the neutron diffraction patterns cannot be separated as the magnetic contributions to the *(hkl)* lines from the rare-earth and Mn sublattices overlap below T_C^{Nd} (based on the absence of the (001) peak – see Figure 5.13(d)). Using the method with extrapolated the temperature dependence of Mn moments above T_C^{Nd} to lower temperatures below T_C^{Nd} (see e.g.[56]) where both Nd and Mn order in F*mc*(Mn)+F(Nd) region. This leads to the temperature dependence of the Nd moments as shown by the full line in Figure 5.13(g) leading to moment values μ_{total}^{Mn} = 2.52(3) μ_B and μ_c^{Nd} = 2.10(4) μ_B at 6 K.

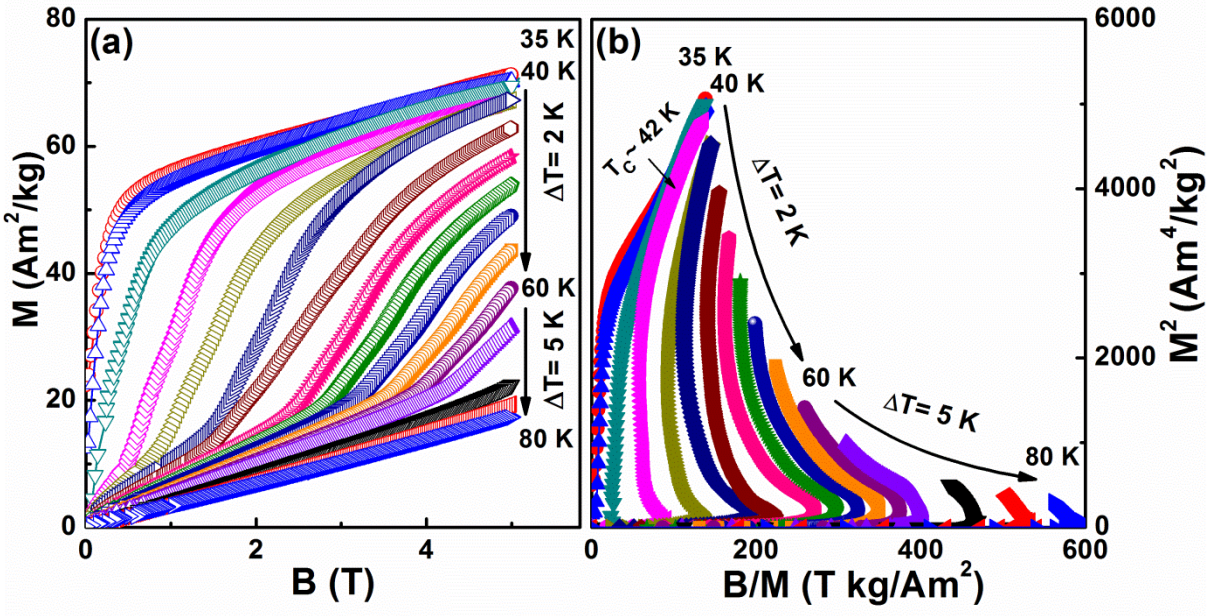

Figure 5.14 (a) Magnetization curves for $NdMn_{1.7}Cr_{0.3}Si_2$ over the temperature range 35–80 K for increasing (closed symbols) and decreasing (open symbols) and (b) the corresponding Arrott plots of M^2 versus B/M.

Comparison of the magnetization curves of $NdMn_{1.7}Cr_{0.3}Si_2$ for both increasing and decreasing fields at 2 K intervals over the temperature region ~ 35-80 K (Figure 5.14(a)) demonstrate that there are effectively negligible magnetic hysteresis effects (< ~ 0.1 T) in this compound. This behaviour indicates that $NdMn_{1.7}Cr_{0.3}Si_2$ has promising performance advantages when cycled over the metamagnetic transition from the antiferromagnetic to the ferromagnetic state for magnetic refrigerator applications [57]. As shown by the Arrott plots in Figure 5.14(b) and in agreement with the magnetic structures determined from the neutron data as above, $NdMn_{1.7}Cr_{0.3}Si_2$ is ferromagnetic below 42 K (positive intercept on M^2 axis) and antiferromagnetic above 42 K (negative intercept on M^2 axis)[39]. The observed negative slope which is nature of the Arrott plots characterize a first order magnetic transition. The absence of thermal (< ~ 0.8 K; Figure 5.11(b)) and magnetic hysteresis effects (< ~ 0.1 T; Figure 5.14(a)) in $NdMn_{1.7}Cr_{0.3}Si_2$ at T_C ~ 42(2) K, compares favourably with other materials such as $Gd_5Si_2Ge_2$ (magnetic hysteresis of ~ 1 T and thermal hysteresis of ~ 2 K at T_C ~ 276 K)[14] and $La_{0.7}Pr_{0.3}Fe_{11.4}Si_{0.6}$ (magnetic hysteresis of ~ 0.08 T and thermal hysteresis of ~ 1.5 K at T_C ~ 180 K)[4].

As shown by the magnetic entropy changes in Figure 5.15(a) (derived from the magnetization curves using the standard Maxwell relation [40]: (equation 5.3) , the $-\Delta S_M$ peak for ΔB=0-5 T gradually broadens towards higher temperatures with increasing magnetic field, which is characteristic of a field induced transition from an antiferromagnetic to a ferromagnetic state. The entropy value at the respective Curie temperatures, $-\Delta S_M$ ~ 15.3 J kg^{-1} K^{-1} at T_C ~ 42(2) K (ΔB=0-5 T) for $NdMn_{1.7}Cr_{0.3}Si_2$, is greater than for Gd (9.5 J kg^{-1} K^{-1}) and near that for the giant magnetocaloric effect $Gd_5Si_2Ge_2$ compound (18.8 J kg^{-1} K^{-1})[14]. The MCE value of $NdMn_{1.7}Cr_{0.3}Si_2$ is comparable to those of other materials, which include: GdCoAl [43] ($-\Delta S_M$=10.4 J kg^{-1} K^{-1} at 100 K) and TbCoAl [43] ($-\Delta S_M$=10.5 J kg^{-1} K^{-1} at 70 K), all of which,

in common with $NdMn_{1.7}Cr_{0.3}Si_2$, importantly exhibit negligible field and thermal hysteresis losses.

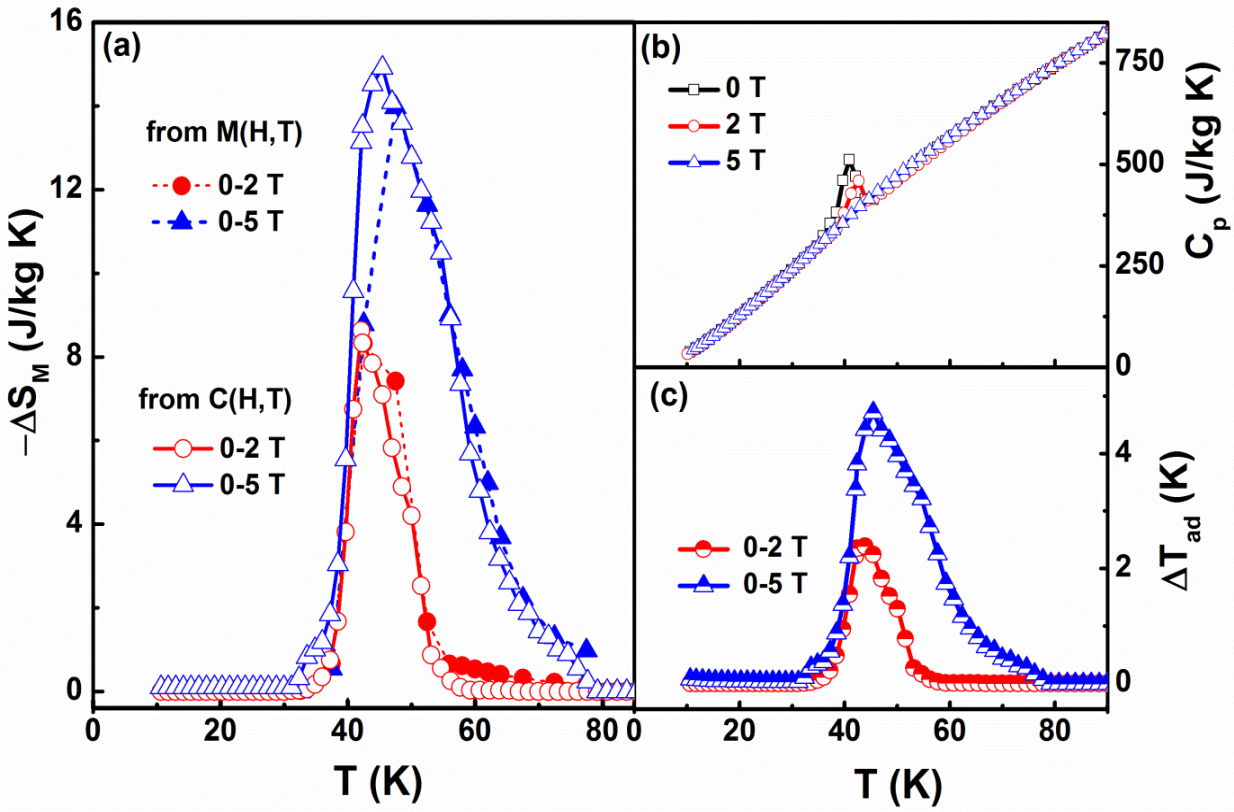

Figure 5.15 (a) Magnetic entropy change, $-\Delta S_M$, of $NdMn_{1.7}Cr_{0.3}Si_2$ determined from heat capacity (open symbols) and magnetization (closed symbols) measurements for ΔB=0-2 T and ΔB=0-5 T; (b) Heat capacity of $NdMn_{1.7}Cr_{0.3}Si_2$ for B=0 T, 2 T, 5 T; (c) Adiabatic temperature change, ΔT_{ad}, as determined from the heat capacity measurements of Figure 5.15(b).

The magnetic entropy change, $-\Delta S_M$ (T, B), has been derived from heat calorimetric measurements of the field dependence of the heat capacity using the expression [44, 45]: - (equation 5.4). The corresponding adiabatic temperature change, ΔT_{ad}, be evaluated from - ΔS_M (T, B) and the zero field heat capacity data as (equation 5.5). Figure 5.15(b) shows the set of heat capacity measurements obtained for $NdMn_{1.7}Cr_{0.3}Si_2$ (B=0 T, 2 T, and 5 T) with the corresponding $-\Delta S_M$ (T, B) and ΔT_{ad} values shown in Figures 5.15(a) and 5.15(c). The peak value of the adiabatic temperature change is $\Delta T_{ad}^{max} \sim 5$ K for ΔB=0-5 T. As shown in Figure 5.15(a), the maximum magnetic entropy change determined from the heat capacity

measurements $-\Delta S_M^{max} \sim 15$ J kg^{-1} K^{-1} is similar to the value $-\Delta S_M^{max} \sim 15.3$ J kg^{-1} K^{-1} determined from the magnetic measurements. This good agreement confirms that the $-\Delta S_M$ values derived for $NdMn_{1.7}Cr_{0.3}Si_2$ from the magnetization measurements represent the MCE behaviour within experimental errors [14, 22]. The contribution to the MCE value for ΔB=0-5 T due to the structural volume expansion is around $-\Delta S_{structural} \sim 1.25$ J kg^{-1} K^{-1} as estimated using the method described by Gschneidner *et al.*[54].

5.1.3.3 $NdMn_{2-x}Cu_xSi_2$

Confirmation that all of the $NdMn_{2-x}Cu_xSi_2$ (x = 0-1.0) samples crystallize in the expected $ThCr_2Si_2$ type structure with space group I4/mmm was provided by analysis of the x-ray powder diffraction patterns. The x-ray diffraction patterns at variable temperatures for x=0.2 are shown in Figure 5.16(a) as a typical example. The measured data from the diffraction patterns were analysed using the Rietveld refinement temperature dependence of the magnetization of $NdMn_{2-x}Cu_xSi_2$ (x = 0-1.0) measured in a magnetic field of B = 0.01 T is shown in Figure 5.16(c) together with the differential scanning calorimetry (DSC). As using calculation in Ref [58], the Néel temperature T_N found to decreases from ~ 380 K to ~ 320 K with increase in Cu concentration from x = 0 to x = 1.0 while Curie temperature T_C increase from ~ 36 K to ~ 100 K. The reduction of unit cell volume due to Cu substitution as shown in Figure 5.16(b) will lead to decrease the Mn-Mn intralayer exchange interaction. Moreover, the change in electronic environment on replacing Mn ($3d^5 4s^2$) by Cu ($3d^{10} 4s^1$) is also expected to influence the magnetic structures and states of the $NdMn_{2-x}Cu_xSi_2$ compounds.

The magnetization curves obtained for $NdMn_{1.8}Cu_{0.2}Si_2$ and $NdMn_{1.4}Cu_{0.6}Si_2$ around their ferromagnetic ordering temperatures are shown in Figures 5.17(a-b). Comparison of the

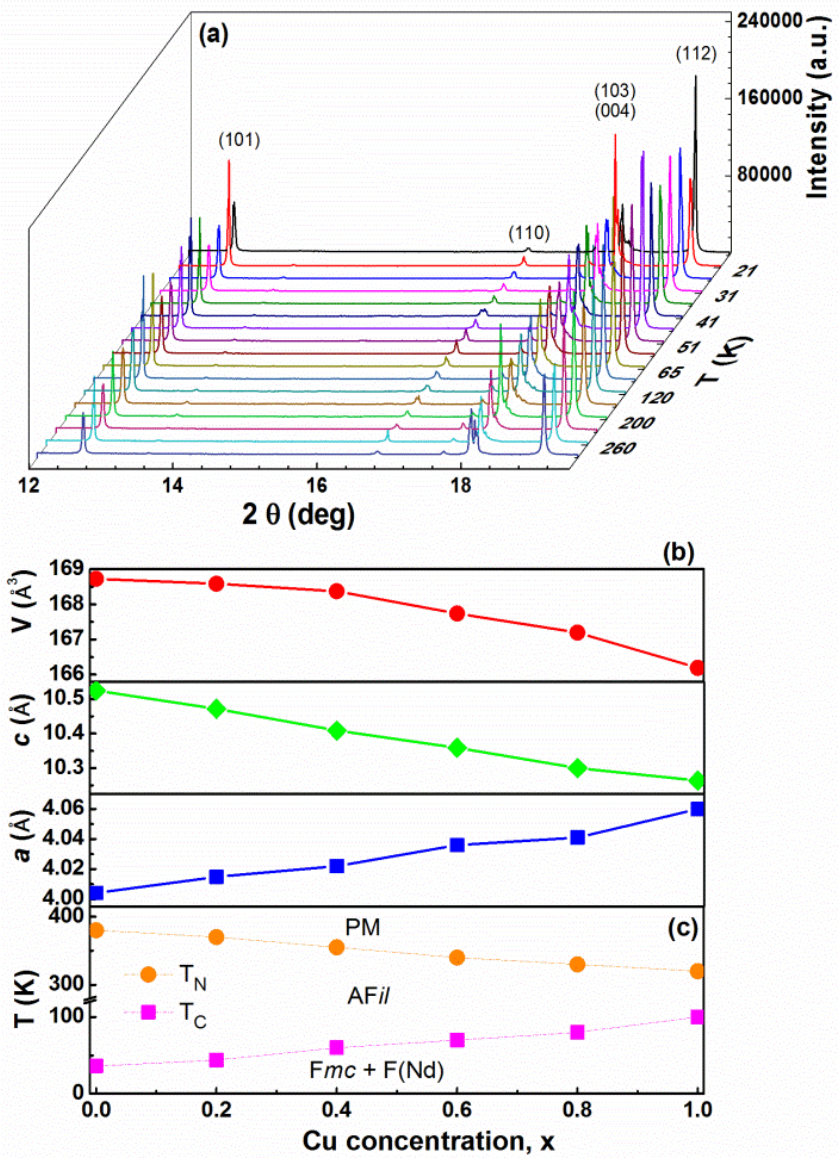

Figure 5.16 (a) XRD pattern for $NdMn_{1.8}Cu_{0.2}Si_2$ compound at range 10-300 K (λ = 0.8265(8) Å) ;(b) Variation of unit cell volume V, *c* and *a* for room temperature with Cu content and (c) Temperature dependence of magnetization, the Néel temperatures (T_N) and the Curie temperatures (T_C) of $NdMn_{2-x}Cu_xSi_2$ compound.

magnetisation curves around the ferromagnetic ordering temperatures for $NdMn_{1.8}Cu_{0.2}Si_2$ and $NdMn_{1.4}Cu_{0.6}Si_2$ reveal pronounced hysteresis losses keep decreasing from ~ 12 J kg^{-1} to no hysteresis loss are observed for $NdMn_{1.4}Cu_{0.6}Si_2$ (indicated values for B = 0 - 5 T as suitable to comparison). It is demonstrated clearly that magnetic hysteresis losses decrease significantly on substitution of Cu for Mn as indicated that increasing Cu concentration contributes to a weakening of the characteristic field induced metamagnetic transition from

the antiferromagnetic to the ferromagnetic state. Figures 2(c) and (d) show the corresponding Arrott plots (M^2 versus B/M) for the x = 0.2 and 0.6 samples, respectively. The Arrott plots

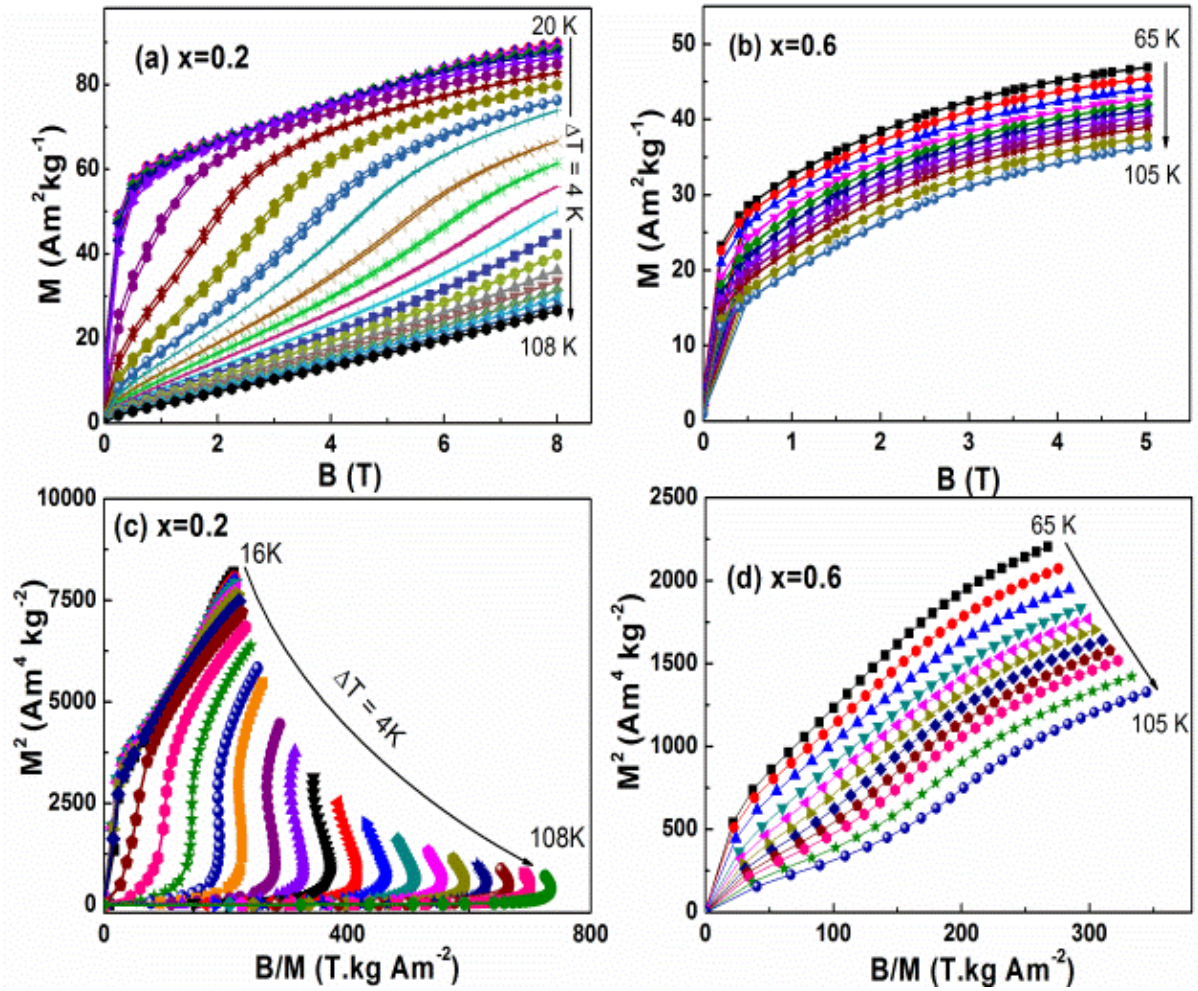

Figure 5.17 Isothermal magnetization curves in the vicinity of the ferromagnetic ordering temperatures for: (a) $NdMn_{1.8}Cu_{0.2}Si_2$, (B = 0 - 8 T) and (b) $NdMn_{1.4}Cu_{0.6}Si_2$ (B = 0 - 5 T) compound respectively. (c) Arrott plots of $NdMn_{2-x}Cu_xSi_2$; x=0.2 and (d) x=0.6 compounds.

are found to exhibit features characteristic of a first order transition for x < 0.6 to second order transition for x ≥ 0.6 as shown in Figures 5.17(c-d). As been determined by particular the nature of the Arrott plot near T_C denotes a negative order of the sign of the coefficient c2(T) in the Landau expansion of the magnetic free energy [39], thereby denoting a first order magnetic transition for x<0.6 and been confirmed with nature of phase transitions method [59].

The magnetic entropy change, $-\Delta S_M$, has been determined for the set of $NdMn_{2-x}Cu_xSi_2$ compounds (x = 0 -1.0) from their magnetization curves for decreasing field values as functions of temperature and magnetic field (ΔB = 0-5 T). The magnetic entropy change has been derived by applying the standard Maxwell relation as used before (equation 5.3).

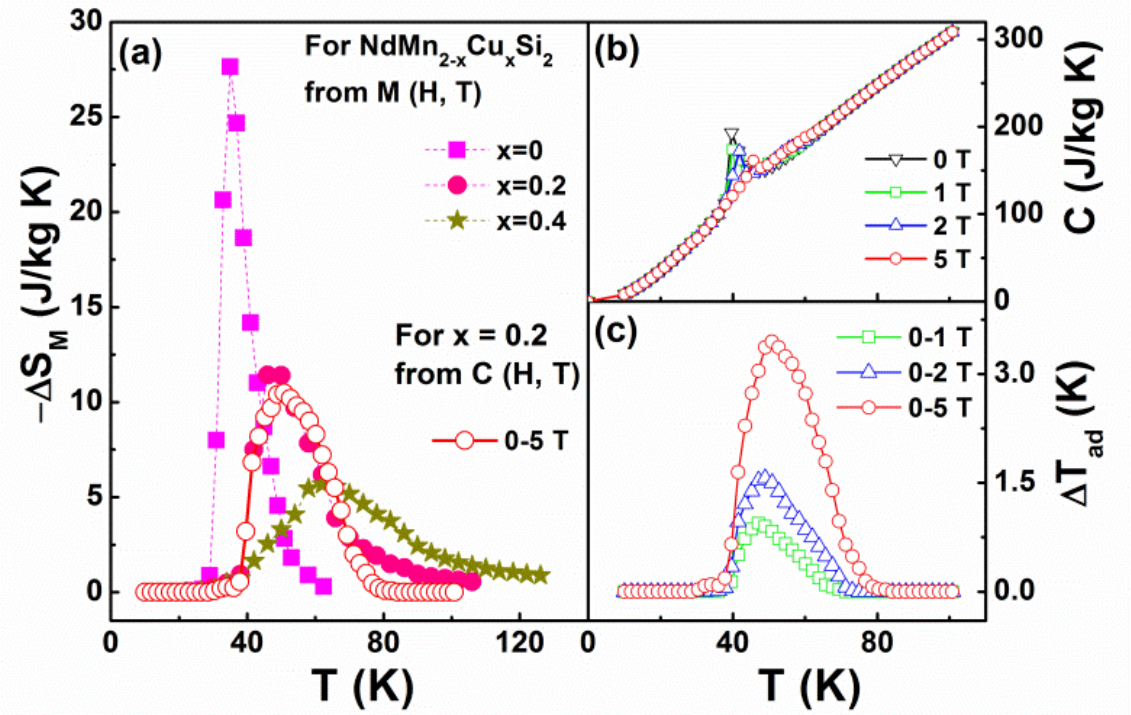

Figure 5.18 (a) The magnetic entropy change, $-\Delta S_M$, determined from magnetization and the heat capacity measurements of Fig. 3(b) for $NdMn_{1.8}Cu_{0.2}Si_2$ (ΔB = 0-5 T). (b) The heat capacity of $NdMn_{1.8}Cu_{0.2}Si_2$ as measured over the temperature range 10-90 K. (c) The adiabatic temperature change, ΔT_{ad}, for $NdMn_{1.8}Cu_{0.2}Si_2$.

As shown by the curves of Figure 5.18(a), the $-\Delta S_M$ peak found consistently decrease with Cu concentration x=0, 0.2, 0.4, 0.6, 0.8 and 1.0 as: $-\Delta S_M \sim 27$ J kg^{-1} K^{-1} at T_C = 36 K; $-\Delta S_M \sim 13$ J kg^{-1} K^{-1} at T_C = 44 K; $-\Delta S_M \sim 6.5$ J kg^{-1} K^{-1} at T_C = 60 K; $-\Delta S_M \sim 3.5$ J kg^{-1} K^{-1} at T_C = 70 K; $-\Delta S_M \sim 1.5$ J kg^{-1} K^{-1} at T_C = 80 K and $-\Delta S_M \sim 0.5$ J kg^{-1} K^{-1} at T_C = 100 K. The decrease in magnetization on substitution of the non-magnetic Cu for Mn, correspondingly reduces the value of $-\Delta S_M$. The magnetic entropy change, $-\Delta S_M$ (T, B) has been derived from heat

calorimetric measurements using the expression (equation 5.4) for comparison with magnetization measurement.

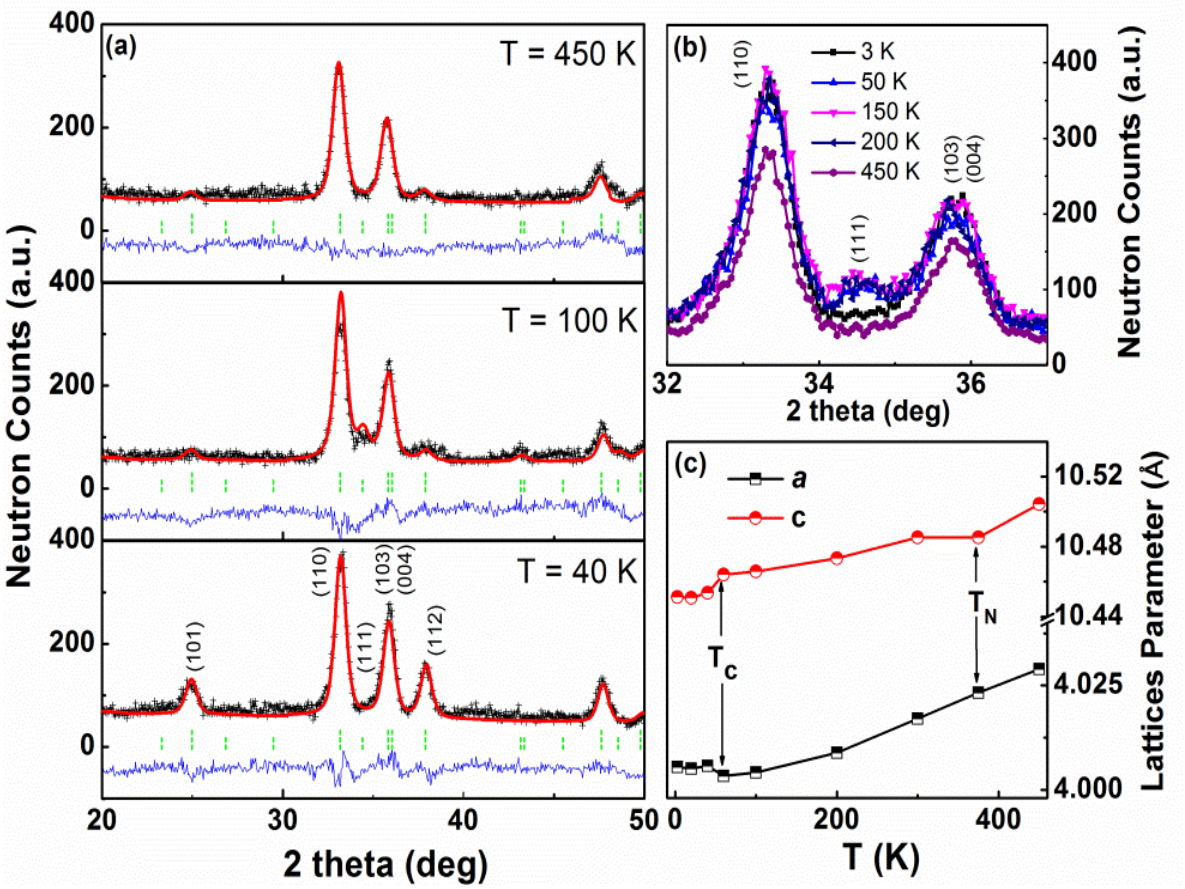

Figure 5.19 (a), Neutron diffraction patterns for $NdMn_{1.8}Cu_{0.2}Si_2$ at 450 K, 100 K, and 40 K respectively. (b) Expanded view of the neutron diffraction pattern for $NdMn_{1.8}Cu_{0.2}Si_2$ at selected temperatures. (c) The lattice parameters of $NdMn_{1.8}Cu_{0.2}Si_2$ as a function of temperature.

The corresponding adiabatic temperature change, ΔT_{ad} were been evaluated from (equation 5.5) as shown in Figure 5.18(b) the set of heat capacity measurement obtained for $NdMn_{1.8}Cu_{0.2}Si_2$ with B = 0, 2, and 5 T. The corresponding $-\Delta S_M(T, B)$ values for $NdMn_{1.8}Cu_{0.2}Si_2$ are shown in Figure 5.18(a) with the ΔT_{ad}^{max} = 3.44 K for ΔB = 0-5 T values in Figure 5.18(c). The $-\Delta S_M^{max}$ for $NdMn_{1.8}Cu_{0.2}Si_2$ as determined from the heat capacity measurement ~ 11.5 J kg^{-1} K^{-1} is comparable to the magnetic measurements using the Maxwell relation ~ 13 J kg^{-1} K^{-1} for ΔB = 0-5 T as shown in Figure 5.18(a).

The diffraction patterns (λ = 1.622(1) Å) and Rietveld refinements obtained for $NdMn_{1.8}Cu_{0.2}Si_2$ at 450 K, 100 K and 40 K are shown in Figure 5.19(a) typify the behaviour of the three magnetic regions (paramagnetic-antiferromagnetic-ferromagnetic) as found similar to $NdMn_{1.9}Ti_{0.1}Si_2$ [55] respectively. Rietveld refinements of the neutron diffraction pattern at 450 K (paramagnetic state) confirm that $NdMn_{1.8}Cu_{0.2}Si_2$ has the $ThCr_2Si_2$ structure and below T_N ~ 375 K, is found to exhibit the antiferromagnetic interlayer coupling structure (AF*il*) down to T_C ~ 44 K (T = 100 K). The AF*il* structure was confirmed by the magnetic scattering observed at the (111), (113) and (201) reflections (extinction rules $h + k = 2n$ and $h + k + l = 2n+1$) indicated a collinear antiferromagnetic structure between adjacent Mn planes in a + - + - sequence along the *c*-axis. When cooling to below T_C ~ 44 K, the magnetic scattering from the (101) and (112) reflections was found to increase (T = 40 K), combined with the eliminate in intensity of the (111) peak as in Figure 5.19(b), confirmed that the interlayer spin components of the Mn moments align parallel, thus contribute to a canted ferromagnetic structure (F*mc*) for the Mn sublattice. The variation in the *a* and *c* lattice parameters with temperature are plotted in Figure 5.19(c). Both the *a* and *c* values exhibit a monotonic decrease with temperature in the region of the antiferromagnetic transition between T_N ~ 375 K and T_C ~ 44 K, while below T_C ~ 44 K, the *a* lattice parameter expands slightly from 4.003(5) Å to 4.005(3) Å whereas the *c* decreases from 10.464(3) Å to 10.451(3) Å at 60 K and at 3 K. The changes in lattice parameter at T_C ~ 44 K according to magnetic state changes from AF*il* to F*mc*+F(Nd) structure, indicates the presence of strong magnetostructural coupling contributing to the total entropy change around T_C.

5.1.3.4 $NdMn_{2-x}V_xSi_2$

All of the $NdMn_{2-x}V_xSi_2$ (x = 0, 0.1, 0.2, 0.3,0.4 and 0.5) samples has been confirm crystallize in the expected $ThCr_2Si_2$ type structure with space group I4/mmm [31] by Rietveld refinement technique [30] analysis of the room temperature x-ray powder diffraction patterns. Substitution of V for Mn does not change the crystal structure but leads to an expansion of the unit cell. The lattice constant *a* sightly decreases but significant increases in *c*, and correspondingly the unit cell volumes, were found with the V concentration. As shown in Table 5.4, $d_{Mn\text{-}Mn}$ decrease from 2.8312(6) Å to 2.8288(6) Å and $d_{Mn\text{-}Nd}$ increase from 3.3063(6) Å to 3.3223(6) Å for x=0 and x=0.5. However $d_{Mn\text{-}Mn}$ remains below $d_{Mn\text{-}Mn}^{crit}$ = 2.87 Å for all compositions similar to other compounds from previous case study.

Table 5.4 Lattice parameters, unit cell volume, and Mn-Mn distance of the $NdMn_{2-x}V_xSi_2$ compounds with x = 0, 0.1, 0.2, 0.3, 0.4 and 0.5 as determined from refinement of the room temperature x-ray diffraction patterns. The errors are shown for $NdMn_2Si_2$ as a typical example.

$NdMn_{2-x}V_xSi_2$	*a* (Å)	*c* (Å)	*V* (Å^3)	*c/a*	$d_{Mn\text{-}Mn}$ (Å)	$d_{Mn\text{-}Nd}$ (Å)
x = 0	4.0039(5)	10.5251(6)	168.73(4)	2.6287(3)	2.8312(6)	3.3063(6)
x = 0.1	4.00302	10.5484	169.03	2.6351	2.8306	3.3106
x = 0.2	4.00219	10.5633	169.20	2.6394	2.8299	3.3134
x = 0.3	4.00115	10.5847	169.45	2.6454	2.8293	3.3173
x = 0.4	4.00098	10.5951	169.60	2.6481	2.8291	3.3193
x = 0.5	4.00056	10.6104	169.81	2.6522	2.8288	3.3223

From other view with high resolution x-ray diffraction, the $NdMn_{1.7}V_{0.3}Si_2$ compound is found single phase and exhibits the body-centred tetragonal $ThCr_2Si_2$-type structure (space group *I4/mmm*) over the temperature range ~10-300 K as shown in Figure 5.20. No change in crystal structure is observed over this temperature range although, as discussed more detail

below, the *a* lattice parameter is found to increase slightly around T_C ~ 24 K while the *c* lattice parameter decreases.

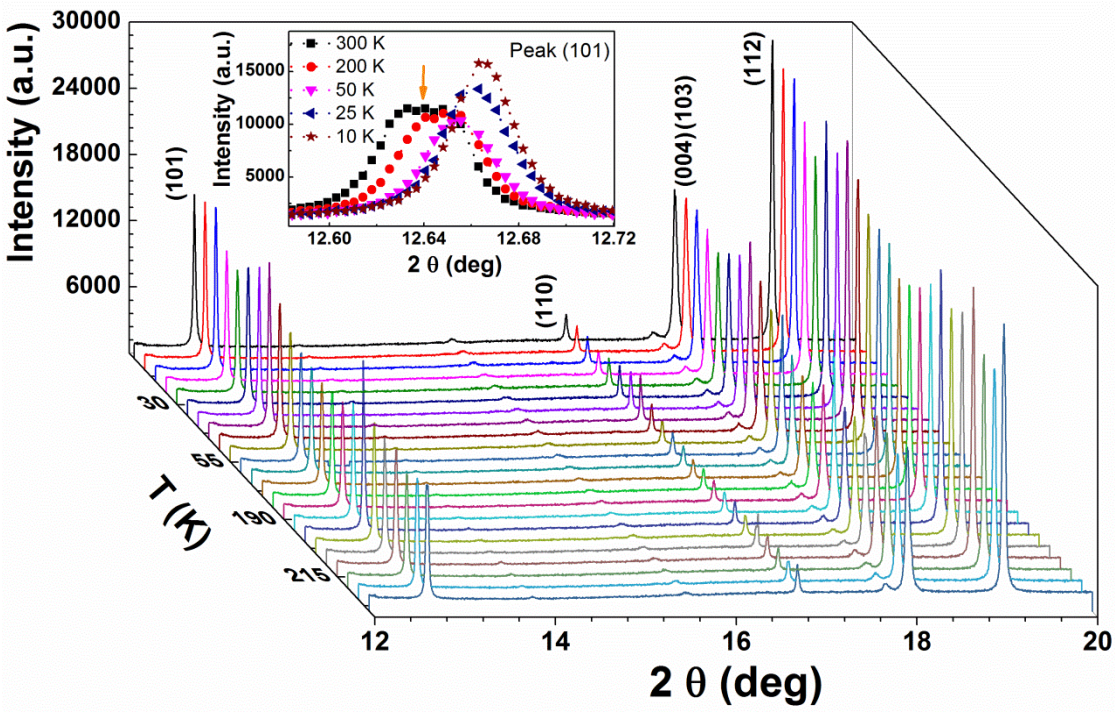

Figure 5.20 (a) X-ray diffraction patterns (synchrotron radiation) of $NdMn_{1.9}V_{0.1}Si_2$ over the temperature range T=10-300 K (λ=0.8265 Å).

The temperature dependence of the magnetization of $NdMn_{2-x}V_xSi_2$ (x = 0, 0.1, 0.2, 0.3,0.4 and 0.5) measured in a magnetic field of B = 0.01 T over the temperature range ~ 10-300 K is shown in Figure 5.21 together with the differential scanning calorimetry (DSC) curves over the temperature range ~ 300-450 K. The inset shows the values of the Néel temperature T_N and the Curie temperature T_C, for the set of compounds as defined by 1/M versus temperature and the maxima of the *d*M/*d*T versus temperature graphs respectively. Inspection of the insert to Figure 5.21, reveals that T_N decreases from ~ 380 K to ~ 345 K with increase in V concentration from x = 0 to x = 0.5 while T_C decreases from ~ 36 K to ~ 16 K. As shown in Table 5.4 $d_{Mn\text{-}Mn}$ and $d_{Mn\text{-}Nd}$ are found to increase from $d_{Mn\text{-}Mn}$ = 2.8312(6) Å, $d_{Mn\text{-}Nd}$ =

3.3063(6) Å at x = 0 to $d_{Mn\text{-}Mn}$ = 2.8341(6) Å, $d_{Mn\text{-}Nd}$ = 3.3180(6) Å at x = 0.3 and this expansion (size effect) will lead to enhancement of the Mn-Mn intralayer exchange interaction.

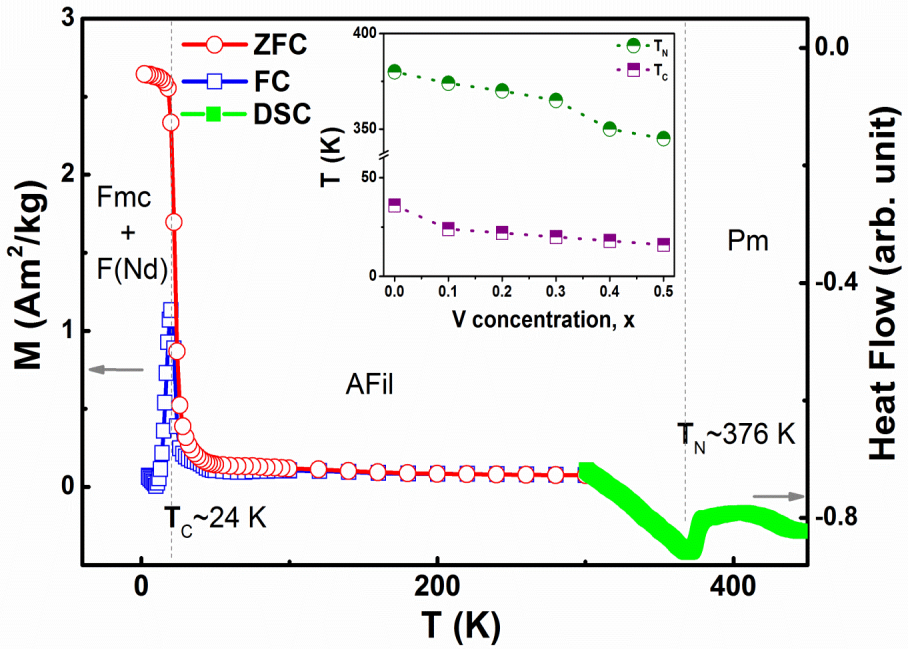

Figure 5.21 Temperature dependence of magnetization of $NdMn_{2-x}V_xSi_2$ compounds (x = 0) as measured in a field of 0.01 T (left axis; red open symbols for zero field cooling, ZFC, and blue open symbol for field cooling, FC); and differential scanning calorimetry measurements for the temperature range 300-450 K (right axis; solid symbols). The inset shows the Néel temperatures (T_N) and the Curie temperatures (T_C) for the set of samples.

On the other hand, increased V concentration is also expected to weaken the exchange interactions of Mn-Mn between layers and the Mn-Nd due to the magnetic dilution effect. Moreover, the change in electronic environment on replacing Mn ($3d^5 4s^2$) by V ($3d^3 4s^2$) is also expected to influence the magnetic structures and states of the $NdMn_{2-x}V_xSi_2$ compounds. These results indicate in Figure 5.22 that for $NdMn_{2-x}V_xSi_2$ compounds over the V concentration range x = 0.0 to 1.0, the electronic effects, rather than atomic size effects produce the observed decrease in magnetic transition temperature.

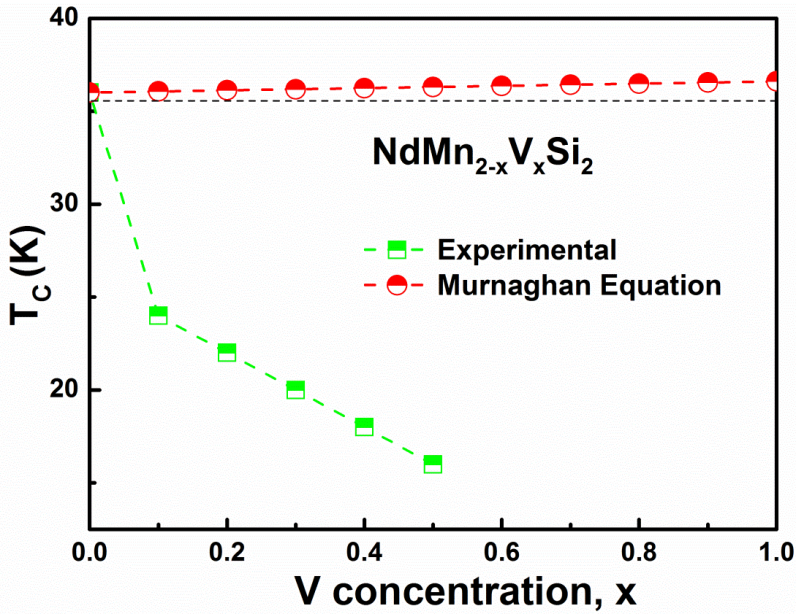

Figure 5.22 Experimental (squares) and calculated values (circles) of the Curie temperature T_C as a function of V concentration for $NdMn_{2-x}V_xSi_2$ (x = 0, 0.1, 0.2, 0.3, 0.4 and 0.5). The T_C values were calculated using the Murnaghan equation and dT_C/dp = -0.6 K/kbar as described in the text. The dashed lines act as a guide to the eye with the horizontal dashed line included to emphasise the slight increase in the calculated T_C values, with increasing V concentration.

The magnetization versus field curves (B = 0-5 T) for $NdMn_{2-x}V_xSi_2$ (x = 0, 0.1, 0.2, 0.3, 0.4 and 0.5) at 10 K are shown in Figure 5.23. The magnetization is not saturated up to 5 T indicating large magnetic anisotropy in these samples as similar to other studies at previous compounds. The saturation magnetization, M_S (at 10 K) is found to decrease with increasing V concentration in the $NdMn_{2-x}V_xSi_2$ compounds. If we assume that the rare earth moment does not change with V content, it can be derived that the substitution of V atoms for Mn leads to a decrease of around -2.2 μ_B per V atom (from linear fitting), which is expected with a simple dilution model (in which the V atoms do not carry magnetic moment).

The magnetization curves obtained for $NdMn_{1.9}V_{0.1}Si_2$ and $NdMn_{1.9}V_{0.5}Si_2$ for fields in the range B = 0 - 8 T and B = 0 - 5 T around their ferromagnetic ordering temperatures are shown in Figures 5.24 (a) and (b), respectively. These data were obtained for increasing and

decreasing fields at 2 K intervals spanning a range around T_C, thus providing information about magnetic hysteresis loss effects has been eliminated which is similar to $NdMn_{2-x}Ti_xSi_2$ compounds from previous study.

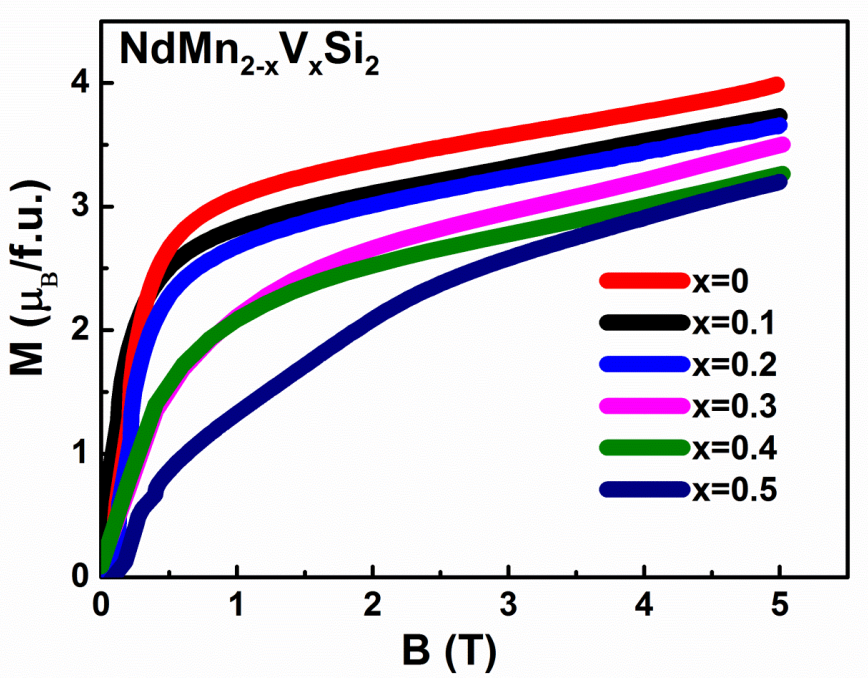

Figure 5.23 Magnetization curves (B = 0 - 5 T) for $NdMn_{2-x}V_xSi_2$ compounds (x = 0, 0.1, 0.2, 0.3, 0.4 and 0.5) at T = 10 K.

As mentioned before, significant MCE values and magnetic entropy changes are usually obtained with a first order magnetic transition due to a large rate of change of magnetisation. Figures 5.24 (c) and (d) show the corresponding Arrott plots (M^2 versus B/M) for the x = 0.1 and 0.5 samples, respectively. The Arrott plots are found to exhibit features characteristic of a first order transition for all of the samples. In particular the nature of the Arrott plot near T_C denotes a negative order of the sign of the coefficient c2(T) in the Landau expansion of the magnetic free energy [39], thereby denoting a first order magnetic transition. The present findings demonstrate that the ferromagnetic transition at T_C in $NdMn_{2-x}V_xSi_2$ remains a first order transition on substitution of V for Mn until V concentration up to x=0.5.

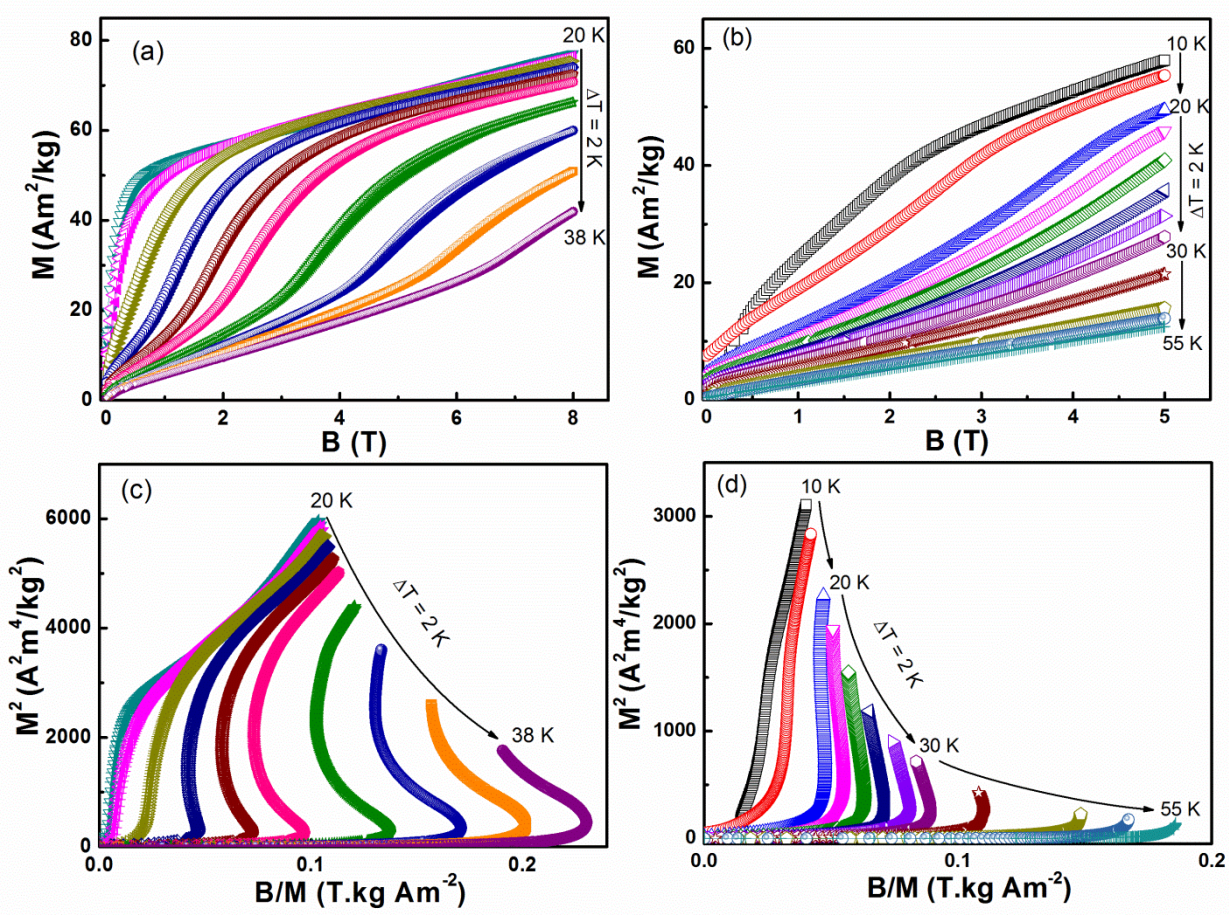

Figure 5.24 Isothermal magnetization curves in the vicinity of the ferromagnetic ordering temperatures for: (a) $NdMn_{1.9}V_{0.1}Si_2$ (T_C = 24 K with B = 0 - 8 T) and (b) $NdMn_{1.5}V_{0.5}Si_2$ (T_C = 16 K with B = 0 - 5 T); Arrott plots of M^2 versus B/M for the set of $NdMn_{2-x}V_xSi_2$ compounds: (c) $NdMn_{1.9}V_{0.1}Si_2$ and (d) $NdMn_{1.5}V_{0.5}Si_2$.

The magnetic entropy change, $-\Delta S_M$, has been determined for the set of $NdMn_{2-x}V_xSi_2$ compounds (x = 0.1) from their magnetization curves for both increasing and decreasing field values as functions of temperature and magnetic field (ΔB = 0-8 T). The magnetic entropy change has been derived by applying the standard Maxwell relation [40] using (equation 5.3) : As shown by the curves of Figure 5.25 (a), the $-\Delta S_M$ peak (closed symbols for increasing field values and open symbols for decreasing field values) gradually broadens towards higher temperatures with increasing magnetic field (from ΔB = 0-5 T), behaviour characteristic of a field induced transition from an antiferromagnetic to a ferromagnetic state.

The changes in magnetic entropy for the set of $NdMn_{2-x}V_xSi_2$ compounds (x = 0, 0.1, 0.2, 0.3, 0.4 and 0.5) around their ferromagnetic ordering temperatures are shown in Figure 5.25 (b) as calculated from decreasing applied fields in order to satisfy the suitability of different experimental and related analytical approaches to establish the isothermal entropy change [41].

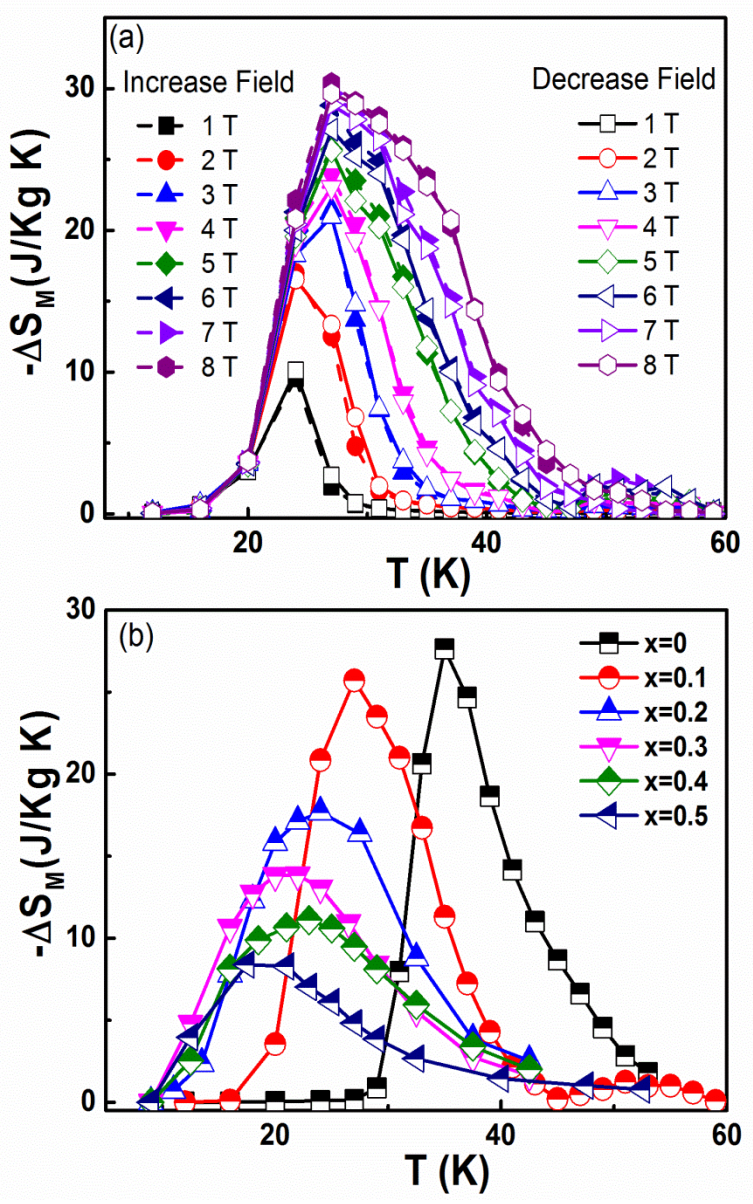

Figure 5.25 (a) The temperature dependence of the isothermal magnetic entropy change, $-\Delta S_M$, for $NdMn_{0.9}V_{0.1}Si_2$ as determined from the magnetization isotherms (closed symbols for increasing fields and open symbols for decreasing fields). (b) The temperature dependence of the isothermal magnetic entropy change, $-\Delta S_M$, for $NdMn_{2-x}V_xSi_2$ compounds with x = 0, 0.1, 0.2, 0.3, 0.4 and 0.5 as measured from magnetization isotherms (ΔB = 0-5 T from decreasing field curves).

The entropy values at the respective Curie temperatures are (ΔB = 0-5 T): $-\Delta S_M$ ~ 27 J kg^{-1} K^{-1} at T_C = 36 K; $-\Delta S_M$ ~ 25.3 J kg^{-1} K^{-1} at T_C = 24 K; $-\Delta S_M$ ~ 17 J kg^{-1} K^{-1} at T_C = 22 K; $-\Delta S_M$ ~ 13.8 J kg^{-1} K^{-1} at T_C = 20 K; $-\Delta S_M$ ~ 10 J kg^{-1} K^{-1} at T_C = 18 K and $-\Delta S_M$ ~ 8 J kg^{-1} K^{-1} at T_C = 16 K for x=0, 0.1, 0.2, 0.3, 0.4 and 0.5 respectively. The decrease in magnetization on substitution of the non-magnetic V for Mn, correspondingly reduces the value of $-\Delta S_M$. Never the less it is noted that the MCE values of $-\Delta S_M$ ~ 25.3 J kg^{-1} K^{-1} for $NdMn_{1.9}V_{0.1}Si_2$ and $-\Delta S_M$ ~ 17 J kg^{-1} K^{-1} for $NdMn_{1.8}V_{0.2}Si_2$ are comparable and higher with MCE values for other materials with small hysteresis that exhibit transitions in the temperature region below 100 K with these materials : $TbCoC_2$ [42] ($-\Delta S_M$ = 15 J kg^{-1} K^{-1} at 28 K), GdCoAl [43] ($-\Delta S_M$ = 10.4 J kg^{-1} K^{-1} at 100 K) and TbCoAl [43] ($-\Delta S_M$ = 10.5 J kg^{-1} K^{-1} at 70 K).

The magnetic entropy change, $-\Delta S_M$ (*T*, *B*) derive from (equation 5.4) as heat calorimetric measurements of the field dependence of the heat capacity and the corresponding adiabatic temperature change, ΔT_{ad} evaluated using the expression [10, 44, 45]. Figure 5.26 (a) shows the set of heat capacity measurement obtained for $NdMn_{1.9}V_{0.1}Si_2$ with B = 0, 2, 5 and 8 T. The corresponding $-\Delta S_M$ (*T*, *B*) values for $NdMn_{1.9}V_{0.1}Si_2$ are shown in Figure 5.26 (b) with the ΔT_{ad} values shown in Figure 5.26 (c). The peak value of the adiabatic temperature change is ΔT_{ad}^{max} = 6.9 K for Δ*B* = 0-8 T using the(equation 5.5). As shown in Figure 5.8(b), the maximum magnetic entropy change for $NdMn_{1.9}V_{0.1}Si_2$ as determined from the heat capacity measurements of $-\Delta S_M^{max}$ ~ 24.9 J kg^{-1} K^{-1} and 11.5 J kg^{-1} K^{-1} for Δ*B* = 0-5 T and 0-2 T are slightly smaller to the maximum entropy change $-\Delta S_M^{max}$ ~ 25.3 J kg^{-1} K^{-1} and 12.8 J kg^{-1} K^{-1} as determined from the magnetic measurements using the Maxwell relation. The good agreement between the two sets of measurements confirms that the $-\Delta S_M$ values derived for $NdMn_{1.9}V_{0.1}Si_2$ from the magnetization measurements represent the MCE behaviour within experimental errors [14, 22, 46].

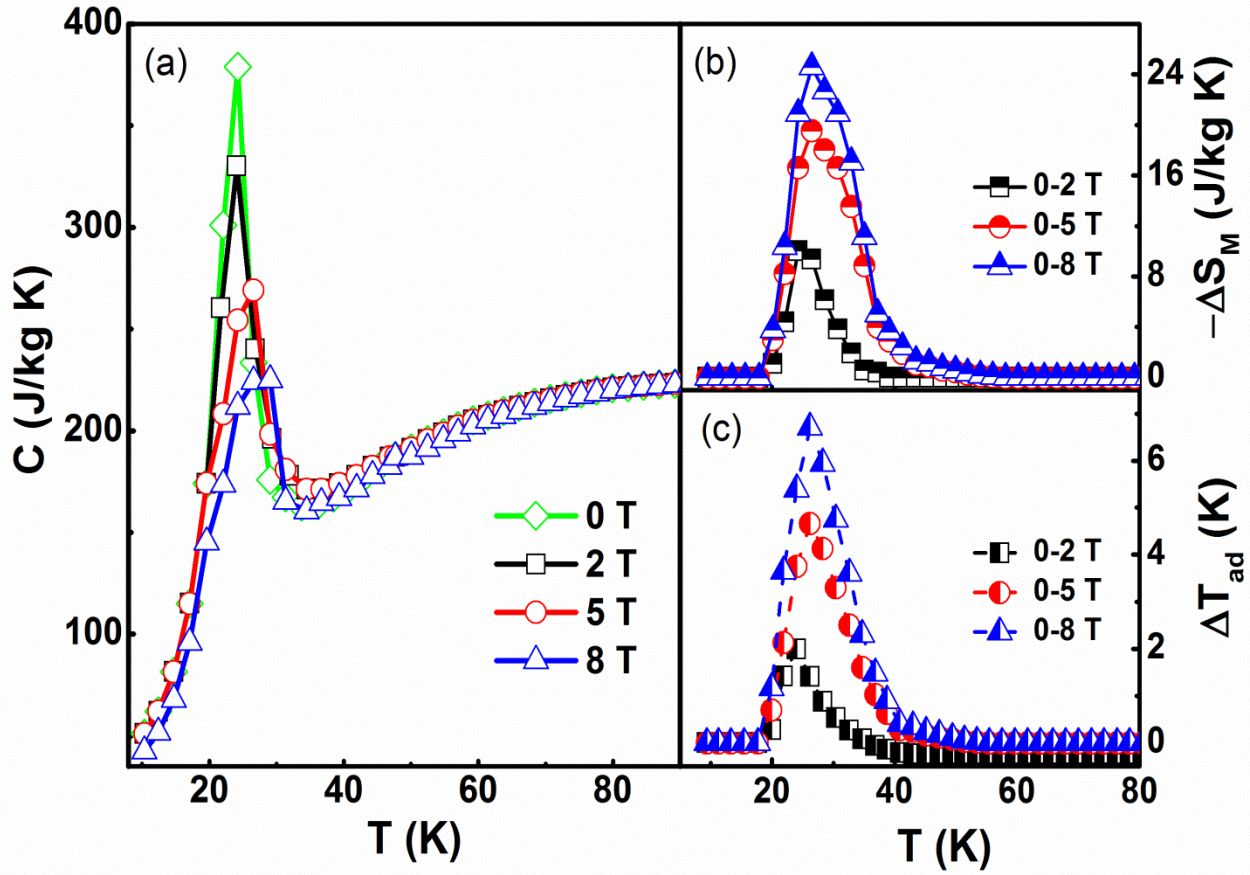

Figure 5.26 (a) The heat capacity of $NdMn_{1.9}V_{0.1}Si_2$ as measured over the temperature range 10-90 K in magnetic fields B = 0 T, 2 T, 5 T and 8 T .(b) The magnetic entropy change, $-\Delta S_M$, determined from the heat capacity measurements of Figure 5.26(a) for $NdMn_{1.9}V_{0.1}Si_2$ (ΔB = 0-2 T, 0-5 T and 0-8 T). (c) The adiabatic temperature change, ΔT_{ad}, for $NdMn_{1.9}V_{0.1}Si_2$ as determined from the heat capacity.

Similarly, the ΔT_{ad} values determined by combing the $-\Delta S_M$ (T, B) (derived from magnetic data) and specific heat results are also drawn in Figure 5.8(c) using closed symbols to make a comparison, which are found to be consistent with the values (open symbols) derived from the specific heat only. By comparison, Nikitin *et al* [47] reported that the value of ΔT_{ad}^{max} in $NdMn_2Si_2$ compound (around T_C ~ 32 K) can be up to 8.2 K with a field change of ΔB=0-6 T. The $NdMn_{1.9}V_{0.1}Si_2$ compound was selected for investigation by neutron diffraction measurements over the temperature range 3-450 K as representative of the magnetic behaviour of the $NdMn_{2-x}V_xSi_2$ samples (Figure 5.27). The aims were to determine the magnetic structures and to explore structural changes at the transition temperatures. It has

been confirmed that magnetic phase structure from PM to AF*il* following with F*mc*(Mn)+F(Nd) as shown in Figure 5.27 (b).

The diffraction patterns (λ = 2.4098 Å) and Rietveld refinements obtained for $NdMn_{1.9}V_{0.1}Si_2$ at 450 K, 100 K and 12 K are shown in Figures 5.28 (a), 5.28 (b) and 5.28 (c), respectively. The selected temperatures typify the behaviour of $NdMn_{1.9}V_{0.1}Si_2$ in the three magnetic regions (paramagnetic-antiferromagnetic-ferromagnetic) as indicated from the magnetisation and DSC measurements of Figure 5.21. Rietveld refinements of the neutron diffraction pattern at 450 K (Figure 5.28 (a)) confirm that $NdMn_{1.9}V_{0.1}Si_2$ has the $ThCr_2Si_2$ structure as expected. The absence of magnetic scattering above T_N ~ 375 K in reflections such as (101), (111) and (112) is consistent with a paramagnetic (PM) state. Below T_N ~ 375 K, $NdMn_{1.9}V_{0.1}Si_2$ is found to exhibit the antiferromagnetic interlayer coupling structure (AF*il*) down to T_C ~ 22 K (see e.g. the 100 K pattern of Figure 5.28 (b)) as indicated collinear antiferromagnetic structure between adjacent Mn planes in a + - + - sequence along the *c*-axis from the magnetic scattering observed at the (111), (113) and (201) reflections. In order to draw out the changes in magnetic structures with temperature, the temperature dependence of the peak intensity for selected magnetic peaks is shown in Figure 5.28 (d). Furthermore, the absence of magnetic scattering from the (111), (113) and (201) reflections at 12 K in Figure 5.28 (c), combined with the increase in intensity of the (112) and (101) peaks as in Figure 5.28 (d), indicate that the interlayer spin components of the Mn moments align parallel, thus leading to a canted ferromagnetic structure (F*mc*) for the Mn sublattice. The presence of the purely magnetic peak (001) below T_C indicates the existence of antiferromagnetic component of Mn moment in the ab-plane [22] as shown inset of Figure 5.28 (c) (pattern from echidna at 3 K with λ = 2.4395 Å) as limitation of wombat at small angle scattering. At lower temperature (e.g. 12 K; Figure 5.28 (d)), the increase in the intensities of the (112)

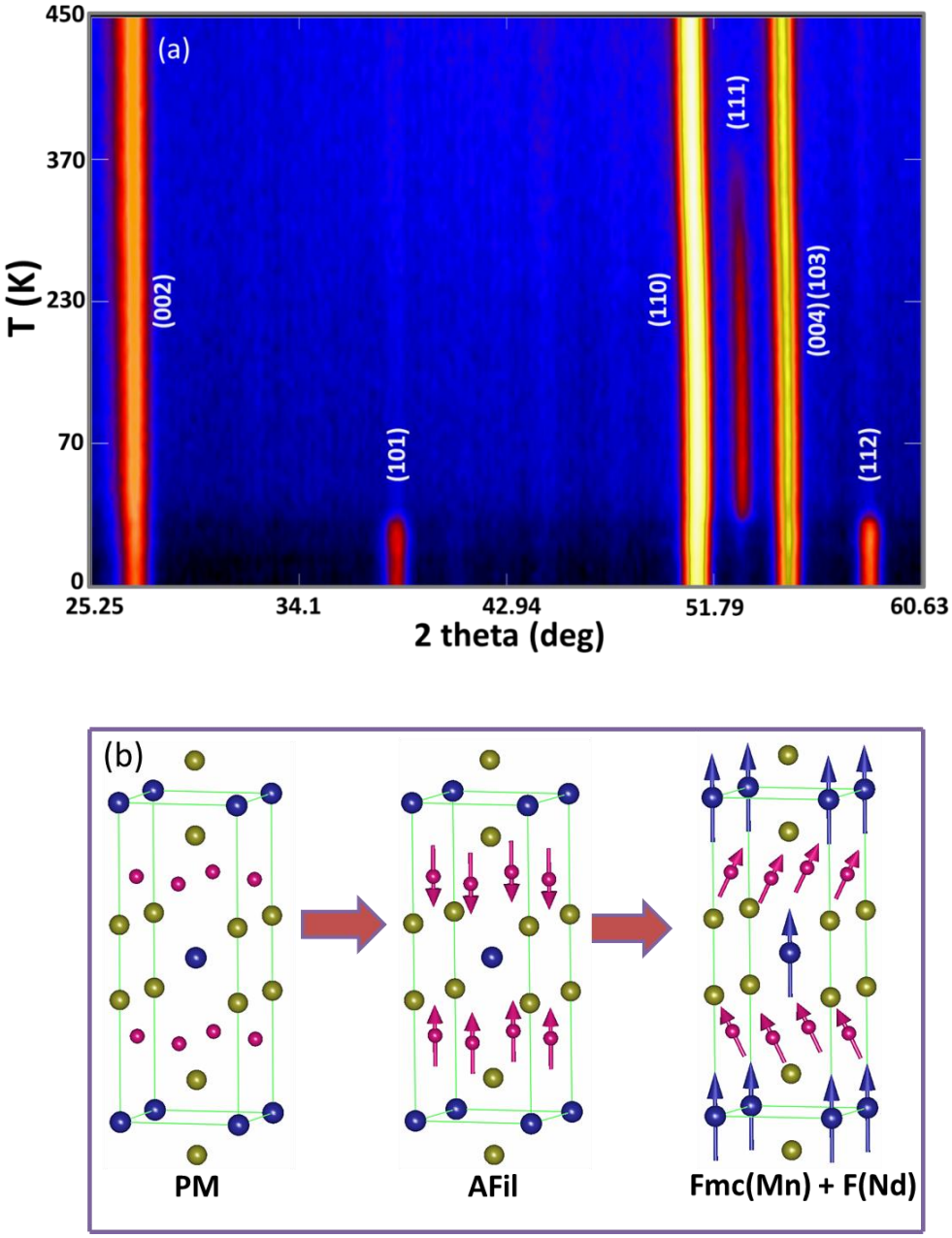

Figure 5.27 (a) Neutron diffraction patterns for $NdMn_{1.9}V_{0.1}Si_2$ over the temperature range 6-450 K (λ= 2.4098 Å). (b) The magnetic structures of $NdMn_{1.9}V_{0.1}Si_2$: paramagnetism for $T > T_N^{intra} \sim 375$ K; AF*il* ordering of the Mn sublattice for $T_N^{intra} > T > T_C \sim 24$ K and combined ferromagnetic state F*mc*(Mn)+F(Nd) for $T < T_C$.

(contributions from both Nd- and Mn-sublattices) and (101) (contribution only from Nd-sublattice [22]) reflections further indicates an additional contribution from Nd moments coupled parallel to the Mn moments along *c*-axis thereby leading to the formation of F*mc*+F(Nd) magnetic structure as depicted in Figures 5.27 (b). This behavior agrees well

with the results of Welter *et al* [51] who demonstrated that in the RMn_2Ge_2 compounds with R= Pr and Nd rare earth moments ferromagnetically coupled with the Mn sublattice at low temperatures. This behavior, also applicable to $NdMn_2Si_2$ [8] and $NdMn_2Si_{1.6}Ge_{0.4}$ [22] compounds, is due to the exchange interaction between the light rare earth elements and 3*d* transition metal as reported by references [52, 53]

Figure 5.28 (e) is a plot of the temperature dependence of the Mn magnetic moments as derived from the refinements. Within the AF*il* state region ($T_N \sim 375$ K > T > $T_C \sim 24$ K), the Mn moment increases to μ^{Mn} = 2.3 (1) μ_B at 100 K with both Nd and Mn ordering magnetically below $T_C \sim 24$ K. The magnetic moments for Mn and Nd have been derived to be μ_{total}^{Mn} = 1.86 μ_B (of basal plane and axial components μ_{ab}^{Mn} =0.86 μ_B and μ_c^{Mn} =1.64 μ_B respectively) and μ^{Nd} = 2.78 μ_B at 6 K. The Nd moment and the ferromagnetic component of the Mn moment along the *c*-axis for $NdMn_{1.9}V_{0.1}Si_2$ are found to be 2.78 μ_B and 1.64 μ_B respectively. The resultant total moment is 4.08 μ_B per formula unit at 6 K which is higher than that obtained from DC magnetization measurement at 10 K (3.8 μ_B per formula unit). This different value of magnetic moment is related to the non-saturation behavior shown by the magnetization curve from DC measurements at 10 K even for a field applied of 5 T.

The variation in the *a* and *c* lattice parameters with temperature are plotted in Figure 5.28 (f). Both the *a* and *c* values exhibit a monotonic decrease with temperature in the region of the antiferromagnetic transition between T_N = 375 K and T_C = 24 K, while below T_C = 24 K, the *a* lattice parameter expands slightly from 3.9967 Å at 30 K to 3.9988 Å at 6 K whereas the *c* lattice parameter decreases from 10.5385 Å at 30 K to 10.5280 Å at 6 K. The variation in lattice parameters *a* and *c* shown in Figure 5.28 (f) for the PM, AF*il*, and F*mc*+F(Nd) states is comparable with the behaviour in $NdMn_2Si_2$ [8]. The changes in lattice parameter at $T_C \sim 24$

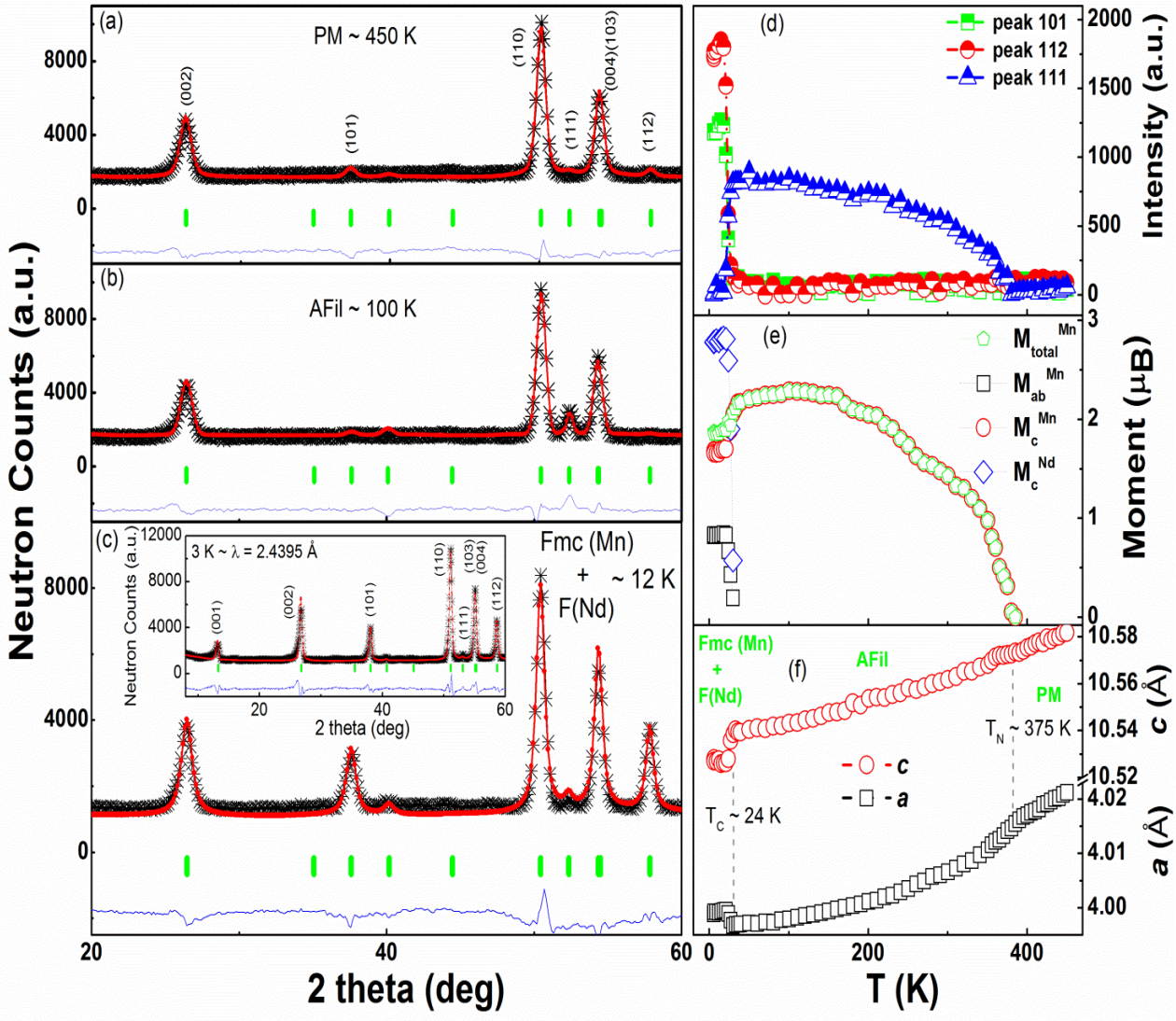

Figure 5.28 Neutron diffraction patterns (λ=2.4098 Å) for $NdMn_{1.9}V_{0.1}Si_2$ at: (a) 450 K; (b) 100 K; (c) 12 K (inset-3 K pattern at λ=2.4395 Å). (d) Temperature dependence of the integrated intensities of the (101), (111) and (112) reflections; (e) Temperature dependence of the Mn and Nd magnetic moments (6-450 K). (f) Lattice parameters as a function of temperature.

K when the magnetic state changes from AF*il* to F*mc*+F(Nd) structure, indicates the presence of strong magnetostructural coupling around T_C. As discussed recently [7, 54], the strong magnetostructural coupling leads to a large structural entropy change around the magnetic phase transition, thereby contributing to the total entropy change around T_C.

5.1.4 Conclusion

A systematic investigation of the structural and magnetic characteristics of $NdMn_{2-x}T_xSi_2$ (T = Ti, Cr, Cu and V) compounds has been carried out. Substitution of Ti for Mn leads to decreases in the Curie temperature and the Néel temperature from $T_C \sim 36$ K and $T_N \sim 380$ K at x=0 to $T_C \sim 14$ K and $T_N \sim 360$ K at x=0.3. The variation in the value of T_C with increasing Ti concentration can be understood in terms of changes in the Mn-Mn exchange interaction together with the effects of magnetic dilution and chemical pressure. A metamagnetic transition from the antiferromagnetic to the ferromagnetic state due to the application of magnetic field was observed above T_C for $NdMn_{1.9}Ti_{0.1}Si_2$. Substitution of Mn by Ti leads to a reduction of the magnetic entropy change from $-\Delta S_M \sim 27$ J kg^{-1} K^{-1} at x = 0; $-\Delta S_M \sim 15.3$ J kg^{-1} K^{-1} at x = 0.1; $-\Delta S_M \sim 13$ J kg^{-1} K^{-1} at x=0.2 and $-\Delta S_M \sim 10$ J kg^{-1} K^{-1} at x = 0.3 respectively. However, analysis of the magnetisation data demonstrates that the first order magnetic transition of $NdMn_2Si_2$ around T_C remains unchanged on replacement of Mn by Ti, and this substitution leads to significant reduction in magnetic hysteresis losses from 28.5 J kg^{-1} for $NdMn_2Si_2$ to 0.8 J kg^{-1} for $NdMn_{1.9}Ti_{0.1}Si_2$ with ΔB = 0-5 T and eliminates thermal hysteresis from $\Delta T = 0.3$ K at x = 0 to $\Delta T = 0$ K at x = 0.1. Neutron diffraction studies demonstrate that $NdMn_{1.9}Ti_{0.1}Si_2$ has the AF*il* antiferromagnetic structure in the temperature range $T_N \sim 374$ K > T > $T_C \sim 22$ K and the combined F*mc*+F(Nd) ferromagnetic state below $T_C \sim 22$ K.

The magnetic structures of $NdMn_{1.7}Cr_{0.3}Si_2$ determined from variable temperature neutron diffraction studies are: layered AF*il* antiferromagnetism for $T_N^{inter} \sim 320(3)$ K<T<$T_N^{intra} \sim 380(3)$ K; canted AF*mc* antiferromagnetism for $T_C \sim 42(2)$ K<T< $T_N^{inter} \sim 320(3)$ K with a combined F*mc*(Mn)+F(Nd) ferromagnetic structure for T<$T_C \sim 42(2)$ K. Values of the magnetic entropy,

magnetocaloric effect and adiabatic temperature change have been determined from magnetization and heat capacity measurements around the first order magnetic transition at T_C. The absence of thermal and magnetic hysteresis in $NdMn_{1.7}Cr_{0.3}Si_2$ at T_C combined with the magnetocaloric values: $-\Delta S_M^{max}$~15.3 J kg^{-1} K^{-1} and ΔT_{ad}^{max}~5 K under ΔB=0-5 T, indicate scope for $NdMn_{1.7}Cr_{0.3}Si_2$ as an active magnetic refrigerator, especially for the helium liquefaction environment.

Substitution of Cu for Mn leads to increase in the Curie temperature and decrease the Néel temperature from T_C ~ 36 K to 100 K and T_N ~ 380 K to 320 K at x=0 and x=1.0. The variation in the value of T_C with increasing Cu concentration can be understood in terms of changes in the Mn-Mn exchange interaction together with the effects of magnetic dilution. Analysis of the magnetisation data demonstrates that the order of magnetic phase transition around T_C changes from first order at x<0.6 to second order transition for x≥0.6 and leads to significant reduction in magnetic hysteresis losses. Substitution of Mn by Cu leads to a reduction of the magnetic entropy change from $-\Delta S_M$ ~ 27 J kg^{-1} K^{-1} at x=0 to ~ 0.5 J kg^{-1} K^{-1} at x=1.0 respectively. Neutron diffraction studies demonstrate that $NdMn_{1.8}Cu_{0.2}Si_2$ has the AF*il* antiferromagnetic structure in the temperature range T_N ~ 375 K > T > T_C ~ 44 K and the combined F*mc*+F(Nd) ferromagnetic state below T_C ~ 44 K.

The replacement Mn by V in $NdMn_{2-x}V_xSi_2$ (x = 0, 0.1, 0.2, 0.3, 0.4 and 0.5) leads to decrease in the Curie and Néel temperature from T_C ~ 36 K to 14 K and T_N ~ 380 K to 345 K at x=0 and x=0.5. Increment of V concentration leads to a reduction of the magnetic entropy change from $-\Delta S_M$ ~ 27 J kg^{-1} K^{-1} at T_C = 36 K for x=0 to $-\Delta S_M$ ~ 8 J kg^{-1} K^{-1} at T_C = 16 K for x=0.5 respectively as did not change the first order magnetic transition behaviour. The neutron diffraction study on $NdMn_{1.9}V_{0.1}Si_2$ compound indicated that magnetic structure

found from paramagnetic PM to the AF*il* antiferromagnetic structure in the temperature range $T_N \sim 375$ K > T > $T_C \sim 24$ K and the combined F*mc*+F(Nd) ferromagnetic state below $T_C \sim 24$ K.

References:

[1] K. A. Gschneidner, Jr., V. K. Pecharsky, E. BrÃ¼ck, H. G. M. Duijn, and E. M. Levin, Physical Review Letters 85 (2000) 4190.

[2] J L Wang, S J Campbell, A J Studer, M Avdeev, R Zeng, and S. X. Dou, Journal of Physics: Condensed Matter 21 (2009) 124217.

[3] T. Samanta, I. Das, and S. Banerjee, Applied Physics Letters 91 (2007) 152506.

[4] M. F. Md Din, J. L. Wang, R. Zeng, P. Shamba, J. C. Debnath, and S. X. Dou, Intermetallics 36 (2013) 1.

[5] G. Venturini, R. Welter, E. Ressouche, and B. Malaman, Journal of Alloys and Compounds 224 (1995) 262.

[6] J. L. Wang, S. J. Campbell, A. J. Studer, M. Avdeev, M. Hofmann, M. Hoelzel, and S. X. Dou, Journal of Applied Physics 104 (2008) 103911.

[7] J. L. Wang, L. Caron, S. J. Campbell, S. J. Kennedy, M. Hofmann, Z. X. Cheng, M. F. Md Din, A. J. Studer, E. Brück, and S. X. Dou, Physical Review Letters 110 (2013) 217211.

[8] R. Welter, G. Venturini, D. Fruchart, and B. Malaman, Journal of Alloys and Compounds 191 (1993) 263.

[9] J. Glanz, Science 279 (1998) 2045.

[10] K. A. Gschneidner Jr and V. K. Pecharsky, International Journal of Refrigeration 31 (2008) 945.

[11] A. Fujita and H. Yako, Scripta Materialia 67 (2012) 578.

[12] N. T. Trung, L. Zhang, L. Caron, K. H. J. Buschow, and E. Bruck, Applied Physics Letters 96 (2010) 172504.

[13] E. Liu, W. Wang, L. Feng, W. Zhu, G. Li, J. Chen, H. Zhang, G. Wu, C. Jiang, H. Xu, and F. de Boer, Nat Commun 3 (2012) 873.

[14] V. K. Pecharsky and J. K. A. Gschneidner, Physical Review Letters 78 (1997) 4494.

[15] A. Yan, K. H. Muller, L. Schultz, and O. Gutfleisch, Journal of Applied Physics 99 (2006) 08K903.

[16] H. Wada and Y. Tanabe, Applied Physics Letters 79 (2001) 3302.

[17] J. Shen, Y. X. Li, Q. Y. Dong, and J. R. Sun, Journal of Magnetism and Magnetic Materials 321 (2009) 2336.

[18] A. Szytuła and J. Leciejewicz, in Handbook on the Physics and Chemistry of Rare Earths, Vol. Volume 12 (Karl A. Gschneidner, Jr. and E. LeRoy, eds.), Elsevier, 1989, p. 133.

[19] B. Emre, S. Aksoy, O. Posth, M. Acet, E. Duman, J. Lindner, and Y. Elerman, Physical Review B 78 (2008) 144408.

[20] G. Venturini, R. Welter, E. Ressouche, and B. Malaman, Journal of Magnetism and Magnetic Materials 150 (1995) 197.

[21] P. Kumar, K. G. Suresh, A. K. Nigam, A. Magnus, A. A. Coelho, and S. Gama, Physical Review B 77 (2008) 224427.

[22] J. L. Wang, S. J. Campbell, J. M. Cadogan, A. J. Studer, R. Zeng, and S. X. Dou, Applied Physics Letters 98 (2011) 232509.

[23] J. L. Wang, S. J. Campbell, J. M. Cadogan, A. J. Studer, R. Zeng, and S. X. Dou, Journal of Physics: Conference Series 303 (2011) 012022.

[24] A. Szytuła and S. Siek, Journal of Magnetism and Magnetic Materials 27 (1982) 49.

[25] H. Fujii, T. Okamoto, T. Shigeoka, and N. Iwata, Solid State Communications 53 (1985) 715.

[26] H. Fujii, M. Isoda, T. Okamoto, T. Shigeoka, and N. Iwata, Journal of Magnetism and Magnetic Materials 54–57, Part 3 (1986) 1345.

[27] Y.G. Wang, F. Yang, C. Chen, N. Tang, and Q. Wang, Journal of Alloys and Compounds 257 (1997) 19.

[28] N. P. Kolmakova, A. A. Sidorenko, and R. Z. Levitin, Low Temperature Physics 28 (2002) 653.

[29] S. M. Yusuf, M. Halder, A. K. Rajarajan, A. K. Nigam, and S. Banerjee, Journal of Applied Physics 111 (2012) 093914.
[30] L. B. McCusker, R. B. Von Dreele, D. E. Cox, D. Louër, and P. Scardi, Journal of Applied Crystallography 32 (1999) 36.
[31] S. Siek, A. Szytuła, and J. Leciejewicz, Solid State Communications 39 (1981) 863.
[32] L. Gelato, J. Appl. Crystallogr. 14 (1981) 151.
[33] T. Fukuhara, K. Maezawa, H. Ohkuni, T. Kagayama, and G. Oomi, Physica B: Condensed Matter 230–232 (1997) 198.
[34] S. Di Napoli, A. M. Llois, G. Bihlmayer, and S. Blügel, Physical Review B 75 (2007) 104406.
[35] T. Kawashima, T. Kanomata, H. Yoshida, and T. Kaneko, Journal of Magnetism and Magnetic Materials 90–91 (1990) 721.
[36] R. Obermyer, S. G. Sankar, and V. U. S. Rao, Journal of Applied Physics 50 (1979) 2312.
[37] Y.-Q. Chen, J. Luo, J.-K. Liang, J.-B. Li, and G.-H. Rao, Chinese Physics B 18 (2009) 4944.
[38] P. Shamba, J. C. Debnath, R. Zeng, J. L. Wang, S. J. Campbell, S. J. Kennedy, and S. X. Dou, Journal of Applied Physics 109 (2011) 07A940.
[39] R. Zeng, J. L. Wang, L. Lu, W. X. Li, S. J. Campbell, and S. X. Dou, Journal of Alloys and Compounds 505 (2010) L38.
[40] H. Feng Xia, S. Bao Gen, S. Ji Rong, C. Zhao Hua, and Z. Xi Xiang, Journal of Physics: Condensed Matter 12 (2000) L691.
[41] L. Caron, Z. Q. Ou, T. T. Nguyen, D. T. Cam Thanh, O. Tegus, and E. Brück, Journal of Magnetism and Magnetic Materials 321 (2009) 3559.
[42] B. Li, W. J. Hu, X. G. Liu, F. Yang, W. J. Ren, X. G. Zhao, and Z. D. Zhang, Applied Physics Letters 92 (2008) 242508.
[43] X. X. Zhang, F. W. Wang, and G. H. Wen, Journal of Physics: Condensed Matter 13 (2001) L747.
[44] V. K. Pecharsky and J. K. A. Gschneidner, Journal of Applied Physics 86 (1999) 565.
[45] B. Ekkes, Journal of Physics D: Applied Physics 38 (2005) R381.
[46] K. A. GschneidnerJr, V. K. Pecharsky, and A. O. Tsokol, Reports on Progress in Physics 68 (2005) 1479.
[47] S. A. Nikitin, Y. F. Popov, R. S. Torchinova, A. M. Tishin, and I. A. Arkharov, Fizika Tverdogo Tela 29 (1987) 572.
[48] M. Balli, M. Rosca, D. Fruchart, and D. Gignoux, Journal of Magnetism and Magnetic Materials 321 (2009) 123.
[49] M. Hofmann, S. J. Campbell, and A. V. J. Edge, Physical Review B 69 (2004) 174432.
[50] I. Dincer, Y. Elerman, A. Elmali, H. Ehrenberg, and G. André, Journal of Magnetism and Magnetic Materials 313 (2007) 342.
[51] R. Welter, G. Venturini, E. Ressouche, and B. Malaman, Journal of Alloys and Compounds 218 (1995) 204.
[52] J. M. D. Coey, Solid State Sciences 7 (2005) 660.
[53] T. Chatterji, J. Combet, B. Frick, and A. Szyula, Journal of Magnetism and Magnetic Materials 324 (2012) 1030.
[54] K. A. Gschneidner Jr, Y. Mudryk, and V. K. Pecharsky, Scripta Materialia 67 (2012) 572.
[55] M. F. M. Din, J. L. Wang, S. J. Campbell, R. Zeng, W. D. Hutchison, M. Avdeev, S. J. Kennedy, and S. X. Dou, Journal of Physics D: Applied Physics 46 (2013) 445002.
[56] I. Dincer, A. Elmali, Y. Elerman, H. Ehrenberg, H. Fuess, and O. Isnard, Journal of Physics: Condensed Matter 16 (2004) 2081.
[57] U. Plaznik, J. Tušek, A. Kitanovski, and A. Poredoš, Applied Thermal Engineering 59 (2013) 52.
[58] M. F. Md Din, J. L. Wang, S. J. Campbell, A. J. Studer, M. Avdeev, S. J. Kennedy, Q. F. Gu, R. Zeng, and S. X. Dou, Applied Physics Letters 104 (2014) 042401.
[59] C. M. Bonilla, J. Herrero-Albillos, F. Bartolomé, L. M. García, M. Parra-Borderías, and V. Franco, Physical Review B 81 (2010) 224424.

5.2 Substitution of Pr with Y in $PrMn_2Ge_2$ Compound

5.2.1 Introduction

The rapid change in magnetisation associated with first order magnetic transitions together with simultaneous field-induced magnetic and structural transformations lead to enhanced entropy values [1]. For example, materials based on the NiMnGa and MnCoGe systems show pronounced entropy behaviour at magnetostructural transitions around room temperature [e.g. 2, 3, and 4]. Layered rare earth compounds in the RMn_2X_2 series (R=rare-earth; X=Ge, Si) are also of interest as they enable the structural and magnetic behaviour to be controlled via substitution of R, Mn, X atoms on the 2a, 4d and 4e sites respectively [5-10]. The overall magnetic behaviour of RMn_2Ge_2 compounds is strongly influenced by two critical intralayer Mn–Mn distances d^a_{Mn-Mn}: d_{crit1} = 2.87 Å (related acrit1=4.06 Å) and d_{crit2} = 2.84 Å (related acrit2=4.02 Å) [5, 8-9]. For compounds with $d^a_{Mn-Mn} > d_{crit1}$, the intralayer in-plane coupling is antiferromagnetic and the interlayer coupling is ferromagnetic [5, 8-9] leading to the F*mc*-type magnetic configuration.

In the case of the $Pr_{1-x}Y_xMn_2Ge_2$ system, given that $PrMn_2Ge_2$ is ferromagnetic and YMn_2Ge_2 antiferromagnetic at room temperature, the $Pr_{1-x}Y_xMn_2Ge_2$ system leads to an extended region of re-entrant ferromagnetism around x~0.5 [8]. The combination of ferromagnetic ordering of the Pr-sublattice and ferromagnetic ordering of the Mn-sublattice in turn leads to enhanced magnetocaloric behaviour. Here, report extension of our studies of the structural and magnetic properties of $Pr_{1-x}Y_xMn_2Ge_2$ using x-ray and neutron diffraction together with magnetic measurements [8-10]. Our investigations have led to construction of the magnetic phase diagram for $Pr_{1-x}Y_xMn_2Ge_2$ as functions of both composition and the Mn–

Mn spacing and exploration of the nature of the magnetic transitions end entropy changes observed at the ferromagnetic. The changes in magnetic states due to Y substitution for Pr are discussed in terms of chemical pressure, external pressure and electronic effects.

5.2.2 Experimental and Procedures

The set of $Pr_{1-x}Y_xMn_2Ge_2$ compounds (with x=0.0 - 1.0) were prepared using conventional argon arc melting. The starting materials contained ~3% excess Mn to compensate for the Mn loss due to evaporation during melting. The ingots were melted five times for improved homogeneity and then annealed at 900°C for one week in an evacuated quartz tube. The samples were characterized at room temperature by x-ray diffraction (CuK_α radiation, λ = 1.5418 Å). The temperature dependences of the DC magnetisation and the AC magnetic susceptibility were measured using a superconducting quantum interference device (SQUID) and a Quantum Design Physical Properties Measurement System (PPMS) Magnetometer from 5 K to 340 K. A search for higher temperature phase transitions in the range 300 K to 570 K was carried out using differential scanning calorimetry (DSC) at a heating rate of 10 K/min. Neutron diffraction experiments were carried out on the GEM time-of-flight diffractometer at ISIS (STFC, UK) from 30-360 K [e.g. 10] and the Echidna and Wombat diffractometers at OPAL (Australia). Rietveld refinements have been carried out using the FULLPROF program package [11] which allows simultaneous refinement of the structural and magnetic parameters.

5.2.3 Result and Discussion

Analysis of the room temperature x-ray diffraction (XRD) patterns of $Pr_{1-x}Y_xMn_2Ge_2$ (Figure 5.29 (a)) indicates that all of the samples are single phase with the expected body-centred tetragonal $ThCr_2Si_2$-type structure (space group I4/mmm). The lattice parameters derived from refinement of the room temperature patterns are presented in Figure 5.29 (b) as a function of composition. The present set of lattice parameters are similar to those reported in reference [12] which are also shown in Figure 5.29 (b). Both the *a* and *c* lattice parameters decrease linearly with increasing Y content with rates of change: d*a*/dx = -0.133 Å and d*c*/dx = -0.053 Å respectively in accord with Vegard's Law.

With respect to $PrMn_2Ge_2$ as the reference, consider the influence of the reduction in unit cell volume due to Y substitution to be analogous to the effects of "chemical pressure". The Murnaghan equation of state and the experimental unit cell volumes of $Pr_{1-x}Y_xMn_2Ge_2$ can be used to derive the related "chemical pressure". It is accepted that Murnaghan equation can be described [13] as:

$$P(V) = \frac{B_o}{B_o'}\left(\left(\frac{V_o}{V}\right)^{B_o'} - 1\right) \qquad (1)$$

where B_0 is the isothermal bulk modulus, B_0' is its pressure derivative, and V_0 and V are the volumes at ambient pressure and pressure p, respectively. Using the values of B_o = 73.5 GPa and B_o' = 11.4 from the closely related compound UGe_2Mn_2 [13], the equivalent "chemical pressure" from $Pr_{1-x}Y_xMn_2Ge_2$ compounds can be derived as shown in Figure 5.29 (c). The distinct change in slope which occurs in the calculated chemical pressure around x=0.5-0.6 at room temperature (Figure 5.29 (c)), may be related to the change in magnetic state from canted ferromagnetism for x <~ 0.6 to canted antiferromagnetism for x >~ 0.6 as discussed

below (see Figure 5.33). This change in slope is drawn out more clearly in the insert to Figure 5.29 (c) which shows the reduced unit cell volume V/V_0 versus Y concentration for $Pr_{1-x}Y_xMn_2Ge_2$ compounds at room temperature (V_0 is the volume of the $PrMn_2Ge_2$ unit cell while V is the volume).

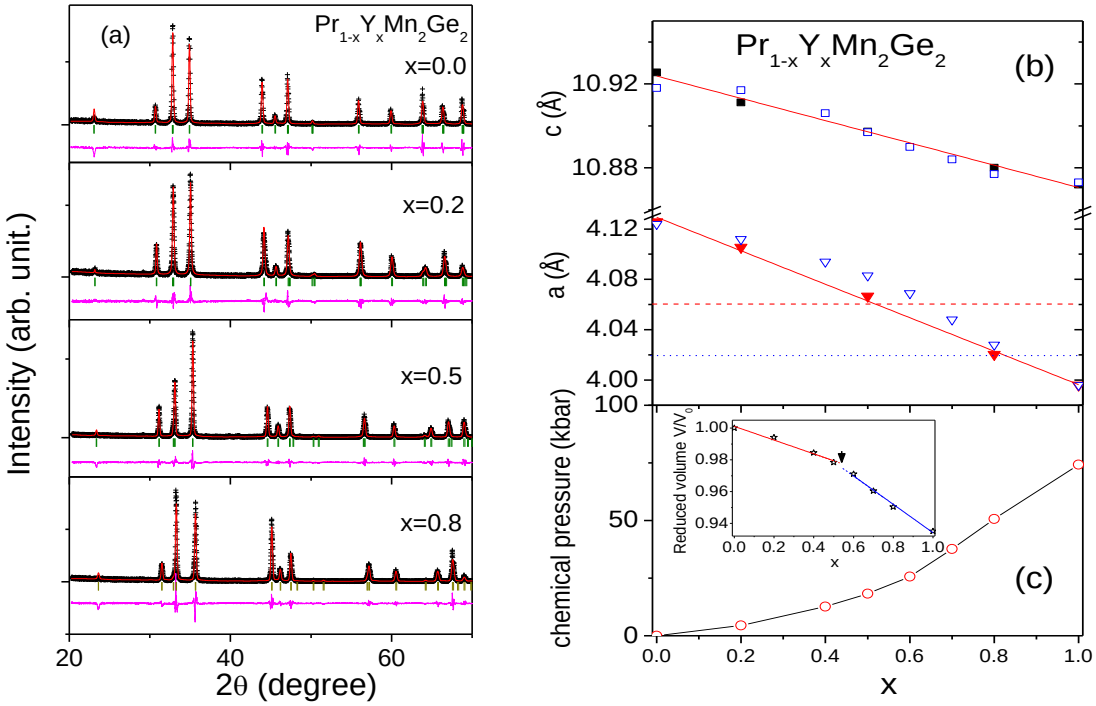

Figure 5.29 (a) Room temperature x-ray diffraction patterns and Rietveld refinements of the $Pr_{1-x}Y_xMn_2Ge_2$ compounds (CuK_α radiation); (b) composition dependence of lattice parameters (open symbols taken from reference [12]). (c) The calculated chemical pressure based on the values of B_0=73.5 GPa and B_0'=11:4 for UMn_2Ge_2 [13] as a function of Y content. The insert shows the composition dependence of the changes in reduced unit cell volume V/V_0 versus Y concentration (V_0 is the volume of the $PrMn_2Ge_2$ unit cell while V is the volume for $Pr_{1-x}Y_xMn_2Ge_2$ compounds at room temperature). The arrow indicates the region where a change in slope is obtained between two linear regions above and below x ~ 0.6.

In considering the magnetic regions for the $Pr_{1-x}Y_xMn_2Ge_2$ samples (x=0.0 – 1.0), the transition temperatures are first identified with their predominant physical influence. In particular with decreasing temperature from the paramagnetic (PM) region: T_N^{intra} defines the magnetic transition from paramagnetism to intralayer antiferromagnetic ordering within the

(001) Mn layers (AF*il*); T_C^{inter} defines the transition from AF*il* to a canted spin structure (F*mc*); $T_{c/c}$ defines the transformation temperature of the magnetic structure from F*mc* to a conical configuration F*mi* type, T_N^{inter} denotes the change from F*mc* to the antiferromagnetic canted structure AF*mc* and T_C^{Pr} defines the transition temperature for onset of the ordering of the Pr sublattice [8, 9]. The magnetization and DSC curves for $Pr_{1-x}Y_xMn_2Ge_2$ compounds were used to determine the possible magnetic phase transitions. As examples, Figure 5.30 (a) shows the composite magnetization and DSC data over the temperature range ~5-500 K for $PrMn_2Ge_2$ with Figure 5.30 (b) showing the DSC data for $Pr_{0.8}Y_{0.2}Mn_2Ge_2$. In the case of the $PrMn_2Ge_2$ compound, four magnetic phase transitions have been observed in the range 5 K to 500 K. The transitions, as marked by arrows in Figure 5.30 (a), are indicated as T_C^{Pr}, $T_{c/c}$, T_C^{inter} and T_N^{intra} with increasing temperature. By comparison, only two transitions are detected in the $Pr_{0.2}Y_{0.8}Mn_2Ge_2$ compound with no transitions occurring below 300 K.

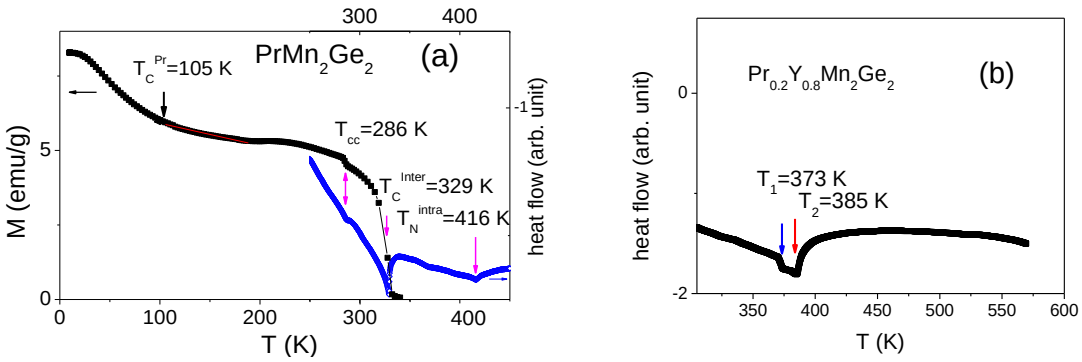

Figure 5.30 (a) Composite figure showing the temperature dependent magnetization obtained on cooling $PrMn_2Ge_2$ in a field of *B*=0.01 T (5-350 K; left part) and the results of DSC measurements (300-500 K; right part). The transition temperatures are indicated by arrows. (b) The DSC results for the $Pr_{0.8}Y_{0.2}Mn_2Ge_2$ compound.

A set of neutron powder diffraction patterns have been obtained for selected $Pr_{1-x}Y_xMn_2Ge_2$ compounds over the temperature range 5-450 K (Figures 5.31 (a) and 5.31 (c)). As noted above, Rietveld refinements were carried out on all patterns using the FULLPROF program package which allows us to derive the structural and magnetic parameters. As explained fully in related articles [5, 8-9], the specific location of Mn atoms on the 4d site in the $ThCr_2Si_2$

structure (space group *I4/mmm*) allows ready identification of various magnetic structures from key indicators in the neutron diffraction patterns as follows.

(1) Ferromagnetic ordering of the Mn atoms – hkl reflections with h + k = 2n and l = 2n; (e.g. (112) reflections);

(2) Antiferromagnetic ordering of the Mn atoms within the (001) planes - reflections with h +k = 2n +1; (e.g. (101), (103) reflections);

(3) Collinear antiferromagnetic structure between adjacent Mn planes - reflections with h + k + l = 2n + 1; (e.g. (111), (113) reflections;

Ferromagnetic mixed incommensurate structure (F*mi*) of wave vector (0, 0, q_z) - satellite reflections with h + k = 2n + 1; (e.g. (101), (103)).

The refinement results for each of the four magnetic states of the $PrMn_2Ge_2$ compound at selected temperatures (*cf.* transition temperatures in Figure 5.30 (a)) are shown as typical examples in Figure 5.31 (a). It is clear that the neutron diffraction pattern characteristic of each magnetic state, matches well with the intensities expected from magnetic contributions to the neutron scattering as outlined above. The refinement results for $PrMn_2Ge_2$ at these selected temperatures are listed in Table 5.5. Figure 5.31 (c) shows the intensities of the (101), (112) and (200) magnetic peaks as a function of temperature with the transitions from the different magnetic phases identified readily from changes in the magnetic scattering. The invariant behaviour of the purely nuclear (002) peak is shown in Figure 5.31 (c) for comparison.

For $Pr_{0.2}Y_{0.8}Mn_2Ge_2$, the lattice parameter *a* at room temperature is derived to be *a* = 4.020(1) Å with $d_{Mn\text{-}Mn}$=2.843 Å (this $d_{Mn\text{-}Mn}$ spacing is very close to the second critical value, $d^{crit2}_{Mn\text{-}}$

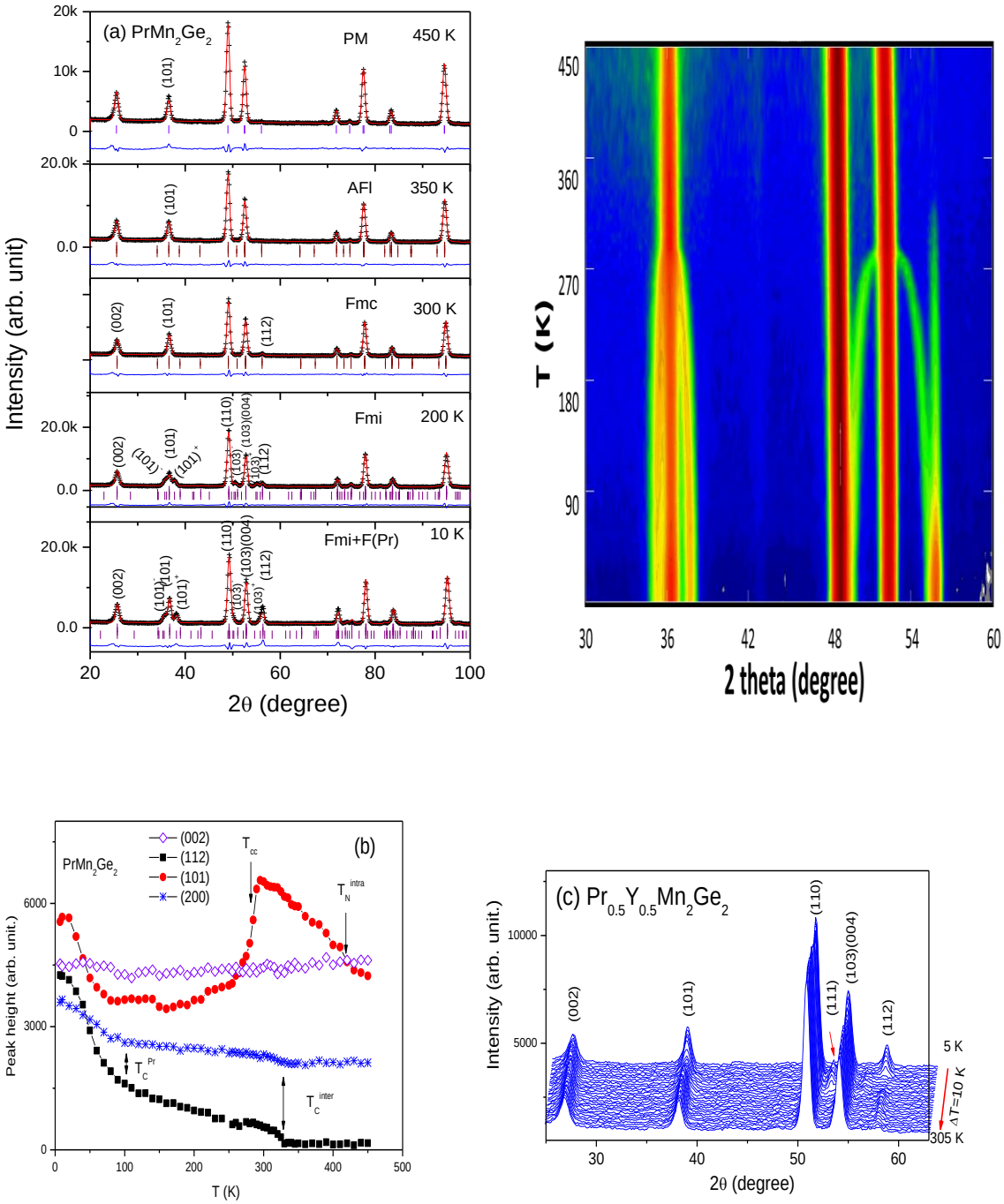

Figure 5.31 (a) Neutron diffraction patterns and Rietveld refinements for $PrMn_2Ge_2$ at 450 K, 350 K, 300 K, 200 K and 10 K (λ=2.4205 Å). These temperatures were selected as characteristic of the neutron diffraction pattern for each magnetic state. (b) Representative diffraction patterns for $Pr_{0.5}Y_{0.5}Mn_2Ge_2$ over the temperature range 5-305 K at 10 K intervals (λ=2.4072 Å). (c) The intensities of the (101), (112) and (200) magnetic peaks as a function of temperature. The temperature variation of the purely nuclear (002) peak is shown for comparison.

$_{Mn}$=2.84 Å, for occurrence of the AF*il* structure as mentioned above). Wang *et al.* [12] reported a value of a=3.996 Å (smaller than a_{crit2}=4.02 Å) for the lattice parameter of YMn_2Ge_2, Szytula and Szott [20] having earlier shown that YMn_2Ge_2 has the AF*il* structure. Given the proximity of the a lattice parameter of $Pr_{0.2}Y_{0.8}Mn_2Ge_2$ to the critical value a_{crit2}, considered two possible magnetic structural models (Figures 5.32 (b) and 5.32 (c)), for refinement of the 300 K neutron diffraction pattern of $Pr_{0.2}Y_{0.8}Mn_2Ge_2$.

The first model is the AF*il* structure which features a collinear antiferromagnetic structure along the *c*-axis. The second model is the AF*mc* structure in which the antiferromagnetic mixed commensurate structure is characterized by antiferromagnetic interplanar coupling of the in-plane ferromagnetic components and by the commensurate ordering of the antiferromagnetic in-plane components. Comparison of the refinements in Figures 5.32 (b) and 5.32 (c) (see inserts for details of the (101) reflection), indicates that at 300 K the AF*mc* structure provides a significantly improved description of the diffraction data compared with the AF*il* structure. This description of the AF*mc* structure for $Pr_{0.2}Y_{0.8}Mn_2Ge_2$ in the temperature region below T_1 (Figure 5.30 (b)) indicates that T_1 can be defined as T_N^{inter} where the AF*il* layered antiferromagnetic structure transforms to the canted AF*mc* structure. Correspondingly T_2 can be assigned as T_N^{intra} where the magnetic state changes from paramagnetism (PM) to the AF*il* antiferromagnetism with decreasing temperature. The refinement for the entire room temperature diffraction pattern of $Pr_{0.2}Y_{0.8}Mn_2Ge_2$ to the AF*mc* structure is shown in Figure 5.32 (a) with the resultant structural and magnetic parameters shown in Figure 5.32 (d).

Combining the present findings with the published results [12, 14-16] has enabled us to construct magnetic phase diagrams for the $Pr_{1-x}Y_xMn_2Ge_2$ system as a function of Y content

as in Figure 5.33 (the phase diagram versus *a* lattice parameter and intralayer distance d^{a}_{Mn-Mn} between Mn-Mn within the ab-plane can be seen in reference [17]). Figure 5.33 demonstrates that, as expected, the magnetic states at room temperature have been modified by Y substitution due to the contraction of the unit cell. Samples with x> ~0.7

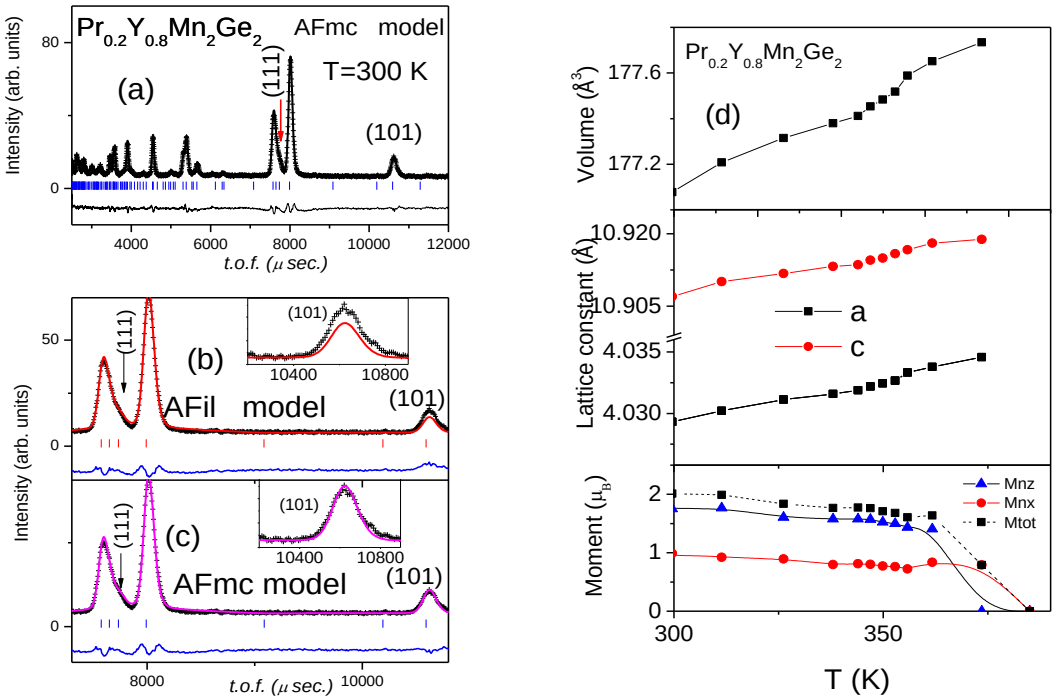

Figure 5.32 (a) Neutron diffraction pattern of $Pr_{0.2}Y_{0.8}Mn_2Ge_2$ at 300 K and Rietveld refinement to the AF*mc* structure; (b) refinement for the AF*il* model shown over an expanded 2θ range and (c) refinement for the AF*mc* model over an expanded 2θ range; (d) temperature dependence of lattice parameters and magnetic moment values of $Pr_{0.2}Y_{0.8}Mn_2Ge_2$ as determined from refinements to the AF*mc* strucutre.

where the lattice constant *a* is below a_{crit1} = 4.06 Å (Figure 5.29 (b)) are antiferromagnetic at room temperature with no ferromagnetic order evident over the entire temperature range, whereas samples of Y content x < ~0.7 are ferromagnetic at room temperature. In RMn_2X_2 compounds there are three magnetic interactions (R-R, R-Mn and Mn-Mn) below T_C^R, the temperature at which the rare earth sublattice orders. In $Pr_{1-x}Y_xMn_2Ge_2$ compounds, the R-R and R-Mn magnetic interactions become weaker with increasing Y content due to the dilution effect caused by introduction of the non-magnetic Y atoms. This behaviour is evident, for

example, in the decrease of T_C^{Pr} with increasing Y concentration from T_C^{Pr} ~ 100 K for $PrMn_2Ge_2$ to T_C^{Pr} ~ 0 K for Y concentration around x ~ 0.7 (Figure 5). As is clear from the phase diagram in Figure 5.33, $Pr_{1-x}Y_xMn_2Ge_2$ compounds with Y content x > 0.7 show a relatively simple magnetic behaviour, transforming from paramagnetism at high temperature to AF*il* followed by AF*mc* with decreasing temperature with no evidence of ordering of the Pr-sublattice. As noted above, YMn_2Ge_2 exhibits the layered AF*il* structure although the boundary between the AF*mc* and AF*il* magnetic structures at high Y contents has yet to be

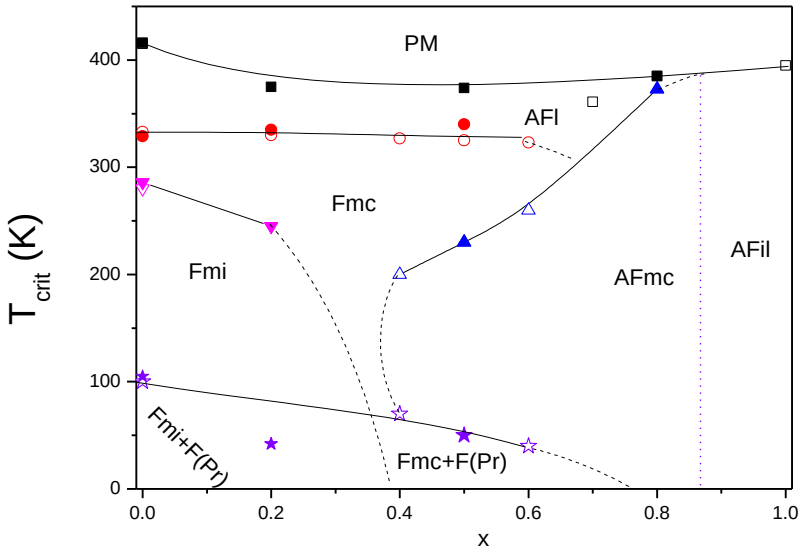

Figure 5.33 Magnetic phase diagram of $Pr_{1-x}Y_xMn_2Ge_2$ as a function of the Y content (closed symbols - present results; open symbols - data from [12, 14-16]). As discussed in the text, T_N^{intra} (squares) defines the transition from paramagnetism to intralayer antiferromagnetic ordering within the (001) Mn layers (AF*il*); T_C^{inter} (circles) defines the transition from AF*il* to a canted spin structure (F*mc*); $T_{c/c}$ (inverted triangle) defines the transformation temperature of the magnetic structure from F*mc* to a conical configuration F*mi* type, T_N^{inter} (triangle) denotes the transition to the antiferromagnetic canted structure AF*mc* and T_C^{Pr} (stars) defines the transition temperature for onset of the ordering of the Pr sublattice. The dashed lines indicate trends in the data. As discussed in the text, the vertical dashed line located around Y concentration of x ~ 0.86 is used as a tentative guide to the boundary between the AF*mc* and AF*il* regions.

delineated. It is assumed that the boundary between the AF*mc* and AF*il* regions originates around the paramagnetic transition for these phases at Y concentration x = ~0.86. By comparison, Pr-rich samples (x<~0.4) successively exhibit four magnetic states – AF*il*, F*mc*, F*mi*, F*mi*+F(Pr) – on cooling from the high temperature paramagnetic phase, while re-entrantferromagnetism has been observed for compounds with Y contents in the range x ~ 0.4-0.6. Figure 5.33 also indicates that the F*mi* structure only occurs for Y content x <~ 0.4. This is reflected by the decrease in wave vector with Y content from q_c = 0.272 for $PrMn_2Ge_2$ at 10 K to q_c = 0.237 for $Pr_{0.8}Y_{0.2}Mn_2Ge_2$ at 10 K. Similar behaviour has been detected in the $PrMn_{2-x}Fe_xGe_2$ [5] and $Pr_{1-y}Lu_yMn_2Ge_2$ [18] systems where the absence of the F*mi* structure is noted for x < 0.38 and y < 0.4, respectively.

Given that the magnetic structure in RMn_2Ge_2 and related systems depends sensitively on the intraplanar Mn-Mn spacing and that both external pressure and the substitution of Y for Pr in $Pr_{1-x}Y_xMn_2Ge_2$ can reduce the Mn-Mn distance, it is interesting to compare the relative impact of chemical pressure and applied pressure on the magnetic order. Here consider the variation of T_N^{inter} with Y content (considered here as equivalent to effects of chemical pressure) and external pressure as detected in $Pr_{0.5}Y_{0.5}Mn_2Ge_2$ [9], where made such a comparasion for T_C^{Pr}. As is evident from Figure 5.33, these two transitions were chosen because of their higher sensitivity to the composition change (and Mn-Mn distance [17]). With increase in Y content, T_N^{inter}, the transition from the canted F*mc* magnetic structure to the canted AF*mc* magnetic structure, increases from ~200 K for x=0.4 to ~373 K for x=0.8 (Figure 5.33). The corresponding chemical pressure changes from ~12.6 kbar for x=0.4 to ~50.7 kbar for x=0.8, leading to a rate of change dT_N^{inter}/dp = 4.5 K/kbar compared with the rate of change in transition temperature with external pressure of dT_N^{inter}/dp = 22.2 K/kbar in $Pr_{0.5}Y_{0.5}Mn_2Ge_2$ [9]. Estimation of the value of chemical pressure due to Y substitution for Pr

using the isothermal bulk modulus B_0 and its pressure derivative $B_0'$of UMn_2Ge_2 [13] is expected to include additional uncertainty because the magnetic states change with pressure from F*mc* to AF*mc* (see [17]) and different magnetic states are expected to have different B_0 and B_0'. Given this additional uncertainty, think the comparison for dT_N^{inter}/dp is consistent with change in T_C^{Pr}, as discussed in [9] where noted the rate of change with mechanical pressure exceeds the change with chemical pressure by a factor of ~2. Comparison of the effects of chemical pressure and applied pressure demonstrates that while the Y substitution for Pr produces changes consistent with the effect of pressure, additional effects occur. These effects are associated with the differences in the electron configurations of Pr^{3+} ($4f^2$) and Y^{3+} ($4d^0$) ions with electronic effects likely to explain the different rates of change for both dT_C^{Pr}/dp and dT_N^{inter}/dp for chemical pressure and external pressure.

Table 5.5 Rietveld refinement results for $PrMn_2Ge_2$ at 10 K, 200 K, 300 K, 350 K and 450 K. These temperatures were selected as characteristic of the neutron diffraction pattern of each magnetic state (*cf.* Figure 5.31(a)). The standard errors derived from the refinements are also listed.

T (K)	10 K	200 K	300 K	350 K	450 K
Magnetic state	*Fmi+F(Pr)*	*Fmi*	F*mc*	AF*il*	PM
a (Å)	4.107(1)	4.114(1)	4.119(1)	4.121(1)	4.126(1)
c (Å)	10.881(1)	10.891(1)	10.905(2)	10.919(2)	10.951(2)
z_{Ge}	0.3820(2)	0.3827(2)	0.3825(2)	0.3826(2)	0.3826(2)
$\mu_{ab}(\mu_B)$	2.51(4)	2.33(4)	2.08(3)	1.86(3)	-
μ_c (μ_B)	2.03(5)	1.95(5)	1.28(6)	-	-
canting angle (°)	51.0(9)	53.6(8)	58.4(6)	90	-
$\mu_{tot}(\mu_B)$	3.23(7)	2.90(4)	2.44(5	1.86(3)	--
q_c	0.272(2)	0.214(1)	-	-	-
$\mu_{Pr}(\mu_B)$	1.53(3)	-			

The magnetocaloric effect around T_C^{inter} have calculated for the set of samples from magnetization data using the standard Maxwell thermodynamic relation [e.g. 19]. The magnetization results for $PrMn_2Ge_2$ in the region of T_C^{inter} ~ 334 K are shown as an example in Figure 5.34 (a) with the corresponding Arrott plots of M^2 versus B/M presented in Figure

5.34 (b). The positive intercepts of the linear extrapolation of the magnetisation data with the M^2 axis below T_C^{inter} (determined from the temperature of zero intercept in Figure 5.34 (b)), demonstrates the ferromagnetic nature of the magnetic phase below T_C^{inter}. The positive slopes of the Arrott plots around T_C^{inter} indicate that the magnetic transition at T_C^{inter} for $PrMn_2Ge_2$ is second order. Similarly, analyses of the Arrott-plots for $Pr_{0.8}Y_{0.2}Mn_2Ge_2$ and $Pr_{0.5}Y_{0.5}Mn_2Ge_2$ demonstrate that the ferromagnetic transitions at T_C^{inter} for these compounds are also second order.

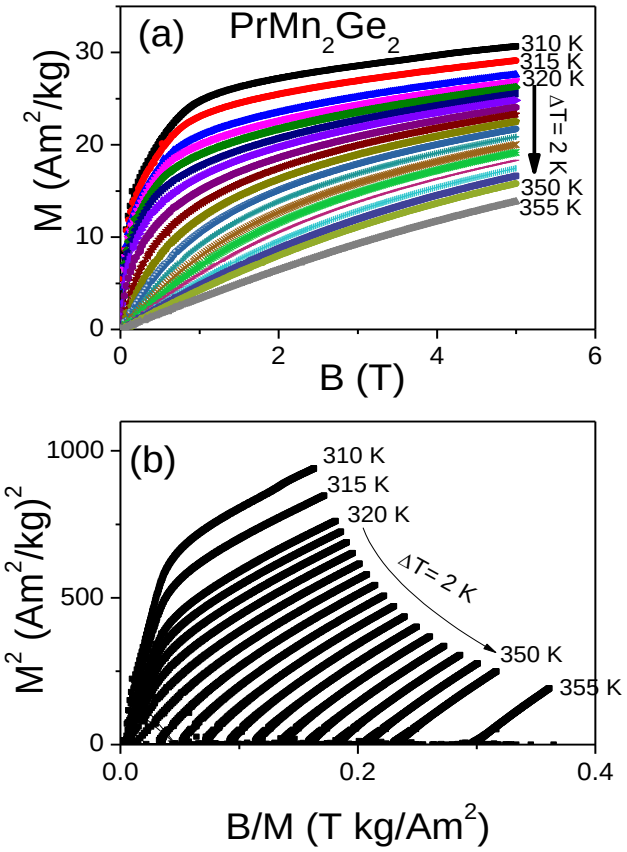

Figure 5.34 (a) Magnetisation versus field curves (B = 0–5 T) for $PrMn_2Ge_2$ over the temperature region around T_C^{inter} ~ 334 K; (b) the corresponding Arrott plots of M^2 versus B/M for $PrMn_2Ge_2$.

The isothermal magnetic entropy change, $-\Delta S_M$, for the $PrMn_2Ge_2$ and $Pr_{0.8}Y_{0.2}Mn_2Ge_2$ samples are shown as a function of temperature in Figures 5.35 (a) and 5.35 (b) respectively.

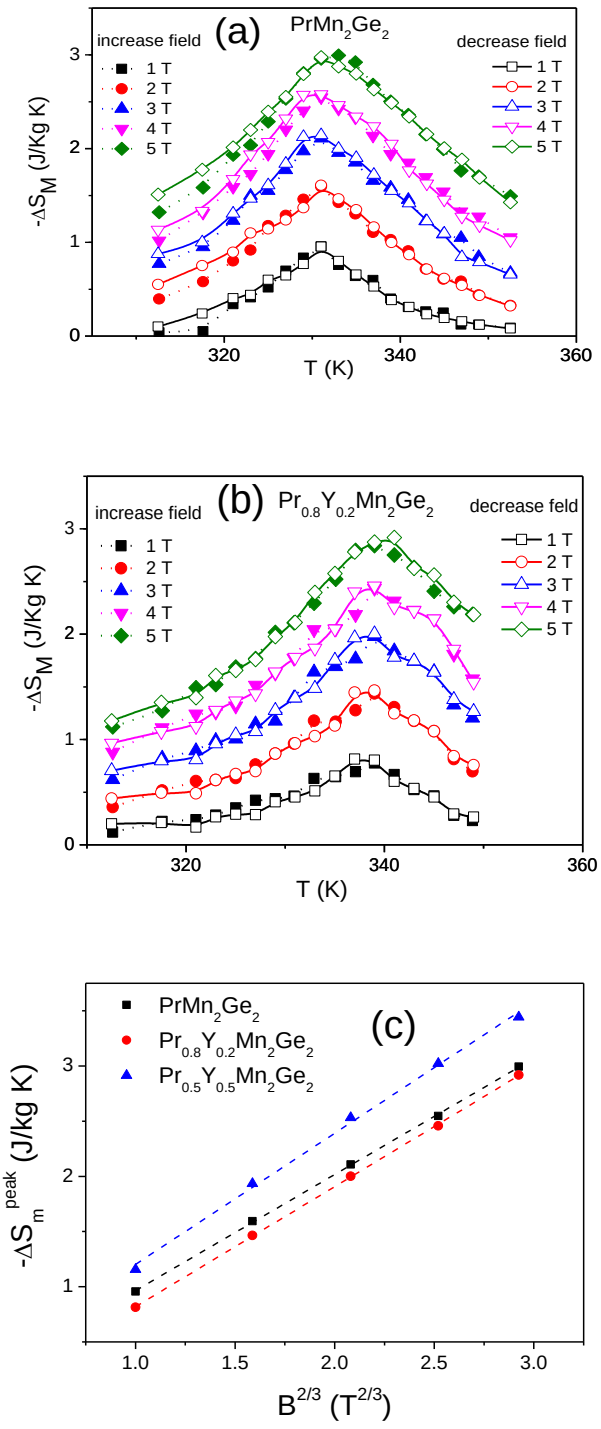

Figure 5.35 Temperature dependence of the isothermal magnetic entropy change $-\Delta S_M$ for: **(a)** $PrMn_2Ge_2$ and **(b)** $Pr_{0.8}Y_{0.2}Mn_2Ge_2$. **(c)** Dependence of $-\Delta S_M^{PK}$ (peak value of the magnetic entropy change at different B) on the parameter $B^{2/3}$ for $Pr_{1-x}Y_xMn_2Ge_2$ compounds with x=0.0, 0.2 and 0.5. The linear fits to the data as shown by the dashed lines are discussed in the text.

The maximum entropy values $-\Delta S_M$ around the ferromagnetic transition temperature T_C^{inter} for the $Pr_{1-x}Y_xMn_2Ge_2$ compounds with x=0.0, 0.2 and 0.5 have been derived to be 3.0 J/kg K, 2.94 J/kg K and 3.47 J/kg K respectively (field change ΔB=0-5 T). Compared with other rare earth intermetallic compounds which also exhibit a second order phase transition around room temperature, the present set of $Pr_{1-x}Y_xMn_2Ge_2$ compounds exhibit moderate isothermal magnetic entropy. As examples, the values of $-\Delta S_M$ for $Ho_2Fe_{17-x}Mn_x$ are 3.2 J $kg^{-1}K^{-1}$ around T_C=336 K (x=0.0) and 2.7 J $kg^{-1}K^{-1}$ around T_C=302 K (x=2.0) respectively [20]. Er_2Fe_{17} has recently been found to exhibit similar entropy value of $-\Delta S_M$=3.6 J $kg^{-1}K^{-1}$ around 300 K for ΔB = 0-5 T [21]. The present set of entropy values are similar to those obtained for related compounds in the RMn_2X_2 series which also exhibit magnetic transitions around ~330 K. Dincer and Elerman [22A] obtained maximum entropy values in the approximate range $-\Delta S_M$ ~ 2-3 J $kg^{-1}K^{-1}$ (ΔB=0-5 T) around the paramagnetic to ferromagnetic Curie temperatures T_C ~ 300-320 K for re-entrant $SmMn_{2-x}Fe_xGe_2$ (x = 0.05, 0.10) and $SmMn_{2-x}Co_xGe_2$ (x = 0.05, 0.15) compounds. On the other hand a reduced entropy value of $-\Delta S_M$ ~ 1.8 J $kg^{-1}K^{-1}$ was obtained for a $Pr_{0.1}Gd_{0.9}Mn_2Ge_2$ sample around the antiferromagnetic to ferromagnetic Curie temperature T_C ~ 340 K [23A].

It is well accepted that the following relationship applies for a magnetic system with a second-order phase transition [22, 23]:

$$|\Delta S_M^{PK}| \propto B^{2/3} \qquad (2)$$

where $-\Delta S_M^{PK}$ is the peak value of the magnetic entropychange at different magnetic fields B. It can be seen from Figure 5.35 (c) that this relationship is valid for the $Pr_{1-x}Y_xMn_2Ge_2$ compounds with x=0.0, 0.2 and 0.5 around T_C^{inter}. This agreement of $-\Delta S_M^{PK}$ with relationship (2) confirms the second order nature of these transitions as demonstrated by the Arrott plot analyses and discussed above (e.g. Figure 5.34 (b) for $PrMn_2Ge_2$).

5.2.4 Conclusions

Replacement of Y for Pr leads to a significant reduction in the lattice parameter of $Pr_{1-x}Y_xMn_2Ge_2$ compounds. The commensurate changes in the intralayer Mn–Mn distances correspondingly lead to a variety of magnetic structures, as also observed in related RMn_2X_2 systems (R – rare earth; X - Ge, Si) [e.g. 24]. The various magnetic structures of $Pr_{1-x}Y_xMn_2Ge_2$ have determined by neutron powder diffraction over the temperature range 5 – 450 K. Together with magnetisation and differential scanning calorimetry measurements, this has enabled us to construct the magnetic phase diagram of $Pr_{1-x}Y_xMn_2Ge_2$. The ferromagnetic transitions at T_C^{inter}, the temperature at which the layered antiferromagnetic structure transforms to the canted F*mc* structure, are found to be second order. The entropy changes around T_C^{inter} have been derived for $Pr_{1-x}Y_xMn_2Ge_2$ compounds of Y contents x = 0.0, 0.2 and 0.5.

References

[1] Z. Arnold, C. Magen, L. Morellon, P.A. Algarabel, J. Kamarad, M.R. Ibarra, V. K. Pecharsky and K. A. Gschneidner, Jr., Phys. Rev. B 79, 144430 (2009)

[2] M. Pasquale, C.P. Sasso, L.H. Lewis, L. Giudici, T. Lograsso and D. Schlagel, Phys Rev B, 72 094435 (2005)

[3] N.T. Trung, L. Zhang, L. Caron, K.H.J. Buschow and E. Brück, Appl Phys Lett, 96 (2010) 172504

[4] J.L. Wang, P. Shamba, W.D. Hutchison, M.F. Md Din, J. C. Debnath, M. Avdeev, R. Zeng, S.J. Kennedy, S.J. Campbell, and S.X. Dou, J. Alloys. Compd. 577 475 (2013); Z. Wang, Z. Nie, J. Zeng, R. Su, Y. Zhang, D.E. Brown, Y. Ren and Y Wang, J Alloys Compd. 577 486 (2013)

[5] J.L. Wang, S.J. Campbell, A.J. Studer, M. Avdeev, M. Hofmann, M. Hoelzel and S.X. Dou, J. Appl. Phys. 104 103911 (2008)

[6] R. Zeng, J.L. Wang, L. Lu, W.X.Li, S.J. Campbell and S X Dou, J. Alloys Compd. 505 L38 (2010)

[7] R. Zeng, S.X. Dou, J.L. Wang, S.J. Campbell J. Alloys Compd. 509 L119 (2011)

[8] J.L. Wang, S.J. Kennedy, S.J. Campbell, M. Hofmann and S.X. Dou, Phys. Rev. B 87, 104401 (2013)

[9] J.L. Wang, L. Caron, S.J. Campbell, S.J. Kennedy, M. Hofmann, Z.X. Cheng, M. F. Md Din, A.J. Studer, E. Brück and S.X. Dou, Phys. Rev. Lett. 110 217211 (2013)

[10] J.L. Wang, S.J. Campbell, M. Hofmann, S.J. Kennedy, M. Avdeev, M.F. Md Din, R. Zeng, Z.X. Chang and S.X. Dou, J. Appl. Phys. 113 17E147 (2013)

[11] L. B. McCusker, R.B. Von Dreele, D.E. Cox, D. Louër, and P. Scardi, J. Appl. Crystallography 32, 36 (1999).

[12] Y.G. Wang, F.M. Yang, C.P. Chen, N. Tang, and Q.D. Wang, J. Phys. Condens. Matter 9, 8539 (1997).

[13] V. Siruguri, S.K. Paranjpe, P. Raj, A. Sathyamoorthy, J.P. Itié, A. Polian, Physica B 344 255 (2004)

[14] A. Szytuła and I. Szott, *Solid State Commun.* 40 199 (1981)

[15] R. Welter, G. Venturini, E. Ressouche, B. Malaman, J. Alloys Compd. 218 204 (1995)

[16] S. Kervan, A. Kilic and A. Gencer, J. Phys.: Condens. Matter 16 4955 (2004)

[17] S.J. Kennedy, J.L. Wang, S.J. Campbell, M. Hofmann and S.X. Dou, J. Appl. Phys. (in press, 2014).

[18] J.L. Wang, S.J. Campbell, A.J. Studer, M. Avdeev, R. Zeng, and S.X. Dou, J. Phys.: Condens. Matter 21 124217 (2009)

[19] J. L. Wang, S. J. Campbell, J. M. Cadogan, A. J. Studer, R. Zeng, and S. X. Dou, Appl. Phys. Lett: 98 232509 (2011)

[20] J.L. Wang, A.J. Studer, S.J. Kennedy, R. Zeng, S.X. Dou, and S.J. Campbell, J. Appl. Phys. 111, 07A911 (2012)

[21] P. Á lvarez-Alonso, P. Gorria, J. A. Blanco, J. Sánchez-Marcos, G.J. Cuello, I. Puente-Orench, J.A. Rodríguez-Velamazán, G. Garbarino, I. de Pedro, J.R. Fernández and J.L. Sánchez Llamazares, Phys. Rev. B 86 184411 (2012)

[22A] I. Dincer and V. Elerman, J. Magn. Magn. Mater, 326 50 (2013)

[23A] I. Dincer and V. Elerman, Phys. Scr., 81 025703 (2010)

[22] A. Biswas, S. Chandra, T. Samanta, B. Ghosh, S. Datta, M.H. Phan, A.K. Raychaudhuri, I. Das and H. Srikanth, Phys. Rev. B 87 134420 (2013) and references therein

[23] J.L. Wang, S.J. Campbell, S.J. Kennedy, R. Zeng, S.X. Dou and G.H. Wu, J. Phys.: Condens. Matter 23 216002 (2011)

[24] A. Szytuła and J. Leciejewicz, Handbook of Crystal Structures and Magnetic Properties of Rare Earth Intermetallics (CRC Press, Boca Raton, 1994)

5.3 Substitution of Ge with Other Metalloid in $CeMn_2Ge_2$ Compound

5.3.1 Introduction

Due to the wide and interesting range of structural and magnetic phenomena - including magnetism, superconductivity, mixed valence, Kondo behavior and heavy fermion - exhibited by layered RT_2X_2 rare earth compounds, (R is a rare earth, T is transition metal and X is Si or Ge) this series has consistently attracted many researchers for further investigation [1-4]. Most of the layered RT_2X_2 crystallize in the body centred tetragonal $ThCr_2Si_2$-type structure with space group *I4/mmm* in which the R, T and X atoms occupy the 2*a*, 4*d* and 4*e* sites respectively with the different atoms stacked along the *c*-axis in the layered sequence R–X–T–X–R [5-7]., The RMn_2X_2 series has continued to attract a great deal of attention over the past two decades due to the fact that the magnetic states of the Mn-sublattice depend sensitively on the inter-planar and intra-planar Mn–Mn distances [8, 9]. Furthermore, intensive studies of RMn_2X_2 compounds have revealed a large variety of magnetic structures and magnetic phase transitions that occur with changes in chemical composition, temperature and mechanical pressure or magnetic field applied [10-12]. As such, from this aspect, RMn_2X_2 compounds provide model systems for study of, for example, the volume dependence of magnetic ordering. They also offer scope for design of critical magnetic parameters — such as the type or order of magnetic phase transitions and ability to shift transition temperatures — by controlling the intra-planar separation distance d^a_{Mn-Mn} with applied mechanical or chemical pressure via replacement with elements of different atomic sizes [13-15].

In this study, we report the findings of an investigation of the effects of substituting Si for Ge in $CeMn_2Ge_{2-x}Si_x$ (x = 0.0-2.0) on their magnetic properties and structures using magnetic, differential scanning calorimetry (DSC), high resolution X-ray synchrotron radiation and neutron diffraction measurements. In addition to exploring the effects of the Si atoms on the metalloid Ge, it is expected that substitution of Ge (atomic radius 1.37 Å) with the smaller Si (atomic radius 1.32 Å) would modify the magnetic structure of $CeMn_2Ge_{2-x}Si_x$. This follows as $d^a_{Mn-Mn} \sim 2.934$ Å in $CeMn_2Ge_2$ while $d^a_{Mn-Mn} \sim 2.806$ Å in $CeMn_2Si_2$ [16]. These values of d^a_{Mn-Mn} are respectively greater than $d_{crit1} \sim 2.87$ Å (of related lattice parameter a_{crit1}=4.06 Å) and less than $d_{crit2} \sim 2.84$ Å (related lattice parameter a_{crit2}=4.02 Å), the first and second critical intralayer Mn–Mn distances which govern the magnetic behaviour in RMn_2Ge_2 compounds [17]. According to Welter *et. al* [18], the d^a_{Mn-Mn} not only affects the intralayer Mn–Mn coupling but also the interlayer exchange interaction and, as summarised below, three general categories can be delineated [19].

(i) The interlayer exchange coupling being ferromagnetic and the intralayer coupling antiferromagnetic for $d^a_{Mn-Mn} > d_{crit1} = 2.87$ Å leading to the canted Fmc-type ferromagnetic structure.

(ii) Both the interlayer and the intralayer coupling being antiferromagnetic (AFmc-type magnetic structure) for $d_{crit2} = 2.84$ Å $< d^a_{Mn-Mn} < d_{crit1} = 2.87$ Å.

(iii) No intralayer in-plane spin component and the interlayer coupling being antiferromagnetic, leading to the AFil-type magnetic structure d^a_{Mn-Mn} in the range $d^a_{Mn-Mn} < d_{crit2} = 2.84$ Å.

This interest in the behaviour of layer structure materials has been enhanced in recent years by the discovery of a giant magnetocaloric effect (MCE) near room temperature in $Gd_5Si_2Ge_2$

compound [20, 21]. $R_5(Si,Ge)_4$ type compounds have a distinct layered structure in which the covalent Si–Si, Si–Ge and Ge–Ge bonds and interlayer distances play a vital role in determining their magnetic and magnetocaloric effect properties attention has therefore increasingly focused on understanding the fundamental properties of this type of layered material. As already noted, the $CeMn_2Ge_{2-x}Si_x$ system has a sequence of atomic layers stacked along the *c*-axis similar to the $R_5(Si,Ge)_4$ system. The relatively simple body centred tetragonal $ThCr_2Si_2$-type structure offers scope for selection of the magnetic state via strong dependence of Mn–Mn intraplanar and interplanar exchange interactions on d^a_{Mn-Mn}, the Mn–Mn separation distance in the *ab*-plane for enhanced understanding of the correlation between magnetic properties and atomic distances. Our comprehensive investigation of the crystallographic, magnetic properties and critical exponent behaviour of $CeMn_2Ge_{2-x}Si_x$ compounds (x=0.0-2.0 has enabled us to establish the magnetic structures across the Ge-Si concentration range and derive the magnetic phase diagram of $CeMn_2Ge_{2-x}Si_x$.

5.3.2 Experimental and Procedures

$CeMn_2Ge_{2-x}Si_x$ alloys with Si concentrations x = 0.0, 0.4, 0.8, 1.0, 1.2, 1.6 and 2.0 were prepared by arc melting the high purity elements on a water-cooled Cu hearth under purified argon gas. The mass loss of Mn during melting was compensated for by adding 3% excess Mn. The ingots were melted five times to attain homogeneity and then annealed at 900 C for one week in an evacuated quartz tube. The samples were characterized by x-ray diffraction (Cu K, λ=1.5418 Å). The temperature dependence of the magnetization, M (T) was measured in a magnetic field of B applied = 0.01 T in a superconducting quantum interference device (SQUID) from 5 to 350 K. All samples were investigated by differential scanning calorimetry (DSC) to check for possible phase transitions in the higher temperature range from 300 to

450 K. Neutron diffraction patterns were collected over the temperature range 6–450 K to cover the temperature range over which long range magnetic order was observed. Further details were obtained on the Wombat (high intensity; with λ= 2.41 Å) diffractometers, OPAL, Australia.

5.3.3 Result and Discussion

5.3.3.1 $CeMn_2Ge_{2-x}Si_x$

Rietveld refinements (FULLPROF package [22]) of the room temperature X-ray diffraction patterns indicate that all of the $CeMn_2Ge_{2-x}Si_x$ samples crystallize in the $ThCr_2Si_2$ structure . The refined results — including lattice parameters *a*, *c*, axial ratio *c*/*a* and unit cell volume V — are shown in Figure 5.36. As expected, substitution of Ge by Si leads to a monotonic decrease of both *a* and *c* along with concomitant contraction of the unit cell volume with increasing Si content; good agreement is obtained with published results [16]. However, it is noted that the variation of the lattice constants and unit cell volume change slope with composition around x = 1.0–1.2, with this behaviour evident in the composition dependence of the axial ratio *c*/*a*.

The change in slope discerned around x = 1.0–1.2 is likely to be related to the change in magnetic ordering of the Mn-sublattice as in discussion of the neutron diffraction results below. At room temperature the x = 1.2 compound exhibits a mixture of ferromagnetic with antiferromagnetic states while compounds with x > 1.2 are purely antiferromagnetic. Similar tendencies in the composition dependence of the lattice constants have been detected in the related $PrMn_2Ge_{2-x}Si_x$ system [23]. As is well known and as indicated above, RMn_2X_2 (X =

Ge or Si) compounds exhibit different magnetic behaviours around two critical values of the lattice parameter a_{crit2} ~ 4.02 Å and a_{crit1} ~ 4.06 Å [9].

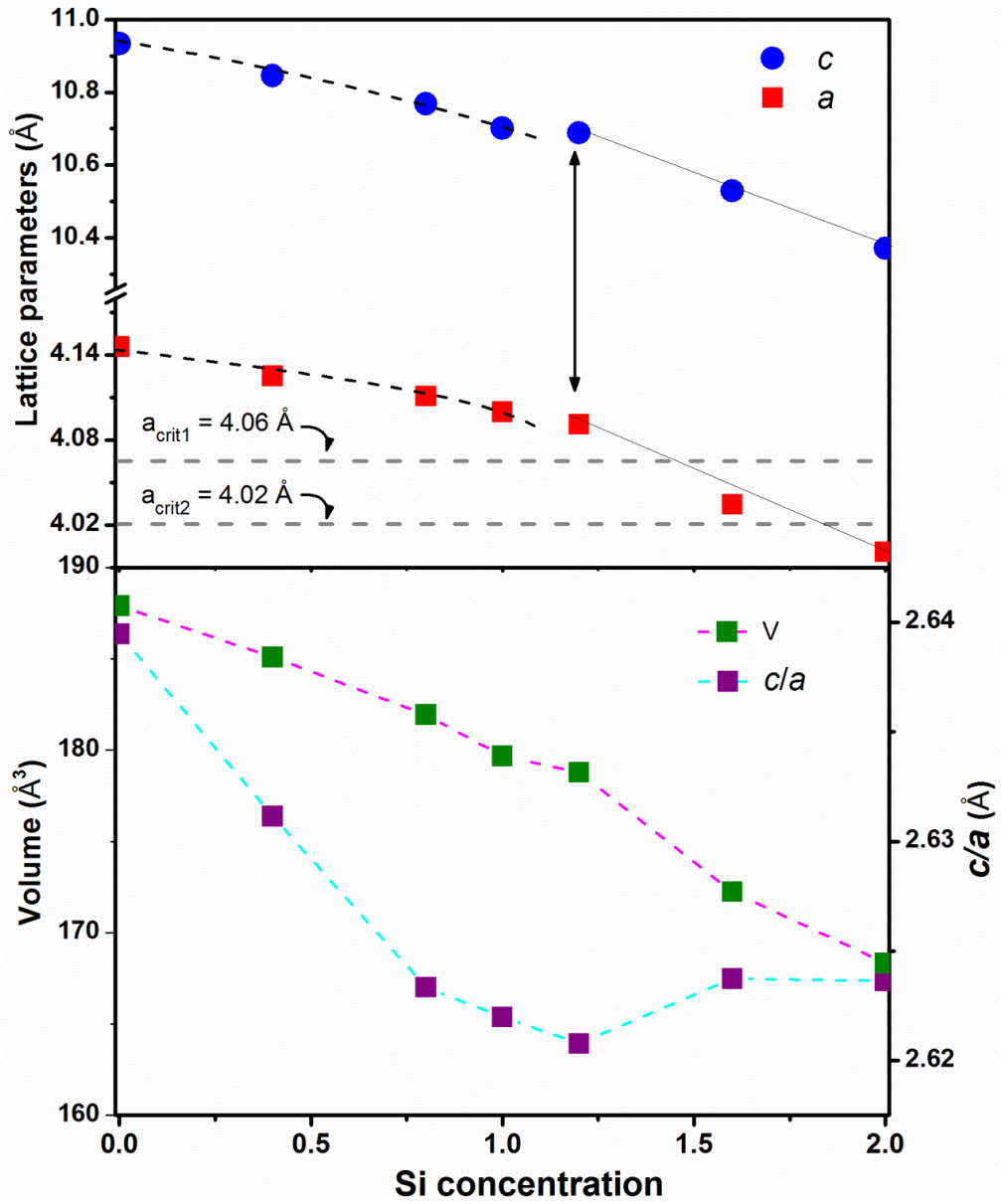

Figure 5.36 Composition dependence of lattice parameters *a* and *c*, axial ratio *c*/*a* and unit cell volume, V, for $CeMn_2Ge_{2-x}Si_x$ at room temperature. The arrows indicate the region where the slope changes. The dashed and full lines are guides to the eye; the a_{crit1} and a_{crit2} values of the upper figure are explained in the text.

The bond lengths between different sites have also been calculated with the BLOKJE program [24] using the structural and positional parameters and the 12-coordinate metallic radii of 1.81 Å, 1.35 Å, 1.37 Å and 1.32 Å for Ce, Mn, Ge and Si, respectively. It was found

that the Mn-Mn intralayer exchange interaction distance decreased from $d_{Mn\text{-}Mn}$ = 2.9306 Å at x=0 to $d_{Mn\text{-}Mn}$ = 2.8307 Å at x=2.0. Moreover if we assume that the contraction of the unit cell volume due to Si substitution (chemical pressure) is equivalent to the influence of external pressure, the corresponding pressures can be derived to be 24.7 kbar and 68.5 kbar for the x = 1.0 and 2.0 samples using the Murnaghan equation as shown in Equation 5.1 In this calculation we used the modulus values B_0 = 819 kbar and B'_0 =4.0 of $LaMn_2Si_2$ [13] as a guide for the modulus values for $CeMn_2Ge_2$ compound ($LaMn_2Si_2$ has the same crystal structure as $CeMn_2Ge_2$).

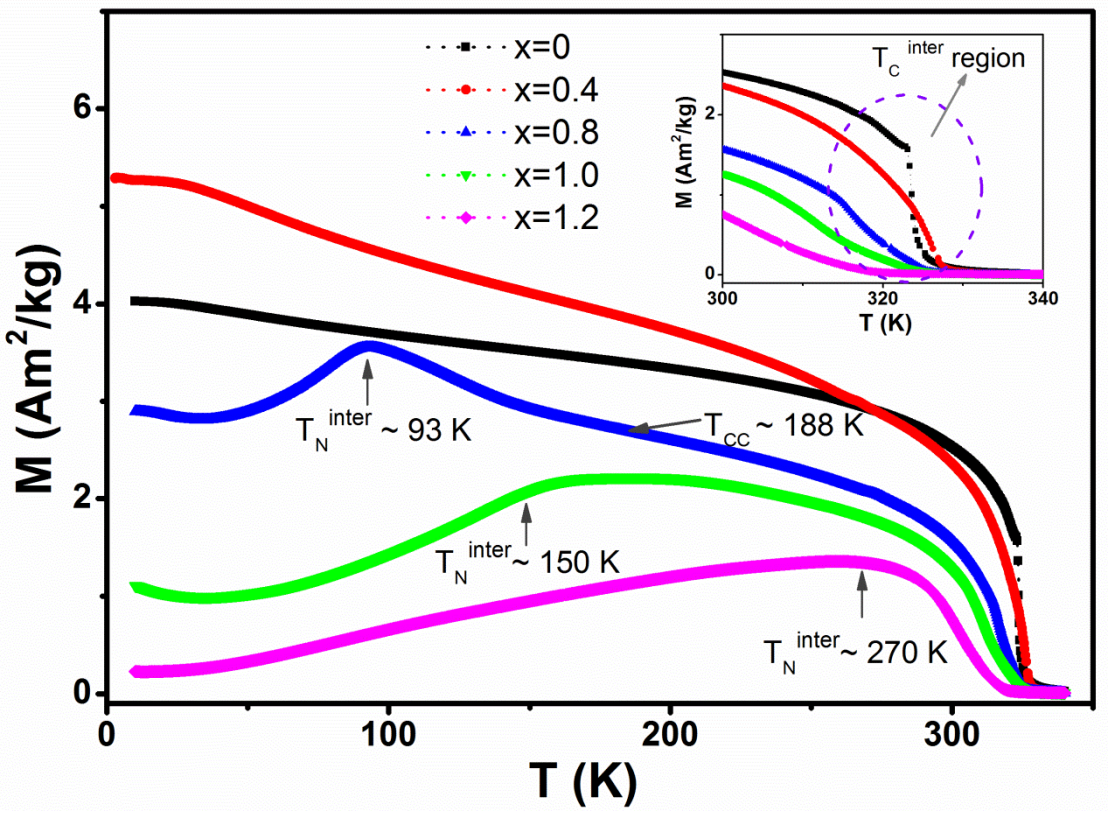

Figure 5.37 Temperature dependence of magnetization of $CeMn_2Ge_{2-x}Si_2$ compounds (x = 0.0- 2.0) as measured in a field of 0.01 T. The inset shows the region of T_C^{inter} for the set of samples.

Figure 5.37 shows the temperature dependence of the magnetization of $CeMn_2Ge_{2-x}Si_x$ as measured in a field of 0.01 T over the temperature range of 5–340 K. DSC measurements have been used to check for possible phase transitions in the temperature region from 340 K

up to 550 K. Figure 5.37 reveals clearly that below 340 K the magnetic phase transition temperatures change with the Si concentration as expected, The T_C^{inter} magnetic phase transition temperature (from interlayer antiferromagnetic AFl to canted ferromagnetic Fmc as discussed below) was found to decrease from T_C^{inter} ~ 320 K for x=0.4 to T_C^{inter} ~ 305 K for x=1.2 (Figure 5.37; inset). This behaviour may be related to the change in electronic environment as replacing Ge ($3d^{10}4s^24p^2$) by Si ($3s^23p^2$) is expected to influence the magnetic structures of the $CeMn_2Ge_{2-x}Si_x$ compounds. This is supported by Density Functional Theory calculations for RMn_2Ge_2 (R = Y or Ca) compounds [25] which indicate that to a large extent, the magnetic moment is determined mainly by the interatomic Mn-Mn distances, while the interstitial electron density contributes to the change in magnetic structures.

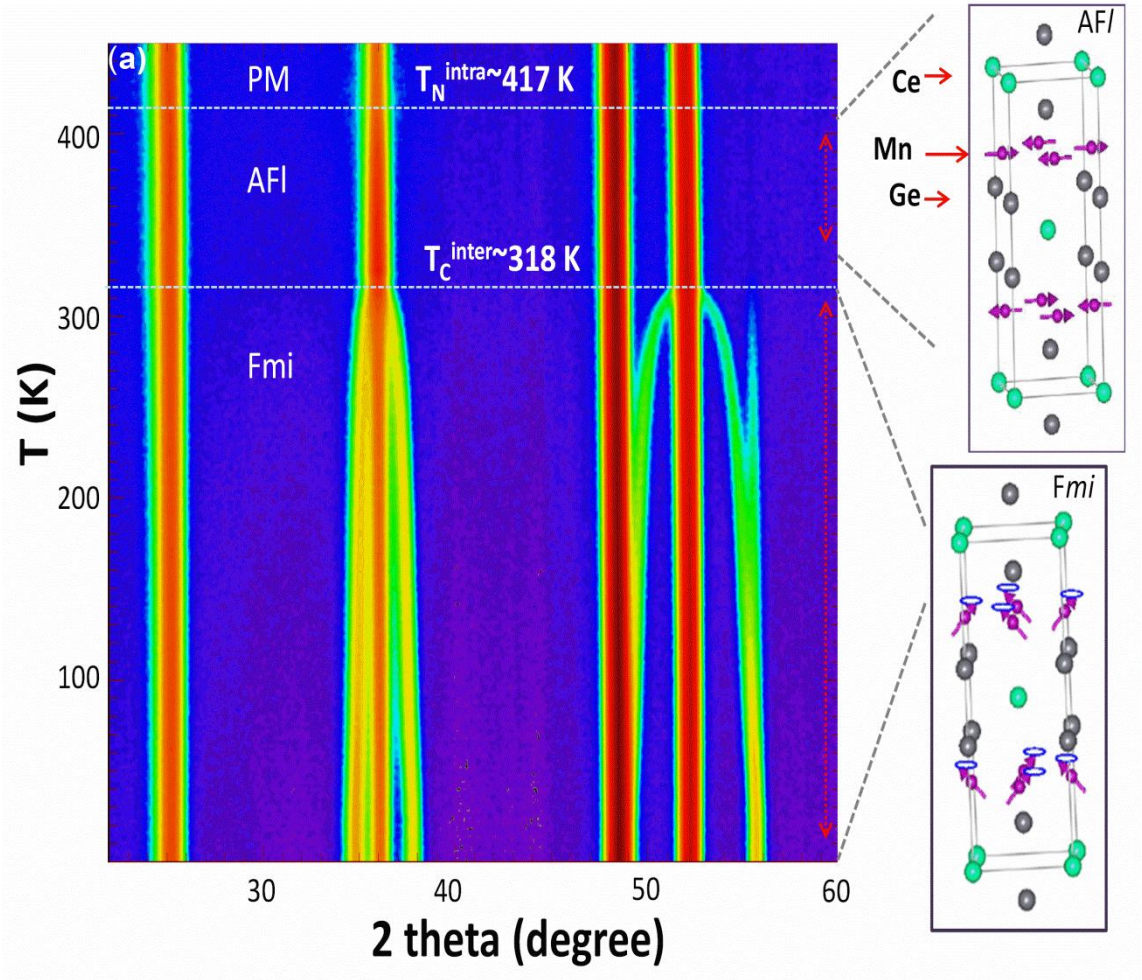

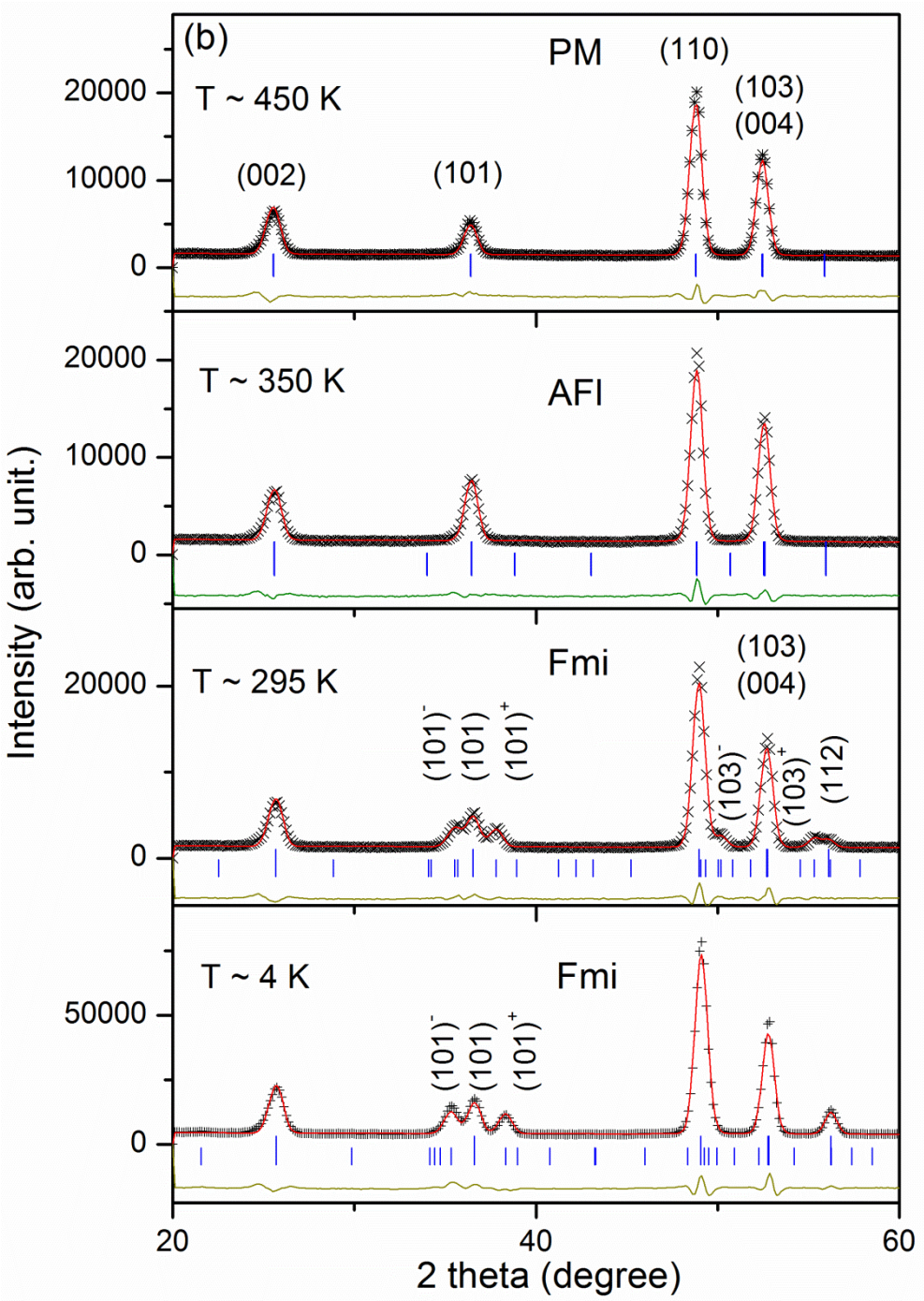

Figure 5.38 (a) Thermal contour plot of $CeMn_2Ge_2$ neutron diffraction measurements over the range of 4–450 K. The AFl and Fmi magnetic structures of $CeMn_2Ge_2$ are also shown; (b) Neutron diffraction patterns and Rietveld refinements for $CeMn_2Ge_2$ at 450 K, 350 K, 295 K, and 4 K (λ=2.4179 Å, Wombat diffractometer, OPAL).

A set of neutron powder diffraction patterns was obtained for $CeMn_2Ge_{2-x}Si_x$ compounds (x =0.0-2.0) over the temperature range 6–450 K. Rietveld refinements were carried out on all patterns using the FULLPROF program package [22] which allows us to derive the structural

and magnetic parameters. As explained fully in related articles [8, 18, 23, 26], the specific location of Mn atoms on the 4*d* site in the $ThCr_2Si_2$ structure (space group *I4/mmm*) allows ready identification of various magnetic structures from key indicators in the neutron diffraction patterns as follows:

(1) Ferromagnetic ordering of the Mn atoms—*hkl* reflections with $h+k = 2n$ and $l = 2n$ (e.g. (112), (200) reflections).
(2) Antiferromagnetic ordering of the Mn atoms within the (001) planes—reflections with $h+k = 2n+1$ (e.g. (101), (103) reflections).
(3) Collinear antiferromagnetic structure between adjacent Mn planes—reflections with $h+k+l = 2n+1$ (e.g. (111), (113) reflections).
(4) Ferromagnetic mixed incommensurate structure (Fmi) of wavevector (0; 0; q_z)—satellite reflections with h+k = 2n+1 (e.g. (101), (103)).

The neutron diffraction thermal contour plot for $CeMn_2Ge_2$ from 4-450 K shown in Figure 5.38(a), covers the various magnetic regions indicated by the magnetic measurements of Figure 5.37. Refinement of the 450 K neutron diffraction pattern confirms that $CeMn_2Ge_2$ is paramagnetic. At 350 K (i.e. below T_N^{intra} ~ 417 K; Figure 3(b)) the intensity of the (101) reflection increases and, consistent with neutron diffraction condition (2) above, $CeMn_2Ge_2$ exhibits the AFl structure. At 295 K, below the transition temperature T_C^{inter} ($T_{C/C}$) ~ 318 K, the appearance of the (112) peak together with the presence of satellite peaks $(101)^+$, $(101)^-$ and $(103)^+$, $(103)^-$ in the patterns and noting condition (4) above, demonstrates that $CeMn_2Ge_2$ has the ferromagnetic mixed incommensurate (Fmi) magnetic structure is below this temperature. The Fmi magnetic structure is found to persist with decrease in temperature

to T ~ 4 K as confirmed by the absence of change in the intensities of the $(101)^{+}$ and $(101)^{-}$ reflections.

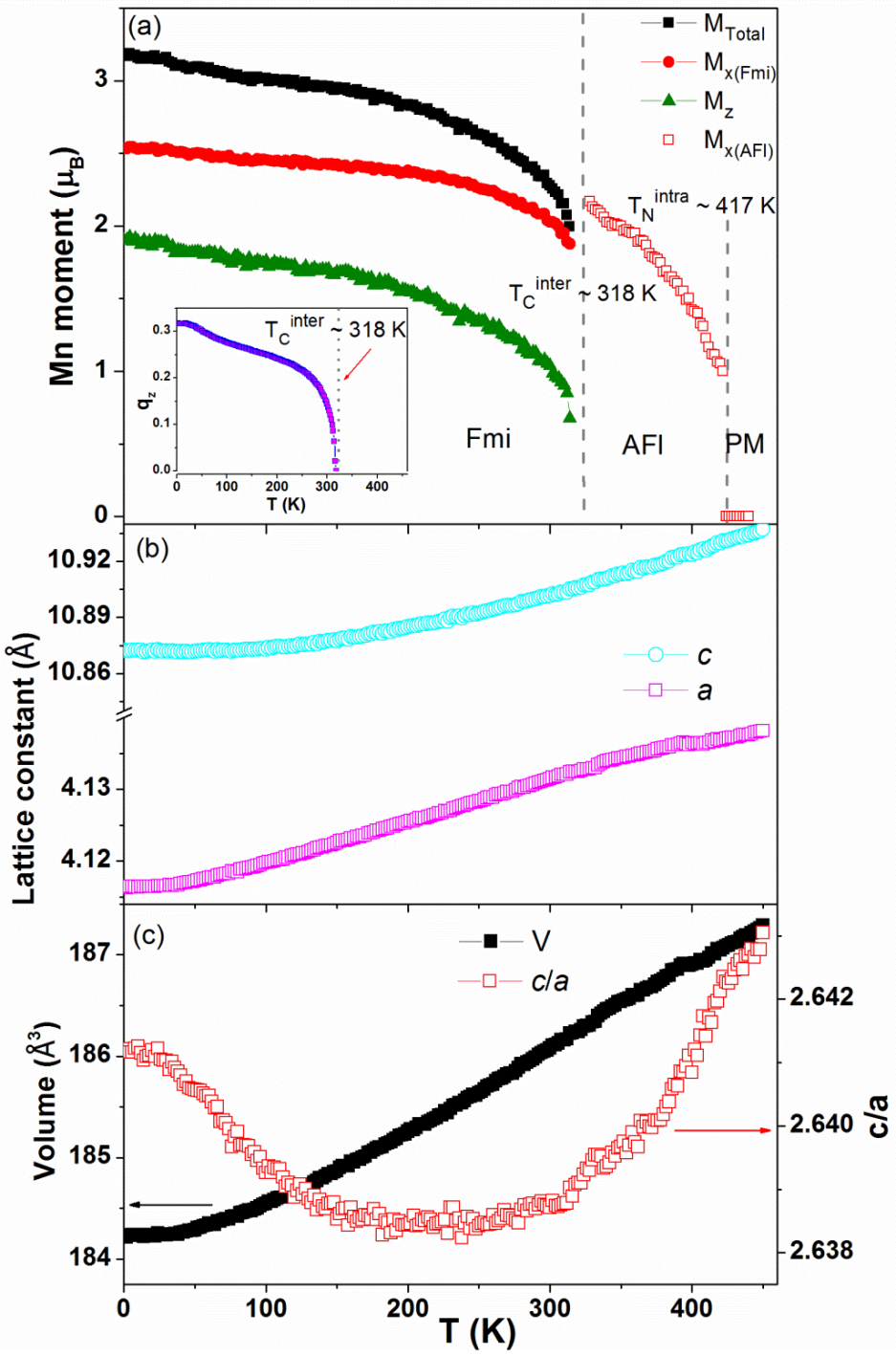

Figure 5.39 Structural and magnetic parameters for $CeMn_2Ge_2$ as derived from refinements of the neutron diffraction patterns: (a) Temperature dependences of the magnetic moment and propagation vector q_z for $CeMn_2Ge_2$ (inset). T_N^{intra} and T_C^{inter} are denoted by arrows with the dotted lines delineating the paramagnetic (PM), antiferromagnetic (AFl-type) and ferromagnetic mixed incommensurate (Fmi) regions. (b) Temperature dependences of lattice parameters *a* and *c* and (c) unit cell volume and axial ratio *c*/*a*.

For $CeMn_2Ge_2$ the values of the magnetic moments at 4 K are derived to be $M_{Total} \sim 3.16\ \mu_B$, $M_x \sim 2.53\ \mu_B$ and $M_z \sim 1.9\ \mu_B$ with the magnitude of the propagation vector $q_z \sim 0.317$ as indicated in Figure 5.39(a). The values of q_z for $CeMn_2Ge_{1.6}Si_{0.4}$ at 4 K are found to decrease to $q_z \sim 0.276$ and continue to reduce with increasing Si concentration. It can be concluded that the replacement of Si for Ge leads to a decrease in q_z; this behaviour is similar to that detected on replacement of Fe for Mn [27] and Y or Lu [9, 28] for Pr in the $PrMn_2Ge_2$ compound. The temperature dependences of the structural and magnetic parameters of $CeMn_2Ge_2$ as derived from the refinements (Figure 5.39 (b)) reveal a significant change from a= 4.145 Å and c=10.934 Å for x=0 to a= 4.001 Å and c=10.371 Å for x=2.0 as reconfirmed in the temperature dependence of the *c*/*a* ratio around T_C^{inter} (Figure 5.39(c)). This phenomena indicates that strong coupling occurs between the magnetism and the crystal lattice in the presence of a *c*-axis component of the Mn moment which is similar to $PrMn_{2-x}Fe_xGe_2$ system [27], where the presence of the interlayer Mn–Mn interactions rather than the intralayer Mn–Mn interactions play the major role in the anomalous thermal expansion observed at the magnetic transition in these layered systems.

Reflecting the changes in magnetisation with temperature for the $CeMn_2Ge_{1.0}Si_{1.0}$ and $CeMn_2Ge_{0.8}Si_{1.2}$ compounds (Figure 5.37), the neutron diffraction patterns of $CeMn_2Ge_{1.0}Si_{1.0}$ and $CeMn_2Ge_{0.8}Si_{1.2}$ were also found to exhibit interesting behaviour. Neutron diffraction patterns were collected for both compounds over the temperature range 6–450 K with temperature steps of around 5 K in order to obtain detailed information around the phase transitions. The set of neutron diffraction patterns for $CeMn_2Ge_{0.8}Si_{1.2}$ are shown as an example in Figure 5.40(a). Among features noted are that the intensity of the (002) nuclear reflection remains effectively unchanged over the whole temperature range and the absence of satellite peak $(101)^+$, $(101)^-$ and $(103)^+$, (103). Magnetic phase transitions at $T_N^{intra} \sim 430$

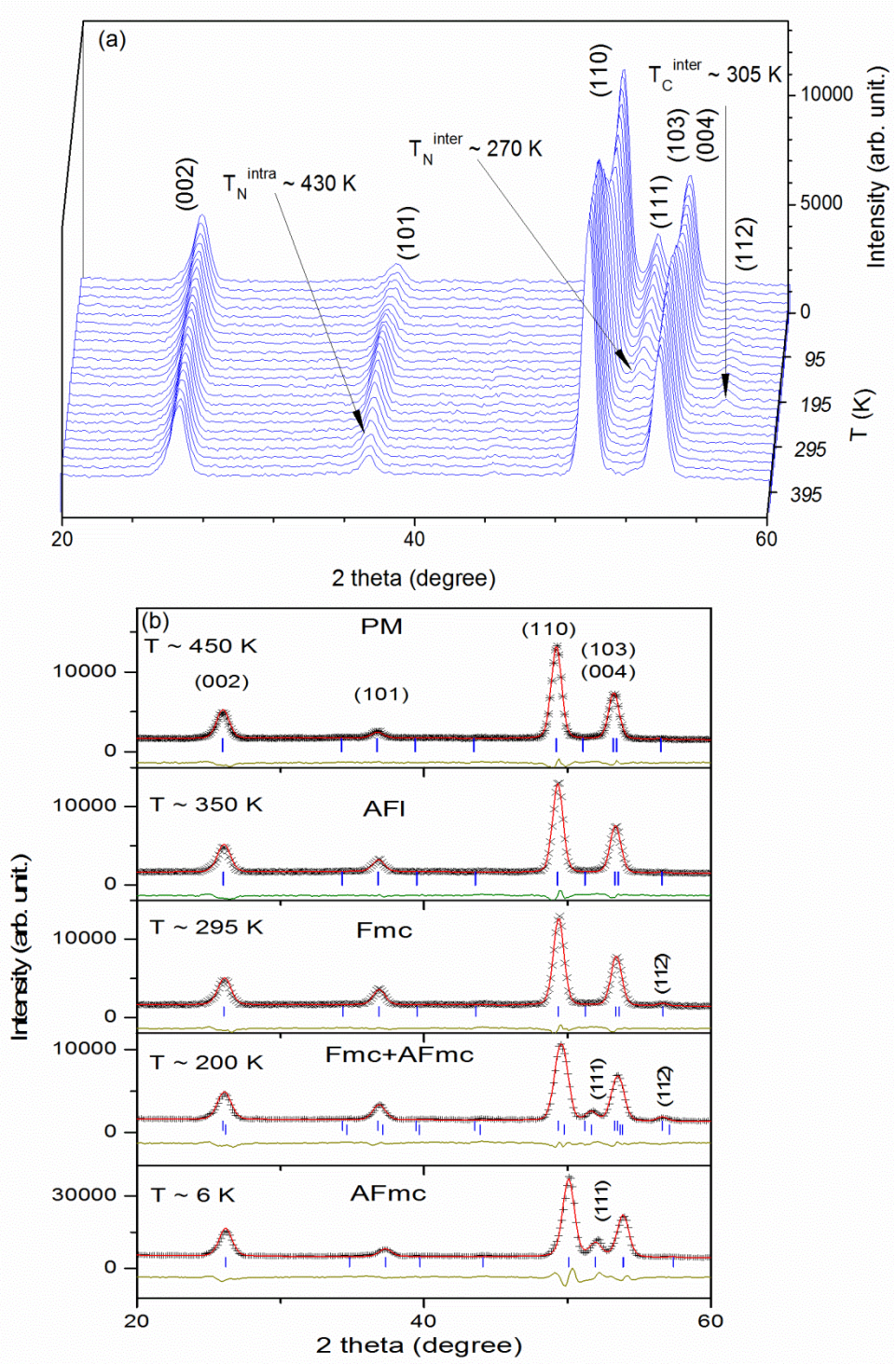

Figure 5.40 (a) Neutron diffraction patterns for $CeMn_2Ge_{0.8}Si_{1.2}$ over the temperature range 6–450 K and (b) Rietveld refinements for $CeMn_2Ge_{0.8}Si_{1.2}$ at 450 K, 350 K, 295 K, 200 K and 6 K (λ=2.4118 Å , Wombat diffractometer, OPAL).

K; T_C^{inter} ~ 305 K; T_N^{inter} ~ 270 K and completed Fmc temperature T* ~ 31 K are clearly marked by changes in the intensities of the (101), (111) and (112) reflections due to magnetic

scattering. According to neutron diffraction condition (3), the appearance of the (111) reflection peak below ~ 270 K at T ~ 200 K in Figure 5.40 (b) indicates the formation of the AFmc state while, based on neutron diffraction condition (2), the fact that the (112) reflection remains indicates that the Fmc state still exists at the same temperature as the mix magnetic state behaviour. However the mix magnetic state start to disappear when cooling to T < 31 K as absent the peak of (112) and consistently unchanged on peak (111) indicated the AFmc state behaviour as shown in Figure 5.40 (b) at T ~ 6 K. Direct evidence for the coexistence of two phases in the $CeMn_2Ge_{1.0}Si_{1.0}$ sample was obtained using high resolution synchrotron X-ray diffraction; Figure 5.41(a) indicates two distinct (101) reflections from ~ 80 K to ~ 180 K with a single (101) reflection observed above ~ 180 K. These structural features are entirely consistent with the occurrence of mixed structures of the ferromagnetic Fmc and antiferromagnetic AFmc states below ~ 180 K. This behaviour was reconfirmed by comparison on the same peak (101) with other Si concentration at 80 K; comparison with $CeMn_2Ge_{2-x}Si_x$ compounds of Si concentrations x = 0.0, x = 0.4, x = 1.0, x = 1.6 and x= 2.0 revealed that only $CeMn_2Ge_{1.0}Si_{1.0}$ present mixed peaks as depicted in Figure 5.41(b). In addition co-existence of the (111) and (112) peaks as observed in the neutron diffraction patterns of $CeMn_2Ge_{0.8}Si_{1.2}$ below T_N^{inter} ~ 270 K (Figure 5.40 at T ~ 200 K), indicates co-existence of two magnetic states corresponding to the ferromagnetic Fmc and antiferromagnetic AFmc states. This behaviour is similar to the co-existence of magnetic phases first reported in $La_{0.8}Y_{0.2}Mn_2Si_2$ [29]. The Rietveld refinements also confirm that the unit cell for the AFmc phase is smaller than the unit cell for the Fmc phase (e.g. at T= 80 K the unit cell volume V ~ 177.2 $Å^3$ for Fmc while V ~ 175.8 $Å^3$ for AFmc). This behaviour agrees well with the other re-entrant ferromagnetism systems [19, 23, 30], with around 0.3% contraction of the unit cell observed when the magnetic state changes at T_N^{inter} from Fmc to AFmc in $SmMn_2Ge_2$ [30].

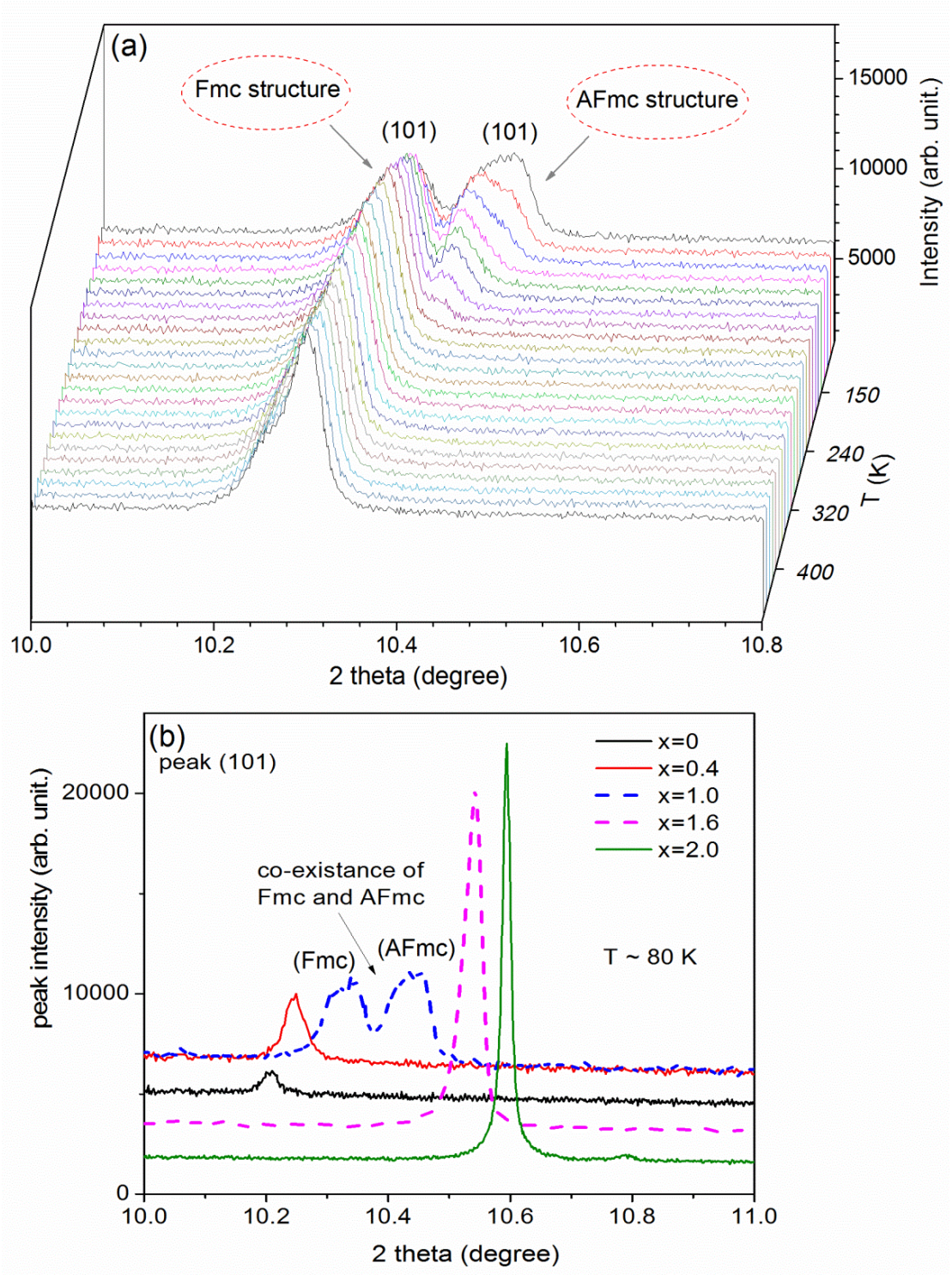

Figure 5.41 (a) X-ray diffraction patterns over the range of 80–450 K for $CeMn_2Ge_{1.0}Si_{1.0}$ in the 2Θ region around the (101) peak position, and (b) comparison of the reflections observed around the (101) peak position for $CeMn_2Ge_{2-x}Si_x$ compounds of Si concentrations x = 0.0, x = 0.4, x = 1.0, x = 1.6 and x= 2.0 at 80 K (λ=0.6887 Å, Powder Diffraction, Australian Synchrotron).

Details about the phase transitions in $CeMn_2Si_2$ over the temperature range 6–450 K were determined from neutron diffraction patterns obtained at temperature step intervals of 2 K (Figure 5.42(a)). Rietveld refinements of the neutron diffraction pattern at 450 K confirm that $CeMn_2Si_2$ has the $ThCr_2Si_2$ structure as expected. The absence of magnetic scattering above $T_N^{intra} \sim 384$ K in reflections such as (101), (111) and (112) is consistent with a paramagnetic (PM) state (see e.g. the disordered magnetic states (PM) observed in $EuMn_2Si_2$ [31] and $LaPrMn_2Si_2$ [32]. Below $T_N^{intra} \sim 384$ K, $CeMn_2Si_2$ is found to exhibit the antiferromagnetic interlayer coupling structure (AFil) down to base temperature T ~ 5 K (Supplementary Fig. S2). The AFil structure — a collinear antiferromagnetic structure between adjacent Mn planes in a + − + − sequence along the *c*-axis — is indicated by the magnetic scattering observed at the (111), (113) and (201) reflections (extinction rules $h + k = 2n$ and $h + k + l = 2n + 1$) in agreement with those reported by Dincer *et al.* [32]. Figure 5.42(b) shows the temperature dependences (5-450 K) of the lattice parameters and *c*/*a* axial ratio as determined from Rietveld refinements of the neutron diffraction patterns. Both the *a* and *c* values exhibit a monotonic decrease with temperature in the region of the paramagnetic to interlayer antiferromagnetic transition. Furthermore, Figure 5.42(b) reveals a significant change in the temperature dependence of the *c*/*a* ratio around $T_N^{intra} \sim 384$ K; this behaviour indicates strong coupling between the magnetism and the crystal lattice in the presence of an *ab*-axis component of the Mn moment and further indicates the presence of strong magnetostructural coupling around $T_N^{intra} \sim 384$ K. As discussed recently [33], the strong magnetostructural coupling leads to a large structural entropy change around the magnetic phase transition, thereby contributing to the total entropy change around the magnetic phase transition.

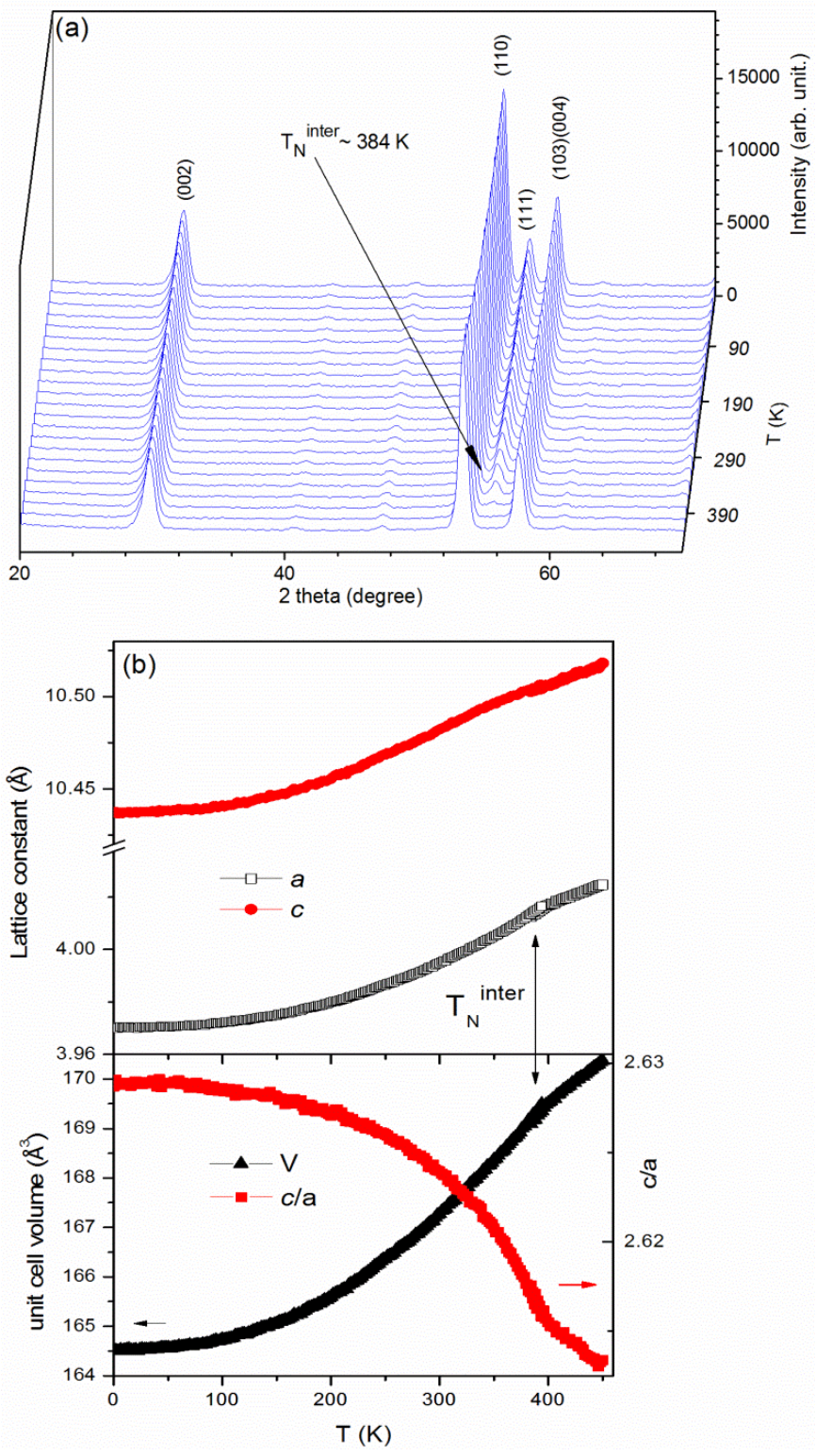

Figure 5.42 (a) Neutron diffraction patterns for $CeMn_2Si_2$ over the range of 6–450 K (λ=2.4118 Å) and (b) Temperature dependences of the lattice parameters *a* and *c* together with the unit cell volume, V, and axial ratio *c*/*a* for $CeMn_2Si_2$ as determined from Rietveld refinements of the neutron diffraction patterns.

The magnetic entropy change, $-\Delta S_M$, has been determined for the set of $CeMn_2Ge_{2-x}Si_x$ compounds (x = 0.0-2.0) from their magnetization curves as functions of temperature and magnetic field (ΔB = 0-5 T) in the region around the ferromagnetic transition T_C^{inter}. The set of $-\Delta S_M$ values was determined by applying the standard Maxwell relation [34] as shown in equation 5.3. As shown by the curves of Figure 5.43(a), the $-\Delta S_M$ peak gradually broadens towards higher temperatures with increasing magnetic field (from ΔB = 0-5 T), behaviour characteristic of a second order magnetic transition. The changes in magnetic entropy for the set of $CeMn_2Ge_{2-x}Si_x$ compounds (x = 0, 0.4 and 0.8) have been derived to be 3.21 J kg^{-1} K^{-1}, 2.86 J kg^{-1} K^{-1} and 2.67 J kg^{-1} K^{-1}, respectively (field change ΔB = 0-5 T) around T_C^{inter}. $CeMn_2Ge_{2-x}Si_x$ compounds exhibit moderate isothermal magnetic entropy accompanied with a second-order phase transition around room temperature comparable with other rare earth intermetallic compound in the RMn_2X_2 series. For example, Dincer and Elerman [35] obtained maximum entropy values in the approximate range $-\Delta S_M \sim 2–3$ J kg^{-1} K^{-1} (ΔB = 0-5 T) around the Curie temperatures $T_C^{inter} \sim 300–320$K for re-entrant $SmMn_{2-x}Fe_xGe2$ (x=0.05, 0.10) and $SmMn_{2-x}Co_xGe_2$ (x=0.05, 0.15) compounds. The present set of entropy values are also similar to other compound such as $Ho_2Fe_{15}Mn_2$ [36] ($-\Delta S_M$ = 2.7 J kg^{-1} K^{-1} at 302 K) and Er_2Fe_{17} [37] ($-\Delta S_M$ = 3.6 J kg^{-1} K^{-1} at 300 K).

The magnetic entropy change, $-\Delta S_M$ (*T, B*) has also been derived from heat calorimetric measurements of the field dependence of the heat capacity using the expression [38-40] (equation 5.4) where *C (T,B)* and *C(T,0)* are the values of the heat capacity measured in field *B* and zero field, respectively. The corresponding adiabatic temperature change, ΔT_{ad} can be evaluated from $-\Delta S_M$ (*T, B*) and the zero field heat capacity data as shown in equation 5.5. Figure 5.43(b) shows the set of heat capacity measurement obtained for $CeMn_2Ge_2$ with B = 0 T, 1 T, 2 T and 5 T. The related peak in specific heat around $T_C^{inter} \sim 318$ K was found to

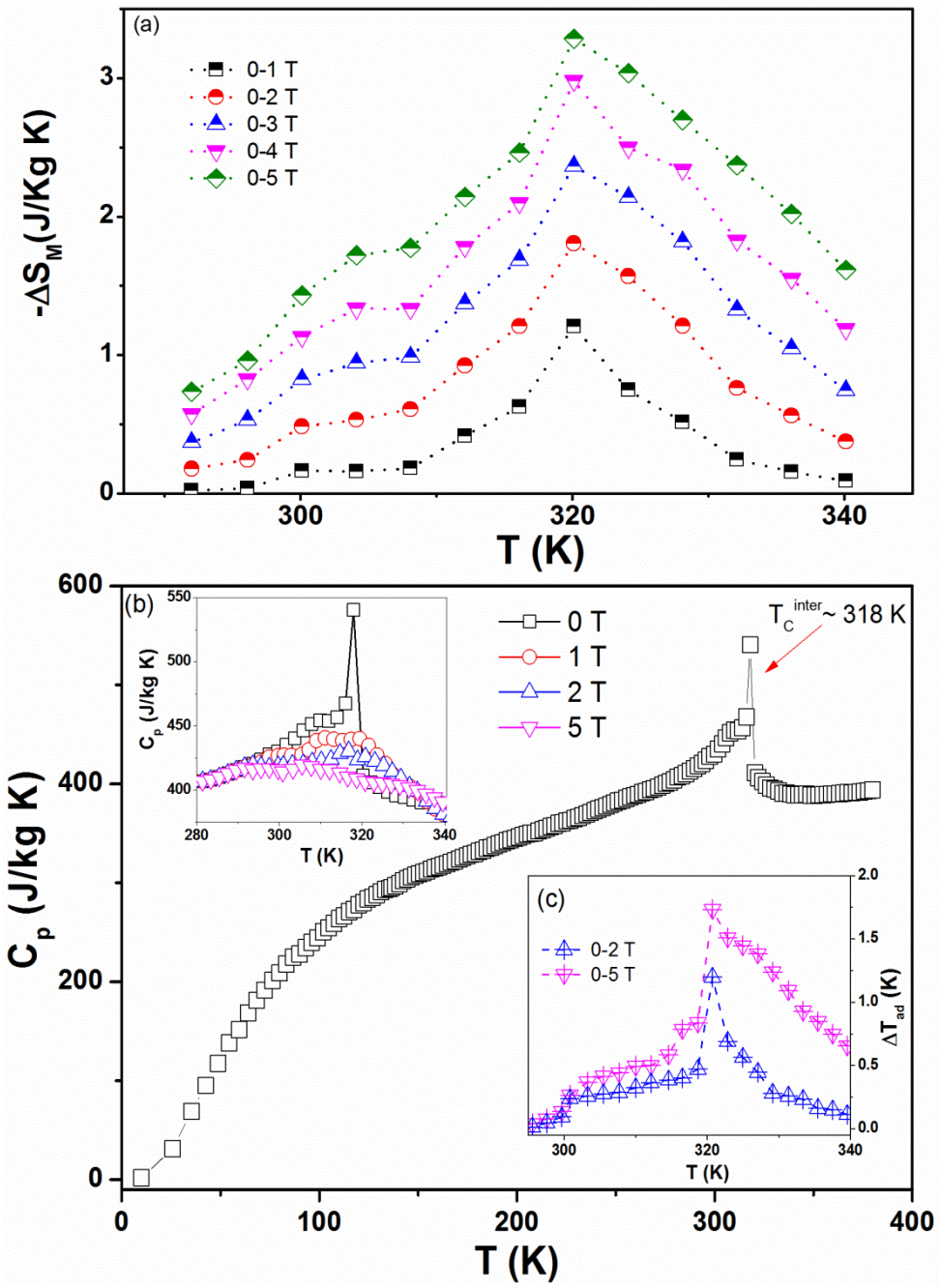

Figure 5.43 (a) Temperature dependence of the isothermal magnetic entropy change $-\Delta S_M$ for $CeMn_2Ge_2$ in the region around the ferromagnetic transition T_C^{inter} as determined from magnetisation measurements. (*b*) The heat capacity of $CeMn_2Ge_2$ as measured over the temperature range 10–340 K in magnetic fields B = 0 T, 1 T, 2 T and 5 T; (*c*) The adiabatic temperature change, ΔT_{ad}^{max}, for the $CeMn_2Ge_2$ compound.

decrease with increasing magnetic field as shown by the upper inset to Figure 5.43(b). The ΔT_{ad} values derived from the specific heat data using equation (4) are shown in Figure 5.43(c). The peak value of the adiabatic temperature change is found to be ΔT_{ad}^{max} = 1.7 K

for ΔB = 0-5 T. Within experimental errors [21, 41, 42], the maximum magnetic entropy change for $CeMn_2Ge_2$ as determined from the heat capacity measurements of $-\Delta S_M^{max}$ ~ 2.9 J kg^{-1} K^{-1} agrees well with the maximum entropy change $-\Delta S_M^{max}$ ~ 3.2 J kg^{-1} K^{-1} determined from the magnetic measurements using the Maxwell relation.

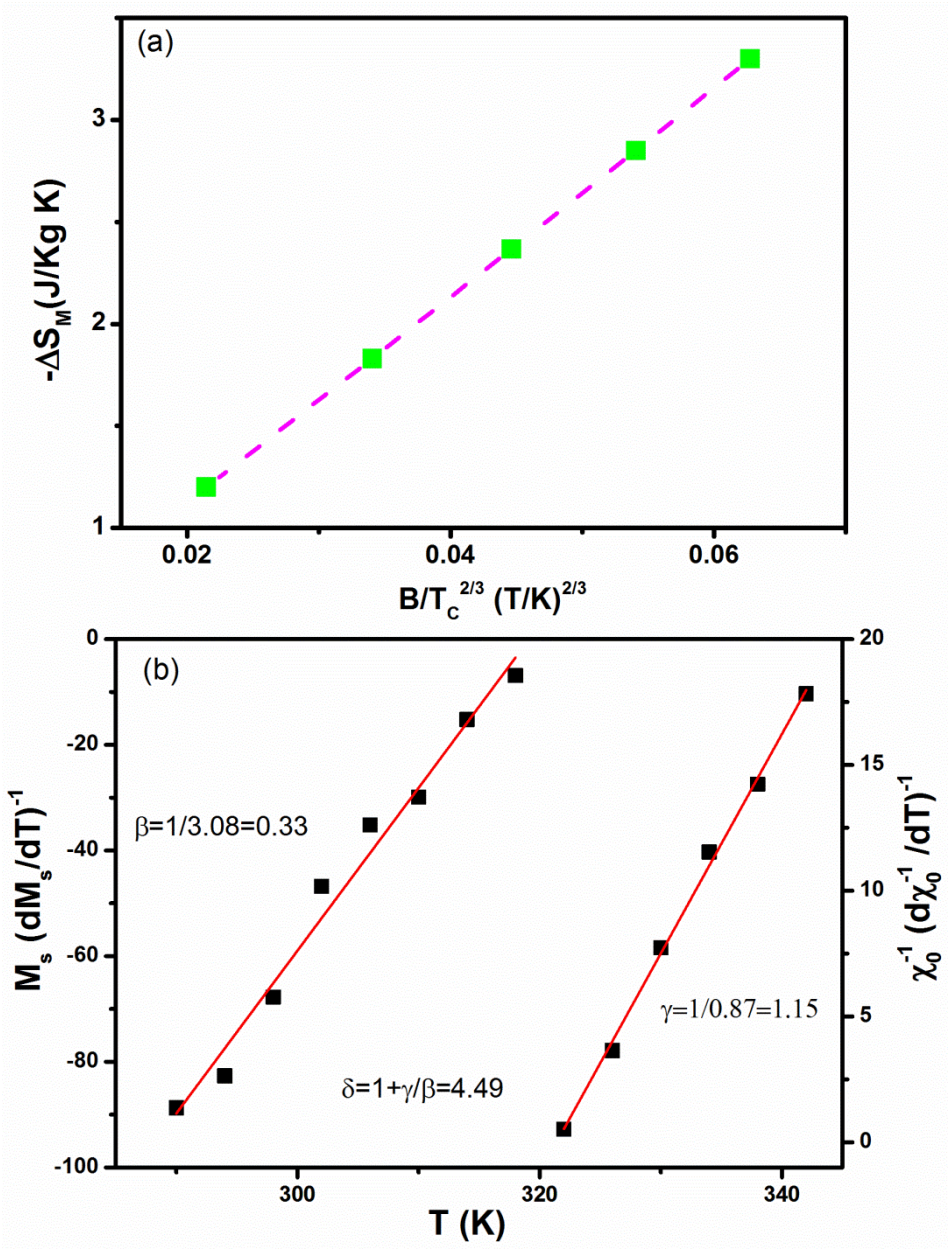

Figure 5.44 (a) Dependence of $-\Delta S_M$ (peak value of the magnetic entropy change at different B values) on the parameter $(B/T_C)^{2/3}$ for $CeMn_2Ge_2$ compound and (b) Kouvel–Fisher plots of $M_S(T)[dM_S/dT]^{-1}$ (left scale) and $\chi_0^{-1}(T)[d\chi_0^{-1}/dT]^{-1}$ (right scale) versus temperature. The lines are fits to the data around T_C as discussed in the text with fits leading to the critical exponent values.

Critical exponent analysis: Mean-field theory predicts that in the vicinity of second-order phase transitions, $-\Delta S_M$ is proportional to $(\mu_0 H/T_C)^{2/3}$ [43, 44]. Figure 5.44(a) shows a graph of $-\Delta S_M$ as a function of $(B/T_C)^{2/3}$ in the region around the transformation at T_C^{inter} ~ 318 K. The linear fit to the data in Figure 5.43(a) clearly demonstrates that the relationship $-\Delta S_M \propto (B/T_C)^{2/3}$ is valid around the transition at T_C^{inter} for $CeMn_2Ge_2$. According to the conventional static scaling law, the critical properties of a second-order magnetic transition can be described by critical exponents β, γ and δ derived from magnetization measurements around the transition temperature. On applying these standard approaches, as shown by the fits to the Kouvel–Fisher plots of $M_S(T)[dM_S/dT]^{-1}$ and $\chi_0^{-1}(T)[d\chi_0^{-1}/dT]^{-1}$ versus temperature in Figure 5.44(b), the critical exponents around T_C in $CeMn_2Ge_2$ have been determined to be β = 0.33±0.03 and γ = 1.15±0.22. Hence, on applying the relationship δ = 1 + γ/β, with β = 0.33, γ = 1.15, the critical exponent δ = 1 + γ/β = 4.49±0.25. The critical exponents derived from the analyses are similar to the theoretical values - β = 0.365, γ = 1.386 and δ = 4.80 - based on the three-dimensional Heisenberg model corresponding to short range interactions [45]. Thus, the critical behaviour analysis in the vicinity of T_C^{inter} indicates that the magnetism of the $CeMn_2Ge_2$ compound is governed by short range interactions.

5.3.4 Conclusion

The total magnetic moment of $CeMn_2Ge_{2-x}Si_x$ compounds at base temperature ~ 5 K is found to decrease with increasing Si content. This behaviour indicates that contraction of the unit cell leads to a reduction in the Mn moment value (e.g. M_{Total} ~ 3.16 μ_B for x = 0.0 and M_{Total} ~ 2.02 μ_B for x = 2.0) and agrees well with the tendency detected for both $LaMn_2Si_2$ and $LaMn_2Ge_2$ systems where M_{Total} is found to decrease with decrease in the lattice parameter *a* [46]. First principles calculations on $LaMn_2Si_2$ and $LaMn_2Ge_2$ [46] suggest that the reduction

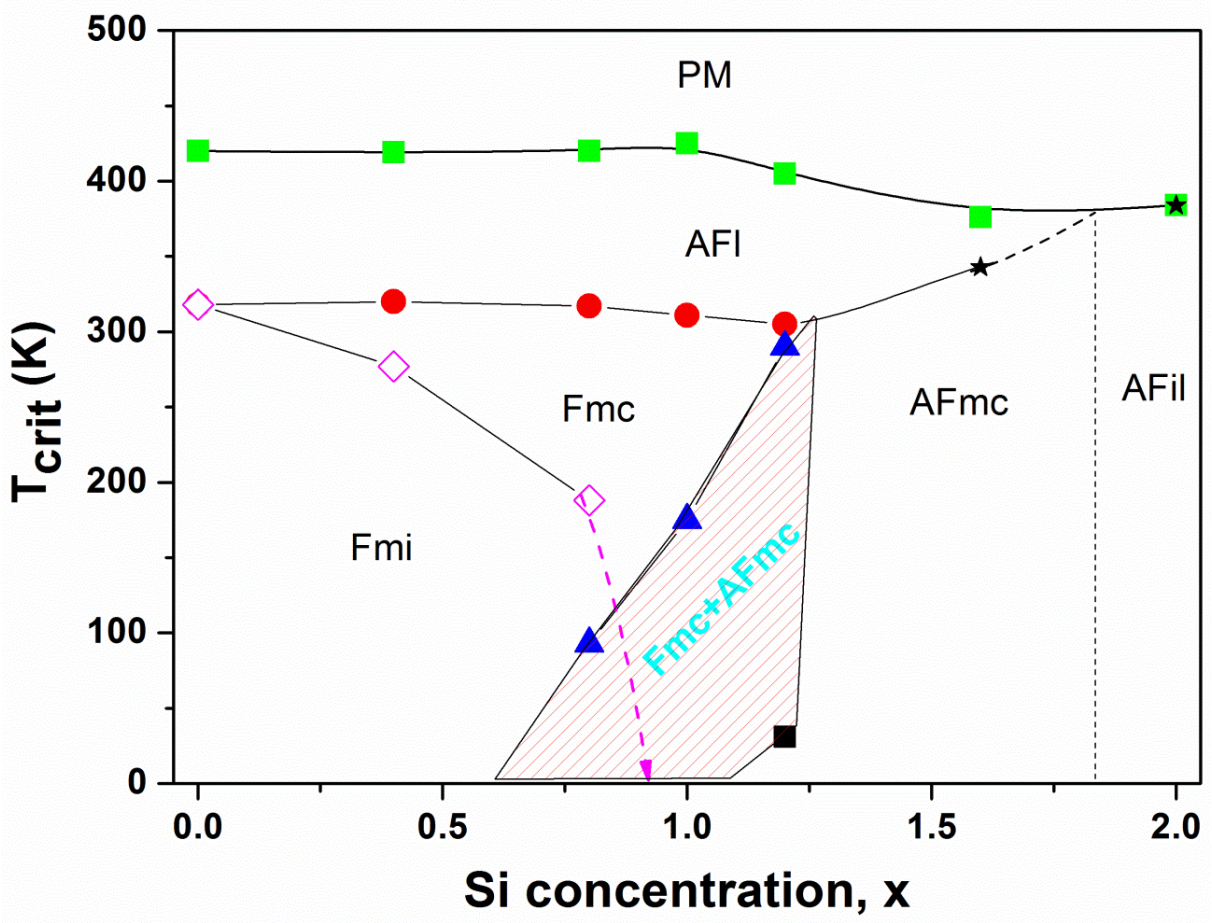

Figure 5.45 Magnetic phase diagram of $CeMn_2Ge_{2-x}Si_x$ as a function of Si content. As discussed in the text, T_N^{intra} (green squares) defines the transition from paramagnetism to intralayer antiferromagnetic ordering within the (001) Mn layers (AFl) (except x=2.0 which exhibits AFil type antiferromagnetic order); T_C^{inter} (red circles) defines the transition from AFl to a canted spin structure (Fmc); Tc/c (open pink diamond) defines the transformation temperature of the magnetic structure from Fmc to a conical configuration Fmi type, T_N^{inter} (blue triangle) denotes the transition to the mixed region with co-existence of the antiferromagnetic canted structure AFmc and the Fmc structure. The dashed lines indicate trends in the data. As discussed in the text, the vertical dashed line located around Si concentration of x=1.85 is used as a tentative guide to the boundary between the AFmc and AFil regions.

of Mn moments in $LaMn_2Si_2$ (a = 4.11 Å) compared with $LaMn_2Ge_2$ (a = 4.19 Å) depends primarily on the Mn–Mn distances (stronger Mn–Mn hybridization due to shorter Mn–Mn distance leads to a smaller local Mn moment [18]). However the larger hybridization strength of Si–Mn in $LaMn_2Si_2$ than Ge–Mn in $LaMn_2Ge_2$ also plays a role. In the present study, the reduction of Mn moments in the $CeMn_2Ge_{2-x}Si_x$ compound with increasing Si content can be

ascribed to these two factors: (1) decrease of the Mn–Mn spacing (at room temperature ~ 300 K, d_{Mn-Mn} = 2.9306 Å at $CeMn_2Ge_2$ to d_{Mn-Mn} = 2.8307 Å at $CeMn_2Si_2$) and (2) increase of Si–Mn hybridization strengths compared with Ge–Mn hybridization [22], similar behaviour to that of $PrMn_2Ge_{2-x}Si_x$ [23].

The temperature dependence of the $CeMn_2Ge_{2-x}Si_x$ lattice parameters demonstrates an anomaly in thermal expansion (as shown in Figure 5.36) and is accompanied with appearance of the interlayer Mn–Mn interactions. This behaviour agrees well with others system as $PrMn_{2-x}Fe_xGe_x$ and $PrMn_2Ge_{2-x}Si_x$ where it is found that the interlayer Mn–Mn interactions rather than the intralayer Mn–Mn interactions, play the major role in the anomalous thermal expansion [26]. The present findings have enabled us to construct the magnetic phase diagram for the $CeMn_2Ge_{2-x}Si_x$ system as shown in Figure 5.45 with more detail now available compared with the previous study [16]. The shaded region in Figure 5.45 indicates the region of co-existence of the Fmc and AFmc phases. The co-existence of different magnetic states at the same temperature is considered to be related to the non-random variation of site concentrations of Si and Ge, and depends sensitively on the Mn–Mn distances in this system; this in turn leads to differences in the local environments throughout the sample [7].

As expected, the magnetic states at room temperature have been modified by Si substitution due to the contraction of the unit cell indicated in Figure 5.36. Samples with $x \geq 1.4$ where the lattice constant a is below a_{crit1} ~ 4.06 Å are antiferromagnetic at room temperature with no ferromagnetic order evident over the entire temperature range, whereas samples of Si content $x \leq 0.4$ are ferromagnetic at room temperature. It is interesting to note that samples with Si concentrations in the range x ~ 1.0–1.2 correspond approximately to the region of co-

existence of the AFmc and Fmc phases around room temperature as shown in Figure 5.45. A smaller unit cell in an antiferromagnetic state than in a ferromagnetic state (as indicated by the deviation from linear behaviour in the composition dependence of the lattice constants at room temperature; Figure 5.36), can be understood in terms of the difference in magnetic states at room temperature for these samples and in turn reflects the large contribution from magnetic effects to thermal expansion [26].

The compounds with rich Si concentration $x \geq 1.85$ have a relatively simple magnetic behaviour, transforming from paramagnetism at high temperature to AFil. By comparison, Ge-rich samples ($x = 2.0$) successively exhibit two magnetic states as AFl and Fmi when cooling from the high temperature paramagnetic phase. The Fmi structure was eliminated when Si concentration $x \geq 1.0$ and co-existence of AFmc and Fmc is detected for $CeMn_2Ge_{2-x}Si_x$ in the intermediate Si concentration range $0.6 < x < 1.25$. This co-existence reflects the incompleteness of the phase transition from Fmc to AFmc with decreasing temperature And agrees well with calculations of the electronic structure of the two magnetic states (AFmc and Fmc) carried out using a spin polarized localized density approximation (LSDA) in the framework of density functional theory (DFT). These calculations show that changes to the magnetic energy of the two states are caused directly by modification of the lattice with temperature [3]. Moreover, critical properties study on the second-order ferromagnetic transition of $CeMn_2Ge_2$ demonstrate that the magnetic interactions around T_C^{inter} can be described with the three dimensional Heisenberg model corresponding to short range interactions. Overall this investigation has demonstrated that, as expected, the Si concentration plays the dominant role in tuning the magnetic structure and properties of the $CeMn_2Ge_{2-x}Si_x$ compounds.

References

[1] S. Siek, A. Szytuła, and J. Leciejewicz, Solid State Communications 39 (1981) 863.
[2] B. Emre, I. Dincer, Y. Elerman, and S. Aksoy, Solid State Sciences 22 (2013) 1.
[3] J. L. Wang, L. Caron, S. J. Campbell, S. J. Kennedy, M. Hofmann, Z. X. Cheng, M. F. Md Din, A. J. Studer, E. Brück, and S. X. Dou, Physical Review Letters 110 (2013) 217211.
[4] J. L. Wang, S. J. Campbell, M. F. Md Din, S. J. Kennedy, and M. Hofmann, physica status solidi (a) 211 (2014) 1092.
[5] I. Dincer, Y. Elerman, A. Elmali, H. Ehrenberg, H. Fuess, E. Duman, and M. Acet, Journal of Magnetism and Magnetic Materials 248 (2002) 268.
[6] I. Dincer, A. Elmali, Y. Elerman, H. Ehrenberg, H. Fuess, and O. Isnard, Journal of Physics: Condensed Matter 16 (2004) 2081.
[7] J. L. Wang, S. J. Kennedy, S. J. Campbell, M. Hofmann, and S. X. Dou, Phys. Rev. B 87 (2013) 104401.
[8] R. Welter, G. Venturini, D. Fruchart, and B. Malaman, Journal of Alloys and Compounds 191 (1993) 263.
[9] J L Wang, S J Campbell, A J Studer, M Avdeev, R Zeng, and S. X. Dou, Journal of Physics: Condensed Matter 21 (2009) 124217.
[10] J. H. V. J. Brabers, K. H. J. Buschow, and F. R. de Boer, Physical Review B 59 (1999) 9314.
[11] R. Welter and B. Malaman, Journal of Alloys and Compounds 354 (2003) 35.
[12] M. F. M. Din, J. L. Wang, S. J. Campbell, R. Zeng, W. D. Hutchison, M. Avdeev, S. J. Kennedy, and S. X. Dou, Journal of Physics D: Applied Physics 46 (2013) 445002.
[13] M. Hofmann, S. J. Campbell, K. Knorr, S. Hull, and V. Ksenofontov, Journal of Applied Physics 91 (2002) 8126.
[14] P. Kumar, K. G. Suresh, A. K. Nigam, A. Magnus, A. A. Coelho, and S. Gama, Physical Review B 77 (2008) 224427.
[15] M. F. Md Din, J. L. Wang, S. J. Campbell, A. J. Studer, M. Avdeev, S. J. Kennedy, Q. F. Gu, R. Zeng, and S. X. Dou, Applied Physics Letters 104 (2014) 042401.
[16] G. Liang and M. Croft, Phys. Rev. B 40 (1989) 361.
[17] G. Venturini, B. Malaman, and E. Ressouche, Journal of Alloys and Compounds 240 (1996) 139.
[18] R. Welter, G. Venturini, E. Ressouche, and B. Malaman, Journal of Alloys and Compounds 218 (1995) 204.
[19] G. Venturini, B. Malaman, and E. Ressouche, Journal of Alloys and Compounds 237 (1996) 61.
[20] V. K. Pecharsky and K. A. Gschneidner Jr, Journal of Magnetism and Magnetic Materials 167 (1997) L179.
[21] K. A. GschneidnerJr, V. K. Pecharsky, and A. O. Tsokol, Reports on Progress in Physics 68 (2005) 1479.
[22] L. B. McCusker, R. B. Von Dreele, D. E. Cox, D. Louër, and P. Scardi, Journal of Applied Crystallography 32 (1999) 36.
[23] J. L. Wang, S. J. Campbell, M. Hofmann, S. J. Kennedy, R. Zeng, M. F. M. Din, S. X. Dou, A. Arulraj, and N. Stusser, Journal of Physics: Condensed Matter 25 (2013) 386003.
[24] L. Gelato, J. Appl. Crystallogr. 14 (1981) 151.
[25] S. Di Napoli, A. M. Llois, G. Bihlmayer, and S. Blügel, Physical Review B 75 (2007) 104406.
[26] J. L. Wang, S. J. Campbell, A. J. Studer, M. Avdeev, M. Hofmann, M. Hoelzel, and S. X. Dou, Journal of Applied Physics 104 (2008)
[27] J. L. Wang, S. J. Campbell, A. J. Studer, M. Avdeev, M. Hofmann, M. Hoelzel, and S. X. Dou, Journal of Applied Physics 104 (2008) 103911.

[28] J. L. Wang, S. J. Campbell, M. Hofmann, S. J. Kennedy, M. Avdeev, M. F. Md Din, R. Zeng, Z. X. Cheng, and S. X. Dou, Journal of Applied Physics 113 (2013)
[29] M. Hofmann, S. J. Campbell, and S. J. Kennedy, Journal of Physics: Condensed Matter 12 (2000) 3241.
[30] M. Duraj, R. Duraj, A. Szytuła, and Z. Tomkowicz, Journal of Magnetism and Magnetic Materials 73 (1988) 240.
[31] M. Hofmann, S. J. Campbell, and A. V. J. Edge, Physical Review B 69 (2004) 174432.
[32] I. Dincer, Y. Elerman, A. Elmali, H. Ehrenberg, and G. André, Journal of Magnetism and Magnetic Materials 313 (2007) 342.
[33] K. A. Gschneidner Jr, Y. Mudryk, and V. K. Pecharsky, Scripta Materialia 67 (2012) 572.
[34] H. Feng Xia, S. Bao Gen, S. Ji Rong, C. Zhao Hua, and Z. Xi Xiang, Journal of Physics: Condensed Matter 12 (2000) L691.
[35] I. Dincer and Y. Elerman, Journal of Magnetism and Magnetic Materials 326 (2013) 50.
[36] J. L. Wang, A. J. Studer, S. J. Kennedy, R. Zeng, S. X. Dou, and S. J. Campbell, Journal of Applied Physics 111 (2012)
[37] X. X. Zhang, F. W. Wang, and G. H. Wen, Journal of Physics: Condensed Matter 13 (2001) L747.
[38] V. K. Pecharsky and J. K. A. Gschneidner, Journal of Applied Physics 86 (1999) 565.
[39] B. Ekkes, Journal of Physics D: Applied Physics 38 (2005) R381.
[40] K. A. Gschneidner Jr and V. K. Pecharsky, International Journal of Refrigeration 31 (2008) 945.
[41] V. K. Pecharsky and J. K. A. Gschneidner, Physical Review Letters 78 (1997) 4494.
[42] J. L. Wang, S. J. Campbell, J. M. Cadogan, A. J. Studer, R. Zeng, and S. X. Dou, Applied Physics Letters 98 (2011) 232509.
[43] H. Oesterreicher and F. T. Parker, Journal of Applied Physics 55 (1984) 4334.
[44] J. L. Wang, S. J. Campbell, R. Zeng, C. K. Poh, S. X. Dou, and S. J. Kennedy, Journal of Applied Physics 105 (2009)
[45] S. N. Kaul, Journal of Magnetism and Magnetic Materials 53 (1985) 5.
[46] S. Di Napoli, A. M. Llois, G. Bihlmayer, Bl¨ugel S, M. Alouani, and D. e. H., Phys. Rev. B 70 (2004) 174418.

Chapter 6

THE MAGNETOCALORIC EFFECT AND CRITICAL BEHAVIOUR OF MnCoGe-based ALLOYS

6.1 Substitution of Ge by other Metalloid in MnCoGe Alloy

MnCoGe, as a typical MM′X (M, M′ = transition metal, X = Si, Ge, Sn) compound, possesses magnetic and structural transitions and has been studied for decades [1]. Stoichiometric MnCoGe crystallizes in the hexagonal Ni_2In-type austenite (A) phase, and at about 420 K, in the paramagnetic state, it undergoes a martensitic structural transformation to another paramagnetic, orthorhombic TiNiSi-type martensite (M) [2]. The austenite and the martensite phases have Curie temperatures T_C^A = 273 K and T_C^M = 355 K, respectively, with both phases featuring collinear ferromagnetism [3].

6.1.1 Introduction

In the last few years, there has been a considerable increase in research on near-room-temperature magnetic cooling [4-6]. This new cooling technology, which is expected to supersede the conventional refrigeration technology based on gas compression/expansion, is of special interest because of its considerable socio-economic benefits. Compared to the refrigeration technology based on gas compression/expansion, which is widely used today, magnetic refrigeration is environmentally friendly and more efficient [7, 8]. Magnetic refrigeration is based on the magnetocaloric effect (MCE), which results from the coupling of

a system of magnetic moments with an external magnetic field, resulting in the cooling or heating of the system [9]. Material systems such as LaFeSi [10], NiMnGa [11], MnAsSb [5], and GdSiGe [12] undergo first-order magnetic transitions and have been found to possess a giant MCE. There are some major drawbacks of these material systems, however, which include large thermal and magnetic hysteresis that is detrimental to the refrigerant capacity, making them undesirable for practical applications. Hence, it is imperative to search for materials that exhibit a giant MCE as well as negligible thermal and magnetic hysteresis. One candidate is MnCoGe [13, 14], which undergoes a second-order phase transition as well as a crystallographic phase transition from the low temperature orthorhombic TiNiSi-type to the high temperature hexagonal Ni_2In-type structure [15]. Previously, scientists have managed to achieve a coupling of the magnetic and crystallographic transitions in the MnCoGe material system through substitution of Cr [16] and addition of boron [17] as an interstitial, thereby leading to the attainment of a giant magnetocaloric effect.

An investigation on substituting other metalloids for Ge in $MnCoGe_{1-x}T_x$ compounds (T = Al and Si) has been implemented in this thesis work, and it was found that an appropriate T concentration successfully shifted the structural change and magnetic phase transition into the temperature range of interest, leading to the attainment of a high contribution to the giant magnetocaloric effect (GMCE). Furthermore, the strong dependence on proper tuning for critical behaviour of the phase transition, which was due to the vacancy induced structural and magnetic transition and the field-induced martensitic transformation, acted as a guide to more interesting phenomena related to the substitution for Ge (atomic radius ≈ 1.37 Å) by Al (atomic radius ≈ 1.43 Å) or Si (atomic radius ≈ 1.32 Å) in $MnCoGe_{1-x}T_x$ compounds. It was recently found that $MnCoGe_{1-x}T_x$ provides the best example for control of the temperature window in order to investigate the effects of the structural and magnetic transition on the total

entropy change, providing an excellent vehicle for investigation of the field-induced martensitic transformation in GMCE materials. Thus, in an effort to understand the nature of the magnetic transition in $MnTiGe_{0.97}Al_{0.03}$, critical exponent analysis in the vicinity of the ferromagnetic (FM)–paramagnetic (PM) region [18-20] has been performed. The outcomes revealed that this material undergoes a structural transition at ~ 420 K as well as a second-order ferromagnetic–paramagnetic transition at ~ 350 K. Finally, a temperature dependent neutron diffraction experiment has been performed to clarify whether there is a coupling of the structural transition and the magnetic phase transition.

6.1.2 Experimental and Procedures

Polycrystalline $MnCoGe_{1-x}T_x$ (T = Al and Si; range x = 0-1.0) ingots were prepared by arc melting the appropriate amounts of Mn (99.9%), Ge (99.999%) powder, Co (99.9%), Al (99.9%), and Si (99.999%) chips in an argon atmosphere. During arc melting, a 3% excess of Mn over the stoichiometric amount was added to compensate for the weight loss of Mn. The polycrystalline ingots were melted five times to achieve good homogeneity. The ingots were then wrapped in tantalum foil, sealed in a quartz ampoule, and subsequently annealed at 900 °C for 120 h and then quenched in water at room temperature. The magnetization measurements were carried out using the vibrating sample magnetometer option of a Quantum Design 14 T physical properties measurement system (PPMS) and a Quantum Design magnetic properties measurement system (MPMS) in the temperature range of 100–340 K at applied fields of up to 5 T. For critical exponent study, magnetization isotherms were measured in the temperature range of 290–340 K with an interval of 2 K at applied fields of up to 5 T. The neutron data were collected in the temperature range of 5–340 K

using the Wombat high intensity powder diffractometer at the Open Pool Australian Lightwater (OPAL) reactor with an incident neutron wavelength of λ = 2.4205 Å.

6.1.3 Results and Discussion

6.1.3.1 $MnCoGe_{1-x}Al_x$

Figure 6.1 presents the X-ray diffraction (XRD) patterns of $MnCoGe_{1-x}Al_x$ (x = 0, 0.03, 0.07, 0.10, and 0.1) collected at room temperature. Most of the peaks could be clearly identified

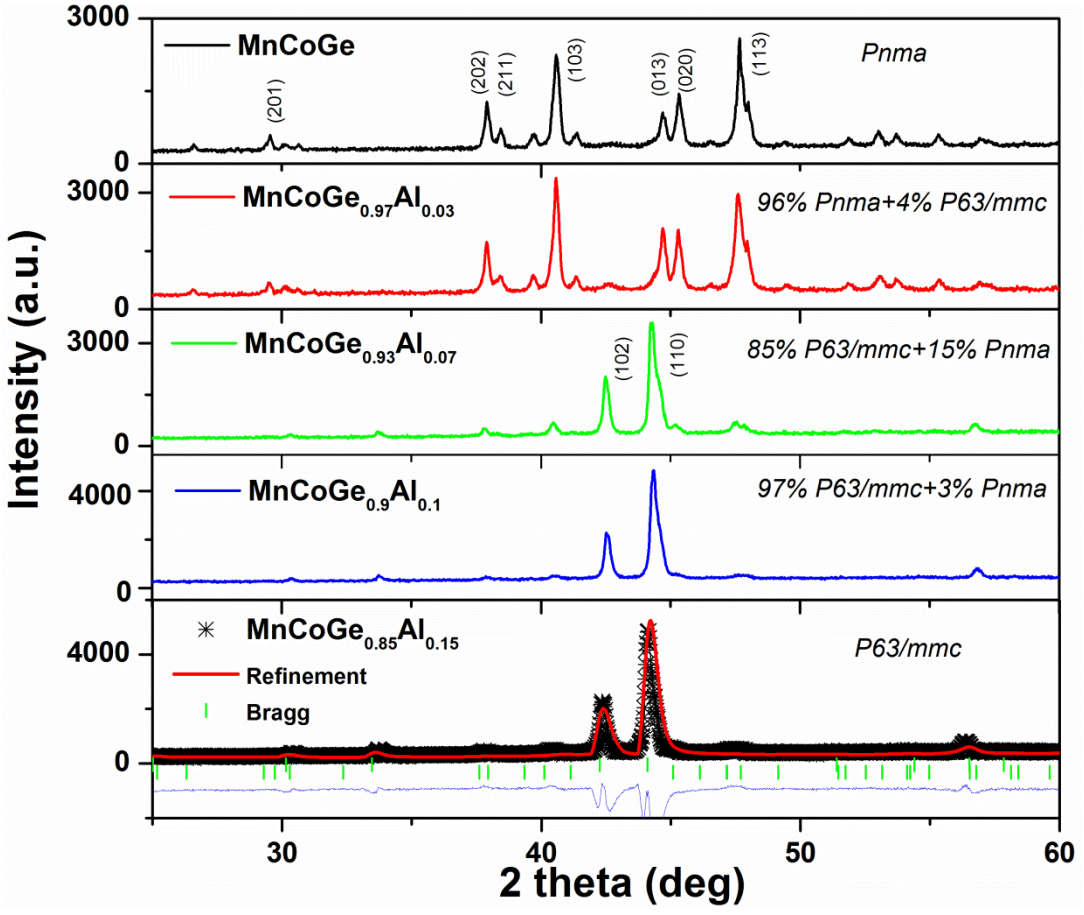

Figure 6.1 Powder XRD patterns of $MnCoGe_{1-x}Al_x$ (x = 0.03, 0.07, 0.1, and 0.15) measured at room temperature. The Miller indices hkl denote the typical Ni_2In-type hexagonal (top) and TiNiSi-type orthorhombic (bottom) structures. The refined pattern at the bottom includes the experimental and calculated results, and their difference is presented for the sample with x = 0.15.

with the TiNiSi-type structure (orthorhombic; space group *Pnma*) for x ≤ 0.03 and the Ni_2In-type structure (hexagonal, space group *P63/mmc*) for x > 0.03. It can be seen that the crystal structure changes from the coexistence of TiNiSi-type and Ni_2In-type structures to the single Ni_2In-type structure with the substitution of Al for Ge atoms. This indicates that the martensitic transformation temperatures of the two series of alloys decrease from higher temperature down to lower temperature. Increasing Al substitution for Ge can effectively change the phase stability of MnCoGe compounds. From refinement analysis, as shown in Figure 6.1, the pattern for x = 0.03 can be indexed as a TiNiSi-type orthorhombic structure, mixed with a small amount of hexagonal phase (4 ± 0.2 wt%). For the sample with x = 0.07, the ratio of hexagonal phase increases, and a mixed ratio of orthorhombic (15.0±0.2 wt%) and hexagonal (85.0±0.11 wt%) phase was found. The other samples ($x \geq 0.07$) are almost single hexagonal phase with Ni_2In-type structure (x = 0.1; 97.4 ± 0.03 wt%, x = 0.15; 99.3 ± 0.02 wt%), indicating that the structural transformation temperatures, T_{str}, of these samples are above room temperature. These results illustrate that the fraction of hexagonal austenite at room temperature increases as the Al-doping level increases. In other words, the substitution of Al for Ge tends to maintain Ni_2In-type austenite and lower the T_{str}.

In order to determine the transition temperature and the nature of the transition, temperature dependent magnetization (M–T curves) under a low field of 0.01 T and differential scanning calorimetry (DSC) measurements of $MnCoGe_{1-x}Al_x$ compounds were conducted in the range of 10-600 K, as shown in Figure 6.2. For the compositions with x = 0.00 and 0.03, there is basically no change in the magnetization below the Curie temperature, indicating that the samples' behaviour is different from that in a previous report [21] which they shown the change of magnetization with increase the Co concentration. This difference behaviour is

probably associated with the fact that the annealing temperature for this experiment is not the same as in ref [21].

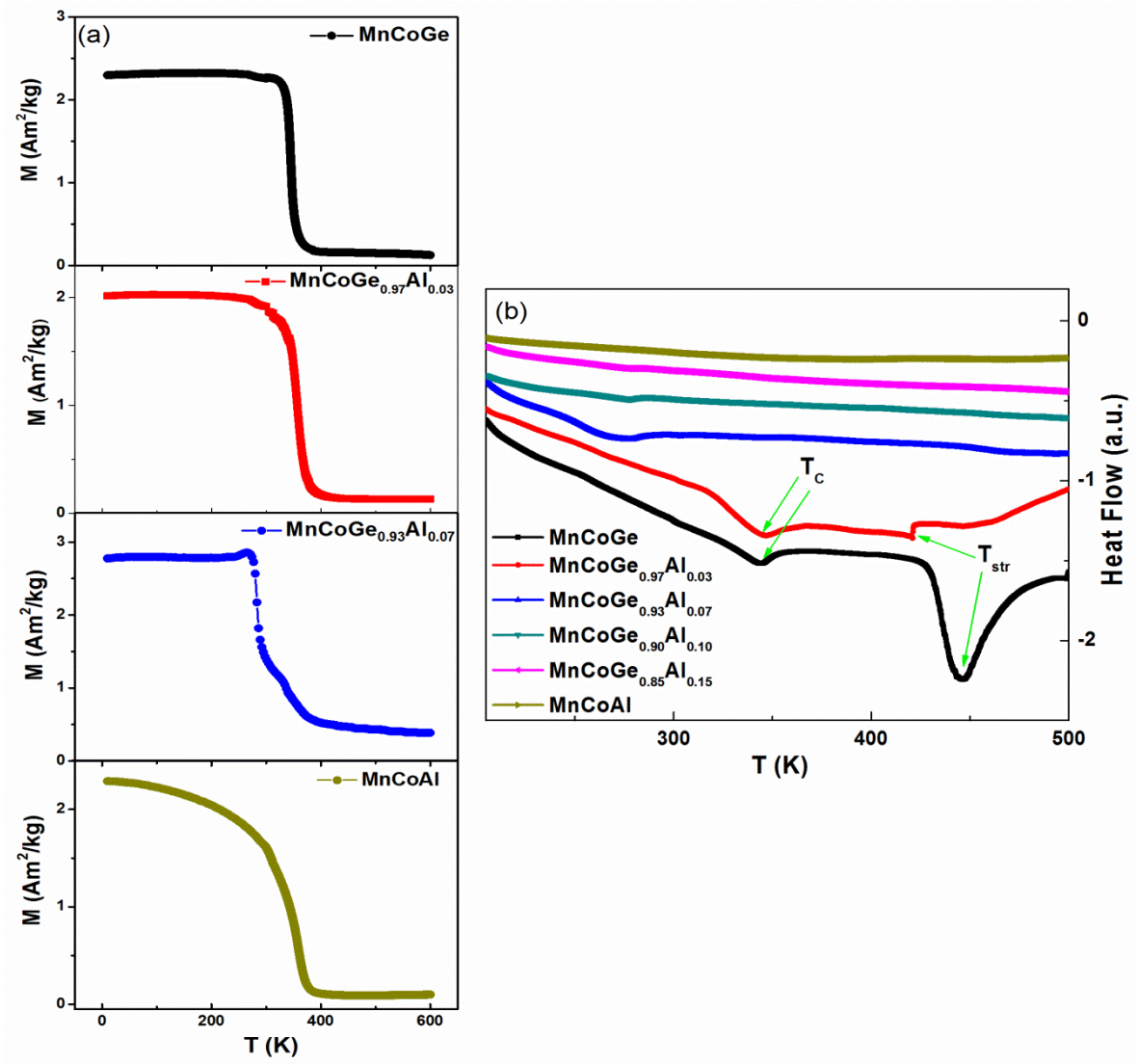

Figure 6.2 (a) M–T curves measured under a magnetic field of 0.01 T for $MnCoGe_{1-x}Al_x$ (x = 0, 0.03, 0.07, and 1.0). (b) DSC curves collected in the range of 250-500 K. The arrows indicate the structural transition and the Curies temperature.

The DSC measurement indicated that the structural transition temperature decreased from T_{str} ≈ 448 K at x = 0 to T_{str} ≈ 420 K at x = 0.03. The $MnCoGe_{0.93}Al_{0.07}$ compound exhibits a visible step-like behaviour in *M-T* curves, indicating the mixed phase, as the temperature of the transition for austenite, T_C^A, is ~ 280 K and that of martensite, T_C^M, is ~ 320 K [22]. This phenomenon is probably attributable to the fact that the MnCoGe-based compounds undergo

a structural transition induced by the replacement of Ge by Al and "temperature change when cooling to low temperature [21]. As for further increasing the Al concentration, MnCoAl has been found in single austenite phase with $T_C^A \approx 380$ K. The DSC measurements agree well with the magnetization measurements as similar transition temperature values were determined by the maxima of the DSC signals (see Figure 6.2(b)).

The magnetization curves obtained for MnCoGe and MnCoAl for fields in the range of B = 0–5 T from the ferromagnetic to the paramagnetic ordering temperatures are shown in Figure 6.3(a) and (b), respectively. These data were obtained for increasing and decreasing fields at 2 K and 4 K intervals spanning a range around the Curie temperature, T_C, thus providing evidence for the lack of magnetic hysteresis loss effects, as is intrinsic to second order magnetic transitions [10]. Moreover, Figure 6.3(c-d) shows the corresponding Arrott plots (M^2 versus B/M) for the x = 0 and 1.0 samples, which are found to exhibit features characteristic of a second order transition for both of the samples. This was particularly confirmed by the absent of negative slope behaviour of the Arrott plot near T_C and denotes a positive sign of the coefficient $c2(T)$ in the Landau expansion of the magnetic free energy [23].

The magnetic entropy change, $-\Delta S_M$, has been determined for the set of $MnCoGe_{1-x}Al_x$ compounds (x = 0, 0.03, 0.07, 0.1, 0.15, and 1.0) from their magnetization curves for both increasing and decreasing field values as functions of temperature and magnetic field (ΔB = 0–5 T). The magnetic entropy change has been derived by applying the standard Maxwell relation [24]:

$$-\Delta S_M(T,H) = \int_0^H \left(\frac{\partial M}{\partial T}\right)_H dH \qquad (6.1)$$

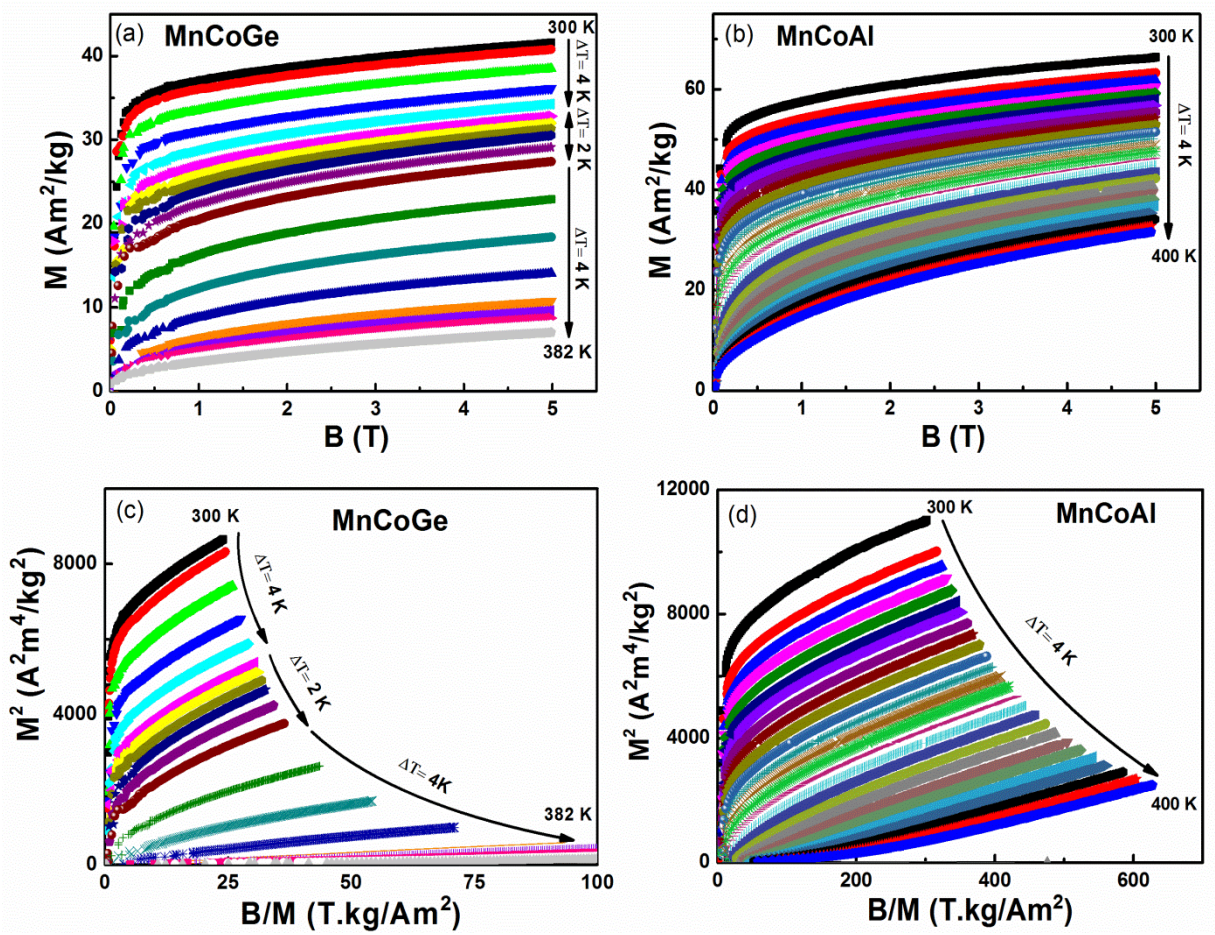

Figure 6.3 Variation in magnetization with applied field of 0-5 T for (a) MnCoGe compound and (b) MnCoAl compound; and (c, d) Arrott plots showing the second order transition type for both compounds.

Although the use of Maxwell's relation for first order systems is still questionable, Caron *et al.* successfully established a method for determining the magnetic entropy change of first order systems by using decreasing field [25]. In this case study, the magnetic entropy change, $-\Delta S_M$, was also evaluated in the decreasing field mode, as is shown by the open symbol curves in Figure 6.4. A comparison of the $-\Delta S_M$ values calculated using increasing and decreasing fields, respectively, shows no difference between these values, which confirms that there is no hysteresis loss occurring in the vicinity of the magnetic transition. With increasing Al content, the temperature corresponding to the maximum $-\Delta S_M$ shifts to lower

temperature first, and then moves to higher temperature, showing the same tendency as the variation of the Curie temperature. The maximal values of the magnetic entropy change are about 4.41, 4.83, 6.23, 7.44, 8.12, and 3.73 $J \cdot kg^{-1}K^{-1}$ for x = 0.00, 0.03, 0.07, 0.1, 0.15, and 1.0, for a field change of 0-5 T, respectively. It is worth pointing out that the compounds

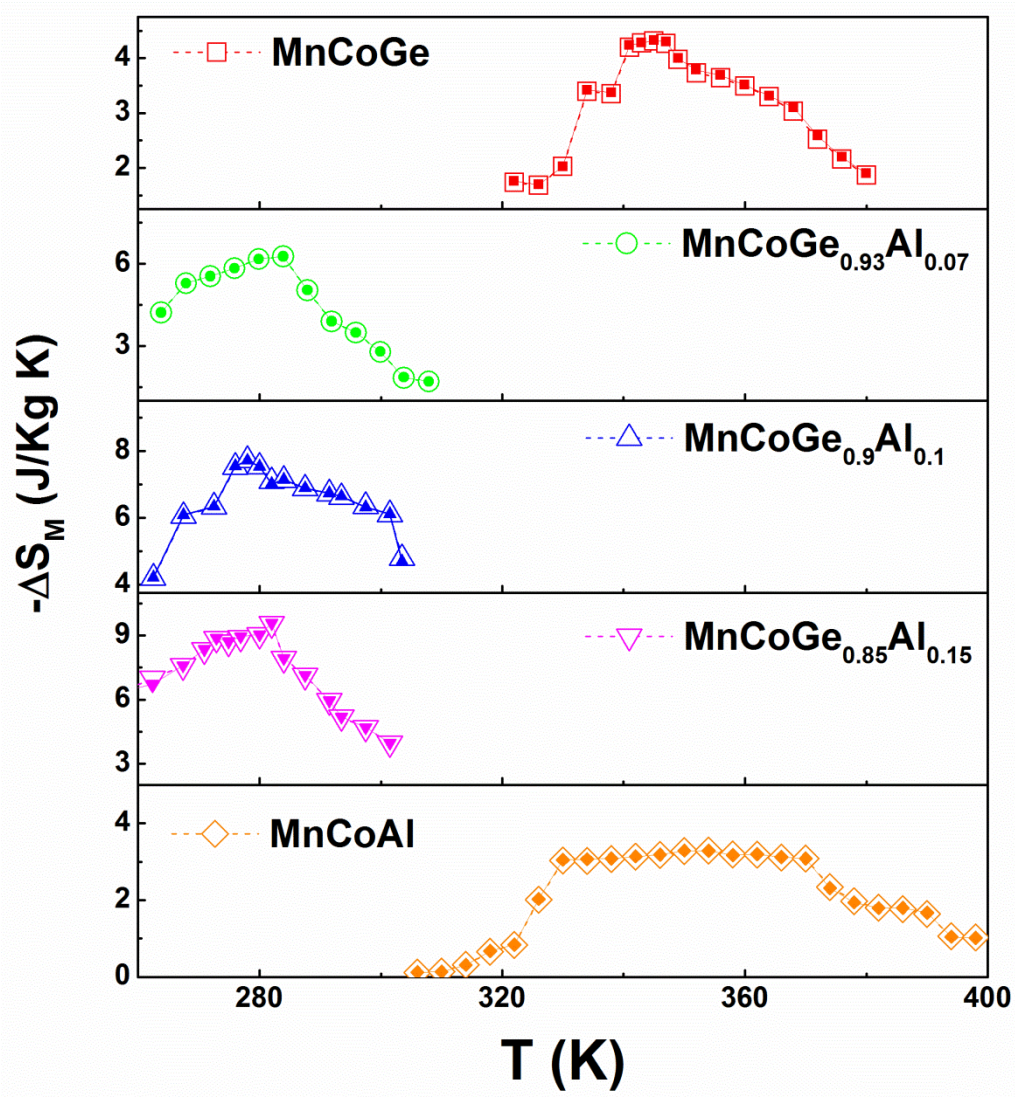

Figure 6.4 Temperature dependence of the isothermal magnetic entropy change, $-\Delta S_M$ (T, H), for $MnCoGe_{1-x}Al_x$ compounds (x = 0, 0.07, 0.1, 0.15, and 1.0) calculated from magnetization isotherms with 0-5 T field change applied. Closed symbols are for increasing and open symbols for decreasing field, respectively.

with high Al content exhibit larger magnetic entropy change than those with low Al content, apart from x = 1.0. The reason can be explained in terms of the effects of the structural variations and the change of the magnetization on the magnetic entropy change. As is well

known for Mn-Co-based compounds, the saturation magnetization of the compounds decreases with increasing Al content [21] for concentrations $x > 0.15$. At low Al content, the increase in the magnetic entropy change in the Al-substituted compounds is probably associated with the structural change from TiNiSi-structure to Ni_2In-structure. On the other hand, for high Al content, the reduced magnetic entropy change may be attributed to the decrease in the magnetization.

In an effort to further clarify the nature of the FM – PM phase transition, an analysis of the critical behaviour near T_C for $MnCoGe_{0.97}Al_{0.03}$ compound was performed. The isothermal magnetization versus the applied field around T_C has been measured using intervals of 4 K and 2 K, as shown in Figure 6.5. A plot of B/M versus M^2, known as the standard Arrott plot, is shown in Figure 6.6 for the temperatures in the vicinity of T_C.

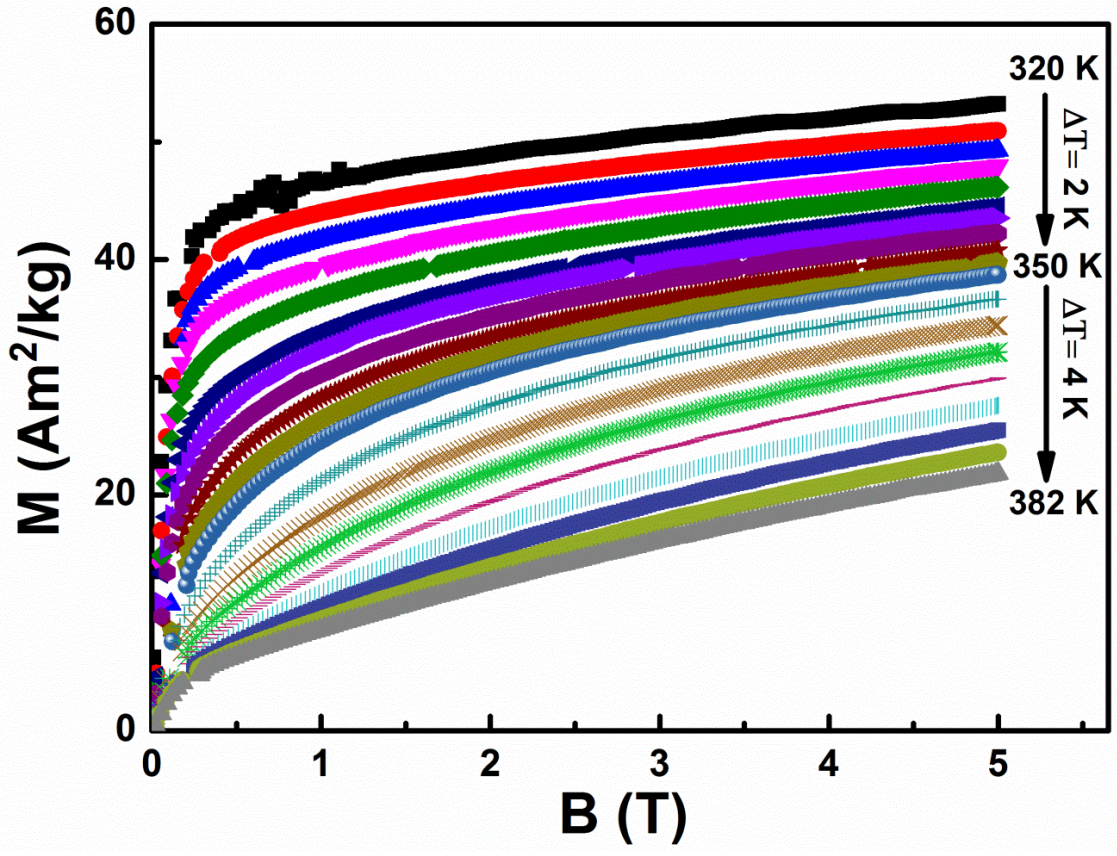

Figure 6.5 Isothermal magnetization curves for $MnCoGe_{0.97}Al_{0.03}$ compound in the vicinity of $T_{C.}$

According to the criterion proposed by Banerjee [26], the order of magnetic transition can be determined from the slope of the isotherm plot. If the B/M versus M^2 curves show a negative slope, the transition is first order, while a positive slope corresponds to a second order transition. For the $MnCoGe_{0.97}Al_{0.03}$ compound, the always positive slope of the B/M, versus M^2 curves throughout the transition temperature range indicates that the phase transition is second order. This result is consistent with the absence of thermal and magnetic hysteresis in the vicinity of the PM – FM transition as discussed, thereby confirming the second order

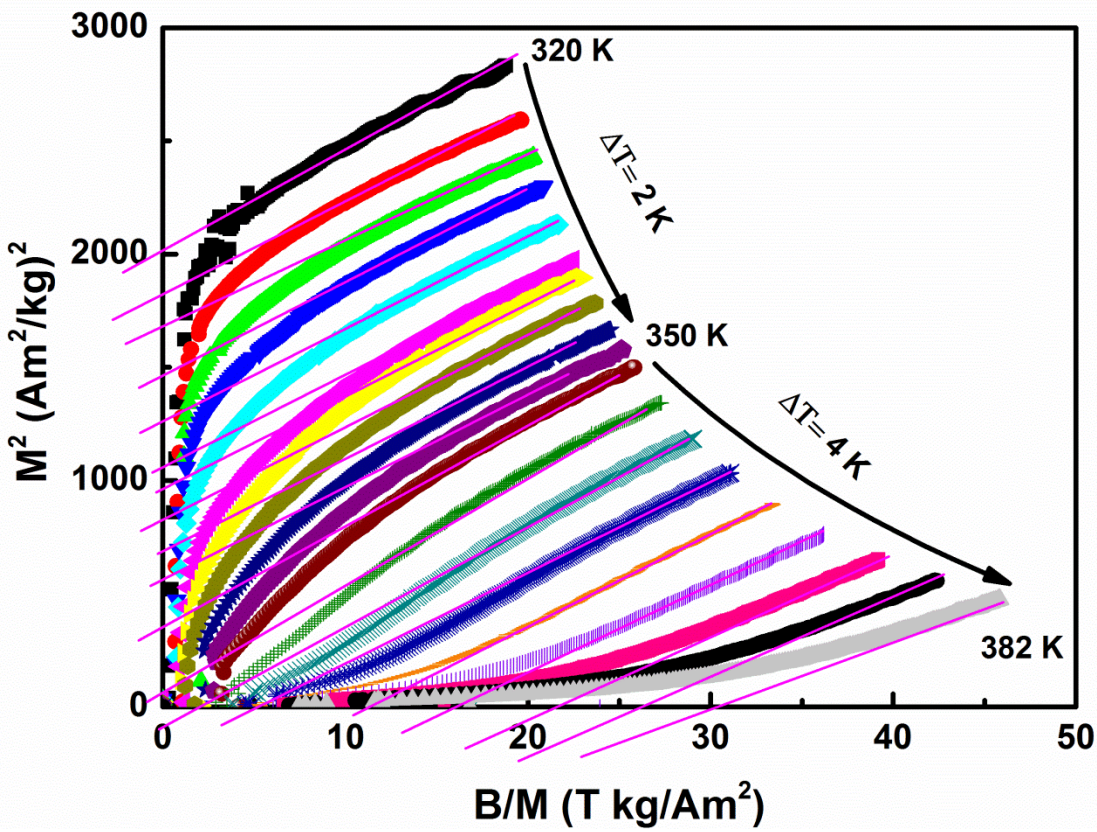

Figure 6.6 Arrott plots (M^2 vs. B/M) at temperatures in the vicinity of T_C for $MnCoGe_{0.97}Al_{0.03}$ compound.

nature of this transition. The scaling hypothesis postulates that a second order magnetic phase transition near T_C is characterized by a set of critical exponents, namely, β, γ, and δ [27]. In this work, different methods have been used to investigate the critical behaviour of $MnCoGe_{0.97}Al_{0.03}$ compound, namely, modified Arrott plots (MAPs), the Kouvel-Fisher

method, critical isotherm analysis, and the the Widom scaling relation. The first method used to calculate the critical exponents is the MAPs method, which is based on the Arrott-Noakes equation of state [27]. Quantitative fits are made to the Arrott plots using the following equations [28].

$$M_S(T) = \lim_{H\to 0}(M) = M_0\,(-\varepsilon)^{\beta}, \varepsilon < 0 \tag{6.2}$$

$$\chi_0{}^{-1}(T) = \lim_{H\to 0}(H/M) = (h_0/M_0)\varepsilon^{\gamma}, \varepsilon > 0 \tag{6.3}$$

where M_0 and h_0 are constants and ε (= (T-T_C)/T_C) is the reduced temperature. Initial values of β and γ are selected, and then a plot of $M^{1/\beta}$ versus $(B/M)^{1/\gamma}$ is obtained. The spontaneous magnetisation, M_S, is then determined from the intersection of the linearly extrapolated curve with the $M^{1/\beta}$ axis. It is imperative to note that only the high field linear region is used for the analysis because MAPs tend to deviate from linearity at low field due to the mutually misaligned magnetic domains [29]. Next, M_S is plotted as a function of temperature. To determine the inverse initial magnetic susceptibility, $\chi_0{}^{-1}(T)$, a similar procedure is used in conjunction with the $(B/M)^{1/\gamma}$ axis. The values of $\chi_0{}^{-1}(T)$ and M_S(T) are plotted as a function of temperature in Figure 6.7 and these plots are then fitted with Equations (6.2) and (6.3), thus obtaining values of β and γ. These new critical exponent values are then used to construct new MAPs. These steps are repeated until the iterations converge to the optimum β, γ, and T_C values. Using Equations (6.2) and (6.3), the MAPs shown in Figure 6.7 yielded critical parameters β = 0.44 and γ = 0.83.

The Kouvel-Fisher (KF) method, which makes use of Equations (6.4) and (6.5) shown below, is a more accurate way of determining the critical exponents β and γ [29].

$$\frac{M_S(T)}{\frac{dM_S(T)}{dT}} = \frac{T-T_C}{\beta} \tag{6.4}$$

$$\frac{\chi_0^{-1}(T)}{d\chi_0^{-1}(T)dT} = \frac{T-T_C}{\gamma} \tag{6.5}$$

According to Equations (6.4) and (6.5), plotting $M_S(T)[dM_S/dT]^{-1}$ and $\chi_0^{-1}(T)[d\chi_0^{-1}/dT]^{-1}$ versus temperature yields straight lines with slopes of 1/β and 1/γ, respectively, as shown in Figure 6.7. The value of T_C is obtained from the intercepts on the x-axis. The critical exponents β, γ, and δ, as well as T_C, obtained using the Kouvel-Fisher method are β = 0.44, γ = 0.83, δ = 2.89, and T_C = 342 K. A comparison of the critical exponents β and γ obtained using the MAPs and those obtained using the KF method reveals that these values match extremely well. The value of the critical component δ can be determined directly from the critical isotherm $M(T_C, H)$ according to Equation (6.6) below.

$$M_{T_C} = DH^{1/\delta}, \varepsilon = 0, T = T_C \tag{6.6}$$

Figure 6.8 shows the magnetic field dependence of the magnetization at T_C = 275 K for the $Mn_{0.94}Ti_{0.06}CoGe$ alloy. The inset shows the critical isotherm on a log – log scale. From Equation (6.6), a plot of log (M) versus log (H) is expected be a straight line with slope 1/δ. The obtained δ value from the critical isotherm is 2.89. Another way of obtaining the critical exponent δ is by using the Widom scaling relation shown in Equation (6.7):

$$\delta = 1 + \frac{\gamma}{\beta} \tag{6.7}$$

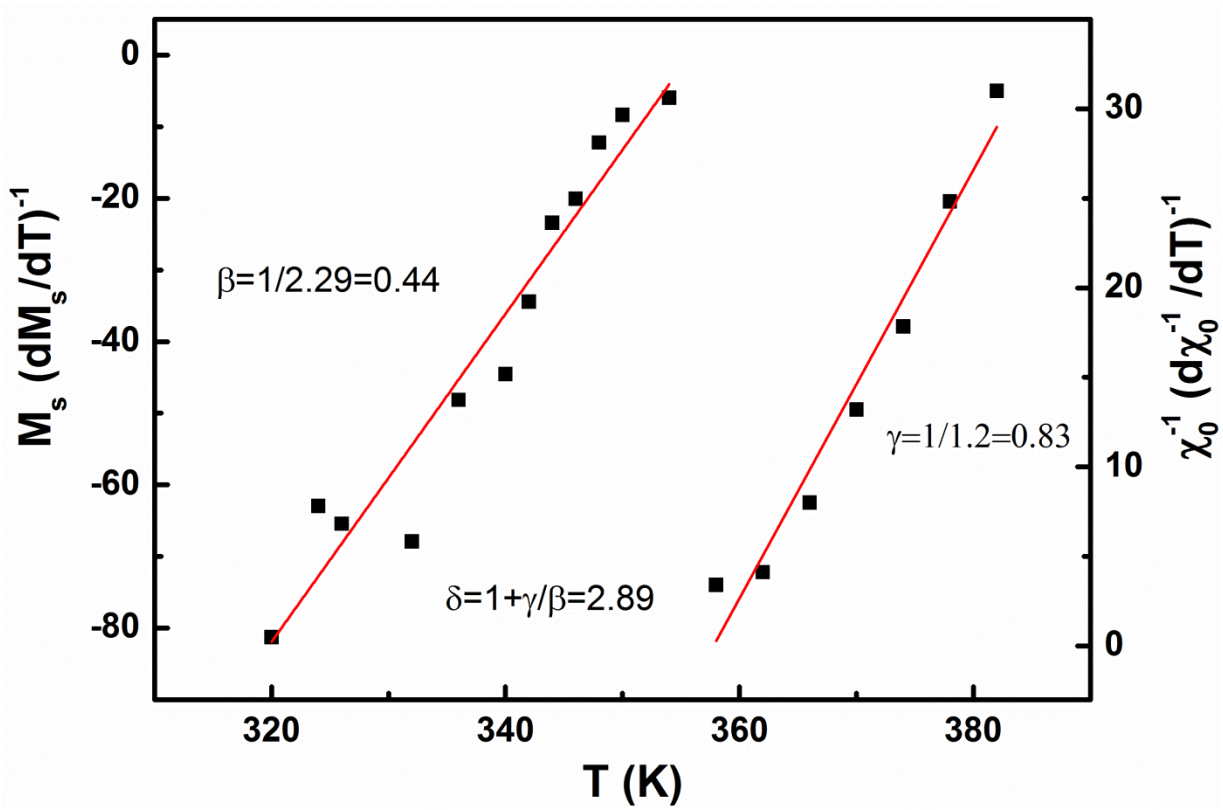

Figure 6.7 Kouvel-Fisher plot for the spontaneous magnetization $M_S(T)$ and the inverse initial susceptibility $\chi_0^{-1}(T)$. (Solid lines are fitted to Equations (6.4) and (6.5).)

Using Equation (6.6) and the critical parameters β and γ obtained using the MAPs and those obtained using the Kouvel-Fisher method, the deduced δ values are 2.92 and 2.89, respectively. Thus, the Widom scaling relation has confirmed the reliability of the critical exponents deduced from the experimental data. The reliability of the calculated exponents β and γ can be confirmed by using the scaling theory. In the critical region, according to the scaling theory, the magnetic equation of state can be written as:

$$M\,(H,\,\varepsilon) = \varepsilon^{\beta} f_{\pm}\,(H\,/\,\varepsilon^{\beta+\gamma}) \tag{6.8}$$

Where ε is the reduced temperature, $(T–T_C)/T_C$, and f_+ and f_- are regular analytical functions above and below T_C, respectively. Using β and γ obtained from the Kouvel-Fisher method, the plots of M/ε^{β} versus $H/\varepsilon^{(\beta+\gamma)}$ (shown in Figure 6.9) yield two universal curves, one for

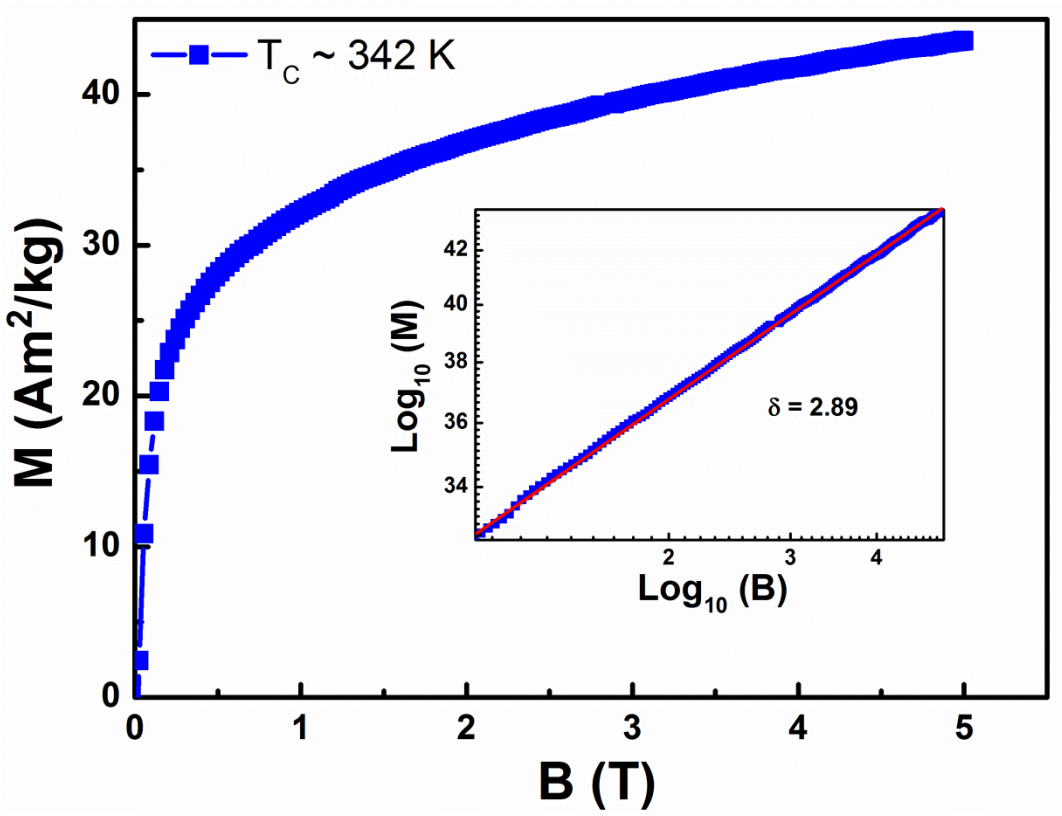

Figure 6.8 Critical isotherm analysis at T_C of the $MnCoGe_{0.97}Al_{0.03}$ sample. The inset shows the same plot on the log – log scale (with the solid line a linear fit to Equation (6.6)).

temperatures above T_C and the other one for temperatures below T_C, in agreement with the scaling theory. This therefore confirms that the obtained values of the critical exponents as well as the T_C are reliable and in agreement with the scaling hypothesis.

It is well accepted that the order parameter of the phase transition around the magnetic transition temperature is fluctuating on all available length scales, and those fluctuations smear out the microscopic details of the interactions in the continuous phase transition system [30]. The mean-field interaction model for long range ordering has theoretical critical exponents of $\beta = 0.5$, $\gamma = 1.0$, and $\delta = 3.0$ [31], while the theoretical values based on the three dimensional Heisenberg model corresponding to short range interactions are $\beta = 0.365$, $\gamma = 1.386$, and $\delta = 4.80$ [32]. The δ, β, and γ values derived for the $MnCoGe_{0.97}Al_{0.03}$ compound are close to the mean-field values, thus indicating that long range interactions dominate the

critical behaviour around T_C in this compound. Thus, the critical behaviour analysis in the vicinity of T_C demonstrates that the magnetism of the $MnCoGe_{0.97}Al_{0.03}$ compound is governed by long range interactions, which is in agreement with the linear fit to the data, which clearly also demonstrates that the relationship $\Delta S_M \propto (\mu_0 H/T_C)^{2/3}$ is valid around T_C.

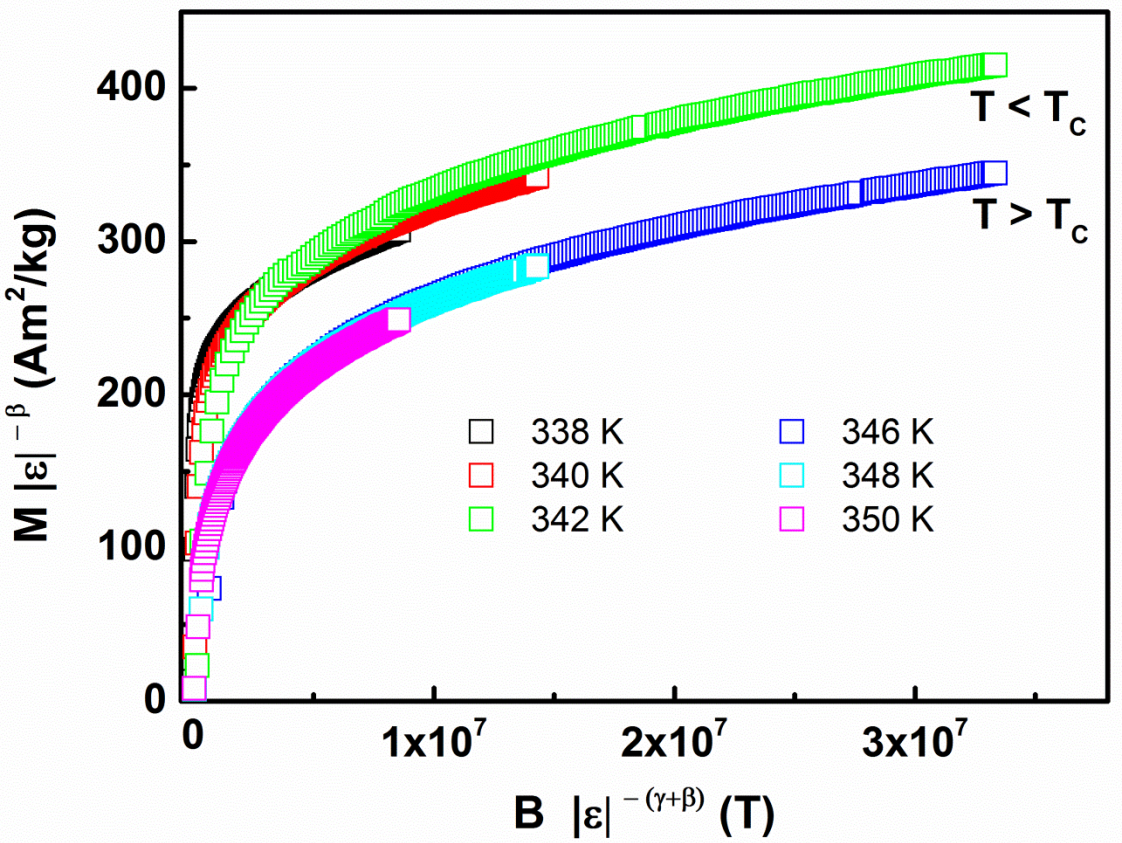

Figure 6.9 Scaling plots indicating universal curves below and above T_C for the $MnCoGe_{0.97}Al_{0.03}$ compound.

Figure 6.10 presents a thermal contour plot of neutron diffraction measurements on $MnCoGe_{0.97}Al_{0.03}$ compound from 6 to 450 K, with the orthorhombic phase (hkl) Miller indices (space group *Pnma*) being marked without * and the hexagonal phase (hkl) Miller indices (space group *P63/mmc*) marked with *. It can be seen clearly that with deceasing temperature, a structural transition takes place, starting from around 430 K and complete 350

K, which agrees well with the DSC and magnetic measurements, revealing a phase transition at approximately 420 K. Compared with the parent MnCoGe compound, which has the

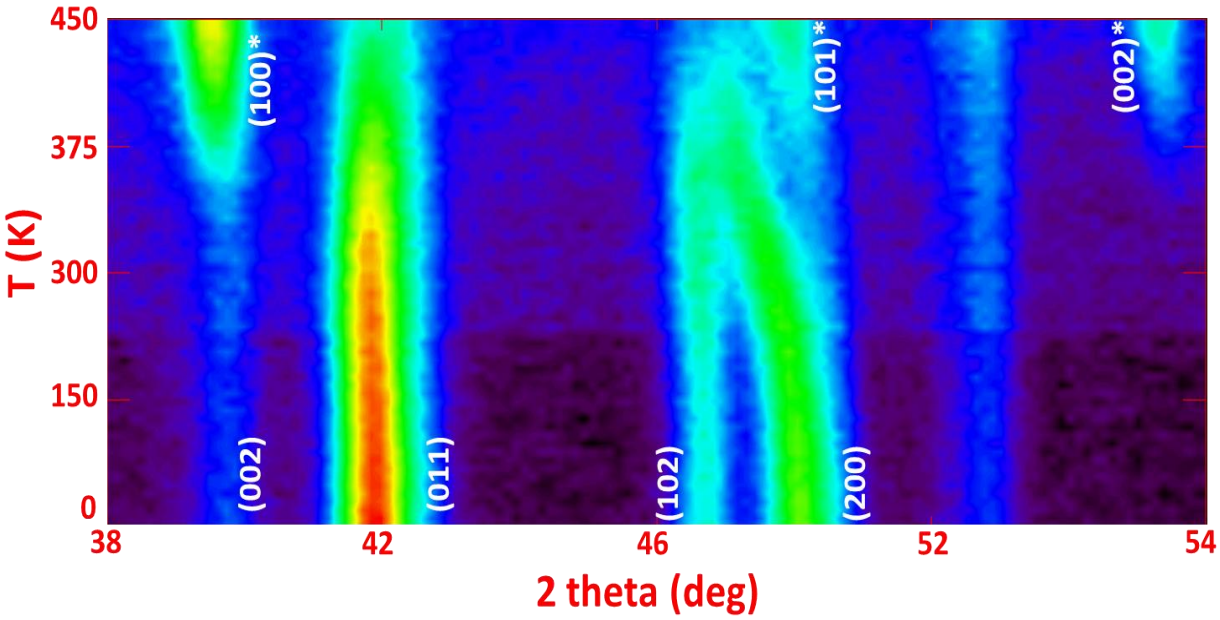

Figure 6.10 Neutron diffraction image for $MnCoGe_{0.97}Al_{0.03}$ collected at 5 K steps over the temperature range of 6 - 450 K.

structure change occurring at $T_{str} \approx 450$ K, the substitution of small amount of Al (3% wt.) for Mn leads to a slightly reduction in T_{str} to ~ 420 K. In order to investigate the crystallographic behaviour of $MnCoGe_{0.97}Al_{0.03}$ compound, neutron diffraction patterns were collected at selected temperatures (T = 450 K, 400 K, 300 K, and 6 K), as shown in Figure 6.11.

Refinement of the neutron diffraction patterns in Figure 6.11 indicated that at 450 K the compound crystallizes in the hexagonal Ni_2In-type structure (space group *P63/mmc*), while at the lowest temperature of 6 K, the crystal structure changes totally to orthorhombic TiNiSi-type structure (space group *Pnma*). At the temperatures of 400 K and 300 K, there is coexistence of both phases, thus confirming our expectations from magnetic measurements.

So, these results indicate again that the stability of hexagonal *P63/mmc* phase is enhanced due to the substitution of Al for Ge.

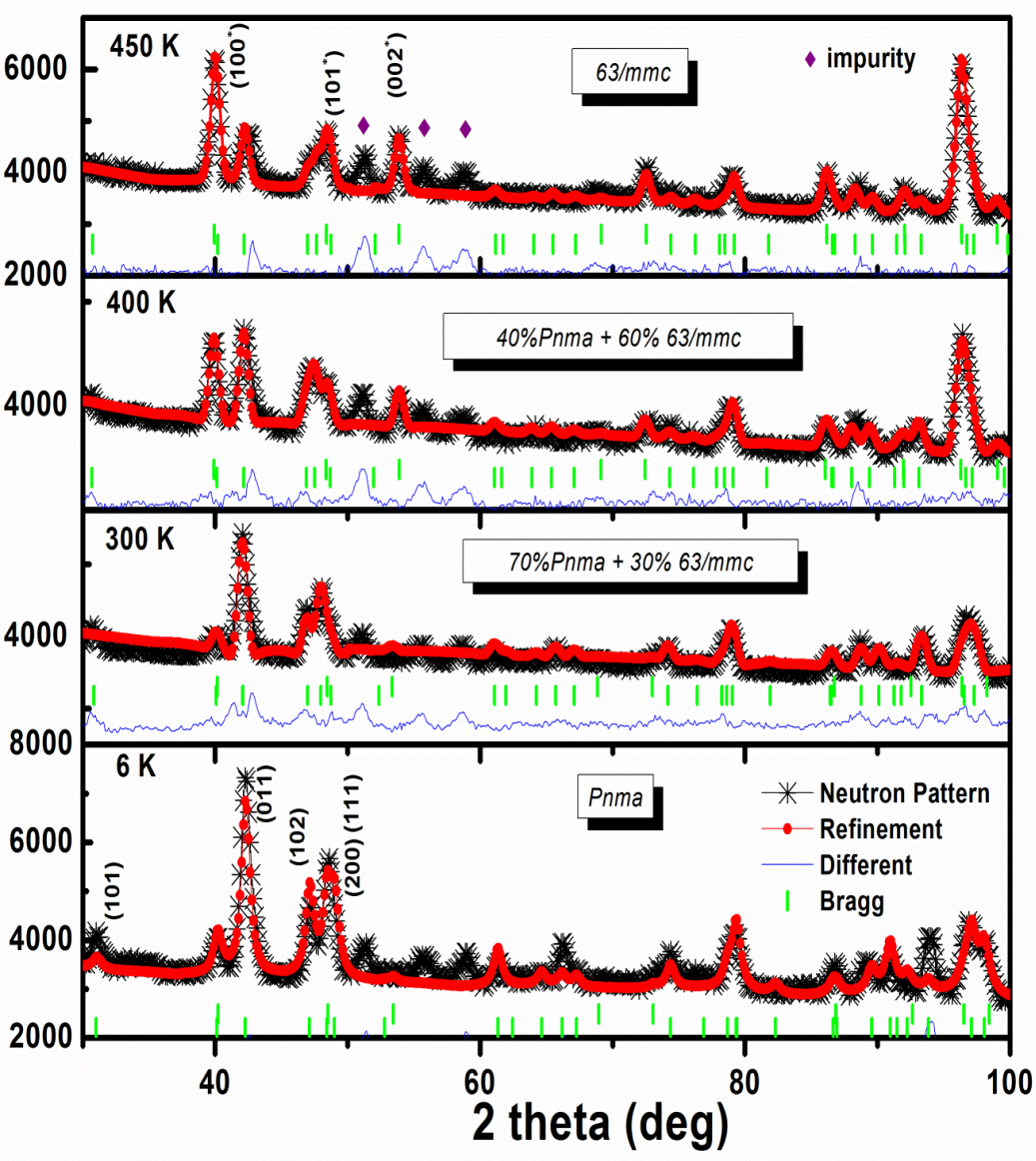

Figure 6.11 Measured and calculated neutron diffraction patterns for the $MnCoGe_{0.97}Al_{0.03}$ compound at 450 K, 400 K, 300 K, and 6 K. The points (marked by crosses) are the experimental data, while the solid lines are the calculated results. The vertical bars indicate the peak positions and the bottom solid line indicates the difference between the experimental and the calculated results.

Further analysis of the neutron diffraction data using Rietveld refinement resulted in the determination of the lattice parameters, as well as the volume phase fractions, for the orthorhombic and hexagonal phases. The peak intensities of the selected reflections (002)*

(for *P63/mmc*) and (011) (for *Pnma*) as a function of temperature are shown in Figure 6.12. The peak intensity of the (011) reflection, which decreases with increasing temperature,

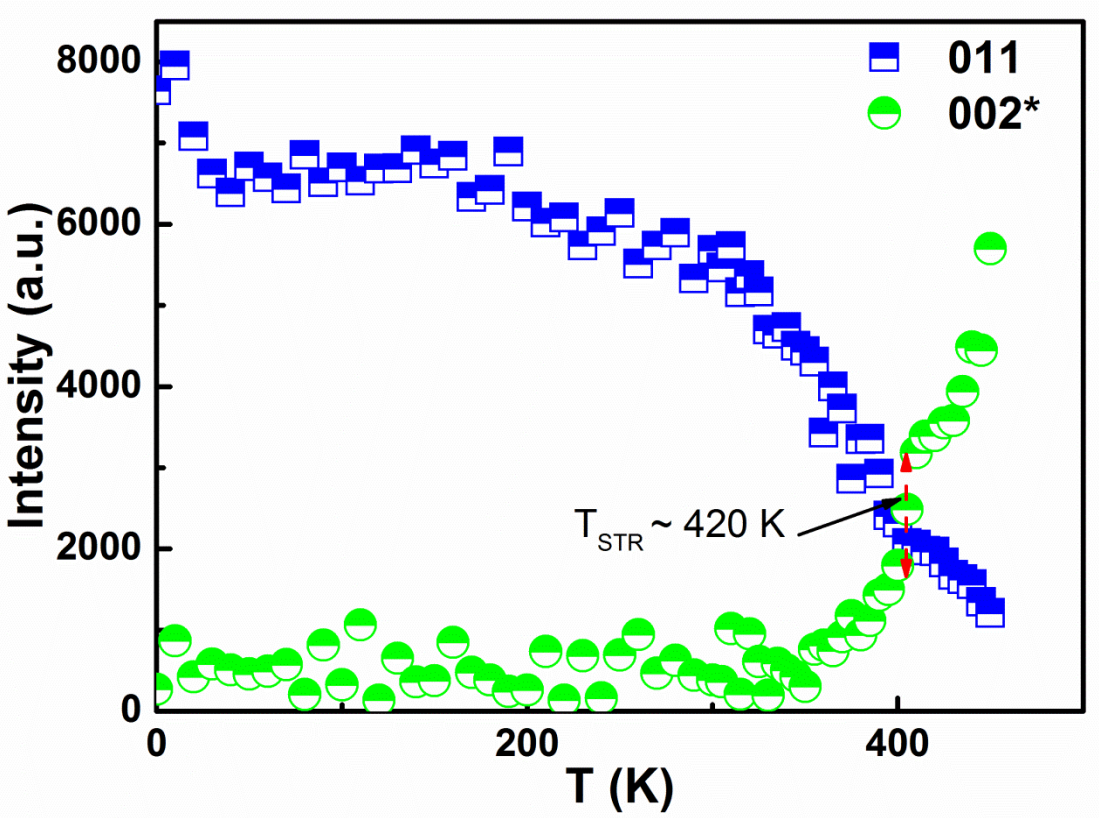

Figure 6.12 Peak intensity as a function of temperature for the (002)* and (011) peaks of the $MnCoGe_{0.97}Al_{0.03}$ compound.

corresponds to the decrease of the *Pnma* phase fraction, whilst the peak intensity of the (002)* reflection, which increases with increasing temperature, corresponds to the increase of the *P63/mmc* phase fraction with temperature.

Figure 6.13 shows the refined structural parameters of the $MnCoGe_{0.97}Al_{0.03}$ compound as a function of temperature from the neutron diffraction data. The appearance of additional impurity peaks has been indicated, however, they do not affect the behaviour of this compound. The lattice parameters and unit cell volumes of these two structures can be denoted as $a = a_{ortho} = c_{hex}$, $b = b_{ortho} = a_{hex}$, $c = c_{ortho} = \sqrt{3}a_{hex}$, and $V = V_{ortho} = 2V_{hex}$ [33]. The

lattice parameter *b* indicates the exchange interaction between the Mn-Mn moments along this axis, and a change in this parameter strongly influences the Curie temperature. Around

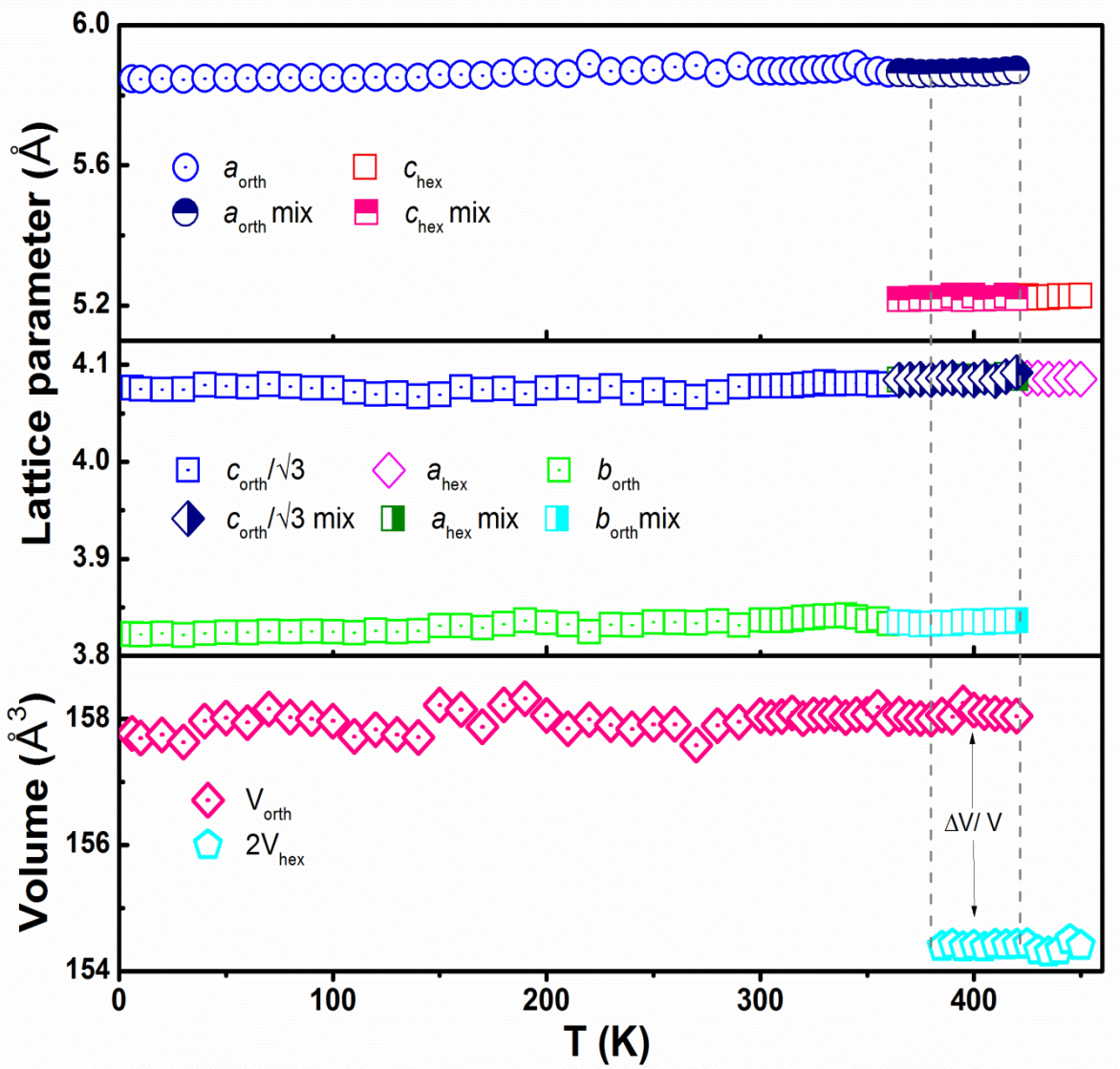

Figure 6.13 Lattice parameters and unit cell volume of $MnCoGe_{0.97}Al_{0.03}$ compound as a function of temperature. Open symbols with dots on the centre denote the orthorhombic phase, open symbols denote the hexagonal phase, and half-filled symbols denote the corresponding phases in the mixed phase region.

the structural transition temperature, $T_{str} \approx 420$ K, it is clearly evident in Figure 6.13 that when the symmetry changes from hexagonal to orthorhombic, there is a large volume change ($\Delta V = 1/2V_{orth}\text{-}V_{hex} = 2.02$ Å^3, so $\Delta V/V \approx 2.35\%$). For comparison, Kanomata *et al.* [22] estimated the difference in the unit cell volume at T_{str} as $\Delta V \approx 3$ Å^3 for MnCoGe compound.

For first order magnetic phase transitions, it is assumed that the total field-induced magnetic entropy change, ΔS_{tot}, can be expressed as the sum of the conventional second-order magnetic entropy change (ΔS_M) and the entropy difference of the two different crystallographic polymorphs (ΔS_{st}), i.e. $\Delta S_{tot} = \Delta S_M + \Delta S_{st}$. It was reported that the structural entropies are proportional to the volume differences of the phases involved in the transition [34]. Such a difference in the volume change around T_{str} for $MnCoGe_{0.97}Al_{0.03}$ compound will lead to a significant structural entropy change, resulting in a change in the total magnetic entropy change. So, the observed MCE around T_{str} (approximately 9 J kg^{-1} K^{-1} for ΔB = 5 T), which is larger than at T_C (approximately 3 J kg^{-1} K^{-1} for ΔB = 5 T) in the $MnCoGe_{0.97}Al_{0.03}$ compound can be attributed to the combined effect of an abrupt change in magnetization as well as in the unit cell volume in the vicinity of the structural transition (structural entropy change).

6.1.3.2 $MnCoGe_{1-x}Si_x$

In order to define the sensitivity from the substitution of another metalloid for Ge, a small amount of Si has been substituted for Ge in $MnCoGe_{1-x}Si_x$ compounds (x = 0, 0.05, 0.1, 0.15, and 0.2). The structural properties of $MnCoGe_{1-x}Si_x$ were investigated by room temperature X-ray diffraction, as shown in Figure 6.14. Predominantly, the orthorhombic TiNiSi-type structure with very small hexagonal Ni_2In-type structure was observed with increasing the Si concentration up to x = 0.2.

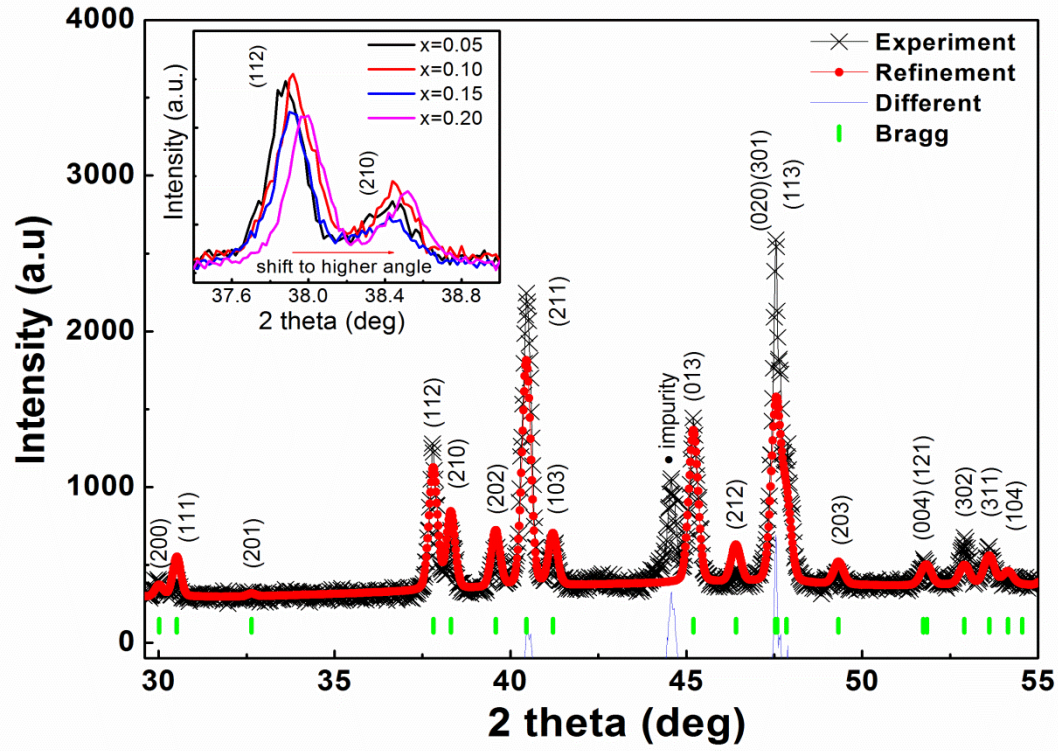

Figure 6.14 Refined XRD pattern of $MnCoGe_{0.80}Si_{0.20}$ measured at room temperature. The Miller indices hkl typically denote the Ni_2In-type hexagonal structure. The refinement pattern includes the experimental and calculated results, and their difference is presented. The inset shows the patterns for the indicated range of the $MnCoGe_{1-x}Si_x$ (x = 0.05, 0.10, 0.15, and 0.20) samples, demonstrating that the Bragg peaks shift to higher angles.

From the refinement analysis, the lattice parameters and unit cell volume of all the compounds were found decrease with increasing Si concentration, as the peaks shift to higher angle positions, which is related to the smaller atomic radius of Si, ~ 1.32 Å, compared to Ge,

~ 1.37 Å . Their lattice parameters and unit cell volumes are related by $a = a_{ortho} = c_{hex}$, $b = b_{ortho} = a_{hex}$, $c = c_{ortho} = \sqrt{3}a_{hex}$, and $V = V_{ortho} = 2V_{hex}$ [14]. Further increasing the Si concentration ($x > 0.2$) needs to be investigated in order to define the effects of the symmetry change from orthorhombic to hexagonal, the unit cell volume change, and the variation in Curie temperature of $MnCoGe_{1-x}Si_x$ compounds.

It is well known that the variation in the distance between the magnetic atoms will directly modify the exchange coupling and lead to a change in the transition temperature [17]. The increase and decrease of the Curie temperature closely follows the changes in the lattice parameter *b*, indicating that exchange interaction between the Mn-Mn moments along this axis plays an important role in determining the Curie temperature. Figure 6.15(a) shows the temperature dependence of the magnetization of $MnCoGe_{1-x}Si_x$ compounds measured in a field of 0.01 T from 10-330 K. For the compositions $x = 0.00$ up to 0.2, the Curie temperature was found to slightly increase with enhanced Si concentration. Moreover, the transition for all compounds was found to be incomplete and did not reach zero moment, as indicated by the fact that the temperatures of the structure transition were higher than 330 K, suggesting that this behaviour is related to the smaller Si atomic radius, which is needed in order to change the symmetry of the orthorhombic TiNiSi-type structure to hexagonal Ni_2In-type structure.

Furthermore, in order to determine the thermal hysteresis, which is a characteristic of the first order transition [12, 18], the temperature dependence of the magnetization of $MnCoGe_{1-x}Si_x$ was measured for heating and cooling. It is clear that the heating and cooling curves overlap completely, which indicates that there is no thermal hysteresis and the transition is second

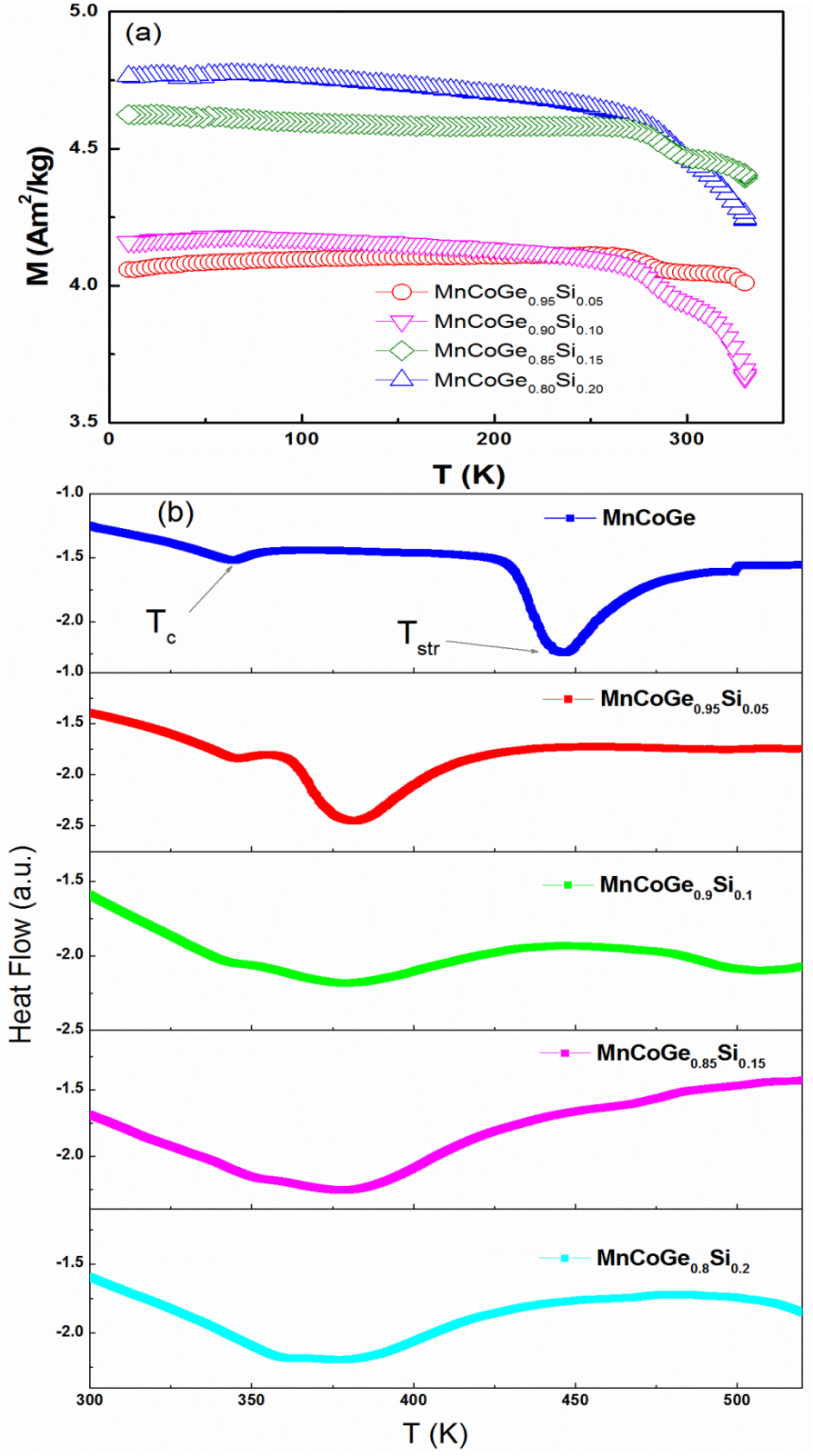

Figure 6.15 (a) *M–T* curves measured under a magnetic field of 0.01 T for $MnCoGe_{1-x}Si_x$ (x = 0.05, 0.1, 0.15, and 0.2). (b) DSC curves collected in the range of 300-500 K with the arrows indicating the structural transition and Curie temperature.

order type. It is well known that the cell volume, magnetic moment, Curie temperature, and structural transition temperature T_{str} all show strong dependence on the Co vacancy concentration rather than on Ge vacancy [35]. It can be seen, however, that the structural transition T_{str} determined from the DSC measurements decreases from 450 K for x = 0 to 360 K for x=0.2, as shown in Figure 6.15(b). This behaviour demonstrates that replacing Ge with a small percentage of Si (20%) leads to a decrease in the structural transition temperature and slightly increases the Curie temperature.

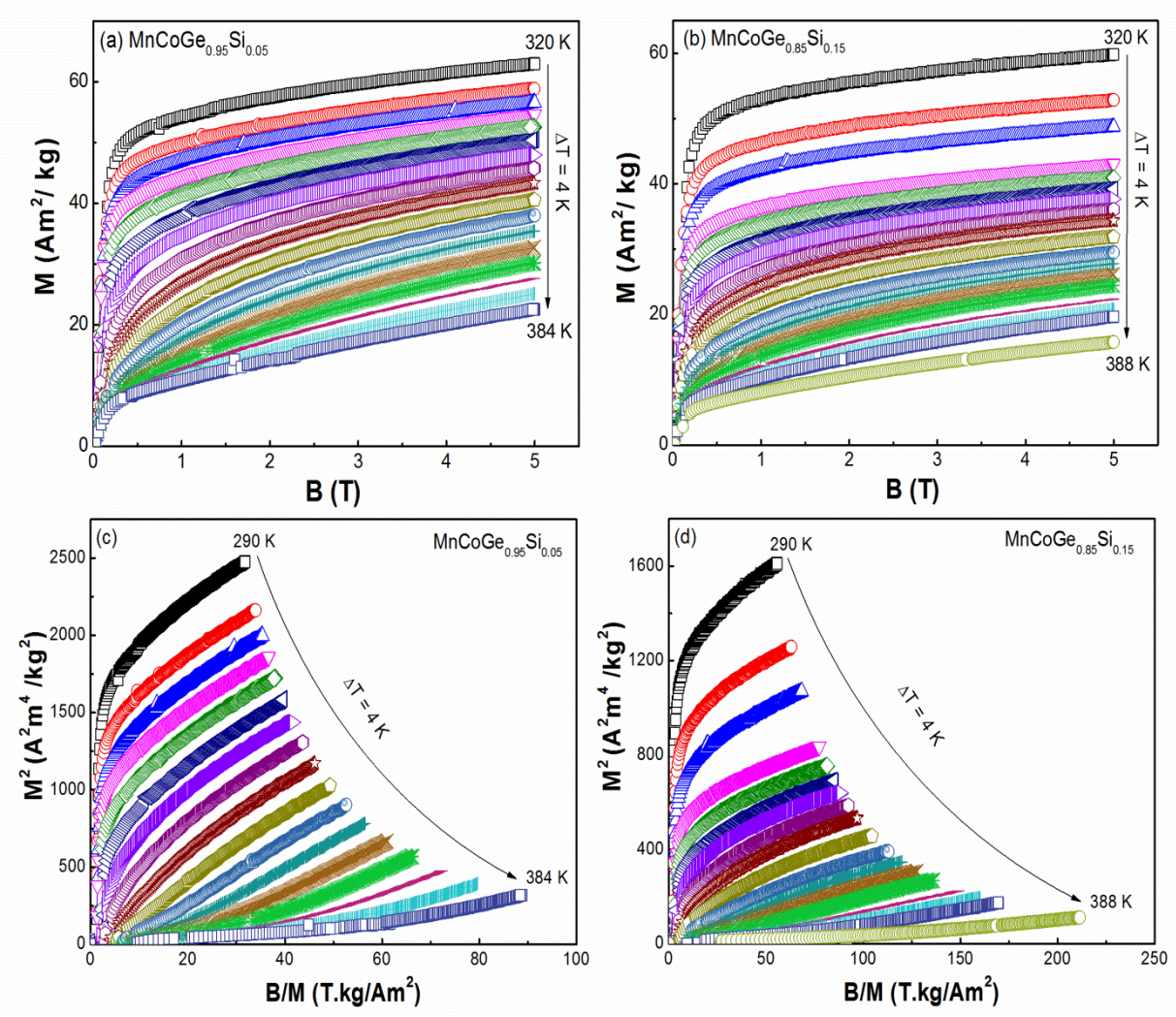

Figure 6.16 Variation in magnetization with applied field of 0-5 T for (a) MnCoGe compound and (b) MnCoAl compound; and Arrott plots showing the second order transition type for both compounds (c, d).

The magnetization curves obtained for $MnCoGe_{0.95}Si_{0.05}$ and $MnCoGe_{0.85}Si_{0.15}$ for fields in the range of B = 0 - 5 T around their Curie temperatures with 4 K interval steps are shown in Figure 6.16(a) and (b), respectively. These measurements show overlapping for increasing and decreasing fields for both compounds, thus indicating that there are no detectable magnetic hysteresis loss effects for increasing Si substitution for Ge in $MnCoGe_{1-x}Si_x$ compounds. Moreover, Figure 6.16(c) and (d) shows the corresponding Arrott plots (M^2 versus B/M) for the $MnCoGe_{0.95}Si_{0.05}$ and $MnCoGe_{0.85}Si_{0.15}$, which were found to exhibit features characteristic of a second order transition for all of the samples. The present findings demonstrate that the ferromagnetic transition at T_C in $MnCoGe_{1-x}Si_x$ remains a second order transition on substitution of Si for Ge for Si concentrations up to x = 0.2.

The magnetic entropy change, $-\Delta S_M$, has been determined for the whole set of $MnCoGe_{1-x}Si_x$ compounds (x = 0-0.2) from their magnetization curves for both increasing and decreasing field values as functions of temperature and magnetic field (ΔB = 0-5 T). The magnetic entropy change has been derived by applying the standard Maxwell relation [36] using Equation 6.1. As shown by the curves in Figure 6.17(a-c), the $-\Delta S_M$ peak gradually broadens towards higher temperatures with increasing magnetic field, behaviour characteristic of a field induced transition from the paramagnetic to a ferromagnetic state. The changes in magnetic entropy for the set of $MnCoGe_{1-x}Si_x$ compounds (x = 0.05, 0.1, 0.15, and 2.0) around their ferromagnetic ordering temperatures have been calculated from decreasing applied fields in order to determine the suitability of different experimental and related analytical approaches to establish the isothermal entropy change [16]. The entropy values at the respective Curie temperatures are found slightly the increase, with ΔB = 0-5 T: $-\Delta S_M \sim 2.1$ J kg^{-1} K^{-1} at T_C = 345 K for $MnCoGe_{0.95}Si_{0.05}$; $-\Delta S_M \sim 3.5$ J kg^{-1} K^{-1} at T_C = 350 K for $MnCoGe_{0.90}Si_{0.10}$; and $-\Delta S_M \sim 5.1$ J kg^{-1} K^{-1} at T_C = 355 K for $MnCoGe_{0.85}Si_{0.15}$. The increase

in magnetization on substitution of Si for Ge, correspondingly enhances the value of -ΔS_M, which is related to the exchange interaction between the Mn-Mn moments.

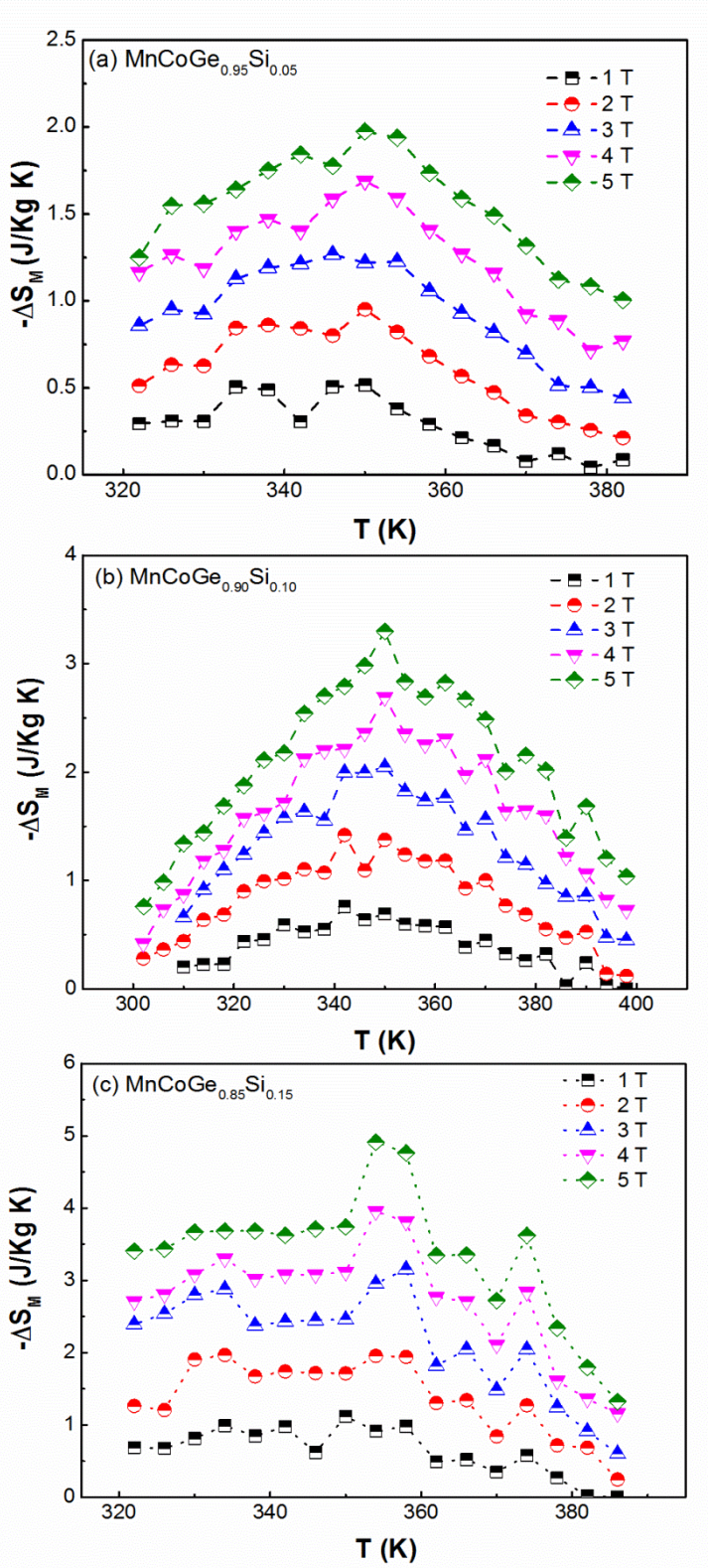

Figure 6.17 Temperature dependence of the isothermal magnetic entropy change, -$\Delta S_M(T, H)$ for $MnCoGe_{1-x}Si_x$ compounds (x = 0.05, 0.10, and 0.15) calculated from magnetization isotherms with 0-5 T field change applied.

6.1.4 Conclusions

In conclusion, the substitution of Al for Ge atoms induces a structural transformation from an orthorhombic structure at $x \cdot < 0.03$ to a hexagonal structure at $x > 0.03$ at room temeprature, and the concentration was employed to tune the structural transition temperature T_{str} in $MnCoGe_{1-x}Al_x$ compounds. It was found that with increasing Al doping, T_{str} decreases and overlaps with the Curie temperature of the martensite phase T^{M}_{C}. As a result, a transition temperature window as wide as 80 K (from 270 to 350 K) is observed, and the Curie temperature changes differently in hexagonal and orthorhombic structures with increasing Al. The origin of the reduction of T_{str} is ascribed to the strengthening of Mn–Mn covalent bonding and the lowering of the c/a ratio due to Al doping. For the optimized compositions, there was a moderate magnetic entropy change $-\Delta S_M$, which was found to represent second order magnetic transition behaviour. The working temperature region from 320 to 350K is favourable for magnetic refrigeration applications in this temperature area. Further substitution of Al for Ge ($x > 0.03$) in $MnCoGe_{1-x}Al_x$ compounds leads to the separation of magnetic and structural transitions.

An excellent agreement of the critical exponents of the $MnCoGe_{0.97}Al_{0.03}$ compound was determined using the isothermal magnetization in the vicinity of T_C, based on various techniques such as the Kouvel-Fisher method, modified Arrott plots, and critical isotherm analysis. Moreover, all critical exponents fulfil the Widom scaling law. The validity of the calculated critical exponents was confirmed by the scaling equation with the obtained magnetization, field, and temperature data below and above T_C, showing a collapse into two different curves. Thus, the scaling of the magnetization data above and below T_C obtained using the respective critical exponents and the consistency in the values of the critical exponents determined by different methods confirm that our calculated exponents are

unambiguous and intrinsic. The determined critical exponents are close to those predicted by the mean-field theory, with long range interactions.

Furthermore, the investigation of the replacement of Ge by Si in $MnCoGe_{1-x}Si_x$ compounds demonstrated the dominant structure to be orthorhombic TiNiSi-type with very small hexagonal Ni_2In-type structure for increasing Si concentration up to x = 0.2. The magnetization and DSC measurements indicated that T_C is slightly increased with increasing Si concentration, although the structural transition temperature, T_{str}, is reduced. The magnetic entropy change, $-\Delta S_M$, shows enhancement with increasing Si concentration up to x = 0.2, accompanied by the lack of any magnetic hysteresis loss, which is characteristic of second order magnetic transition behaviour and very favourable to magnetic refrigerator application. Higher Si concentrations (x > 0.2) need to be investigated, however, in order to clarify and optimise the effects of substitution by Si in $MnCoGe_{1-x}Si_x$ compounds.

6.2 Substitution for Mn by Ti in MnCoGe Alloy

6.2.1 Introduction

Earlier studies of the parent compound MnCoGe indicated that a martensitic structural transformation [15] from the low-temperature orthorhombic TiNiSi-type structure (space group *Pnma*) to the high-temperature hexagonal Ni_2In-type structure (space group *P63/mmc*) occurs at around T_{str} = 650 K. [16]. The orthorhombic TiNiSi-type structure of MnCoGe is reported to be ferromagnetic below the second-order paramagnetic to ferromagnetic transition at $T_C \approx 345$ K, while the hexagonal Ni_2In-type structure exhibits a ferromagnetic transition at $T_C \approx 275$ K [16,17]. Given that a large decrease in the unit cell volume of approximately 3.9% in MnCoGe compound occurs at T_{str} when the crystal symmetry changes from orthorhombic to hexagonal [15], MnCoGe and related compounds are of interest because of the scope they allow to control the temperatures (by causing T_{str} and T_C to coincide or be close enough) at which the magnetic and structural transitions occur and thereby capitalise on both magnetic and structural entropies.

In this section, the substitution of Ti into $Mn_{1-x}Ti_xCoGe$ compounds was investigated, and it was found that the one with the x = 0.06 substitution most successfully shifted the structural change and magnetic phase transition into the temperature range of interest, leading to the attainment of a giant magnetocaloric effect. Furthermore, the magnetic properties and critical behaviour of the $Mn_{0.94}Ti_{0.06}CoGe$ and $Mn_{0.99}Ti_{0.01}CoGe$ compounds were also investigated. Thus in an effort to understand the nature of the magnetic transition in both compounds, critical exponent analysis in the vicinity of the ferromagnetic (FM) – paramagnetic (PM) region [19–21] was performed. The results reveal that these materials undergo a structural

transition as well as a second-order ferromagnetic–paramagnetic transition, which will be discussed in more detail later.

6.2.2 Experimental and Procedures

Polycrystalline $Mn_{1-x}Ti_xCoGe$ compound ingots were prepared by arc melting the appropriate amounts of Mn (99.9%), Ti (99.999%) powder, Co (99.9%), and Ge (99.999%) chips in an argon atmosphere. During arc melting, 3% excess Mn over the stoichiometric amount was added to compensate for the weight loss of Mn. The polycrystalline ingots were melted many times to achieve good homogeneity. The ingots were then wrapped in tantalum foil, sealed in a quartz ampoule, and subsequently annealed at 850 °C for 120 h and then quenched in water at room temperature. Magnetization measurements were carried out using the vibrating sample magnetometer option of a Quantum Design 14 T physical properties measurement system (PPMS) in the temperature range of 10–600 K at applied fields of up to 5 T. Differential scanning calorimetry (DSC) measurements were carried out using a TA instrument DSC-Q100 over the range of 300-450 K to check for possible phase transitions in the higher temperature range.

6.2.3 Results and Discussion

6.2.3.1 $Mn_{1-x}Ti_xCoGe$

The temperature dependence (100–340 K) of the magnetization of the $Mn_{1-x}Ti_xCoGe$ (x = 0.1 and 0.06) compounds was measured in various magnetic fields, as shown in Figure 6.18. A decoupling of the structural and magnetic transitions is clearly observed in the *M–T* curves as

a two-step transition, which can be discerned at $T_C \approx 270$ K and $T_{str} \approx 235$ K for $x = 0.06$, t\and $T_C \sim 178$ K and $T_{str} \sim 280$ K for $x = 0.1$, respectively. Based on the analogous magnetic behaviour between $Mn_{0.9}Ti_{0.1}CoGe$ [37] and $Mn_{0.94}Ti_{0.06}CoGe$ [38], these transitions can be described as representing the change from orthorhombic to hexagonal structure at T_{str}, with T_C indicating the paramagnetic to ferromagnetic transition in the hexagonal phase. The inset in Figure 6.18(b) shows a plot of M^2 versus T, which reveals a magnetic transition from FM to PM at the ordering temperature, $T_C \approx 270$ K, as well as a plot of dM/dT showing the

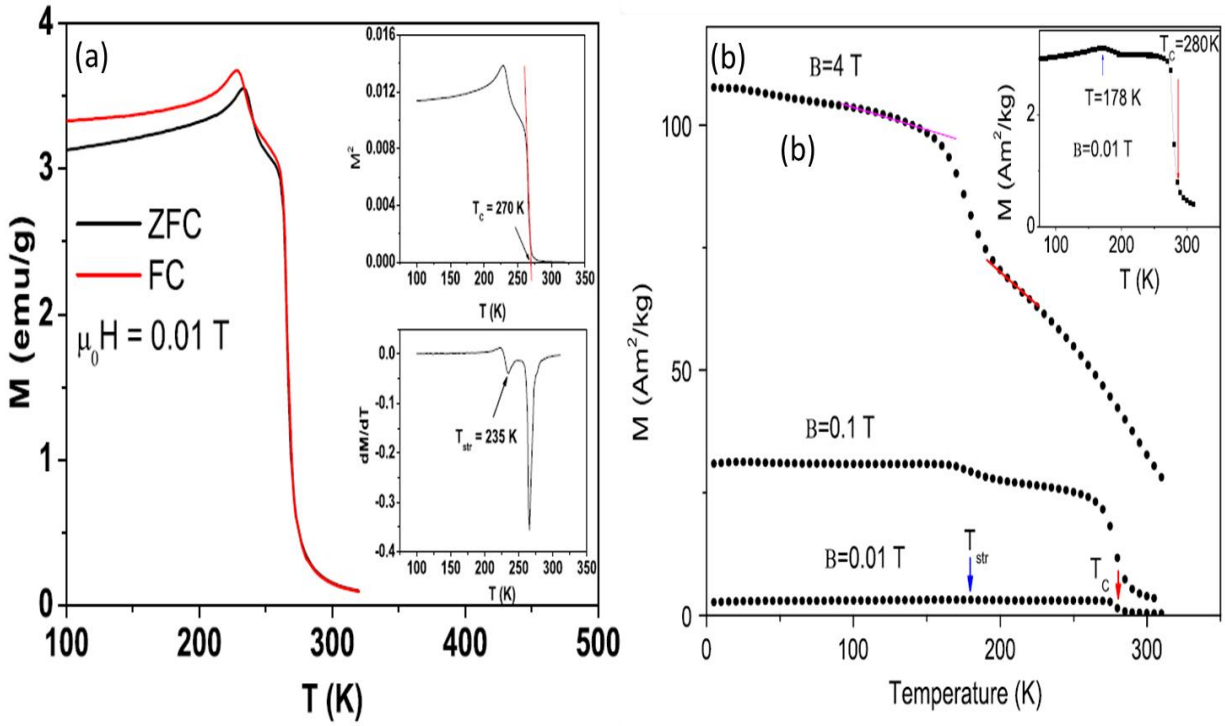

Figure 6.18 Temperature dependence of the magnetization (a) for $x = 0.06$ and (b) for $x = 0.1$. The insets show dM/dT versus T, used for the determination of T_{str}, as well as M^2 versus T, used for the determination of T_C.

structural transition at $T_{str} \sim 235$ K. The absence of thermal hysteresis in the vicinity of the magnetic PM to FM transition is clear evidence of the second-order nature of this transition. A notable thermal hysteresis is observed, however, in the vicinity of the magnetostructural transition from the antiferromagnetic TiNiSi-type to the ferromagnetic Ni_2In-type structure,

confirming its first-order nature. It has been previously established that the presence of a small hysteresis at T_{str} is indicative of a magnetoelastic character of the FM to antiferromagnetic (AFM) transition [17].

The magnetic entropy changes, $-\Delta S_M$, of the materials have been calculated using the Maxwell relation in Equation 6.1 [23] and are shown in Figure 6.19 as a function of temperature and field. The magnetic entropy change, $-\Delta S_M$, was also evaluated in the decreasing field mode, which is shown by the dotted and open symbol curves in Figure 6.19(a). A comparison of the $-\Delta S_M$ values calculated using increasing and decreasing fields for both compounds shows that the difference between these values is very small, which confirms that there is negligible hysteresis loss occurring in the vicinity of the structural transition, thus demonstrating the applicability of the Maxwell relation. As expected, $-\Delta S_M$ increases with increasing applied magnetic field. The temperature dependence of the magnetic entropy changes in the vicinity of T_{str} and T_C for $Mn_{0.9}Ti_{0.1}CoGe$ and $Mn_{0.94}Ti_{0.06}CoGe$ is shown in Figure 6.19.

Figure 6.19(a) reveals that the entropy change is significantly higher at T_{str} with a maximum value of $-\Delta S_M$ of ~ 6.6 J/kg K, compared with the value at T_C of $-\Delta S_M \approx 4.2$ J/ kg K for a field change of $\Delta B = 8$ T for $Mn_{0.9}Ti_{0.1}CoGe$. The inset in Figure 6.19(b) showing the variation of the magnetic entropy with temperature at 1 T clearly displays two maxima for $Mn_{0.94}Ti_{0.06}CoGe$, one occurring at the structural transition and the other at the magnetic transition. Interestingly, the maximum magnetic entropy change is found to be in the vicinity of T_{str} and is $-\Delta S_M \approx 11.3$ J kg^{-1} K^{-1} for a magnetic field change ΔB of 5 T, which is about one order of magnitude higher than that found for the undoped MnCoGe (~ 4.8 J kg^{-1} K^{-1} for a

change from 0-5 T) [17]. Around the FM to PM transition temperature T_C, $-\Delta S_M$ is found to be ~3 J kg^{-1} K^{-1} for a magnetic field change ΔB of 0-5 T. The difference in the $-\Delta S_M$ values at T_{str} and T_C can be understood in terms of the difference in order of the phase transitions. Compared with findings for some alloys with a second-order magnetic transition, the $-\Delta S_M$ peak of $Mn_{0.94}Ti_{0.06}CoGe$ is comparable to that of Gd [25] (~ 10.2 J kg^{-1} K^{-1} for a change of

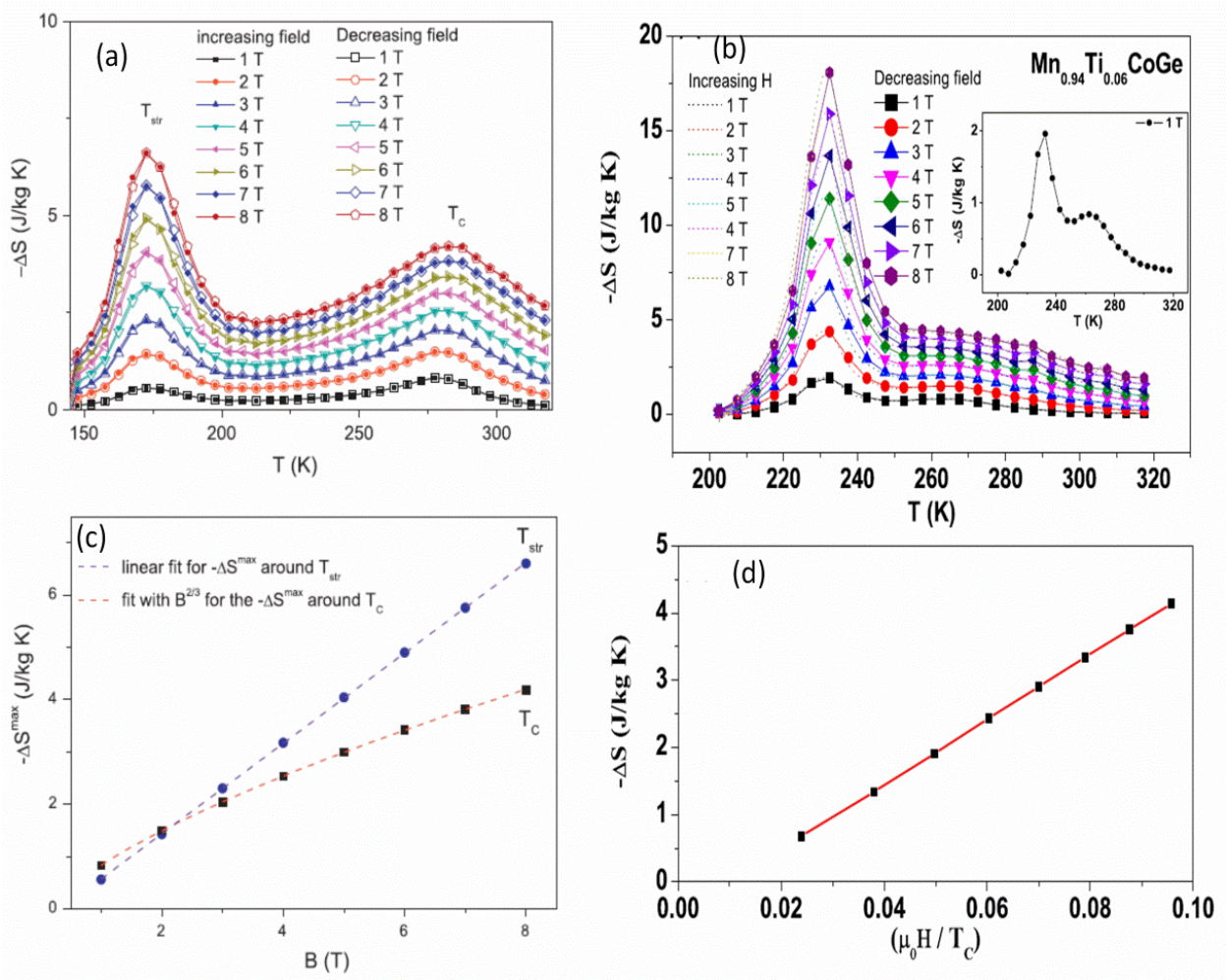

Figure 6.19 Temperature dependence of the isothermal magnetic entropy change $-\Delta S_M$ for (a) $Mn_{0.9}Ti_{0.1}CoGe$ and (b) $Mn_{0.94}Ti_{0.06}CoGe$ calculated from magnetization isotherms, with the inset showing the variation of magnetic entropy at 1 T; (c) dependence of the maximum magnetic entropy change on $B(T)$ for $Mn_{0.9}Ti_{0.1}CoGe$ and (d) on the parameter $(\mu_0 H/T_C)^{2/3}$ for $Mn_{0.94}Ti_{0.06}CoGe$. The solid line represents a linear fit to the data.

0-5 T). Figure 6.19(c) shows that for the region around the structural transformation at $T_{str} \approx$ 178 K, the maximum values of the entropy change $-\Delta S_M$ vary linearly with magnetic field, indicating the existence of the proportional relationship $-\Delta S_M \propto B$ at this transition for

$Mn_{0.9}Ti_{0.1}CoGe$. On the other hand, it was found that the dependence of the magnetic entropy change on the parameter $(\mu_0 H/T_C)^{2/3}$ for $Mn_{0.94}Ti_{0.06}CoGe$ in Figure 6.19(d) was linear. The mean-field theory predicts that in the vicinity of second-order phase transitions, $-\Delta S_M$ is proportional to $(\mu_0 H/T_C)^{2/3}$ [26, 27]. The linear fit to the data in Figure 6.2(d) clearly demonstrates that the relationship $-\Delta S_M \propto (\mu_0 H/T_C)^{2/3}$ is valid around T_C.

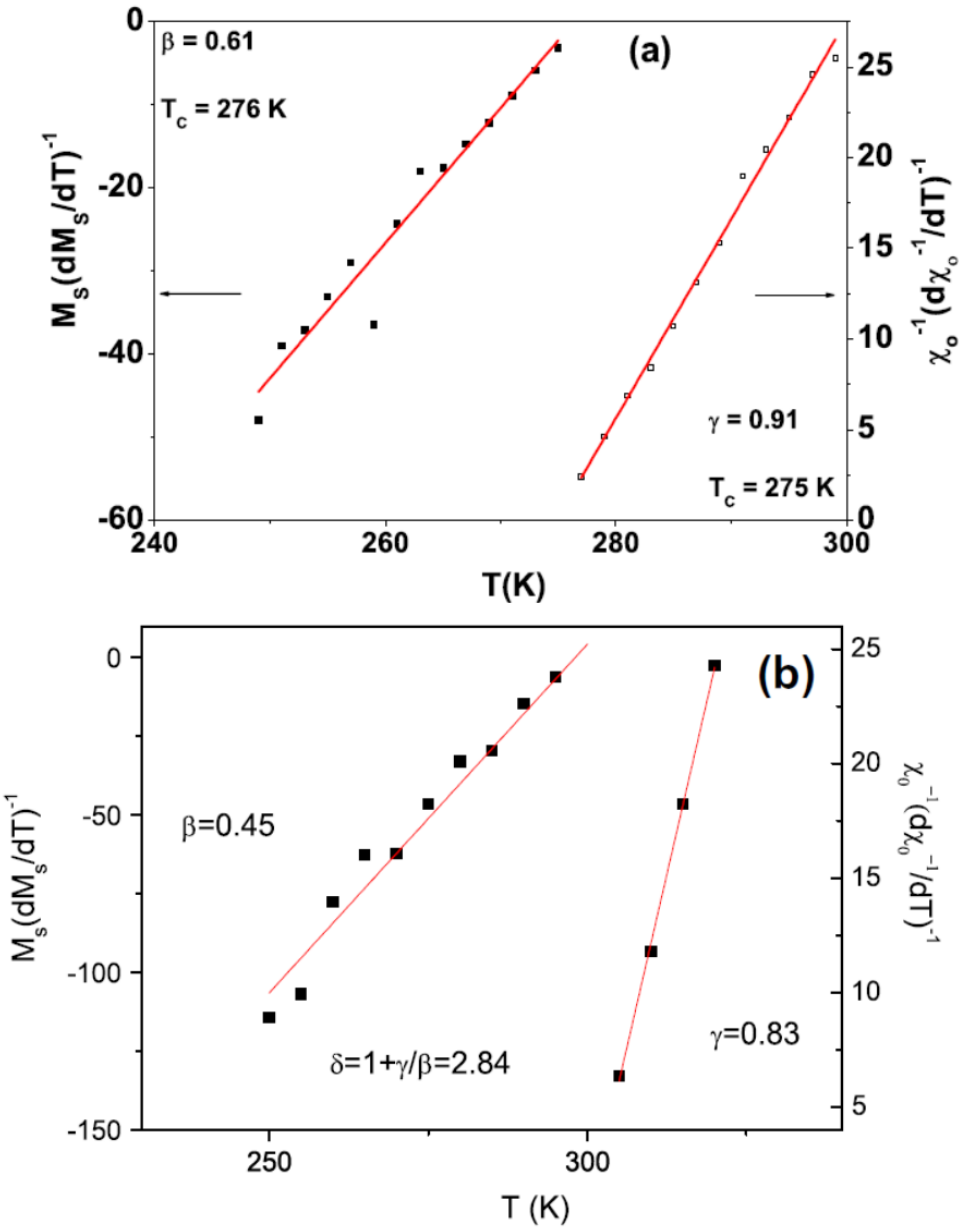

Figure 6.20 Kouvel–Fisher plots for the spontaneous magnetization of $M_S(T)[dM_S/dT]^{-1}$ (left scale) and $\chi_0^{-1}(T)[d\chi_0^{-1}/dT]^{-1}$(right scale) versus temperature for (a) $Mn_{0.94}Ti_{0.06}CoGe$ and (b) $Mn_{0.9}Ti_{0.1}CoGe$ compounds. The lines are fits to the data around T_C, as discussed in the text, with the fits leading to the critical exponent values.

According to the conventional static scaling law, the critical properties of a second-order magnetic transition can be described by the critical exponents β, γ, and δ derived from magnetization measurements around the transition temperature, as in the previous section. On applying these standard approaches, as shown by the fits to the Kouvel–Fisher plots of $M_S(T)[dM_S/dT]^{-1}$ and $\chi_0^{-1}(T)[d\chi_0^{-1}/dT]^{-1}$versus temperature in Figure 6.20, the critical exponents around T_C in $Mn_{0.94}Ti_{0.06}CoGe$ have been determined to be β = 0.61 and γ = 0.91. Hence, on applying the relationship δ = 1 + γ / β, with β = 0.61, γ = 0.91, the critical exponent δ = 1 + γ / β = 2.49. For the $Mn_{0.94}Ti_{0.06}CoGe$ compound, the critical exponents have been found to be β = 0.45, γ = 0.83, and δ = 2.84, respectively. The critical exponents determined for both compound are similar to the theoretical values from the mean-field model, for which β = 0.5, γ = 1.0, and δ = 3.0, consistent with the existence of long-range ferromagnetic interactions [27]. Thus, the critical behaviour analysis in the vicinity of T_C demonstrates that the magnetism of the $Mn_{0.94}Ti_{0.06}CoGe$ and $Mn_{0.9}Ti_{0.1}CoGe$ compounds is governed by long range interactions. This is in agreement with the linear fit to the data in Figure 6.19(d), which clearly demonstrates that the relationship $-\Delta S_M \propto (\mu_0 H/T_C)^{2/3}$ is valid around T_C.

6.2.4 Conclusion

The structural and magnetic properties of $Mn_{1-x}Ti_xCoGe$ compounds have been investigated by magnetic measurements and critical exponent analysis. Substitution of Ti for Mn in the parent MnCoGe compound leads to a significant reduction in both T_{str} (from ~ 645 K for MnCoGe to ~ 235 K for $Mn_{0.94}Ti_{0.06}CoGe$ and ~ 178 K for $Mn_{0.9}Ti_{0.1}CoGe$) and T_C (from ~ 345 K for MnCoGe to ~ 270 K for $Mn_{0.94}Ti_{0.06}CoGe$ and ~ 280 K for $Mn_{0.9}Ti_{0.1}CoGe$). Moreover, all the critical exponents for $Mn_{0.94}Ti_{0.06}CoGe$ and $Mn_{0.9}Ti_{0.1}CoGe$ fulfil the Widom scaling law. The validity of the calculated critical exponents was confirmed by the

scaling equation, with the magnetization, field, and temperature data obtained below and above T_C collapsing onto two different curves. Thus, the scaling of the magnetization data above and below T_C was obtained using the respective critical exponents, and the consistency of the values of the critical exponents determined by different methods confirm that the calculated exponents are unambiguous and intrinsic. The critical exponents determined are close to those predicted by the mean-field theory for long range interactions.

References

[1] S. Nizioł, A. Wesełucha, W. Bażela, and A. Szytuła, Solid State Communications 39 (1981) 1081.

[2] S. Nizioł, A. Bombik, W. Bażela, A. Szytuła, and D. Fruchart, Journal of Magnetism and Magnetic Materials 27 (1982) 281.

[3] V. Johnson and W. Jeitschko, Journal of Solid State Chemistry 4 (1972) 123.

[4] V. K. Pecharsky and J. K. A. Gschneidner, Physical Review Letters 78 (1997) 4494.

[5] H. Wada and Y. Tanabe, Applied Physics Letters 79 (2001) 3302.

[6] H. Wada, S. Tomekawa, and M. Shiga, Cryogenics 39 (1999) 915.

[7] J. L. Wang, S. J. Campbell, O. Tegus, E. Brück, and S. X. Dou, Journal of Physics: Conference Series 217 (2010) 012132.

[8] M. Patra, S. Majumdar, S. Giri, Y. Xiao, and T. Chatterji, Journal of Physics: Condensed Matter 26 (2014) 046004.

[9] J. L. Wang, L. Caron, S. J. Campbell, S. J. Kennedy, M. Hofmann, Z. X. Cheng, M. F. Md Din, A. J. Studer, E. Brück, and S. X. Dou, Physical Review Letters 110 (2013) 217211.

[10] M. F. Md Din, J. L. Wang, R. Zeng, P. Shamba, J. C. Debnath, and S. X. Dou, Intermetallics 36 (2013) 1.

[11] F.X. Hu, B.-g. Shen, and J.-r. Sun, Applied Physics Letters 76 (2000) 3460.

[12] K. A. GschneidnerJr, V. K. Pecharsky, and A. O. Tsokol, Reports on Progress in Physics 68 (2005) 1479.

[13] N. T. Trung, V. Biharie, L. Zhang, L. Caron, K. H. J. Buschow, and E. Brück, Applied Physics Letters 96 (2010)

[14] N. T. Trung, L. Zhang, L. Caron, K. H. J. Buschow, and E. Brück, Applied Physics Letters 96 (2010)

[15] N. T. Trung, Z. Q. Ou, T. J. Gortenmulder, O. Tegus, K. H. J. Buschow, and E. Brück, Applied Physics Letters 94 (2009)

[16] L. Caron, Z. Q. Ou, T. T. Nguyen, D. T. Cam Thanh, O. Tegus, and E. Brück, Journal of Magnetism and Magnetic Materials 321 (2009) 3559.

[17] N. T. Trung, J. C. P. Klaasse, O. Tegus, D. T. C. Thanh, K. H. J. Buschow, and E. Brück, Journal of Physics D: Applied Physics 43 (2010) 015002.

[18] J. Fan, L. Ling, B. Hong, L. Zhang, L. Pi, and Y. Zhang, Phys. Rev. B 81 (2010) 144426.

[19] K. Ghosh, C. J. Lobb, R. L. Greene, S. G. Karabashev, D. A. Shulyatev, A. A. Arsenov, and Y. Mukovskii, Phys. Rev. Lett 81 (1998) 4740.

[20] R. Cabassi, F. Bolzoni, A. Gauzzi, and F. Licci, Phys. Rev. B 74 (2006) 184425.

[21] L. Song, O. Tegus, E. Bruck, W. Dagula, T. J. Gortenmulder, and K. H. J. Buschow, Magnetics, IEEE Transactions on 42 (2006) 3776.

[22] T. Kanomata, H. Ishigaki, T. Suzuki, H. Yoshida, S. Abe, and T. Kaneko, Journal of Magnetism and Magnetic Materials 140–144, Part 1 (1995) 131.
[23] R. Zeng, S. X. Dou, J. L. Wang, and S. J. Campbell, Journal of Alloys and Compounds 509 (2011) L119.
[24] M. F. Md Din, J. L. Wang, S. J. Campbell, A. J. Studer, M. Avdeev, S. J. Kennedy, Q. F. Gu, R. Zeng, and S. X. Dou, Applied Physics Letters 104 (2014) 042401.
[25] M. F. M. Din, J. L. Wang, S. J. Campbell, R. Zeng, W. D. Hutchison, M. Avdeev, S. J. Kennedy, and S. X. Dou, Journal of Physics D: Applied Physics 46 (2013) 445002.
[26] B. K. Banerjee, Physics Letters 12 (1964) 16.
[27] A. Arrott, Noakes, and J. E., Phys. Rev. Lett. 19 (1967) 786.
[28] M. Sahana, U. K. R"ossler, N. Ghosh, S. Elizabeth, H. L. Bhat, K. D"orr, D. Eckert, M. Wolf, and K. H. M"uller, Phys. Rev. B 68 (2003) 144408.
[29] J. S. Kouvel and M. E. Fisher, Phys. Rev. 136 (1964) A1625.
[30] M. Ahlberg, P. Korelis, G. Andersson, and B. o. Hj"orvarsson, Phys. Rev. B 85 (2012) 224425.
[31] V. Franco, A. Conde, J. M. Romero-Enrique, and J. S. Blázquez, Journal of Physics: Condensed Matter 20 (2008) 285207.
[32] Đ. Drobac, Journal of Magnetism and Magnetic Materials 159 (1996) 159.
[33] J. T. Wang, D. S. Wang, C. Chen, O. Nashima, T. Kanomata, H. Mizuseki, and Y. Kawazoe, Applied Physics Letters 89 (2006)
[34] K. A. Gschneidner Jr, Y. Mudryk, and V. K. Pecharsky, Scripta Materialia 67 (2012) 572.
[35] K. G. Sandeman, R. Daou, S. "Ozcan, J. H. Durrell, N. D. Mathur, and D. J. Fray, Phys. Rev. B 74 (2006) 224436.
[36] H. Feng Xia, S. Bao Gen, S. Ji Rong, C. Zhao Hua, and Z. Xi Xiang, Journal of Physics: Condensed Matter 12 (2000) L691.
[37] J. L. Wang, P. Shamba, W. D. Hutchison, M. F. Md Din, J. C. Debnath, M. Avdeev, R. Zeng, S. J. Kennedy, S. J. Campbell, and S. X. Dou, Journal of Alloys and Compounds 577 (2013) 475.
[38] P. Shamba, J. L. Wang, J. C. Debnath, S. J. Kennedy, R. Zeng, M. F. M. Din, F. Hong, Z. X. Cheng, A. J. Studer, and S. X. Dou, Journal of Physics: Condensed Matter 25 (2013) 056001.

CHAPTER 7

CONCLUSIONS AND OUTLOOK

In the summary, structural, magnetic and magnetocaloric properties of some selected magnetic materials withdifferent crystal structures such as cubic $NaZn_{13}$-type structure, body centred tetragonal $ThCr_2Si_2$-type structure; hexagonal Ni_2In-type structure and orthorhombic TiNiSi-type structure have been systematically investigated. The aim of this study was to contribute towards a better understanding of the fundamental material characteristics, with an emphasis on understanding the relationship between a defined structure, the crystallographic phase and magnetic phase structure, and alteration in the magnetic properties. This work has important contributions towards an understanding of the role of atomic substitution as chemical pressure effect in tuning the magnetocaloric properties, magnetic phase transition and magnetic structure. The main outcomes of the thesis are summarized as follows:

- A systematic investigation of the structural and magnetic characterization of $La_{0.7}Pr_{0.3}Fe_{11.4-x}Cu_xSi_{1.6}$ (x = 0, 0.06, 0.12, 0.23, 0.34) for high temperature annealing (HTA) and low temperature annealing (LTA) samples has been carried out. The results show that the HTA process resolves the problem of non-equilibrium solidification behaviour due to the incomplete peritectic reaction γ-Fe+L $\rightarrow$ $La(Fe,Si)_{13}(\tau_{1a})$ that occurs in the LTA process. The HTA sample with x = 0 shows promising values of $-\Delta S_M$ and RCP with very small hysteresis loss. This indicates the

elevated temperature in HTA plays an important role to form the $NaZn_{13}$ type structure in the $La_{0.7}Pr_{0.3}Fe_{11.4}Si_{1.6}$ compound.

- Substitution of Cu for Fe leads to a decrease in the magnetic entropy change and eliminates hysteresis loss. Increasing the Cu concentration (starting from x = 0.06) also results in a change in the magnetic phase transition type from first to second order and reduces the characteristics of the IEM transition. The Curie temperature, T_C, increases with increasing Cu content, which can be ascribed to the increase in the lattice parameter and the modification of the composition. The compound with a small amount of Cu substitution shows a promising magnetic performance for magnetic refrigerator application, with no hysteresis loss and reasonable RCP.

- Replacement of Fe by Cr in $La_{0.7}Pr_{0.3}Fe_{11.4-x}Cr_xSi_{1.6}$ compounds leads to decreases in lattice parameter but variation behaviour on temperature transition, T_C. The variation in the value of T_C with increasing Cr concentration can be understood in terms of sensitive changes of Fe1-Fe2 and Fe2-Fe2 distances. Analysis of the magnetisation data demonstrates that the order of magnetic phase transition around T_C is consistent on first order type even x=0.34 for $La_{0.7}Pr_{0.3}Fe_{11.4-x}Cr_xSi_{1.6}$ compounds. Replacement of Fe by Cr leads to a reduction of the magnetic entropy change from beginning at x=0; ($-\Delta S_M$ =17 J kg^{-1} K^{-1}) to x=0.06; ($-\Delta S_M$ = 12 J kg^{-1} K^{-1}), however starts to enhance again when keep increasing Cr concentration until x=0.34; ($-\Delta S_M$ = 17.5 J kg^{-1} K^{-1}).

- High intensity neutron and X-ray diffraction studies demonstrate that $La_{0.7}Pr_{0.3}Fe_{11.06}Cr_{0.34}Si_{1.6}$ compound has contraction in unit cell from ferromagnetic to

paramagnetic structure which contributes to produce high magnetic entropy change. However this investigation is still incomplete as it will be the platform for us to further study, particularly further increase Cr concentration in this compound in order to confirm the ultimate of the beneficial in Cr substitution.

- A systematic investigation of the structural and magnetic characteristics of $NdMn_{2-x}T_xSi_2$ (T = Ti, Cr, Cu and V) compounds has been carried out. Substitution of Mn by Ti leads to a reduction of the magnetic entropy change. However, analysis of the magnetisation data demonstrates that the first order magnetic transition of $NdMn_2Si_2$ around T_C remains unchanged on replacement of Mn by Ti, and this substitution leads to significant reduction in magnetic hysteresis losses and eliminates thermal hysteresis. Neutron diffraction studies demonstrate that $NdMn_{1.9}Ti_{0.1}Si_2$ has the AF*il* antiferromagnetic structure in the temperature range $T_N \sim 374$ K > T > $T_C \sim 22$ K and the combined F*mc*+F(Nd) ferromagnetic state below $T_C \sim 22$ K.

- The magnetic structures of $NdMn_{1.7}Cr_{0.3}Si_2$ determined from variable temperature neutron diffraction studies are: layered AF*il* antiferromagnetism for T_N^{inter}~320(3) K<T<T_N^{intra}~380(3) K; canted AF*mc* antiferromagnetism for T_C~42(2) K<T< T_N^{inter}~320(3) K with a combined F*mc*(Mn)+F(Nd) ferromagnetic structure for T<T_C~42(2) K. Values of the magnetic entropy, magnetocaloric effect and adiabatic temperature change have been determined from magnetization and heat capacity measurements around the first order magnetic transition at T_C.

- Substitution of Cu for Mn leads to increase in the Curie temperature and decrease the Néel temperature. The variation in the value of T_C with increasing Cu concentration

can be understood in terms of changes in the Mn-Mn exchange interaction together with the effects of magnetic dilution. Analysis of the magnetisation data demonstrates that the order of magnetic phase transition around T_C changes from first order at $x<0.6$ to second order transition for $x\geq0.6$ and leads to significant reduction in magnetic hysteresis losses. Substitution of Mn by Cu leads to a reduction of the magnetic entropy change and neutron diffraction studies demonstrate that $NdMn_{1.8}Cu_{0.2}Si_2$ has the AF*il* antiferromagnetic structure in the temperature range T_N ~ 375 K > T > T_C ~ 44 K and the combined F*mc*+F(Nd) ferromagnetic state below T_C ~ 44 K.

- The replacement Mn by V in leads to decrease in the Curie and Néel temperature from. Increment of V concentration leads to a reduction of the magnetic entropy change respectively as did not change the first order magnetic transition behaviour. The neutron diffraction study on $NdMn_{1.9}V_{0.1}Si_2$ compound indicated that magnetic structure found from paramagnetic PM to the AF*il* antiferromagnetic structure in the temperature range T_N ~ 375 K > T > T_C ~ 24 K and the combined F*mc*+F(Nd) ferromagnetic state below T_C ~ 24 K.

- Replacement of Y for Pr leads to a significant reduction in the lattice parameters of $Pr_{1-x}Y_xMn_2Ge_2$ compounds. The commensurate changes in the intralayer Mn–Mn distances correspondingly lead to a variety of magnetic structures, as also observed in related RMn_2X_2 systems (R – rare earth; X - Ge, Si) [e.g. 24]. The various magnetic structures of $Pr_{1-x}Y_xMn_2Ge_2$ have determined by neutron powder diffraction over the temperature range 5 – 450 K. Together with magnetisation and differential scanning calorimetry measurements, this has enabled us to construct the magnetic phase

diagram of $Pr_{1-x}Y_xMn_2Ge_2$. The ferromagnetic transitions at T_C^{inter}, the temperature at which the layered antiferromagnetic structure transforms to the canted F*mc* structure, are found to be second order. The entropy changes around T_C^{inter} have been derived for $Pr_{1-x}Y_xMn_2Ge_2$ compounds of Y contents x = 0.0, 0.2 and 0.5.

- The temperature dependence of lattice parameters for $CeMn_2Ge_{2-x}Si_x$ demonstrates an anomaly in thermal expansion which is accompanied with appearance of the interlayer Mn–Mn interactions. The co-existence of different magnetic states at the same temperature is considered to be related to the non-random variation of site concentrations of Si and Ge, and depends sensitively on the Mn–Mn distances in this system. Moreover, critical properties study on the second-order ferromagnetic transition of $CeMn_2Ge_2$ demonstrate that the magnetic interactions around T_C^{inter} can be described with the three dimensional Heisenberg model corresponding to short range interactions. Overall this investigation has demonstrated that, as expected, the Si concentration plays the dominant role in tuning the magnetic structure and properties of the $CeMn_2Ge_{2-x}Si_x$ compounds.

- The substitution of Al for Ge atoms in MnCoGe induces a structural transformation from an orthorhombic structure at $x \cdot < 0.03$ to a hexagonal structure at $x > 0.03$, and the varation in concentration was employed to tune the structural transition temperature T_{str} in $MnCoGe_{1-x}Al_x$ compounds. The origin of the reduction of T_{str} is ascribed to the strengthening of Mn–Mn covalent bonding and the lowering of the *c*/*a* ratio due to Al doping. Further substitution of Al for Ge ($x > 0.03$) in $MnCoGe_{1-x}Al_x$ compounds leads to the separation of magnetic and structural transitions.

- Furthermore, the investigation of the replacement of Ge by Si in $MnCoGe_{1-x}Si_x$ compounds indicated that the dominant structure is orthorhombic TiNiSi-type with very small hexagonal Ni_2In-type structure being present for increasing Si concentration up to $x = 0.2$. The magnetization and DSC measurements indicated that T_C is slightly increased with increasing Si concentration, although the structural transition temperature, T_{str}, is reduced. The samples with higher Si concentrations ($x > 0.2$) are needed to be further investigated in order to clarify and optimise the effects of substitution by Si in $MnCoGe_{1-x}Si_x$ compounds.

- Finally, the structural and magnetic properties of $Mn_{1-x}Ti_xCoGe$ compounds have been investigated by magnetic measurements and critical exponent analysis. Substitution of Ti for Mn in the parent MnCoGe compound leads to a significant reduction in both T_{str} and T_C. Moreover, all the critical exponents for $Mn_{0.94}Ti_{0.06}CoGe$ and $Mn_{0.9}Ti_{0.1}CoGe$ fulfil the Widom scaling law. The validity of the calculated critical exponents was confirmed by the scaling equation, with the magnetization, field, and temperature data obtained below and above T_C collapsing onto two different curves. Thus, the scaling of the magnetization data above and below T_C was obtained using the respective critical exponents, and the consistency of the values of the critical exponents determined by different methods confirm that the calculated exponents are unambiguous and intrinsic. The critical exponents determined are close to those predicted by the mean-field theory for long range interactions.

The overall of this intensive study has provided an insight on the effect of atomic substitutions in term of chemical pressure for tuning the magnetic structure and magnetocaloric effect properties as well as the magnetic phase transitions. It is ambition

that this work may act as a foundation for further research in order to development of new materials that can fulfil specific requirements of cooling devices. Future work may include:

- It would be very favourable to tune the $La_{0.7}Pr_{0.3}Fe_{11.4}Si_{1.6}$ compound with substitution Fe with other transition metal in order to produce room temperature transition belonging with higher magnetic entropy change.

- There is a need to perform pressure dependent magnetisation measurements of the layered RT_2X_2 rare earth compounds, (R is a rare earth, T is transition metal and X is Si or Ge) in the diamond anvil cell up to a pressure of 10 GPa. Such an experiment will help to explain if at all, it's possible to physically tune (by the application of pressure) the structural and magnetic transitions to enable them to coincide, giving rise to a giant magnetocaloric effect and change magnetic properties.

- Further study on critical concentration by doping or substitution need to be done in order to combine 2 different structure temperature transition on MnCoGe, as a typical MM′X (M, M′ = transition metal, X = Si, Ge, Sn). This compound shown the strong dependence on proper tuning for critical behaviour of the phase transition, which was due to the vacancy induced structural and magnetic transition and the field-induced martensitic transformation, acted as a guide to more interesting phenomena related to the substitution for Ge.

List of Publications

1. M. F. Md Din, J. L. Wang, S. J. Campbell, A. J. Studer, M. Avdeev, S. J. Kennedy, Q. F. Gu, R. Zeng, and S. X.Dou , "Magnetic phase transitions and entropy change in layered $NdMn_{1.7}Cr_{0.3}Si_{2.}$" (***Applied Physics Letters***) **104, 042401 (2014)**

2. M. F. Md Din, J. L. Wang, A. J. Studer, Q. F Gu, R. Zeng, J. C Debnath, P. Shamba, S. J. Kennedy, and S. X. Dou "Effects of Cr substitution on structural and magnetic properties in $La_{0.7}Pr_{0.3}Fe_{11.4}Si_{1.6}$ compound" **(*Journal of Applied Physics*) 115, 17A942 (2014)**

3. M. F. Md Din, J. L. Wang, M. Avdeev, Q. F. Gu, R. Zeng, S. J. Campbell, S. J. Kennedy and S. X. Dou, "Magnetic properties and magnetocaloric effect of $NdMn_{2-x}Cu_xSi_2$ compounds" **(*Journal of Applied Physics*) 115, 17A921 (2014)**

4. M.F. Md Din, J.L. Wang, S.J. Kennedy, S.J. Campbell and S.X. Dou. "Magnetic properties and magnetocaloric effect in layered $NdMn_{1.9}Ti_{0.1}Si_2$". **(*Atom Indonesia*) 40, 1 (2014)**

5. Jiantie Xu, Shu-Lei Chou, Qin-Fen Gu, **Md-Din Muhamad**, Hua-Kun Liu and Shi-Xue Dou "Study on Vanadium Substitution to Iron in $Li_2FeP_2O_7$ as Cathode Material for Lithium-ion Batteries", **(*Electrochimica Acta*) 141, 195-202 (2014)**

6. J. L. Wang, S. J. Campbell, **M. F. Md Din**, S. J. Kennedy and M. Hofmann "Magnetic transitions and the magnetocaloric effect in the $Pr_{1-x}Y_xMn_2Ge_2$ system". **(*Phys. Status Solidi A*) 211, 1092-1100 (2014)**

7. J. L. Wang, **M. F. Md Din**, S. J. Kennedy, F. Hong, S. J. Campbell, A. J. Studer, G. H. Wu, Z. X. Cheng, and S.X. Dou "A comparative study of magnetic behaviors in $TbNi_2$, $TbMn_2$ and $TbNi_2Mn$". (***Journal of Applied Physics)*** **115, 17E135 (2014)**

8. J. L. Wang, L. Ma, M. Hofmann, M. Avdeev, S. J. Kennedy, S. J. Campbell, **M. F. Md Din**, M. Hoelzel, G. H. Wu and S. X. Dou "Neutron diffraction study of $MnNiGa_2$—Structural and magnetic behaviour". **(*Journal of Applied Physics)* 115, 17A904 (2014)**

9. M.F. Md Din, J.L. Wang1, R. Zeng, S.J. Kennedy, S.J Campbell and S.X. Dou**,** "Magnetic Properties and Magnetocaloric Effect in Layered $NdMn_{1.9}V_{0.1}Si_2$" (***EPJ Web of Conferences***) **75, 04001 (2014)**

10. J. L. Wang, L. Caron, S. J. Campbell, S. J. Kennedy, M. Hofmann, Z. X. Cheng, **M. F. Md Din**, A. J. Studer, E. Bru¨ck, and S. X. Dou "Driving Magnetostructural Transitions in Layered Intermetallic Compounds" **(*Physical Review Letters*) 110, 217211 (2013)**

11. J. L. Wang, S. J. Campbell, M. Hofmann, S. J. Kennedy, M Avdeev, **M. F. Md Din**, R. Zeng, Z. X. Cheng and S. X. Dou "Substitution of Y for Pr in $PrMn_2Ge_2$—The magnetism of $Pr_{0.8}Y_{0.2}Mn_2Ge_2$" **(*Journal of Applied Physics)* 113, 17E147 (2013)**

12. M.F. Md Din, J.L. Wang, R. Zeng, P. Shamba, J.C. Debnath and S.X. Dou "Effects of Cu substitution on structural and magnetic properties of $La_{0.7}Pr_{0.3}Fe_{11.4}Si_{1.6}$ compounds" **(*Intermetallics)* 36, 1-7 (2013)**

13. P Shamba, J LWang, J C Debnath, S J Kennedy, R Zeng, **M F Md Din**, F Hong, Z X Cheng, A J Studer and S X Dou "The magnetocaloric effect and critical behaviour of the $Mn_{0.94}Ti_{0.06}CoGe$ alloy". **(*Journal of Physics: Condensed Matter*) 25, 056001 (2013)**

14. **M F Md Din**, J L Wang, S J Campbell, R Zeng, W D Hutchison, M Avdeev, S J Kennedy and S X Dou "Magnetic properties and magnetocaloric effect of $NdMn_{2-x}Ti_xSi_2$ compounds". **(*Journal of Physics D: Applied Physics*) 46, 445002 (2013)**

15. J L Wang, S J Campbell, M Hofmann, S J Kennedy, R Zeng, **M F Md Din**, S X Dou, A Arulraj and N Stusser "Magnetism and magnetic structures of $PrMn_2Ge_{2-x}Si_x$". **(*Journal of Physics: Condensed Matter*) 25, 386003 (2013)**

16. J.L. Wanga, P. Shamba, W.D. Hutchison, **M.F. Md Din**, J.C. Debnath, M. Avdeev, R. Zeng, S.J. Kennedy, S.J. Campbell and S.X. Dou "Ti substitution for Mn in MnCoGe – The magnetism of $Mn_{0.9}Ti_{0.1}CoGe$". **(*Journal of Alloy and Compound)* 577, 475-479 (2014)**

17. **M. F. Md Din**, J. L. Wang, R. Zeng, P. Shamba, W.D Hutchison, M. Avdeev, S.J. Kennedy, S.J Campbell and S. X. Dou "Magnetic and Structural Properties of Intermetallic $NdMn_{2-x}Ti_xSi_2$ Compounds". **(*Conference Proceeding)* Australian Institute of Physics Congress, Sydney, Australia, 9-13 December 2012.**

18. **M. F. Md Din**, J. L. Wang, Z. X. Cheng, S. X. Dou, S. J. Kennedy and S. J. Campbell "Tuneable Magnetic Phase Transitions in Layered $CeMn_2Ge_{2-x}Si_x$ Compounds" **(*Scientific Report*) (Accepted)**

19. J.L. Wang, **M.F. Md Din**, S.J. Campbell, S.J. Kennedy, F.M. Yang, G.H. Wu and S.X. Dou "^{57}Fe Mössbauer and Magnetic studies of $Nd_3Fe_{24.5}Cr_{4.5}$".**(*Hyperfine Interactions*)**

Hyperfine Interactions 231, 65–74 (2015)

20. J.L. Wang, P. Shamba, W.D. Hutchison, Q.F. Gu, **M.F. Md Din**, Q.Y. Ren, Z.X. Cheng, S.J. Kennedy, S.J. Campbell and S.X. Dou "Magnetocaloric effect and magnetostructural coupling in $Mn_{0.92}Fe_{0.08}CoGe$ compounds" **(*Journal of Applied Physics*) 117**, 17D103 (2015)

21. J.L. Wang, **M.F. Md Din,** S.J. Kennedy, Z.X. Cheng, S.J. Campbell, J. Kimpton and S.X. Dou "Anomalies in magnetoelastic properties of $DyFe_{11.2}Nb_{0.8}$ compound" **(*Journal of Applied Physics*) 117**, 17C109 (2015);

22. **M. F. Md Din**, J. L. Wang, S. X. Dou, S. J. Kennedy and S. J. Campbell "Magnetic Properties and Magnetocaloric Effect of $NdMn_{2-x}V_xSi_2$ Compounds" **(In preparation)**

23. **M. F. Md Din**, J. L. Wang, S. X. Dou, S. J. Kennedy and S. J. Campbell "Magnetic Properties and Structure Contribution for Magneticaloric Effect of $MnCoGe1-_xAl_x$ Compounds" **(In preparation)**